Cover Page

Universiteit Leiden

The handle http://hdl.handle.net/1887/19028 holds various files of this Leiden University dissertation.

Author: Heinle, Ingo Matthias
Title: Application of evolutionary strategies to industrial forming simulations for the identification and validation of constitutive laws
Date: 2012-05-29

Application of Evolutionary Strategies to Industrial Forming Simulations for the Identification and Validation of Constitutive Laws

Ingo Matthias Heinle

Application of Evolutionary Strategies to Industrial Forming Simulations for the Identification and Validation of Constitutive Laws

PROEFSCHRIFT

ter verkrijging van
de graad van Doctor aan de Universiteit Leiden,
op gezag van Rector Magnificus prof. mr. P.F. van der Heijden,
volgens besluit van het College voor Promoties
te verdedigen op dinsdag 29 mei 2012
klokke 15:00 uur

door
Ingo Matthias Heinle
geboren te Augsburg, Duitsland in 1975

Promotiecommissie:

Prof. dr. T.H.W. Bäck	Promotor
Prof. dr. M. Wagner (Regensburg University)	Overige leden
Prof. dr. J.N. Kok	
Prof. dr. B. Katzy	
Dr. M.T.M. Emmerich	

Application of Evolutionary Strategies to Industrial Forming Simulations for the Identification and Validation of Constitutive Laws.
Ingo Matthias Heinle.
Thesis University Leiden.
ISBN: 978-94-6191-260-2
Printed in the Netherlands.

To my parents, Öykü and Luna

Contents

1 Introduction **11**

2 Optimization **15**
2.1 Introduction . . . 15
2.1.1 Object variables . . . 15
2.1.2 Objective function . . . 16
2.1.3 Global, local minimum . . . 16
2.1.4 Multicriteria optimization . . . 16
2.1.5 Pareto optimization . . . 17
2.1.6 Scalarization . . . 20
2.2 One dimensional strategies . . . 23
2.2.1 Simultaneous optimization . . . 23
2.2.2 Sequential methods . . . 24
2.2.3 Interpolation methods . . . 25
2.3 Evolutionary algorithms . . . 27
2.4 Evolutionary strategies . . . 28
2.4.1 Selection . . . 29
2.4.2 Recombination . . . 30
2.4.3 Mutation . . . 30
2.4.4 Adaptation of endogenous strategy parameters . . . 34
2.4.5 Derandomized self adaptation . . . 38
2.4.6 Cumulative step-size adaptation . . . 40
2.4.7 Covariance matrix adaptation . . . 43
2.4.8 (1+λ)-CMA-ES . . . 46
2.5 Newton method . . . 48
2.6 Sequential quadratic programming . . . 50
2.7 Summary . . . 52

3 Production process of sheet metal parts **55**
3.1 Introduction . . . 55
3.2 The stamping operation . . . 55
3.3 Development of production processes . . . 59
3.4 Example . . . 61

3.5 Industrial production process 62

4 Steels for car bodies **63**
4.1 The crystalline structure of metals 63
4.2 The elastic behavior of metals 63
4.3 The plastic behavior of metals 63
4.4 Metallurgy of steels 65
4.5 Steelmaking 67
4.6 Steels for the automotive industry 68
4.7 Summary 69

5 Forming simulation **71**
5.1 Continuum mechanics 71
5.1.1 Introduction 71
5.1.2 Kinematics 71
5.1.3 Balance relations 73
5.1.4 Stress tensor 76
5.1.5 Initial and boundary conditions 77
5.2 Constitutive laws - stress-strain relation 78
5.2.1 Introduction 78
5.2.2 Formulation of constitutive laws 78
5.2.3 Split of the strain tensor 79
5.2.4 Infinitesimal deformations 79
5.2.5 Elasticity 80
5.2.6 Plastic incompressibility 81
5.2.7 Clausius-Duhem inequality 81
5.2.8 Elasto-plastic constitutive law 83
5.2.9 Yield loci 84
5.2.10 Strain hardening 88
5.2.11 Strain rate dependent hardening 89
5.2.12 The Bauschinger effect 89
5.3 Constitutive laws - friction 92
5.4 Failure criterion - Forming limit curve 94
5.4.1 Introduction 94
5.4.2 Prediction of localized necking 94
5.5 Finite element method 96
5.5.1 Shape functions 96
5.5.2 Continuity of shape functions 96
5.5.3 Weak form of the differential equations 98
5.5.4 The discrete differential equations 98
5.5.5 Shell elements 102
5.5.6 The explicit solution procedure 107
5.5.7 The implicit solution procedure 109
5.5.8 Discussion explicit, implicit methods 112
5.5.9 Stress update algorithm 113

5.5.10 Plane stress constraint 116
5.6 Summary 117

6 Experiments **119**
6.1 Fundamental experiments 121
6.1.1 Tensile test 121
6.1.2 Bulge test 122
6.1.3 Miyauchi test 124
6.1.4 Nakajima test 125
6.2 Complementary experiments 126
6.2.1 YLIT-Experiments 126
6.2.2 Bending experiment 128
6.2.3 Friction experiment 129
6.3 Validation experiments 130
6.3.1 U-Profile experiment 130
6.3.2 Hole extrusion experiment 132
6.3.3 Cylindrical deepening experiment 135

7 Determination of the model parameters **137**
7.1 Tensile test 138
7.2 Bulge test 141
7.3 Shear test 142
7.4 Calibration of the Barlat 2000 yield locus 143
7.4.1 Objective function 144
7.4.2 Harrington desirability functions 144
7.4.3 Additive aggregation of the objectives 145
7.4.4 Termination of the optimization 146
7.4.5 Weighting of the objectives 146
7.4.6 Investigation of the calibration procedure 148
7.5 Calibration of the Barlat ´89 yield locus 153
7.6 Summary 155

8 Calibration of the constitutive laws **157**
8.1 Introduction 157
8.2 YLIT-Experiments 166
8.2.1 Barlat 2000 yield locus; A generalized parameter identification 172
8.2.2 Barlat ´89 yield locus 179
8.2.3 Discussion of the results 180
8.3 Bending experiment 182
8.4 Friction experiment 186
8.5 Discussion of the results of the sensitivity analysis 190
8.6 Determination of the unknown model parameters 190
8.7 Noise in numerical solutions 198
8.8 Discussion of the complementary experiments 199
8.8.1 YLIT-Experiments 199

8.8.2 Bending experiment . . . 201
8.8.3 Friction experiment . . . 203

9 Validation experiments 207
9.1 Introduction . . . 207
9.2 U-Profile experiment . . . 208
9.3 Cylindrical deepening experiment . . . 216
9.4 Hole extrusion experiment . . . 220
9.5 Discussion of the results . . . 224
9.6 Noise in numerical solutions . . . 224
9.7 Discussion of the experiments . . . 224
9.7.1 U-Profile experiment . . . 224
9.7.2 Cylindrical deepening experiment . . . 226
9.7.3 Hole extrusion experiment . . . 227

10 Uncertainties in the input data 229
10.1 An optimization based approach . . . 230
10.2 Treatment of the modified input data . . . 231
10.3 Investigation of the optimization algorithm . . . 232
10.4 Experiments . . . 234
10.4.1 YLIT-4-BMW . . . 234
10.4.2 Bending experiment . . . 234
10.4.3 Friction experiment . . . 234
10.4.4 U-Profile experiment . . . 235
10.4.5 Cylindrical deepening experiment . . . 235
10.4.6 Hole extrusion experiment . . . 235
10.5 Summary . . . 236

11 Summary and outlook 239
11.1 Outlook . . . 243

A Additional figures 245

B Tensor analysis 249
B.1 Symbols . . . 249
B.2 Tensors . . . 250

C Shape functions 251

D Numerical parameters LS-Dyna 252

Bibliography 252

Samenvatting 263

Chapter 1

Introduction

In the last decade, the deployment of simulation systems in the automotive industry on the basis of the finite element method (FEM) became a standard for the evaluation of sheet metal forming processes. The scope of application begins with the car development phase and ends with the engineering phase of the production process. During the product design phase, the forming simulation enables to evaluate the producibility of parts and to derive necessary part modifications as early as possible. Another application in this phase is the investigation of the springback behavior that allows identifying actions for reducing this effect, which decreases the scattering of part shape in the press shop. Furthermore, the prediction of the process forces on the basis of the FEM supports the selection of the best possible press line for each part and the computed forming history increases the quality of simulations regarding the product functionality. During the engineering phase of the production process the forming simulation is applied for optimizing its design. Possibly, the springback is compensated by deriving a tool modification from the predicted part geometry. The mentioned applications of the finite element method in the field of the production of sheet metal parts underline its economic importance. Nevertheless, the benefit of the FEM based simulation strongly depends on the accuracy of the computed prediction.

The prediction of the forming simulation is based on laws, which originate from theoretical physics. *The aim of theoretical physics is to construct mathematical models such as to enable us, from use of knowledge gathered in a few observations, to predict by logical processes the outcome in many other circumstances* [1]. Consequently, the predictive capability of FEM based simulations is mainly determined by the chosen physical theory and its numerical solution. The laws, utilized for forming simulations, can be grouped in universal and non-universal laws of nature. This thesis focuses on constitutive laws, which are material specific and therefore non-universal laws of nature. The universal laws of nature are the balance relations for mass, linear momentum, rotational momentum and energy. In this context, the term material represents the sheet metal, which is shaped

by a forming operation. For each material a specific stress-strain relation has to be identified and calibrated, which belongs to the group of the constitutive laws. Additionally, a constitutive law for modeling the frictional response between the material and the tool surface is needed. In order to follow the fundamental idea of theoretical physics, the mentioned constitutive laws, which are mathematical models, have to be calibrated on the basis of a few experiments and should be predictive for their field of application. Consequently, in this thesis, the calibration of given constitutive laws is performed by considering the minimum possible experimental data. Additional experiments are applied solely for investigating the predictive capability of the calibrated constitutive laws. The applied numerical solution of the physical laws based on the finite element method is considered to be sufficiently accurate in this thesis.

Subsequently, the term material model is used as a synonym for the stress-strain relation. In the last decades, manifold material models have been proposed for modeling the elasto-plastic material behavior of sheet metals (For example: [2], [3], [4], [5], [6], [7], [8] and [9]). Unfortunately, a general recommendation regarding the choice of the material model for a given material is not available. Generally, it is expected that the best choice of the material model depends on the considered steel grade or aluminum alloy. In order to treat all aspects concerning material modeling, which are introduced below, this thesis is limited to the investigation of the interstitial free mild steel DX54. However, it is expected that the findings of this thesis are transferable to other materials.

Microstructural models are not considered in this thesis[1]. The investigations are limited to hypo-elasto-plastic material models. Furthermore, thermodynamic effects are neglected. These stress-strain relations comprise a model for the elasticity, the yield locus and the material hardening. Regarding the yield locus models, only phenomenological ones are considered, which are not directly derived from microstructure-based models [11]. This choice is made, as these yield loci are not computationally expensive and therefore enable the solution of elasto-plastic mechanical problems for industrial applications. A major focus of this thesis is the choice of the yield locus model and its calibration. Apart from the commonly applied Hill ´48 [8] model also the Barlat ´89 [2] and the Barlat 2000 [3] yield locus are investigated. This set of yield loci represents different levels of complexity regarding the model parameters. Today, yield loci have been published, which comprise much more parameters as the Barlat 2000 model [5]. Such models are able to reflect the input data of the calibration experiments highly accurate. However, the amount of necessary calibration experiments rises, which leads to an additional cost for the model calibrations. One has to bear in mind that material model calibrations of various steel grades and aluminum alloys need to be provided for the application of the forming simulation in the engineering phase of the product and the production process. Consequently, at the moment the complexity of the Barlat 2000 or similar yield loci is assumed to be the limit, which

[1] An approach for modeling a forming process based on microstructural plasticity is given by Thieme-Marti [10].

can be treated for the mentioned application. The findings regarding the choice of the yield loci and the calibration procedure are assumed to be transferable with respect to other yield loci. Hence, only the mentioned yield loci are investigated. Additionally, the need for the consideration of the strain rate dependency of the hardening effect of the material and the Bauschinger effect are analyzed. Thereby, only simple isotropic models are applied, which can be calibrated based on tensile tests. Finally, steels can show a significant dependency of the Young's modulus with respect to the forming history [12]. This effect can affect the quality of the prediction of the elastic springback and is, therefore, analyzed too. As mentioned above, constitutive laws of forming simulations also comprise the modeling of the frictional response between the sheet metal and the tool surface. Hence, also a friction law needs to be analyzed. However the treatment of the friction model is in this context aligned to the temperature conditions, which hold for the experiments, considered in this thesis. Also the dependency of friction with respect to the contact pressure and the relative velocity between the sheet metal and the tool surface are neglected.

The objective of this thesis is threefold: Firstly, the identification of potentials regarding material models in order to maximize the benefit of the FEM simulation and, secondly, the development of an identification and validation procedure for material models. Thirdly, the investigation of the effect of the deviations between the measured data and the true values of the calibration experiments on the predictive capabilities of material models.

Authoritative for the evaluation of the accuracy of the predictions of the simulation is the press shop process. Unfortunately, the FEM cannot capture all effects influencing the production process. Examples are wear, thermodynamic effects and scattering material properties. Furthermore, the material model should be validated in advance for the application in the product and production process development, which excludes the press shop process as a source for the model identification and validation in the case a new material is introduced for the car body. Some of the non treatable effects, occurring in the press shop, are avoided, if the prediction of the simulation is investigated on the basis of experiments, performed under laboratory conditions. This implies the application of the same batch of the material for all calibration and validation experiments. It has to be mentioned that the calibration of the constitutive laws on the basis of another batch of the same material may lead to other model parameters. However, for the subsequent investigations it is assumed that a representative batch is selected for the calibration and validation of the constitutive laws. Apart from the standard calibration experiments (tensile test, bulge test, shear test), which are also referred to as fundamental experiments in this thesis, further experiments are introduced for the identification of the model parameters (complementary experiments) and the validation of the constitutive laws (validation experiments).

The parts, produced in the press shop, should not show any material failure. In order to avoid the occurrence of material failure, the design of the production process needs to be optimized. Thereby, failure criteria, which are based on the

results of the forming simulation, are deployed. These failure criteria are also considered by the validation experiments. However, the evaluations are limited to the failure mode localized necking. The failure is analyzed on the basis of an experimentally determined forming limit curve, as the applied experiments do not show a pronounced non-linear strain path.

The design and the commissioning of the experiments are parts of this thesis. However, more emphasis is given to the mathematical procedures, which are applied to reach the above mentioned objectives.

Both, the complementary and the validation experiments, introduced in this thesis, are designed for the investigation of constitutive laws and their parameters. Under ideal conditions, each experiment shows a different sensitivity with respect to the constitutive laws and the associated parameters regarding the prediction of the measured quantities. However, this desired property of the complementary and validation experiments has to be assured. Generally, it is difficult to predict all these sensitivities solely by theoretical considerations. As the identification of the model parameters depends on the chosen constitutive laws, this choice is made first. Subsequently, the sensitivities of the model parameters with respect to the deviation between the prediction of the simulation and the measured data of the experiments are investigated. Based on the determined sensitivities and the knowledge about the choice of the model parameters, leading to an accurate prediction of the measured data, allows selecting the investigated experiments for the identification and validation of the selected constitutive laws. For the determination of the desired information, an optimization problem can be formulated. The objective is to minimize the deviation between the prediction of the simulation and the measured data by searching for the best possible choice of the model parameters. A second component of this solution is the application of evolutionary strategies. As these optimization algorithms are based on statistical methods, also information regarding the sensitivity of the object variables (model parameters) is given. Another aspect for choosing evolutionary strategies is that these minimization problems are expected to be multimodal. Generally, it is indented to add only model parameters to the search space of the optimization, which cannot be determined by the fundamental experiments. These parameters will be referred to as unknown model parameters in this thesis. In this context it has to be mentioned that the procedures for evaluating the results of the fundamental experiments are not investigated in this thesis. Therefore, the quantities, derived from these experiments are assumed to be given. One should consider that this set of unknown model parameters and the above introduced distinction between complementary and validation experiments depends on the applied constitutive laws. Originating from the selected constitutive laws and the determined unknown model parameters, the validation experiments are applied for analyzing the predictive capability of the calibrated constitutive laws.

Chapter 2

Optimization

2.1 Introduction

2.1.1 Object variables

A frequently arising problem in the field of engineering is the optimization of the performance of a system. In this thesis the location of the optimum is assumed to be invariant with respect to time (static optimization). The parameters, which are modified in order to obtain the desired performance, are referred to as object variables x_i ($x_i \in \mathbb{R}$). It is convenient to assemble these variables into a vector $\mathbf{x} = [x_1, x_2, \ldots, x_n]^T$. Depending on the optimization task, the domain of the object variables may be restricted. Expression (2.1) defines the term feasible region M [13]:

$$M := \{\mathbf{x} \in \mathbb{R}^n | g_i(\mathbf{x}) \leq 0,\ \forall i \in \{1, \ldots, k\}\}. \tag{2.1}$$

k is the number of the functions g_i, which are referred to as constraints. Expression (2.2) summarizes the possible states of these functions:

$$\begin{aligned} g_i(\mathbf{x}) \leq 0 \quad &\Rightarrow \quad satisfied, \\ g_i(\mathbf{x}) = 0 \quad &\Rightarrow \quad active, \\ g_i(\mathbf{x}) < 0 \quad &\Rightarrow \quad inactive, \\ g_i(\mathbf{x}) > 0 \quad &\Rightarrow \quad violated. \end{aligned} \tag{2.2}$$

If M is identical to $\mathbb{R}^n$, the optimization problem is called unconstrained.

2.1.2 Objective function

For comparing the performance of a system under different choices of the objective variables, a measure is needed, which is termed objective function f. Depending on the problem, an appropriate objective function has to be formulated, which gives a minimum or a maximum value for the best possible performance of the system. Such an objective function enables transforming the optimization task into a search for a minimum or maximum respectively

$$\min f(\mathbf{x}), \quad \max f(\mathbf{x}), \quad \mathbf{x} \in M, \quad f : M \subseteq \mathbb{R}^n \to \mathbb{R}. \tag{2.3}$$

2.1.3 Global, local minimum

The term global minimum of an objective function is defined by [13]

$$\begin{aligned} \forall \mathbf{x} \in M : f(\mathbf{x}^*) \leq f(\mathbf{x}), \\ M \neq \emptyset, \mathbf{x}^* \in M, \\ f(\mathbf{x}^*) > -\infty. \end{aligned} \tag{2.4}$$

M, as introduced above, is the feasible region and $\mathbf{x}^*$ the global minimum. The problem of finding such a global minimum is termed global optimization problem. Any maximization problem can be transformed into a minimization problem, since the identity

$$\max \{f(\mathbf{x}) | \mathbf{x} \in M\} = -\min \{-f(\mathbf{x}) | \mathbf{x} \in M\} \tag{2.5}$$

holds [13]. Hence, without loss of generality only minimization problems are considered in this chapter. A local minimum $\hat{f}(\hat{\mathbf{x}})$ is defined as

$$\exists \epsilon \in \mathbb{R}, \ \epsilon > 0 : \forall \mathbf{x} \in M : \|\mathbf{x} - \hat{\mathbf{x}}\| < \epsilon \Rightarrow \hat{f} \leq f(\mathbf{x}). \tag{2.6}$$

2.1.4 Multicriteria optimization

Optimization problems can comprise multiple objectives. Equation (2.7) shows a minimization problem consisting of q objectives:

$$\min \mathbf{f}(\mathbf{x}) = \begin{bmatrix} \min f_1(\mathbf{x}) \\ \min f_2(\mathbf{x}) \\ \vdots \\ \min f_q(\mathbf{x}) \end{bmatrix} \mathbf{x} \in M \quad \mathbf{f} : M \subseteq \mathbb{R}^n \to \mathbb{R}^q. \tag{2.7}$$

The vector $\mathbf{f}$ combines the values of the objectives f_i with respect to the solution $\mathbf{x}$. If $\mathbf{x}^*$ is the minimum of each f_i, the solution is referred to as ideal.

Provided that conflicts between the objectives f_i exist (2.8), a unique solution cannot be determined:

$$\min f_i(\mathbf{x}) \rightarrow \mathbf{x}_i^*,\ \min f_j(\mathbf{x}) \rightarrow \mathbf{x}_j^*\ \wedge \mathbf{x}_j^* \neq \mathbf{x}_i^*. \tag{2.8}$$

In this section, an extract of the methods will be introduced for dealing with multi-objective optimization problems.

2.1.5 Pareto optimization

An approach for treating multi-objective problems is the Pareto optimization. A solution $\mathbf{x}'$ dominates a solution $\mathbf{x}''$ if expression (2.9) applies [14]:

$$\begin{aligned} \mathbf{x}' \prec \mathbf{x}'' \Leftrightarrow: \qquad \forall\, i \quad &\in \quad \{1,\ldots,q\}: \quad f_i(\mathbf{x}') \leq f_i(\mathbf{x}'') \\ \wedge \exists\, j \quad &\in \quad \{1,\ldots,q\}: \quad f_j(\mathbf{x}') < f_j(\mathbf{x}'')\,. \end{aligned} \tag{2.9}$$

This definition, which is referred to as the principle of Pareto-Dominance, compares two solutions $\mathbf{x}'$ and $\mathbf{x}''$ in consideration of each objective of the vector $\mathbf{f}$. Consequently, a solution $\mathbf{x}'$ is referred to as non-dominated, if no $\mathbf{x}''$ exists, which dominates $\mathbf{x}'$. The set of non-dominated solutions are termed either Pareto-Set PS (2.10) or efficient set [14]:

$$PS = \{\mathbf{x}' \in M |\ \nexists \quad \mathbf{x}'' \in M:\ \mathbf{x}'' \prec \mathbf{x}'\}\,. \tag{2.10}$$

This set contains the best solutions of the multi-objective optimization problem. The term Pareto-Front is defined as the mapping of the Pareto-Set into the objective function space. In this thesis, the treatment of constraints in association with the Pareto optimization is omitted. Figure 2.1 illustrates five solutions in the objective function space of a minimization problem consisting of two objectives. Both components of the vectors $f(\mathbf{x}_1)$ and $f(\mathbf{x}_2)$ are superior to the associated values of $f(\mathbf{x}_3)$, $f(\mathbf{x}_4)$ and $f(\mathbf{x}_5)$. In other words, the solutions $\mathbf{x}_1$ and $\mathbf{x}_2$ are non-dominated by $\mathbf{x}_3$, $\mathbf{x}_4$ and $\mathbf{x}_5$. The solutions $\mathbf{x}_1$ and $\mathbf{x}_2$ are incomparable; as neither $\mathbf{x}_1$ dominates $\mathbf{x}_2$ nor $\mathbf{x}_2$ dominates $\mathbf{x}_1$.

For the determination of the Pareto-Front diverse solutions have to be identified, which differ sufficiently from each other. As each of these solutions is a compromise, finally one has to make a choice on the basis of additional, a posteriori defined, experience based preferences, which are difficult to formulate as an objective function. A procedure for finding a Pareto-Front is the weighted Tchebycheff method. First of all, for each objective f_i, a single-objective optimization is performed

$$f_i^* = \min_{\mathbf{x} \in M}\ f_i(\mathbf{x})\,. \tag{2.11}$$

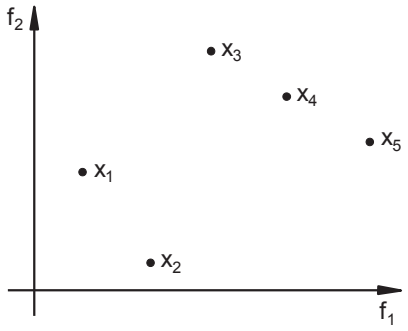

Figure 2.1: Example of non-dominated and dominated solutions.

As a next step, several vectors $\mathbf{w}$ are chosen and for each vector the optimization, defined by expression (2.12), is performed:

$$\sum \omega_i = 1, \min_{\mathbf{x}\in M} \max_{i=1,\ldots,q} \omega_i \left| f_i(\mathbf{x}) - f_i^* \right|. \tag{2.12}$$

The Tchebycheff method minimizes the maximum deviation between each objective f_i and the related result of the single-objective optimization f_i^*. Expression (2.12) aggregates the results of the multiple objectives to a scalar value. Each of these optimizations gives a point of the Pareto-Front [15]. The Tchebycheff method allows to compute all points on the Pareto-Front by changing the weights ω_i [16]. A downside of this method is the computational cost for determining the Pareto-Front. First of all, q single-objective optimizations are necessary in order to identify all f_i^*. Moreover for each point on the Pareto-Front an additional single-objective optimization has to be performed.

Evolutionary algorithms, which are introduced in chapter 2.3, are especially suitable for the determination of a Pareto-Set. This type of optimization algorithm deals simultaneously with different solutions. Hence, in combination with some extensions, Evolutionary Algorithms are able to identify a Pareto-Set within a single run. As an example the fundamental idea of the Strength Pareto Evolutionary Algorithm 2 (SPEA2), which was published by Zitzler in 2001, is given in this section [17]. Further algorithms can be found in [18] and [19]. The applied Evolutionary Algorithm is complemented by an archive P, which includes a prescribed number of $\bar{N}$ solutions, containing the so far detected promising solutions. At the beginning of the optimization, the archive is an empty set and t is equal to 0. Subsequently, the optimization step $t+1$ is discussed. A raw fitness value, as defined by

$$R(i) = \sum_{j\in P_t \cup \overline{P_t}, j \prec i} S(j),\ S(i) = \left| \left\{ j | j \in P_t \cup \overline{P_t} \wedge i \prec j \right\} \right|, \tag{2.13}$$

is assigned for each solution of the current population P_t and the members

of the archive $\bar{P}_t$. In this section, $|A|$ gives the number of the elements of a set A. A high value of the raw fitness $R(i)$ indicates that the associated solution is dominated by many other ones. If the raw fitness $R(i)$ is equal to 0.0, the solution is non-dominated. For maximizing the diversity of the generated solutions, a density is introduced, which is assigned to each solution. Mathematically, the density is defined as given by

$$D\left(i\right) = \frac{1}{\sigma_i^k + 2}. \tag{2.14}$$

The formulation of (2.14) implies that $D(i) < 1$. For the determination of σ_i^k, the distance in the objective function space of the solution i to all the solutions of the population and the archive is computed and sorted in an increasing order. σ_i^k denotes the distance of the solution i to its k-th nearest neighbor. Zitzler recommends choosing k as given by

$$k = \sqrt{N + \overline{N}} \tag{2.15}$$

(N: Population size; $\overline{N}$: Archive size). Consequently, an accumulation of solutions in a region of the Pareto-Front is identified by high values of the associated density. In SPEA2, both, the raw fitness and the density are additively combined to a scalar fitness value

$$F\left(i\right) = R\left(i\right) + D\left(i\right). \tag{2.16}$$

Equation (2.17) illustrates the update of the archive:

$$\overline{P}_{t+1} = \left\{ i | i \in P_t \cup \overline{P_t} \wedge F\left(i\right) < 1 \right\}. \tag{2.17}$$

According to (2.17) all non-dominated solutions are transferred to the archive. If the number of known non-dominated solutions is smaller than the prescribed archive size, dominated solutions are copied to the archive. In this case, these dominated solutions are taken, implying the best fitness values (2.16). If the number of non-dominated solutions exceeds the archive size, solutions are iteratively sorted out. Thereby, a solution i is discarded, if $i \leq_d j$ for all j of $\bar{P}_{t+1}$:

$$\begin{aligned} i \leq_d j \Leftrightarrow \quad & \forall \quad 0 < k < \left|\overline{P}_{t+1}\right| \; : \; \sigma_i^k = \sigma_j^k \vee \\ & \exists \quad 0 < k < \left|\overline{P}_{t+1}\right| \; : \; \left[\left(\forall\, 0 < l < k \; : \; \sigma_i^l = \sigma_j^l\right) \wedge \sigma_i^k < \sigma_j^k\right]. \end{aligned} \tag{2.18}$$

Alternatively stated, the solution, which is located closest to another solution, is discarded from the archive. Additionally, equation (2.18) considers the distance to the second closest solution and so forth. The selection within the EA is performed on the basis of the fitness function (2.16). It has to be mentioned that additional modifications with respect to the EA-Algorithm are necessary in order to obtain the desired search performance. For example, the strategy parameters

of an ES-Algorithm (evolutionary strategy), which will be introduced in the next chapter, should be individually adapted for each member of the population [20]. The individual adaptation of the strategy parameters is necessary, as diverse solutions are desired and the associated optimal strategy parameters may be different. If the stopping criterion for the optimization is satisfied, the set P_t contains the non-dominated solutions.

2.1.6 Scalarization

Another technique for treating multicriteria optimization problems are the scalarization methods [16]. The idea of scalarization is to transform multiple objectives to a single one by applying an aggregation of the objectives. Two of these methods are shown below.

Additive weighted aggregation

Firstly, the well known additive aggregation of the objectives is discussed. For each objective a weight w_i is introduced, which has to be defined a priori. As shown by (2.19) the weighted objectives are added in order to generate a single-objective function $F(\mathbf{x})$ [21]:

$$F(\mathbf{x}) = \sum_{i=1}^{q} \omega_i f_i(\mathbf{x}). \tag{2.19}$$

A drawback of this method is that the result of the optimization depends on the choice of the weights. Additionally, a poor performance induced by the choice of the object variables with respect to a single objective in combination with a small weight may not be reflected by the result of the objective function $F(\mathbf{x})$. Hence, for real-live problems the selection of the weights might be a difficult task.

From expression (2.20) follows, that a point, which is non-dominated with respect to (2.9) is also non-dominated with respect to (2.19) [16] ($\mathbf{x}' \prec \mathbf{x}'' \longleftrightarrow \mathbf{f}'(\mathbf{x}') \prec \mathbf{f}''(\mathbf{x}'')$):

$$\forall \mathbf{f}', \mathbf{f}'' \in \mathbb{R}^q \; : \; \mathbf{f}' \prec \mathbf{f}'' \rightarrow \sum_{i=1}^{q} f_i' < \sum_{i=1}^{q} f_i''. \tag{2.20}$$

Consequently, also the question arises, whether this type of aggregation enables to determine all points on the Pareto-Front. For introducing theorem 1, which answers this question, the definitions 1,2 and 3 are necessary.

Definition 1 *A subset $C \subseteq \mathbb{R}^q$ is called a cone, if $\alpha \boldsymbol{d} \in C$ for all $\boldsymbol{d} \in C$ and for all $\alpha \in \mathbb{R}, \alpha > 0$ [21].*

Definition 2 *A cone C in $\mathbb{R}^q$ is called convex, if $\alpha \boldsymbol{d}_1 + (1-\alpha)\boldsymbol{d}_2 \in C$ for all $\boldsymbol{d}_1, \boldsymbol{d}_2 \in C$ and for all $0 < \alpha < 1$ [21].*

Definition 3 *Given a Pareto optimization problem (Expression 2.7), then a solution* $\boldsymbol{x}$ *is called efficient in the Geoffrion sense or properly efficient, if (a) it is efficient, and (b) there exists a number* $N > 0$ *such that* $\forall i = 1, \ldots, q$ *and* $\forall \boldsymbol{x} \in M$ *satisfying* $f_i(\boldsymbol{x}) < f_i(\boldsymbol{x}^*)$*, there exists an index* j *such that* $f_j(\boldsymbol{x}^*) < f_j(\boldsymbol{x})$ *and* $\frac{f_i(\boldsymbol{x}^*) - f_i(\boldsymbol{x})}{f_j(\boldsymbol{x}) - f_j(\boldsymbol{x}^*)} \leq N$ *[16].*

Theorem 1 *Let us assume a Pareto optimization problem (Expression 2.7) with a Pareto-Front that is cone convex with respect to the positive orthant* $\left(\mathbb{R}^q_{\geq}\right)$*. Then for each properly efficient point* $\boldsymbol{x} \in M$ *there exist weights* $\omega_1 > 0, \ldots, \omega_q > 0$ *such that* $\boldsymbol{x}$ *is one of the solutions of* $\sum_{i=1}^{q} w_i f_i(\boldsymbol{x}) \rightarrow min$ *[16].*

Therefore, by variation of the weights ω_i, all points on the Pareto-Front can be obtained, if the Pareto-Front is cone convex.

Desirability functions

Another method to transform a multi-objective optimization problem into a single-objective one is to aggregate the objectives multiplicatively in combination with Harrington desirability functions. Expression (2.21) illustrates the one-sided and (2.22) the two-sided Harrington desirability function [22]:

$$d_1\left(f\left(\mathbf{x}\right), b_0, b_1\right) = e^{\left(-e^{\left(-\left(b_0 + b_1 f(x)\right)\right)}\right)}, \tag{2.21}$$

$$d_2\left(f\left(\mathbf{x}\right), U, L, n\right) = e^{\left(-\left|\frac{2f(x) - (U+L)}{U-L}\right|^n\right)}. \tag{2.22}$$

The expressions (2.21) and (2.22) map the objective function f to the interval $[0; 1]$ (figure 2.2). If the objective function is equal to the desired value, the corresponding value of the desirability function is 1.0. For a non-satisfying result of the objective function f, the desirability function gives values close to 0.0. The mapping according to (2.21) and (2.22) implies a gray-zone, which is determined by the parameters n, U, L, b_0 and b_1. The gray-zone enables the user to weight deviations of the objective function from the desired value.

This approach is especially suitable, if the corresponding values f of the optimum and the non-acceptable values of f are a priori known. Figure 2.3 shows three different choices of the parameter n. According to the example, deviations from the optimum are stronger penalized, if n is chosen to be small.

Nevertheless, the choice of the exponent is arbitrary and has to be performed based on experience. Additionally, the desirability function can be applied to model constraints. A violation of the constraint corresponds to a value close to 0.0. If the constraint is fulfilled, the desirability function is equal to 1.0. Finally, the objectives and the constraints can be multiplicatively aggregated

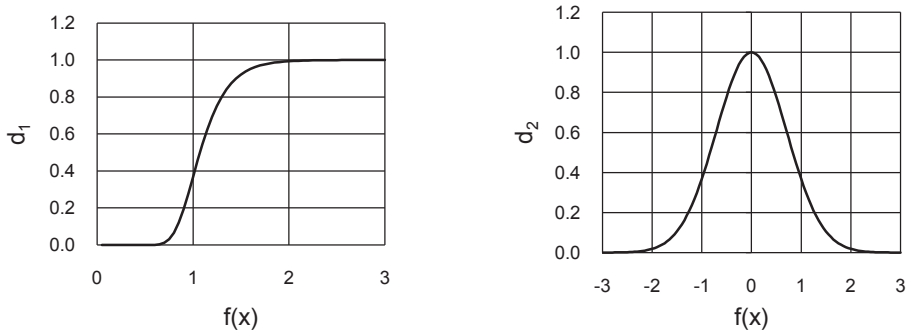

Figure 2.2: Left: Visualization of a one-sided Harrington desirability function; Right: Visualization of a two-sided Harrington desirability function.

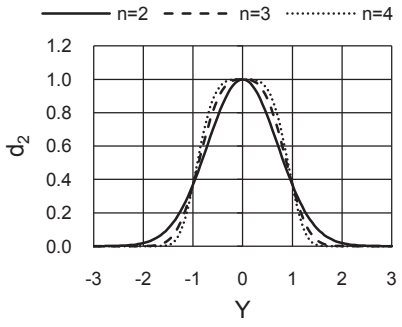

Figure 2.3: Effect of n on the shape of the two-sided Harrington desirability function.

$$d_A(x) = \prod_{i=1}^{r} d_1\left(f_i\left(\mathbf{x}\right), b_{0i}, b_{1i}\right) \prod_{j=1}^{s} d_2\left(f_j\left(\mathbf{x}\right), U_j, L_j, n_j\right) \prod_{k=1}^{t} d_1\left(g_k\left(\mathbf{x}\right), b_{0k}, b_{1k}\right) \prod_{l=1}^{u} d_2\left(g_l\left(\mathbf{x}\right), U_l, L_l, n_l\right). \tag{2.23}$$

This type of aggregation gives pessimistic results, as shown by

$$d_A(x) \leq \min_{i=1,...,r;j=1,...,s;k=1,...,t;l=1,...,u} (d_1\left(f_i\left(\mathbf{x}\right), b_{0i}, b_{1i}\right); d_2\left(f_j\left(\mathbf{x}\right), U_j, L_j, n_j\right); d_1\left(g_k\left(\mathbf{x}\right), b_{0k}, b_{1k}\right); d_2\left(g_l\left(\mathbf{x}\right), U_l, L_l, n_l\right)). \tag{2.24}$$

Expression (2.25) shows the transformation of (2.23) into a minimization problem:

$$F\left(\mathbf{x}\right) = 1 - d_A(x). \tag{2.25}$$

A similar type of desirability functions can be found in [23].

2.2 One dimensional strategies

The discussion of one dimensional strategies is limited to functions $f(x) : \mathbb{R} \to \mathbb{R}$, which are unimodal in $x \in [a, b] \subseteq \mathbb{R}$, and the desired minimum is located within this interval.

2.2.1 Simultaneous optimization

A possible solution is to create a set of points $P = \{x_i \in [a; b]\}, i \in \{1, ..., n\}$ and to compute the corresponding objective function values $f(x_i)$. The point $\overline{x} = \min_{x_i \in P} \left(f\left(x_i\right)\right)$ is assumed to be the minimum of $f(x)$. It can be theoretically shown that an equidistant distribution of the search points is the best choice [24]. The interval of uncertainty regarding the true minimum x^* is defined by $x^* \in [c; d] \subseteq [a; b]$. For a given number n of uniformly distributed points, the size of the interval of uncertainty is given by expression

$$u_n = \frac{2(b-a)}{n+1} < \epsilon \tag{2.26}$$

[24]. Thereby, n refers to the amount of points inside of the interval $]\,a;b\,[$. Expression (2.27) shows the determination of the equidistant distributed points x_i, needed for seeking the optimum:

$$x_i = a + \left(\frac{b-a}{n+1}\right) i,\ i = 1, ..., n. \tag{2.27}$$

The interval of uncertainty is given with respect to smallest computed objective function value by $\left[\overline{x} - \frac{u_n}{2}; \overline{x} + \frac{u_n}{2}\right]$. An estimation of an appropriate choice of n for a given accuracy ϵ is shown by expression

$$\frac{2(b-a)}{\epsilon} - 1 < n. \tag{2.28}$$

An advantage of this method is the possibility of computing the objective function values simultaneously. However, depending on the needed accuracy ϵ the method can be computationally expensive. In order to reduce the needed amount of objective function evaluations, it is advantageous to adapt the search according to the information, available during the optimization, regarding the location of the optimum. Therefore, sequential methods are introduced subsequently, which possess this property.

2.2.2 Sequential methods

The above shown equidistant minimum search method can be applied multiple times. Each time the search is repeated, the original interval is reduced by a factor α. Consequently, after k repetitions, the interval shrinks by the factor α^k. The factor α depends on the amount of objective function evaluations per repetition $\alpha = \frac{2}{n+1}$. It is more advantageous to reduce n and to perform more repetitions than vice versa [24], as the shrinking of the investigated interval depends exponentially on k. The minimum number of objective function evaluations per step (repetition) is $n = 2$. As the reduced interval is defined by the lowest objective function value $\overline{x}^{(k)}$ with respect to the actual step k and both neighbor points, the value of n cannot be smaller than $n = 2$. If n is chosen to be equal to three, only in the first step three computations of the objective function are necessary. For the following steps, $f(x)$ needs to be evaluated only two times, as one of the points $x_i^{(k)}$ is coincident with a point $x_i^{(k-1)}$ of the previous step.

By giving up the constraint of using equidistant points, it is possible to enforce on the basis of two points ($n = 2$) that each step comprises a point of the previous one. Consequently, only one evaluation of the objective function is needed for each step, which leads to a better performance compared with the equidistant interval division methods.

Figure 2.4, taken from [25], shows the interval division for the steps $k-1$ and k. τ defines the relative position of the points $x_1^{(k)}, x_2^{(k)}$ with respect to the interval $\left[a^{(k)}; b^{(k)}\right]$. The equation (2.29), which leads to coincident points between the steps, can be directly derived from this figure:

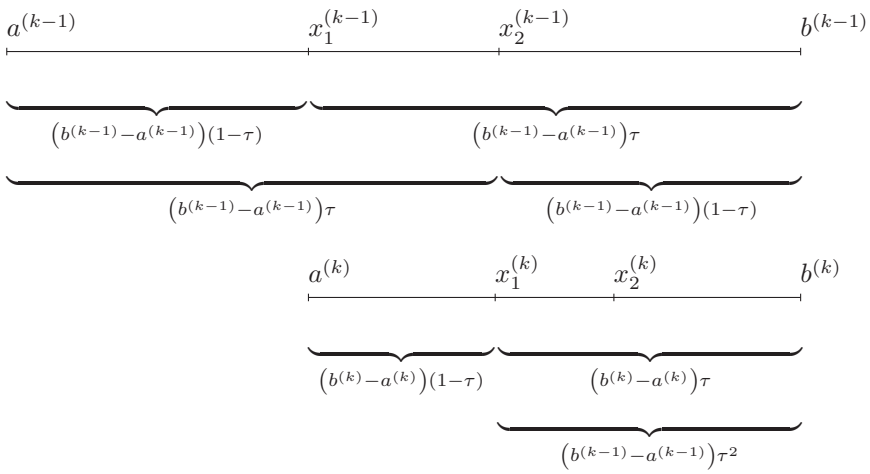

Figure 2.4: Derivation of τ for the golden section interval division.

$$\tau^2 = (1 - \tau). \tag{2.29}$$

The positive root of (2.29) is $\tau = \frac{\sqrt{5}-1}{2} \approx 0.618$. Consequently, using this value of τ leads to an interval division, which comprises only one evaluation of $f(x)$ per step. This procedure is referred to as golden section interval division.

2.2.3 Interpolation methods

Newton method

A root of the function $f(x)$ can be computed by applying the Newton method, provided the function is differentiable. The method estimates the root starting from a linearization of $f(x)$ at $x^{(k)}$. The root of the linear function $x^{(k+1)}$ is taken as an improved value for a further iteration. Expression (2.30) summarizes both steps and gives $x^{(k+1)}$:

$$x^{(k+1)} = x^{(k)} - f(x^{(k)}) \left[\left. \frac{df(x)}{dx} \right|_{x=x^{(k)}} \right]^{-1}. \tag{2.30}$$

If the function $f(x)$ is linear, the Newton method gives the exact solution within one iteration.

Regula Falsi iteration

Expression (2.31) illustrates an approximation of the derivative at the point $x^{(k)}$ [26]:

$$\left.\frac{df(x)}{dx}\right|_{x=x^{(k)}} \approx \frac{f(x^{(k)}) - f(x^{(m)})}{x^{(k)} - x^{(m)}} \ , \ m < k. \tag{2.31}$$

An exchange of the derivative of (2.30) by expression (2.31) leads to the Regula Falsi iteration

$$x^{(k+1)} = x^{(k)} - f(x^{(k)}) \left[\frac{f(x^{(k)}) - f(x^{(m)})}{x^{(k)} - x^{(m)}}\right]^{-1}. \tag{2.32}$$

A root of a continuous function $f(x)$ within the interval $[a; b]$ exists, if $f(a)$ and $f(b)$ are of opposite sign. Therefore, the sign of the corresponding function values of the initial values $x^{(0)}$ and $x^{(1)}$ has to be different.

Provided $f(x)$ is linear, expression (2.31) gives the exact derivative and therefore also (2.32) leads to the exact solution by one iteration. For a stable convergence of the Regula Falsi iteration, $f(x^{(k)})$ and $f(x^{(m)})$ have to be of opposite sign [26], which is achieved by selecting an appropriate value of m.

Lagrangian interpolation

Finally, the Lagrangian interpolation is introduced. For searching a minimum, the function $f(x)$ is interpolated by a pth order polynomial, which is fitted on the basis of $p + 1$ evaluations of $f(x)$. The optimum is derived from the stationary point of the interpolated polynomial. Expression (2.33) shows the computation of the stationary point of a second order polynomial [24]:

$$\begin{aligned}
A^{(k)} &= \left[\left(b^{(k)}\right)^2 - \left(c^{(k)}\right)^2\right] f\left(a^{(k)}\right) \\
B^{(k)} &= \left[\left(c^{(k)}\right)^2 - \left(a^{(k)}\right)^2\right] f\left(b^{(k)}\right) \\
C^{(k)} &= \left[\left(a^{(k)}\right)^2 - \left(b^{(k)}\right)^2\right] f\left(c^{(k)}\right) \\
d^{(k)} &= \frac{1}{2} \frac{A^{(k)} + B^{(k)} + C^{(k)}}{\left[b^{(k)} - c^{(k)}\right] f\left(a^{(k)}\right) + \left[c^{(k)} - a^{(k)}\right] f\left(b^{(k)}\right) + \left[a^{(k)} - b^{(k)}\right] f\left(c^{(k)}\right)}.
\end{aligned} \tag{2.33}$$

The stationary value is a minimum, if the denominator is positive. In order to improve the computed minimum, the procedure can be repeated. It is recommended to choose the initial value $b^{(0)}$ in the middle of the interval $\left[a^{(0)}; c^{(0)}\right]$ [24]. Each further iteration needs only one additional objective function evaluation, as

shown by table 2.1. If the function $f(x)$ is a quadratic function, the Lagrange interpolation gives the exact minimum within one iteration.

Table 2.1: Recursion algorithm for the Lagrange interpolation.

$if\ a^{(k)} < d^{(k)} < b^{(k)} \wedge f(d^{(k)}) < f(b^{(k)})$	$\begin{cases} a^{(k+1)} = a^{(k)} \\ b^{(k+1)} = d^{(k)} \\ c^{(k+1)} = b^{(k)} \end{cases}$
$if\ a^{(k)} < d^{(k)} < b^{(k)} \wedge f(d^{(k)}) > f(b^{(k)})$	$\begin{cases} a^{(k+1)} = d^{(k)} \\ b^{(k+1)} = b^{(k)} \\ c^{(k+1)} = c^{(k)} \end{cases}$
$if\ b^{(k)} < d^{(k)} < c^{(k)} \wedge f(d^{(k)}) < f(b^{(k)})$	$\begin{cases} a^{(k+1)} = b^{(k)} \\ b^{(k+1)} = d^{(k)} \\ c^{(k+1)} = c^{(k)} \end{cases}$
$if\ b^{(k)} < d^{(k)} < c^{(k)} \wedge f(d^{(k)}) > f(b^{(k)})$	$\begin{cases} a^{(k+1)} = a^{(k)} \\ b^{(k+1)} = b^{(k)} \\ c^{(k+1)} = d^{(k)} \end{cases}$

2.3 Evolutionary algorithms

Evolutionary algorithms are methods, inspired by the natural evolution, for solving optimization problems. According to the Darwinian theory of evolution, the adaptive change of species is explained by the principle of natural selection. Species are favored, which are best adapted to their environmental conditions. Furthermore, Darwin recognized that offspring are subject to mutation, in which the occurrence of small, apparently random and undirected variations of the genetic material occurs. The copying process of the genetic information between the parents and the offspring works highly accurately, however not perfect [13]. These slight imperfections are equivalent to the mutation. The fitness in the sense of evolution of an individual is measured indirectly by its ability to survive and to reproduce in its environment. Mutation enables genetic changes, which optimize in combination with selection the fitness. In nature, selection is based on the fitness of the individual. The fitter the individual, the higher is the chance to bring its genetic information to the next generation ("survival of the fittest"). The objective of natural evolution is to find continuously an appropriate adaption of the species with respect to the environmental conditions. In literature, recombination, which describes the combination of the parental genetic material, is not

considered as an essential contribution to the evolution, because this process does not induce any new information.

As mentioned above, evolutionary algorithms (EA), which are applied for optimizing fitness functions, imitate natural evolution. In the field of evolutionary algorithms, the term fitness function is usually applied, which is equivalent to the above introduced objective function. For the solution of the numerical optimization problem, the objective function is interpreted as a so-called adaptive landscape in the context of evolutionary algorithms [13]. During the optimization, the development of the initial population subject to genetic operators (selection, mutation and recombination) is simulated. In contrast to natural evolution, the fitness of individuals can be directly quantified. The objective is to find a choice of the object variables, which minimizes the fitness function. The term evolutionary algorithm summarizes three main streams of algorithms. The origins of two of them are in the United States of America. Holland (1965; 1975) has developed the genetic algorithms (GA) and Fogel (1962; 1966) published another variant of EA called evolutionary programming (EP). Finally, evolutionary strategies (ES) were developed by students at the Technical University of Berlin (Rechenberg, 1965; 1971; Schwefel, 1965, 1975) [27]. Subsequently, only evolutionary strategies are discussed, because these are the most powerful variants of evolutionary algorithms for real-valued and mixed-integer variables.

2.4 Evolutionary strategies

Typically, evolutionary strategies (ES) are applied for optimizations of non-linear fitness functions. During the optimization procedure, trial choices of the object variables, called individuals, are created. The set of individuals is referred to as a population. The term generation is introduced for distinguishing between different populations. Usually, the initial population is generated randomly. As a next step, the fitness of the individuals of the first population is computed. In order to obtain a progress, only the best individuals with respect to the fitness are selected for creating the subsequent population. The optimization enters at this state into a loop. The termination condition of this loop is either a resource (maximum number of generations, maximum CPU time) or a convergence (in the space of fitness values, object variables, strategy parameters) criterion. The offspring of the selected individuals is generated by recombination and mutation operators. The first mentioned operator combines the parental genetic information. The mutation operator generates, on the basis of the result of recombination, stochastic variations, which have to comply with the boundary conditions of the optimization problem. The occurrence of small mutations should be more likely. This operator introduces alterations regarding the object variables into the optimization process, which is essential for finding an optimum. Again, the fitness of the members of the new generation is evaluated and only those individuals are selected, which show promising properties. The loop is repeated until the termination condition is fulfilled. Figure 2.5 summarizes the general form of an evolutionary strategy.

```
1  t = 0        P : Population
2  P_t ← Init ()
3  Evaluate (P_t)
4  while (termination criterion is not fulfilled) do
5     G_t ← Generate (P_t)
6     Evaluate (G_t)
7     P_{t+1} ← Select (G_t ∪ P_t)
8     t ← t + 1
9  end while
```

Figure 2.5: A general scheme of evolutionary strategies [28].

ES do not use any information regarding the structure of the optimization problem. Only the associated fitness value of a given choice of the objective variables is needed. Hence, from the perspective of the optimizer, the fitness function acts as a black box. Because of this property, the ES belong to the zero-order optimization algorithms. A first-order optimization algorithm also takes the first derivative of objective function into account and a second-order one the second derivative respectively.

The evaluation of the fitness values of each individual, belonging to a population, can be performed independently. If the determination of the fitness of individuals is time consuming, this property of evolutionary strategies offers the potential to perform the evaluation of the fitness function simultaneously, i. e., to exploit parallelism.

The standard notation $(\mu/\rho+, \lambda)$-ES describes the selection strategy (plus, comma strategy), the number of parents involved in the creation of one offspring ρ, the amount of the created offspring λ and the number of parents μ. For the special case $\rho = 1$, the offspring is generated without any recombination (cloning). For the remaining cases $\rho > 1$, the offspring is procreated on the basis of more than one parent. λ, μ and ρ are referred to as exogenous parameters, as these quantities are defined in advance and are kept constant during the optimization.

2.4.1 Selection

After creating λ descendants and computing the related fitness values, the comma strategy chooses the best μ individuals of the offspring for the new generation. The plus strategy selects the best μ individuals out of the set, consisting of parents and offspring. Hence, the latter mentioned strategy enables individuals to survive several generations. Consequently, in both cases the population size remains constant. Furthermore, the presented selection schemes are strictly deterministic [29]. The comma strategy even discards good solutions, if all offspring is worse than the parents. Because of this behavior the scheme is able to overcome local minima. This property is especially for multimodal landscapes advantageous [13]. Additionally, in contrast to the plus strategy, the comma strategy is suitable for

the application to changing environments. The plus strategy preserves solutions and is therefore not able to follow a moving optimum. A drawback of the comma scheme is its convergence behavior. In the worst case, the comma strategy can even diverge, whereas the plus strategy shows only a premature stagnation [27]. Nevertheless, the comma selection mechanism is usually applied in ES [29], due to the fact that it is advantageous for the self-adaptation of the strategy parameters.

2.4.2 Recombination

Inspired by nature, the recombination combines parental genetic information for the creation of individuals. The term multirecombination is applied for the case, if more than two parents are involved in the creation of offspring $\rho > 2$ [27]. The recombination operator is only used for populations, which consist of at least two or more individuals $\mu > 1$. Generally, this operator causes in ES the creation of a single offspring. The recombination is performed on the basis of ρ parental vectors $\mathbf{a}$. The recombination is termed discrete, if each component of the resultant vector $\mathbf{r}$ is obtained by a random selection from the corresponding components of the parental vectors $\mathbf{a}$. Expression (2.34) illustrates the introduced procedure [27] (n dimension of the parameter space):

$$(r)_k := (a_{m_k})_k \,, \text{ with } m_k = \text{random}\{1, \ldots, \rho\} \,, \; k \in [1; n]. \tag{2.34}$$

Another approach is the intermediate recombination, which takes all ρ parents into account. The computation of the resultant vector $\mathbf{r}$ is performed in analogy with the center of mass

$$(r)_k := \frac{1}{\rho} \sum_{i=1}^{\rho} (a_i)_k \,. \tag{2.35}$$

2.4.3 Mutation

The selection guides the optimization into promising search space regions, whereas mutation is needed for exploring the search space. Generally, the variation of the parental state should not depend on any fitness information. The performance of the mutation operator depends on the optimization problem. A general method for designing such an operator has not been established yet. Subsequently, the recommendations of Beyer [27] are given, which have been derived from theoretical considerations and analyses of ES-implementations.

The first principle requires the reachability of an arbitrary point in the search space, independent of the position of the parental point, within a finite number of mutations. Another principle is referred to as scalability, which formulates the need for an adaptation of the mutation operator with respect to the properties of the fitness landscape. Finally, the variation of the parental state should not introduce any bias (principle of unbiasedness). A violation of the presented design

principles does not necessarily indicate that the considered operator will generally fail.

A search space can consist of combinations of real-valued, integer-valued or binary object variables. Subsequently, a pure real-valued search space is assumed. A discussion of the remaining types of object variables is omitted in this work. A comprehensive introduction regarding the treatment of these types of variables can be found in [30]. Commonly, the standard normal distribution plays a crucial role in formulating mutation operators

$$\mathrm{N}\left(\mu, \sigma^2\right) = \frac{1}{\left(2\pi\sigma^2\right)^{\frac{1}{2}}} \exp\left(-\frac{1}{2\sigma^2}\left(x-\mu\right)^2\right). \tag{2.36}$$

The offspring $\mathbf{x}^{(g+1)}$ is created by adding a mutation to a parent $\mathbf{x}^{(g)}$

$$\mathbf{x}^{(g+1)} = \mathbf{x}^{(g)} + \mathbf{z}. \tag{2.37}$$

Equation (2.38) shows a possible mutation operator, consisting of standard normal distributions (2.36) for each dimension

$$\mathbf{z} \sim \sigma\left(\mathrm{N}_1\left(0,1\right), \mathrm{N}_2\left(0,1\right), \ldots, \mathrm{N}_n\left(0,1\right)\right)^T. \tag{2.38}$$

The symbol $\sim$ denotes the equality in distribution. According to the scalability principle, the parameter σ enables the adaptation of (2.38) with respect to the fitness landscape. Strategy parameters, like σ, which are continuously changed during the optimization, are referred to as endogenous. Procedures for adapting the endogenous parameters are shown in the next section.

Each component of the random vector $\mathbf{z}$ (2.38) is drawn independently from the normal distribution with a zero mean and a variance of one. In this case, the surfaces of equal probability density are concentric spheres in the search space (figure 2.6 (left)). The midpoint of these spheres coincides with the parental state $\mathbf{x}^{(g)}$. Expression (2.38) is also termed isotropic mutation operator. For a n-dimensional vector $\mathbf{x}$, the multivariate Gaussian distribution takes the form

$$\mathrm{N}\left(\mathbf{m}, \mathbf{C}\right) = \frac{1}{\left(2\pi\right)^{\frac{n}{2}}} \frac{1}{\left|\mathbf{C}\right|^{\frac{1}{2}}} \exp\left(-\frac{1}{2}\left(\mathbf{x}-\mathbf{m}\right)^T \mathbf{C}^{-1}\left(\mathbf{x}-\mathbf{m}\right)\right). \tag{2.39}$$

The eigenvalues of the covariance matrix $\mathbf{C}$ must be strictly positive, otherwise the distribution cannot be normalized properly [31]. A covariance matrix, implying this property, is said to be positive definite. Additionally, the covariance matrix has to be symmetric [32]. Therefore, surfaces of constant densities are hyper ellipsoids, which are aligned along the principal axes of the covariance matrix. The center of these hyper ellipsoids is coincident with $\mathbf{m}$. As the eigenvectors, obtained from solving the standard eigenvalue problem of a symmetric matrix, are orthogonal [26], the principal axes system of the covariance matrix $\mathbf{C}$ is also orthogonal. Generally, the covariance matrix $\mathbf{C}$ can be decomposed into a diagonal matrix $\mathbf{D}^2$, containing the eigenvalues, and an orthogonal matrix $\mathbf{B}$:

$$\begin{aligned} \mathbf{C} &= \mathbf{B}\mathbf{D}^2\mathbf{B}^T,\ \mathbf{B}\mathbf{B}^T = \mathbf{I}, \\ \mathbf{D}^2 &= diag\left(d_1, d_2, \ldots, d_n\right)^2 = diag\left(d_1^2, d_2^2, \ldots, d_n^2\right). \end{aligned} \tag{2.40}$$

The expressions (2.40) are only valid for a positive definite and symmetric matrix. The matrix $\mathbf{D}$, containing n independent components, scales the spherical distribution with respect to the principal axes, whereas the matrix $\mathbf{B}$ defines the rotation between the coordinate system of the search space and the principal axes. The latter mentioned matrix implies n(n-1)/2 degrees of freedom [33]. For generating a Gaussian normal distributed random vector $\mathrm{N}\left(\mathbf{m}, \mathbf{C}\right)$, the following expression can be applied

$$\mathrm{N}\left(\mathbf{m}, \mathbf{C}\right) \sim \mathbf{m} + \mathbf{B}\mathbf{D}\mathrm{N}\left(\mathbf{0}, \mathbf{I}\right). \tag{2.41}$$

According to (2.41), the desired random vector can be obtained by realizing $(0, 1)$-normally distributed numbers, which can be easily realized on a computer. Expression (2.42) shows the relation between the distribution of the vector $\mathbf{z}$ and the distribution of its components z_i

$$p\left(\mathbf{z}\right) = \prod_{i=1}^{n} p_i\left(z_i\right). \tag{2.42}$$

On the basis of (2.38) and (2.39) an alternative formulation of (2.38) can be derived:

$$\mathbf{z} \sim \mathrm{N}\left(\mathbf{0}, \mathbf{C}_1\left(\sigma\right)\right),\ \mathbf{C}_1\left(\sigma\right) = \sigma^2\mathbf{I}, \tag{2.43}$$

$$\mathbf{D}_1^2 = \mathbf{C}_1,\ \mathbf{B} = \mathbf{I}. \tag{2.44}$$

Expression (2.45) illustrates an extended version of (2.38), which introduces for each dimension an endogenous parameter σ_i:

$$\mathbf{z} \sim \left(\sigma_1\mathrm{N}_1\left(0, 1\right), \sigma_2\mathrm{N}_2\left(0, 1\right), \ldots, \sigma_n\mathrm{N}_n\left(0, 1\right)\right)^T. \tag{2.45}$$

As a consequence, the surfaces of equal probability density are in this case ellipsoidal. This approach enables a better adaption of the mutation operator with respect to the fitness landscape. Provided, the endogenous strategy parameters σ_i are well determined, the probability density reflects promising directions. Hence, the likelihood of generating successful mutations is higher, than it would be if an isotropic mutation operator were applied. Expression (2.46) shows an alternative form of (2.45):

$$\mathbf{z} \sim \mathrm{N}\left(\mathbf{0}, \mathbf{C}_2\left(\sigma_i\right)\right),\ \mathbf{C}_2\left(\sigma_i\right) = \begin{pmatrix} \sigma_1^2 & 0 & 0 & \cdots & 0 \\ 0 & \sigma_2^2 & 0 & \cdots & 0 \\ 0 & 0 & \sigma_3^2 & \cdots & 0 \\ \vdots & \vdots & \vdots & \ddots & \vdots \\ 0 & 0 & 0 & \cdots & \sigma_n^2 \end{pmatrix}. \tag{2.46}$$

As $\mathbf{C}_2$ is a diagonal matrix, the eigenvectors of $\mathbf{C}_2$ are orthogonal and identical to the coordinate system of the search space. Therefore, the ellipsoidal surfaces are orientated along the axes of the search space (figure 2.6 (middle)). Expression (2.47) shows the eigendecomposition of $\mathbf{C}_2$:

$$\mathbf{D}_2^2 = \mathbf{C}_2,\ \mathbf{B} = \mathbf{I}. \tag{2.47}$$

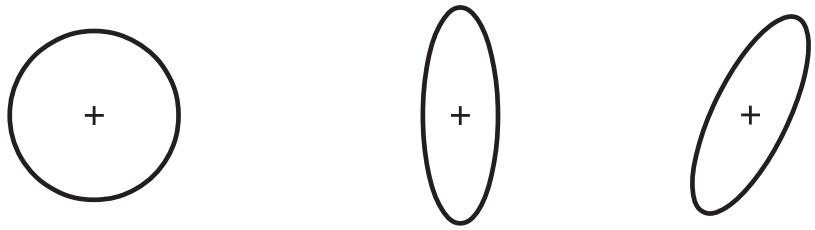

$\mathrm{N}\left(\mathbf{0}, \mathbf{C}_1(\sigma)\right)$ $\mathrm{N}\left(\mathbf{0}, \mathbf{C}_2\left(\sigma_i\right)\right)$ $\mathrm{N}\left(\mathbf{0}, \mathbf{C}_3\left(\sigma_i, \alpha_{ij}\right)\right)$

Figure 2.6: Equal density of different normal distributions.

An improved adaptation of the mutation operator with respect to the fitness landscape can be obtained by introducing orthogonal rotations of the eigenvectors (figure 2.6 (right)). This procedure assures, that the covariance matrix remains positive definite. Expression (2.48) and (2.49) define the rotation matrix $\mathbf{B}$ [13]:

$$\mathbf{B}\left(\boldsymbol{\alpha}\right) = \left(\prod_{i=1}^{n-1} \prod_{j=i+1}^{n} \mathbf{R}\left(\alpha_{ij}\right)\right), \tag{2.48}$$

$$\mathbf{R}\left(\alpha_{ij}\right) = \left(r_{kl}\right),\ r_{ii} = r_{jj} = \cos\alpha_{ij},\ r_{ij} = -r_{ji} = -\sin\alpha_{ij}. \tag{2.49}$$

The endogenous strategy parameters α_{ij} define the angles of the rotation with respect to the axes i and j. In the most general case, $n(n-1)/2$ rotation angles are applied. Consequently, all degrees of freedom of the orthogonal matrix $\mathbf{B}$ are defined by a rotation angle. The expressions (2.50) illustrate the mutation operator, which comprises a scaling of each diagonal element and a rotation:

$$\mathbf{z} \sim \mathrm{N}\left(\mathbf{0}, \mathbf{C}_3\left(\sigma_i, \alpha_{ij}\right)\right),\ \mathbf{C}_3 = \mathbf{B}\mathbf{C}_2\mathbf{B}^T,\ \mathbf{C}_3 = \mathbf{B}\mathbf{D}_2^2\mathbf{B}^T. \tag{2.50}$$

2.4.4 Adaptation of endogenous strategy parameters

The adaptation of the endogenous strategy parameter plays a crucial role in evolutionary strategies. Generally, without changing the strategy parameters a poor performance is expected [34]. On the basis of the strategy parameters, the size of mutation steps (step-size) in the search space is varied. At the beginning of this section, the original $1/5th$-rule is introduced, which is applied for the adaption of an isotropic Gaussian mutation operator (2.38) in $(1+1)$-ES. The performance of such an ES strongly depends on the choice of the mutation strength σ [27]. According to (2.38), the expected length of the mutation with respect to the search space is proportional to σ. The smaller the mutation strength σ is, the smaller the expected length of the mutation step in the search space is. The term success probability is introduced for describing the likelihood that the offspring replaces the parent. The success probability becomes approximately 50%, if the mutation strength is assumed to be very small (i. e., asymptotically approaching zero) and the fitness landscape is smooth. On the one hand, such a mutation strength leads to a remarkable evolvability. On the other hand, the expected length of the mutation steps is small and therefore the number of necessary optimization steps for finding the optimum is inacceptable high. In case the mutation strength is very large, the success probability reduces and, consequently, a progress is not obtained anymore. Thus, the success probability is very low. Again, such a selection of the mutation strength would lead to an unsatisfying search performance. The term evolutionary window, introduced by Rechenberg (1973), describes a range of mutation strengths between the discussed extreme cases, which maximize the performance of the ES. Rechenberg has performed investigations on the basis of a sphere and a corridor test problem for $n \gg 1$. For both problems the success probability, leading to an optimum regarding the ES performance ($P_{s_{Sphere}} \approx 0.27$; $P_{s_{Corridor}} \approx 0.184$), was determined. Rechenberg regarded these test problems as representative for real-world fitness functions. On the basis of these results he recommended to execute the ES under a success probability of 0.2 ($1/5th$ rule), which is a compromise between the results of the investigated test problems. The desired success probability can be obtained by adapting the mutation strength during the optimization. Figure (2.7) shows the implementation of the $1/5th$ rule. For the computation of the success probability, G generations are created by a constant mutation strength and the successful mutations G_s are counted. The obtained success probability is compared with the desired value of 0.2 and, if necessary, the step size is multiplicatively adapted. This procedure assures a positive sign of the mutation strength, as the modification is performed multiplicatively. The best possible value of the exogenous parameter depends on the fitness function, the choice of G and the dimension of the search space. Schwefel recommended using $0.85 \leq a < 1$, provided the search space consists of more than 30 dimensions and G is selected to be equal to n [27]. Finally, one has to bear in mind, that the 1/5th-rule is only suitable for the adaptation of a single strategy parameter. Additionally, this adaptation procedure is usually only applied for a $(1+1)$-ES.

1. perform the $(1+1)$ ES for a number G of generations:
   -keep σ constant during this period
   -count the number G_s of successful mutations during this period

2. determine an estimate of P_s by
   $P_s = \frac{G_s}{G}$

3. change σ according to

$$\sigma = \begin{cases} \sigma/a & \text{if} \quad P_s > 1/5 \\ \sigma a & \text{if} \quad P_s < 1/5 \\ \sigma & \text{if} \quad P_s = 1/5 \end{cases}$$

4. goto 1

Figure 2.7: Implementation of the $1/5th$ rule [27].

The self-adaptation, which is not restricted to a single strategy parameter, is another procedure for changing the endogenous parameters. For applying this method, each individual is extended by a set of strategy parameters. Both the position of the individual in the search space and the strategy parameters undergo variation. Nevertheless, the decision whether an individual becomes a parent of the next generation is only performed on the basis of the fitness value, which is determined by the object variables. It is assumed that successful individuals are an indication for a good quality of the parental strategy parameters. In other words, well adapted strategy parameters with respect to the fitness landscape should produce on average fitter individuals and therefore have a higher chance to survive. The above mentioned variation of the strategy parameters consists of recombination and mutation. An intermediate recombination is recommended for the adaptation of the strategy parameters [13]. The self-adaptation approach is suitable for all of the introduced mutation operators. First of all, the procedure for mutating the strategy parameter of an isotropic Gaussian mutation operator is shown (2.38). The space of the individuals I consists of the search space in conjunction with the space of the strategy parameter σ

$$I = \mathbb{R}^n \times \mathbb{R}. \tag{2.51}$$

The parameter σ of (2.38) has to remain positive. Thus, the mutation of σ is performed multiplicatively. In order to avoid any deterministic drift without selection, the distribution, applied for the mutation of the strategy parameter, should give 1.0 as mean value. Furthermore, the distribution should lead to a higher probability of small changes than of large ones. Finally, the probability of the occurrence of a value and its associated reciprocal value should be equal. All the mentioned requirements are fulfilled by the log-normal distribution [24]. Ex-

pression (2.52) shows the density function of the log-normal distribution $Ln(\mu, \sigma^2)$ [32]:

$$f(x) = \begin{cases} \frac{1}{\sigma\sqrt{2\pi}} \frac{1}{x} \exp[-\frac{(\ln x - \mu)^2}{2\sigma^2}] & \text{if} \quad x > 0 \\ 0 & \text{if} \quad x \leq 0 \end{cases}, \\ \mu \in \mathbb{R},\ \sigma \in \mathbb{R}^+. \tag{2.52}$$

In order to draw a $\mathrm{Ln}(\mu, \sigma^2)$ distributed random number, relation

$$x = \exp(\mu + \sigma y) \sim \mathrm{Ln}(\mu, \sigma),\ y \sim \mathrm{N}(0, 1) \tag{2.53}$$

can be applied [32]. Expression (2.53) transforms a $\mathrm{N}(0, 1)$ distributed random number y to a $\mathrm{Ln}(\mu, \sigma^2)$ distributed one. The update of the mutation strength for an isotropic Gaussian mutation operator is performed on the basis of a product, consisting of a $Ln(0, 1)$ random number and the mutation strength of the generation g

$$\sigma^{(g+1)} \sim \sigma^{(g)} \exp(\tau \mathrm{N}(0, 1)). \tag{2.54}$$

The exogenous strategy parameter τ, which is referred to as learning parameter [27], determines the rate of the self-adaptation. Schwefel (1975) and Beyer (1996) suggested choosing τ to be inversely proportional to the square root of the problem dimension

$$\tau \propto \frac{1}{\sqrt{n}}. \tag{2.55}$$

For avoiding a mutation strength σ close to zero, which would lead to negligible mutations on average, a threshold is introduced

$$\sigma < \varepsilon_0 \rightarrow \sigma = \epsilon_0. \tag{2.56}$$

If the mutation strength σ reaches a value below the threshold ϵ_0, σ is set equal to the threshold.

Now, the update procedure of the endogenous parameters for the mutation operator implying n strategy parameters is introduced. This scheme implies an extension of the space of the individuals as given by

$$I = \mathbb{R}^n \times \mathbb{R}^n. \tag{2.57}$$

Schwefel (1977) suggested the expression (2.58) for computing the vector $\sigma^{(g+1)} = (\sigma_1, \ldots, \sigma_n)^T$:

$$\sigma_i^{(g+1)} \sim \sigma_i^{(g)} \exp(\tau_0 \mathrm{N}(0, 1) + \tau \mathrm{N}_i(0, 1)). \tag{2.58}$$

Expression (2.59) shows recommended values for the learning parameters (Schwefel, 1977):

$$\tau_0 \propto \frac{1}{\sqrt{2n}},\ \tau \propto \frac{1}{\sqrt{2\sqrt{n}}}. \tag{2.59}$$

Again, as for the isotropic Gaussian mutation operator, a threshold is introduced for avoiding σ_i values close to zero. The threshold ϵ_0 is applied for each component of the vector $\boldsymbol{\sigma}$

$$\sigma_i < \epsilon_0 \rightarrow \sigma_i = \epsilon_0. \tag{2.60}$$

Finally, the strategy parameter adaptation of the most general mutation operator (2.50) is discussed. This approach consists, as mentioned above, of n σ_i values and $n(n-1)/2$ rotation angles. Expression (2.61) shows the space of the individuals:

$$I = \mathbb{R}^n \times \mathbb{R}^n \times \mathbb{R}^{n(n-1)/2}. \tag{2.61}$$

The adaption of the rotation angles differs from the σ_i values, as the desired expected change of these angles is zero. Additionally, expression (2.62) should be complied:

$$p(\alpha_i) = p(-\alpha_i). \tag{2.62}$$

These requirements are fulfilled by a Gaussian normal distribution and an additive mutation scheme. Expression (2.63) summarizes the adaptation of the σ_i values and the rotation angles:

$$\begin{aligned} \sigma_i^{(g+1)} &\sim \sigma_i^{(g)} \exp\left(\tau_0 \mathrm{N}(0,1) + \tau \mathrm{N}_i(0,1)\right), \\ \alpha_j^{(g+1)} &\sim \alpha_j^{(g)} + \beta \mathrm{N}_j(0,1). \end{aligned} \tag{2.63}$$

Schwefel recommends to choose the factor β equal to 0.0873. The rotation angles α_j are defined within the interval $[-\pi, \pi]$. Whenever an angle α_j is outside the permissible interval, a mapping is performed as shown by (2.64) [13]:

$$\left|\alpha_j^{(g+1)}\right| > \pi \rightarrow \alpha_j^{(g+1)} = \alpha_j^{(g+1)} - 2\pi sign\left(\alpha_j^{(g+1)}\right). \tag{2.64}$$

Experimental studies showed that the presented self-adaptation mechanism of the strategy parameters is a noisy process, which can show remarkable fluctuations during the optimization [27]. The above mentioned intermediate recombination is able to reduce these fluctuations. Nevertheless, the introduced self-adaptation can fail. In this case the evolution gets stuck in a local optimum because the mutation operator is unable to create superior offspring with respect to their parents. One has to bear in mind that there is no general solution for this problem. In the

subsequent sections advanced techniques are introduced, which take the history of the search process into account.

2.4.5 Derandomized self adaptation

Ostermeier [35] analyzed the self-adaptation mechanism on the basis of an $(1, \lambda)$-ES. The investigated algorithm comprises for each offspring k $(1 \leq k \leq \lambda)$ a global mutation strength variation parameter ξ^k, which takes two possible states with equal probability $(\alpha, 1/\alpha; \alpha \in [1.1; 1.5])$ and a vector $\boldsymbol{\xi}^k$ for the independent variation of the object variables (Individual strategy parameter ξ_i^k). The components of the vector $\boldsymbol{\xi}^k$ are drawn from an appropriate distribution. Expression (2.65) shows the mutation operator (O: Offspring, P: Parent):

$$\mathbf{x}_{O_k}^{(g)} = \mathbf{x}_P^{(g)} + \xi^k \boldsymbol{\xi}^k \boldsymbol{\delta}^g \mathbf{z}^k. \tag{2.65}$$

Each component of the random vector $\mathbf{z}$ is drawn from a normal distribution with zero mean and a variance of one. The random vector $\mathbf{z}$ is modified multiplicatively by the strategy parameters of the previous generation $\boldsymbol{\delta}^{(g)}$, the global mutation strength variation ξ^k and the individual strategy parameter variation $\boldsymbol{\xi}^k$. The fittest individual is selected as a parent for the following generation ($sel \in 1, \ldots, \lambda$, index of the selected individual)

$$\mathbf{x}_P^{(g+1)} = \mathbf{x}_{O_{sel}}^{(g)}. \tag{2.66}$$

The individual strategy parameters for the next generation are computed on the basis of the parameter variation of the selected offspring

$$\boldsymbol{\delta}^{(g+1)} = \xi^{sel} \boldsymbol{\xi}^{sel} \boldsymbol{\delta}^{(g)}. \tag{2.67}$$

The multiplications of (2.65) and (2.67) are performed component wise.

Ostermeier identified two basic shortcomings of the presented self-adaption mechanism. First of all, the scheme does not relate the size of the mutation of the objective variables of the selected individual with the variation of the individual strategy parameters for the following generation. As the components of $\mathbf{z}$ are drawn from a normal distribution, a large mutation is possible, even when a small value of the related individual strategy parameter variation occurs. However, in such a case, the individual strategy parameter variation should reflect the large mutation. Furthermore, the variation of the strategy parameter within a generation is the same as the one between different generations. On the one hand, a distinct variation is necessary for assuring a successful selection procedure. On the other hand, for reducing random fluctuations of the strategy parameters in the generation sequence the inter-generational variation should be much smaller.

Ostermeier suggested a derandomized mutative step-size control in order to overcome the mentioned shortcomings. In this case, the modification of the individual strategy parameters is derived from the sampled random vector $\mathbf{z}$ of the

selected offspring and not drawn from a distribution. The expected values of $\mathrm{E}(|z_i|)$ and $\mathrm{E}(x_i)$ are equal, as shown by

$$z_i \sim \mathrm{N}(0,1), \tag{2.68}$$

$$y_i \sim \chi^2 \sim z_i^2, \tag{2.69}$$

and

$$x_i \sim \chi \sim \sqrt{y_i}. \tag{2.70}$$

The distribution of the absolute value of each component of $\mathbf{z}$ is given by (2.70) [36]. Expression (2.71) [32] shows the computation of the expected value of a χ distributed random variable x_i:

$$\mathrm{E}(x_i) = \sqrt{2}\frac{\Gamma((k+1)/2)}{\Gamma(k/2)}. \tag{2.71}$$

As the value $|z_i|$ is a scalar, the degree of freedom k is equal to one (The results of the gamma function Γ can be found in [26]):

$$\mathrm{E}(x_i) = \sqrt{\frac{2}{\pi}},\ \Gamma\left(\frac{1}{2}\right) = \sqrt{\pi},\ \Gamma(1) = 1. \tag{2.72}$$

As the adaptation of the individual strategy parameter is performed multiplicatively, the exponential function is applied for transforming the expected value to one and to obtain an equal probability for the occurrence of a variation and its associated reciprocal variation

$$\xi_i = \exp\left(\left|z_i^{sel}\right| - \sqrt{\frac{2}{\pi}}\right). \tag{2.73}$$

The update of the strategy parameters is given by

$$\boldsymbol{\delta}^{(g+1)} = \left(\xi^{sel}\right)^{\beta} \left(\boldsymbol{\xi}_{\mathbf{z}_{sel}}\right)^{\beta_{scal}} \boldsymbol{\delta}^{(g)}. \tag{2.74}$$

For each component of the vector $\mathbf{z}$, the absolute value $|z_i|$ is computed. According to expression (2.73), the individual strategy parameter δ_i^g is increased or decreased, if $|z_i|$ is bigger or smaller than the expected value $\sqrt{\frac{2}{\pi}}$.

Ostermeier also introduced two exogenous strategy parameters β $(0 < \beta < 1)$ and $\beta_{scal} (0 < \beta_{scal} < 1)$ for reducing the random inter-generational fluctuations without affecting the variation between competing offspring. These parameters allow decreasing the modification of the individual strategy parameters. Finally, the expressions (2.75) summarize the discussed modifications. Again, all the multiplications and powers of vectors refer to components:

$$\begin{aligned}
\mathbf{x}_{O_k}^{(g)} &= \mathbf{x}_P^{(g)} + \xi^k \boldsymbol{\delta}^g \mathbf{z}^k, \\
\mathbf{x}_P^{(g+1)} &= \mathbf{x}_{O_{sel}}^{(g)}, \\
\boldsymbol{\delta}^{(g+1)} &= \left(\xi^{sel}\right)^{\beta} \left(\boldsymbol{\xi}_{\mathbf{z}_{sel}}\right)^{\beta_{scal}} \boldsymbol{\delta}^{(g)}, \\
\boldsymbol{\xi}_{\mathbf{z}_{sel}} &= \left(\xi_1, \xi_2, \ldots, \xi_n\right)^T, \text{ with } \xi_i = \exp\left(\left|z_i^{sel}\right| - \sqrt{\frac{2}{\pi}}\right).
\end{aligned} \tag{2.75}$$

2.4.6 Cumulative step-size adaptation

The following section deals with a further generalized derandomized procedure for the adaptation of the global mutation strength in consideration of intergenerational information. In [37] the cumulative step-size adaptation is presented on the basis of a $(\mu/1, \lambda)$-CSA-ES and a $(\mu/\mu, \lambda)$-CSA-ES. The latter mentioned algorithm is discussed in this section, which uses an intermediate recombination. The core of the cumulative step-size adaptation (CSA) is the evolution path. Figure 2.8 [33] shows three different evolution paths in an idealized representation, consisting each of five generations. The solid vectors illustrate the connection between the resultant centroids of the intermediate recombination from one generation to the next one and the dashed vector shows the resultant from the initial state to the last generation. As opposed to the vectors connecting the generational sequence of the centroids, the resultant ones differ significantly in length. A long evolution path (length of the resultant vector), shown by 2.8 (right), in comparison with a path obtained by random selection, illustrated by 2.8 (middle), leads under the application of the CSA to an increased mutation strength and vice versa. A mathematical definition of the reference state for assessing the path length is given below. If the evolution path is too short, the search is probably close to an optimum. Hence, the mutation strength is reduced in order to focus the optimization on this region. In the other case, a long evolution path indicates a long distance to the optimum. In such a case it is reasonable to increase the mutation strength.

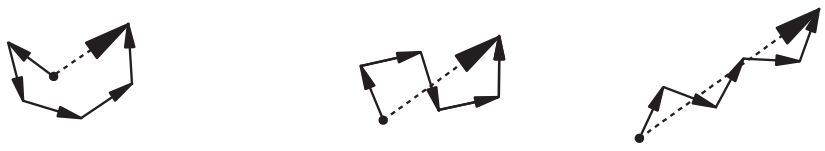

Figure 2.8: Evolution paths of different length [33].

Expression

$$\mathbf{x}_k^{(g+1)} = \langle \mathbf{x} \rangle_\mu^{(g)} + \delta^{(g)} \mathbf{z}_k \tag{2.76}$$

illustrates the isotropic mutation of the offspring k $(1 \leq k \leq \lambda)$ originating from the centroid $\langle \mathbf{x} \rangle_\mu^{(g)}$ of the previous generation

$$\langle \mathbf{x} \rangle_\mu^{(g)} = \frac{1}{\mu} \sum_{i \in I_{sel}^{(g)}} \mathbf{x}_i^{(g)}. \tag{2.77}$$

$I_{sel}^{(g)}$ contains the μ indices, selected within the generation g. $\delta^{(g)} \in \mathbb{R}$ is the mutation strength of the generation g $(\delta^{(g)} > 0)$ and $\mathbf{z}_k$ is a normal distributed random vector. The components of $\mathbf{z}_k$ are drawn independently on the basis of a zero mean and a variance of one. Each $\mathbf{z}_k$ is determined independently from the other random vectors of the generation $g+1$. A mathematical formulation of the evolution path is given by

$$\mathbf{s}^{(g+1)} = (1-c)\, \mathbf{s}^{(g)} + c_u \frac{\sqrt{\mu}}{\delta^{(g)}} \left(\langle \mathbf{x} \rangle_\mu^{(g+1)} - \langle \mathbf{x} \rangle_\mu^{(g)} \right), \tag{2.78}$$

which is a weighted sum of the consecutive centroids and

$$\delta^{(g+1)} = \delta^{(g)} \exp \left(\frac{\left\| \mathbf{s}^{(g+1)} \right\| - \mathrm{E}\left(\left\| \mathrm{N}\left(\mathbf{0}, \mathbf{I} \right) \right\| \right)}{D \mathrm{E}\left(\left\| \mathrm{N}\left(\mathbf{0}, \mathbf{I} \right) \right\| \right)} \right) \tag{2.79}$$

defines the update of the mutation strength. Expression (2.79) compares the Euclidean norm of the evolution path $\mathbf{s}^{(g+1)}$ with the expected value of the Euclidean norm of a normal distributed random vector with zero mean and a identity matrix as a covariance matrix $(\mathrm{E}\left(\left\| \mathrm{N}\left(\mathbf{0}, \mathbf{I} \right) \right\| \right))$.

The expressions

$$\mathbf{z} \sim N\left(\mathbf{0}, \mathbf{I} \right), \tag{2.80}$$

$$y \sim \chi^2 \sim \mathbf{z}^T \mathbf{z} \tag{2.81}$$

and

$$x \sim \chi \sim \sqrt{y} \tag{2.82}$$

show the equivalence of the random variables $\|\mathbf{z}\|$ and x. $\mathrm{E}\left(\left\| \mathrm{N}\left(\mathbf{0}, \mathbf{I} \right) \right\| \right)$ is the expected value of a χ distribution

$$\mathrm{E}\left(\|\mathbf{z}\| \right) = \mathrm{E}\left(\left\| \mathrm{N}\left(\mathbf{0}, \mathbf{I} \right) \right\| \right) = \mathrm{E}\left(x \right) = \sqrt{2} \frac{\Gamma\left((k+1)/2 \right)}{\Gamma\left(k/2 \right)}. \tag{2.83}$$

The degree of freedom k of this distribution is identical to the dimension of the search space. If the length of the evolution path $\mathbf{s}^{(g+1)}$ is smaller than

$\mathrm{E}\left(\|\mathrm{N}\left(\mathbf{0},\mathbf{I}\right)\|\right)$, the global mutation strength is decreased according to (2.79). In the opposite case, the mutation strength is increased. The expected length of a normal distributed random vector is the above mentioned reference state for assessing the evolution path length, which is obtained from random selection. If the Euclidean norm of $\mathbf{s}^{(g+1)}$ is equal to $\mathrm{E}\left(\|\mathrm{N}\left(0,\mathbf{I}\right)\|\right)$, the global mutation strength remains unchanged. The successful steps are expected to be perpendicular to each other [33]

$$\mathbf{z}_{sel}^{(g)^T}\mathbf{z}_{sel}^{(g+1)} \approx 0 \; ; \; \mathbf{z}_{sel}^{(g+1)} = \frac{\sqrt{\mu}}{s^{(g)}}\left(\langle\mathbf{x}\rangle_{\mu}^{(g+1)} - \langle\mathbf{x}\rangle_{\mu}^{(g)}\right). \tag{2.84}$$

Large values of the exogenous damping parameter D lead to a slow adaptation of the mutation strength. The exogenous parameter c weights the influence of the history with respect to the evolution path. In the limit case $c = 1$ the history of the evolution path is ignored. Hansen 1998 recommended for the mentioned parameters the values

$$c = \frac{1}{\sqrt{n}},\; D = \sqrt{n}. \tag{2.85}$$

Originating from

$$z = ax,\; x \sim \mathrm{N}(0,\sigma_x^2),\; z \sim \mathrm{N}(0,a^2\sigma_x^2) \tag{2.86}$$

and

$$x \sim \mathrm{N}(0,\sigma_x^2),\; y \sim \mathrm{N}(0,\sigma_y^2),\; x+y \sim \mathrm{N}(0,\sigma_x^2+\sigma_y^2), \tag{2.87}$$

which gives the rule for the addition of variances of normal distributions,

$$\frac{1}{\mu}\sum_{i=1}^{\mu}\mathbf{z}_i \sim \frac{1}{\sqrt{\mu}}\mathrm{N}\left(\mathbf{0},\mathbf{I}\right),\; \mathbf{z}_k \sim \mathrm{N}\left(\mathbf{0},\mathbf{I}\right) \tag{2.88}$$

can be derived [38]. Expression

$$\langle\mathbf{x}\rangle_{\mu}^{(g+1)} \sim \langle\mathbf{x}\rangle_{\mu}^{(g)} + \delta^{(g)}\frac{1}{\mu}\sum_{i=1}^{\mu}\mathbf{z}_i \tag{2.89}$$

is derived from (2.76) and (2.77). The expressions (2.88), (2.89) and (2.90) are derived under the assumption of a random selection. Inserting (2.88) into (2.89) leads to (2.90), which shows that the difference vector of the centroids between the generations g and $g+1$ is normally distributed:

$$\frac{\sqrt{\mu}}{\delta^{(g)}}\left(\langle\mathbf{x}\rangle_{\mu}^{(g+1)} - \langle\mathbf{x}\rangle_{\mu}^{(g)}\right) \sim \mathrm{N}\left(\mathbf{0},\mathbf{I}\right). \tag{2.90}$$

As (2.90) is normally distributed under random selection, $\mathbf{s}^{(g+1)}$ is also equally distributed, if the constant c_u is chosen according to (2.91) and $\mathbf{s}^{(0)} \sim \mathrm{N}\left(\mathbf{0},\mathbf{I}\right)$

$$\mathbf{s}^{(g+1)} \sim \mathbf{s}^{(g)} \sim \mathrm{N}\left(\mathbf{0}, \mathbf{I}\right) \Rightarrow \left(1-c\right)^2 + c_u^2 = 1^2. \tag{2.91}$$

This expression is derived by applying (2.87). An extension of the introduced cumulative step-size adaptation is shown in the next section, which is not restricted to an isotropic mutation operator.

2.4.7 Covariance matrix adaptation

The best adaptation of the mutation operator with respect to the fitness landscape is obtained by deploying a covariance matrix implying a global scaling, a scaling for each eigenvector and an orthogonal rotation of the coordinate system defined by the eigenvectors. As introduced above, the related covariance matrix can be derived from a set of strategy parameters. Another approach is to learn the covariance matrix directly from the optimization sequence. The adaptation of it is determined by the history of successful steps and the selected individuals of the current population. This procedure is referred to as covariance matrix adaptation (CMA). The introduction of the CMA is mainly taken from [33].

The offspring is drawn from a Normal distribution, as given by

$$\mathbf{x}_k^{(g+1)} \sim \sigma^{(g)} \mathrm{N}\left(\mathbf{m}^{(g)}, \mathbf{C}^{(g)}\right). \tag{2.92}$$

For the numerical computation of the random vector, expression (2.41) is applied. $\sigma^{(g)} \in \mathbb{R}^+$ is the global mutation strength. $\mathbf{x}_k^{(g+1)}$ the k-th offspring of the generation $g+1$, whereas $\mathbf{m}^{(g)} \in \mathbb{R}^n$ is the centroid of the generation g and $\mathbf{C}^{(g)}$ the covariance matrix of the generation g.

The following section treats the update procedures for $\mathbf{m}$, $\mathbf{C}$ and σ. Hansen applies an extended intermediate recombination, which implies additional weights for each parent

$$\mathbf{m}^{(g+1)} = \sum_{i=1}^{\mu} w_i \mathbf{x}_{i:\lambda}^{(g+1)} \tag{2.93}$$

for updating $\mathbf{m}$. All parents are involved in the recombination process, therefore ρ is equal to μ. The expression $i:\lambda$ ranks the individuals according to their fitness value as shown by

$$f\left(\mathbf{x}_{1:\lambda}^{(g+1)}\right) \leq f\left(\mathbf{x}_{2:\lambda}^{(g+1)}\right) \leq \cdots \leq f\left(\mathbf{x}_{\lambda:\lambda}^{(g+1)}\right). \tag{2.94}$$

The higher the fitness of the parents the higher their weight for the recombination is. Expression (2.95) defines the weight factors:

$$\sum_{i=1}^{\mu} w_i = 1,\ w_1 \geq w_2 \geq \cdots \geq w_\mu,\ w_i \in \mathbb{R}^+. \tag{2.95}$$

The expression (2.96) is a useful definition for the subsequent presentation of the CMA-ES:

$$\mu_{eff} = \left(\frac{\sum_{i=1}^{\mu} w_i}{\|\mathbf{w}\|} \right)^2 = \left(\sum_{i=1}^{\mu} w_i^2 \right)^{-1}. \tag{2.96}$$

The lowest possible value of μ_{eff} is 1.0. In this case, one parent has a weight of 1.0 and the remaining parents a weight of 0.0. If all parents have the same weight $\frac{1}{\mu}$, μ_{eff} is equal to μ, which is the highest possible value of μ_{eff}.

Generally, a fast search is desired, which implies a small population size λ. Under this condition, it is difficult to obtain a reliable estimation of the covariance matrix. Hansen suggested deploying information from previous generations in order to improve the computation of the covariance matrix. Expression (2.97) illustrates the estimation of the covariance matrix within the generation $g+1$:

$$\mathbf{C}_{\mu}^{(g+1)} = \sum_{i=1}^{\mu} w_i \left(\mathbf{x}_{i:\lambda}^{(g+1)} - \mathbf{m}^{(g)} \right) \left(\mathbf{x}_{i:\lambda}^{(g+1)} - \mathbf{m}^{(g)} \right)^T. \tag{2.97}$$

The same weights are applied as for the extended intermediate recombination. Hansen [33] interprets (2.97) as an estimation of the variances of the sampled steps, because the mean is taken from the previous generation. Expression (2.98) demonstrates the assignment of prior information to the covariance matrix:

$$\mathbf{C}^{(g+1)} = (1 - c_{\mu})\, \mathbf{C}^{(g)} + \frac{c_{\mu}}{{\sigma^{(g)}}^2} \mathbf{C}_{\mu}^{(g+1)}. \tag{2.98}$$

The recent generations possess a higher weight than the older ones. The exogenous parameter c_{μ} controls the significance of the older information with respect to the current covariance matrix and is referred to as learning rate. If c_{μ} is chosen to be zero, the initial covariance matrix is preserved. A value of $c_{\mu} = 1$ means that any prior information is discarded. Inserting (2.97) into (2.98) and applying

$$\mathbf{y}_{i:\lambda}^{(g+1)} = \frac{\mathbf{x}_{i:\lambda}^{(g+1)} - \mathbf{m}^{(g)}}{\sigma^{(g)}} \tag{2.99}$$

gives

$$\mathbf{C}^{(g+1)} = (1 - c_{\mu})\, \mathbf{C}^{(g)} + c_{\mu} \sum_{i=1}^{\mu} w_i \mathbf{y}_{i:\lambda}^{(g+1)} \mathbf{y}_{i:\lambda}^{(g+1)^T}. \tag{2.100}$$

The parameter c_{μ} balances between two extreme cases. If c_{μ} is chosen too big, the covariance matrix could degenerate and a small value of c_{μ} leads to slow learning. Usually, as an initial covariance matrix $\mathbf{C}^{(0)}$ the unity matrix $\mathbf{I}$ is utilized.

A drawback of the presented estimation of the covariance matrix is that the sign information of the steps is not reflected $\mathbf{y}\mathbf{y}^T = (-\mathbf{y})(-\mathbf{y})^T$. Hansen proposed to overcome this shortcoming by introducing a so-called evolution path. Successful steps are accumulated and stored in a vector $\mathbf{p}_c$. Expression (2.101) defines this vector:

$$\mathbf{p}_c^{(g+1)} = (1 - c_c)\,\mathbf{p}_c^{(g)} + \sqrt{c_c\,(2 - c_c)\,\mu_{eff}}\left(\frac{\mathbf{m}^{(g+1)} - \mathbf{m}^{(g)}}{\sigma^{(g)}}\right). \tag{2.101}$$

The factor of the second summand on the right hand side is a normalization constant and c_c defines the significance of the previous generations similar as c_μ. Expression (2.102) shows the generation of a covariance matrix on the basis of an evolution path:

$$\mathbf{C}^{(g+1)} = (1 - c_1)\,\mathbf{C}^{(g)} + c_1 \mathbf{p}_c^{(g+1)} \mathbf{p}_c^{(g+1)^T}. \tag{2.102}$$

Both approaches for adapting the covariance matrix can be combined as given by

$$\mathbf{C}^{(g+1)} = (1 - c_1 - c_\mu)\,\mathbf{C}^{(g)} + c_1 \mathbf{p}_c^{(g+1)} \mathbf{p}_c^{(g+1)^T} + c_\mu \sum_{i=1}^{\mu} w_i \mathbf{y}_{i:\lambda}^{(g+1)} \mathbf{y}_{i:\lambda}^{(g+1)^T}. \tag{2.103}$$

Thereby the information of each generation (estimation of the covariance matrix) and the correlations between the generations (evolution path) are efficiently used for updating the covariance matrix. The constants c_1 and c_μ control the significance of the information of the previous generations. Hansen [33] recommends to choose c_1 and c_μ according to

$$c_1 \approx \frac{2}{n^2} \tag{2.104}$$

and

$$c_\mu \approx \min\left(\frac{\mu_{eff}}{n^2}, 1 - c_1\right). \tag{2.105}$$

Additionally, the CMA-ES comprises an overall scale of the mutation operator, which is similar to the above introduced cumulative step-size adaptation. This mechanism is introduced, as the largest reliable learning rate for the covariance matrix update (2.103) is too slow for achieving the desired change rates of the global mutation strength. Expression

$$\mathbf{p}_\sigma^{(g+1)} = (1 - c_\sigma)\,\mathbf{p}_\sigma^{(g)} + \sqrt{c_\sigma\,(2 - c_\sigma)\,\mu_{eff}}\,\mathbf{C}^{(g)^{-\frac{1}{2}}}\frac{\mathbf{m}^{(g+1)} - \mathbf{m}^{(g)}}{\sigma^{(g)}} \tag{2.106}$$

shows a slightly modified version of (2.78), which is adapted to the weighted intermediate recombination and contains a rescaling of the eigenvalues. For the

exogenous parameter c_σ, which weights the influence of the previous generations on the evolution path, Hansen recommends the same range as for c_c.

The matrix $\mathbf{C}^{(g)^{-\frac{1}{2}}}$, defined as

$$\mathbf{C}^{(g)^{-\frac{1}{2}}} = \mathbf{B}^{(g)}\mathbf{D}^{(g)^{-1}}\mathbf{B}^{(g)^T}, \tag{2.107}$$

eliminates the scaling of the axes, which is caused by the covariance matrix $\mathbf{C}^{(g)}$ within the mutation. However, the rotation of the axis is not affected by $\mathbf{C}^{(g)^{-\frac{1}{2}}}$. On the basis of this rescaling, it is possible to compare the length of the evolution path with the expected length of a $N(\mathbf{0}, \mathbf{I})$ distributed normal vector. The fundamental idea of the adaption of the global mutation strength is the same as mentioned in the section about the cumulative step-size adaptation. A successful adaptation of the global mutation strength is obtained, if the vectors, connecting the centroids of each generation are in expectation perpendicular to each other in the rescaled space. If the centroids of each generation are considered in the search space, expression

$$\left(\mathbf{m}^{(g)} - \mathbf{m}^{(g-1)}\right)^T \mathbf{C}^{(g)^{-1}} \left(\mathbf{m}^{(g+1)} - \mathbf{m}^{(g)}\right) \approx 0 \tag{2.108}$$

holds. In other words, the vectors $\mathbf{m}^{(g+1)} - \mathbf{m}^{(g)}$ and $\mathbf{m}^{(g)} - \mathbf{m}^{(g-1)}$ are in expectation $\mathbf{C}^{-1}$ conjugate. The derivation of (2.108) can be found in [33]. Apart from the constant c_σ and the formula signs, the adaptation of the global mutation strength is identically computed as (2.79):

$$\sigma^{(g+1)} = \sigma^{(g)} exp\left[\frac{c_\sigma}{d_\sigma}\left(\frac{\left\|\mathbf{p}_\sigma^{(g+1)}\right\|}{\mathrm{E}\left\|\mathrm{N}\left(\mathbf{0}, \mathbf{I}\right)\right\|} - 1\right)\right]. \tag{2.109}$$

2.4.8 (1+λ)-CMA-ES

Subsequently, a (1+λ)-CMA-ES is introduced, which is developed by Igel et al. [20]. The offspring is procreated in the same way, as shown for the $(\mu/\mu, \lambda)$-CMA-ES (Expression (2.92)). The best fitness value of each generation, comprising λ offspring, is denoted by the symbol $\mathbf{x}_{1:\lambda}^{(g+1)} \in \mathbb{R}^n$. For the adaptation of the step size σ, a procedure similar to the $1/5th$ rule (Rechenberg 1973) is applied. Thereby, $\lambda_{succ}^{(g+1)}$ is defined as the number of offspring concerning a generation, whose fitness is better than the one of the parent. The success probability $p_{succ}^{(g+1)} = \frac{\lambda_{succ}^{(g+1)}}{\lambda}$ is smoothed, as given by

$$\overline{p}_{succ}^{(g+1)} = (1 - c_p)\overline{p}_{succ}^{(g)} + c_p p_{succ}^{(g+1)}. \tag{2.110}$$

The adaptation of the step size σ (2.111) is performed multiplicatively:

$$\sigma^{(g+1)} = \sigma^{(g)} exp\left(\frac{1}{d}\frac{\overline{p}_{succ}^{(g+1)} - p_{succ}^{target}}{1 - p_{succ}^{target}}\right). \tag{2.111}$$

In order to limit the adaptation of the step size by the damping factor, the result of the sub term $\frac{\overline{p}_{succ}^{(g+1)} - p_{succ}^{target}}{1 - p_{succ}^{target}}$ must lie within the interval $]-1;1[$. For obtaining the desired interval, $p_{succ}^{target} < 0.5$ must hold. This restriction of the mentioned sub term leads to an argument of the exponential function, which is larger than $-\frac{1}{d}$ and smaller than $\frac{1}{d}$.

Provided $\mathbf{x}_{1:\lambda}^{(g+1)}$ corresponds to a better fitness value than the parent $\mathbf{x}_{parent}^{(g)}$, this offspring is taken as a parent of the next generation and the covariance matrix is updated. The update procedure of the covariance matrix also depends on the smoothed success probability $\overline{p}_{succ}^{(g+1)}$, as shown by the expressions

$$\begin{aligned} &if\ \overline{p}_{succ}^{(g+1)} < p_{thresh} \\ &\mathbf{p}_c^{(g+1)} = (1 - c_c)\,\mathbf{p}_c^{(g)} + \sqrt{c_c\,(2 - c_c)}\left[\frac{\mathbf{x}_{parent}^{(g+1)} - \mathbf{x}_{parent}^{(g)}}{\sigma_{parent}^{(n)}}\right] \\ &if\ \overline{p}_{succ}^{(g+1)} \geq p_{thresh} \\ &\mathbf{p}_c^{(g+1)} = (1 - c_c)\,\mathbf{p}_c^{(g)} \end{aligned} \tag{2.112}$$

and

$$\begin{aligned} &if\ \overline{p}_{succ}^{(g+1)} < p_{thresh} \\ &\mathbf{C}^{(g+1)} = (1 - c_{cov})\,\mathbf{C}^{(g)} + c_{cov}\mathbf{p}_c^{(g+1)}\mathbf{p}_c^{T\,(g+1)} \\ &if\ \overline{p}_{succ}^{(g+1)} \geq p_{thresh} \\ &\mathbf{C}^{(g+1)} = (1 - c_{cov})\,\mathbf{C}^{(g)} + c_{cov}\left(\mathbf{p}_c^{(g+1)}\mathbf{p}_c^{T\,(g+1)} + c_c\,(2 - c_c)\,\mathbf{C}^{(g)}\right) \end{aligned} \quad . \tag{2.113}$$

Thereby, the update of the covariance matrix takes the actual step into account, if the smoothed success probability is below the threshold. In this case, the evolution path and the adaptation of the covariance matrix is computed in the same way as shown for the $(\mu/\mu, \lambda)$-CMA-ES. The term $\sqrt{c_c\,(2 - c_c)}$ normalizes the variance of $\mathbf{p}_c$, which is considered to be a random variable (see [20]).

According to (2.112), the evolution path shrinks, if the smoothed success probability exceeds the threshold. For preserving the variance of $\mathbf{C}$ in this case, which is affected by the shrinking evolution path, the update of the covariance matrix is complemented by the term $c_c\,(2 - c_c)\,\mathbf{C}^{(g)}$. The threshold p_{thresh} limits the adaptation of the covariance matrix in the case of small step sizes. Table 2.2 summarizes recommendations regarding the choice of the exogenous parameters, as given in [20]. The suggestion of the success probability p_{succ}^{target} lies in the same dimension as $1/5th$ rule of Rechenberg.

Table 2.2: Recommended values of the exogenous parameters of the (1+λ)-CMA-ES algorithm.

Adaptation Step Size
$d = 1 + \frac{n}{2\lambda}$ $\quad p_{succ}^{target} = \frac{1}{5+\frac{\sqrt{\lambda}}{2}}$ $\quad c_p = \frac{p_{succ}^{target}\lambda}{2+p_{succ}^{target}\lambda}$
Adaptation Covariance Matrix
$c_c = \frac{2}{n+2}$ $\quad c_{cov} = \frac{2}{n^2+6}$ $\quad p_{thresh} = 0.44$

2.5 Newton method

The Newton method is an optimization procedure, which is based on the second derivative of the objective function. The application of this algorithm is limited to differentiable and unconstrained minimization problems as given by:

$$\text{minimize: } f(\mathbf{x}),\ \mathbf{x} \in \mathbb{R}^n,\ f \in \mathbb{R}. \tag{2.114}$$

Thereby, the optimization procedure identifies the root of the first derivative

$$\nabla f(\overline{\mathbf{x}}) = \mathbf{0}. \tag{2.115}$$

It has to be mentioned that this root could also correspond to a local maximum or a saddle point of $f(\mathbf{x})$. For investigating the computed stationary point, the Hessian matrix $\nabla^2 f(\mathbf{x})$ can be calculated. Provided this matrix is positive definite, the considered stationary point is a local minimum. The expressions

$$\nabla f = \frac{\partial f(\mathbf{x})}{\partial \mathbf{x}} = \left[\frac{\partial f(\mathbf{x})}{\partial x_1}, \frac{\partial f(\mathbf{x})}{\partial x_2}, ..., \frac{\partial f(\mathbf{x})}{\partial x_n}\right]^T \tag{2.116}$$

and

$$\nabla^2 f(\mathbf{x}) = \left(\frac{\partial^2 f(\mathbf{x})}{\partial x_i \partial x_k}\right)_{i,k=1,...,n} \tag{2.117}$$

define the first and second derivative respectively. The root of the first derivative is computed based on a linearization of the stationary condition with respect to the current position $\mathbf{x}^{(n)}$ (2.115). The desired stationary point is iteratively determined. Expression

$$\nabla f(\mathbf{x}^{(n)}) + \nabla^2 f(\mathbf{x}^{(n)}) \Delta \mathbf{x}^{(n+1)} = \mathbf{0} \tag{2.118}$$

shows the linearization of the nth iteration. This expression is solved for the vector $\Delta \mathbf{x}^{(n+1)}$, which gives, in consideration of

$$\mathbf{x}^{(n+1)} = \mathbf{x}^{(n)} + \Delta\mathbf{x}^{(n+1)}, \tag{2.119}$$

the update of the solution $\mathbf{x}^{(n+1)}$ regarding the nth iteration

$$\mathbf{x}^{(n+1)} = \mathbf{x}^{(n)} - \left[\nabla^2 f(\mathbf{x}^{(n)})\right]^{-1} \nabla f(\mathbf{x}^{(n)}). \tag{2.120}$$

In order to apply the Newton method for constrained problems, as defined by

$$\begin{array}{lll} \text{minimize:} & f(\mathbf{x}), & f \in \mathbb{R}, \qquad \mathbf{x} \in \mathbb{R}^n, \\ & g_j(\mathbf{x}) \leq 0, & j = 1, ..., n_g, \\ & h_i(\mathbf{x}) = 0, & i = 1, ..., n_h, \end{array} \tag{2.121}$$

the objective function can be exchanged by a Lagrange function. This function, as defined by the expression (2.122), enables to transform the constrained problem to an unconstrained one:

$$L(\mathbf{x}, \boldsymbol{\lambda}, \boldsymbol{\mu}) = f(\mathbf{x}) + \sum_{j=1}^{n_g} \lambda_j g_j(\mathbf{x}) + \sum_{k=1}^{n_h} \mu_k h_k(\mathbf{x}). \tag{2.122}$$

Provided, the problem comprises only equality constraints $n_g = 0; n_h > 0$, the stationary point of the Lagrange function

$$\nabla L(\overline{\mathbf{x}}, \overline{\boldsymbol{\lambda}}, \overline{\boldsymbol{\mu}}) = \mathbf{0} \tag{2.123}$$

is a necessary condition of a local minimum. However, the stationary point is only a local minimum, if the Hessian matrix is positive definite.

In the general case, comprising equality and inequality constraints ($n_g > 0; n_h > 0$), the Kuhn-Tucker optimality conditions (2.124), (2.125), (2.126) and (2.127) have to be applied for the determination of a local minimum:

$$\overline{\lambda}_j \geq 0, \tag{2.124}$$
$$\nabla_x L(\overline{\mathbf{x}}, \overline{\boldsymbol{\lambda}}, \overline{\boldsymbol{\mu}}) = \mathbf{0}, \tag{2.125}$$
$$\overline{\lambda}_j g_j(\overline{\mathbf{x}}) = 0, \tag{2.126}$$
$$h_i(\overline{\mathbf{x}}) = 0. \tag{2.127}$$

Expression

$$\nabla_x L(\mathbf{x}, \boldsymbol{\lambda}, \boldsymbol{\mu}) = \nabla_x f(\mathbf{x}) + \sum_{j=1}^{n_g} \lambda_j \nabla_x g_j(\mathbf{x}) + \sum_{i=1}^{n_h} \mu_i \nabla_x h_i(\mathbf{x}) \tag{2.128}$$

gives the partial derivative of $L(\mathbf{x}, \boldsymbol{\lambda}, \boldsymbol{\mu})$ with respect to $\mathbf{x}$. For solving the optimization problem on the basis of the Kuhn-Tucker optimality conditions, the equations (2.125),(2.126) and (2.127) need to be linearized as given by (2.129), (2.130) and (2.131) [26]:

$$\begin{aligned}
&\nabla_x L(\mathbf{x}^{(n)}, \boldsymbol{\lambda}^{(n)}, \boldsymbol{\mu}^{(n)}) + \\
&(\nabla_x^2 f(\mathbf{x}^{(n)}) + \sum_{j=1}^{n_g} \lambda_j^{(n)} \nabla_x^2 g_j(\mathbf{x}^{(n)}) + \sum_{i=1}^{n_h} \mu_i^{(n)} \nabla_x^2 h_i(\mathbf{x}^{(n)}))\Delta\mathbf{x}^{(n+1)} + \\
&\sum_{j=1}^{n_g} \nabla_x g_j(\mathbf{x}) \Delta\lambda_j^{(n+1)} + \sum_{i=1}^{n_h} \nabla_x h_i(\mathbf{x}) \Delta\mu_i^{(n+1)} = \mathbf{0}, \qquad (2.129)
\end{aligned}$$

$$\lambda_j^{(n)} g_j(\mathbf{x}^{(n)}) + g_j(\mathbf{x}^{(n)}) \Delta\lambda_j^{(n+1)} + \lambda_j^{(n)} \nabla_x g_j(\mathbf{x}^{(n)})^T \Delta\mathbf{x}^{(n+1)} = 0, \qquad (2.130)$$

$$h_i(\mathbf{x}^{(n)}) + \nabla_x h_i(\mathbf{x}^{(n)})^T \Delta\mathbf{x}_i^{(n+1)} = 0. \qquad (2.131)$$

For the linearization, the variables $\Delta\mathbf{x}$,$\Delta\lambda_j$ and $\Delta\mu_i$ are introduced. Now, apart from $\mathbf{x}$, also the Lagrange multipliers λ_j and μ_j need to be updated as given by the expressions:

$$\mathbf{x}^{(n+1)} = \mathbf{x}^{(n)} + \Delta\mathbf{x}^{(n+1)}, \qquad (2.132)$$

$$\lambda_j^{(n+1)} = \lambda_j^{(n)} + \Delta\lambda_j^{(n+1)}, \qquad (2.133)$$

$$\mu_i^{(n+1)} = \mu_i^{(n)} + \Delta\mu_i^{(n+1)}. \qquad (2.134)$$

On the basis of the shown equation system (2.129), (2.130) and (2.131) the desired solution can be computed iteratively.

2.6 Sequential quadratic programming

Unfortunately, the Newton method can converge to a solution, which violates the constraints [25]. In order to avoid this shortcoming of the Newton method, Sequential Quadratic Programming algorithms can be deployed. The introduction of these algorithms is mainly taken from [25]. As a first step, additional constraints are defined:

$$\begin{aligned}
\lambda_i^{(n+1)} &\geq 0, \\
g_j(\mathbf{x}^{(n)}) + \nabla_x g_j(\mathbf{x}^{(n)})^T \Delta\mathbf{x}^{(n+1)} &\leq 0. \qquad (2.135)
\end{aligned}$$

By applying the relation $\lambda_j^{(n+1)} = \lambda_j^{(n)} + \Delta\lambda_j^{(n+1)}$ expression (2.130) can be rearranged as given by

$$\lambda_j^{(n+1)} g_j(\mathbf{x}^{(n)}) + \lambda_j^{(n)} \nabla_x g_j(\mathbf{x}^{(n)})^T \Delta\mathbf{x}^{(n+1)} = 0. \tag{2.136}$$

Additionally, if $\lambda_j^{(n)}$ of the second summand of (2.136) is exchanged by $\lambda_j^{(n+1)}$, expression

$$\lambda_j^{(n+1)} (g_j(\mathbf{x}^{(n)}) + \nabla_x g_j(\mathbf{x}^{(n)})^T \Delta\mathbf{x}^{(n+1)}) = 0 \tag{2.137}$$

is obtained. Expression

$$\begin{aligned} &\nabla_x f(\mathbf{x}^n) + \sum_{j=1}^{n_g} \lambda_j^{(n)} \nabla_x g_j(\mathbf{x}^{(n)}) + \sum_{i=1}^{n_h} \mu_i^{(n)} \nabla_x h_i(\mathbf{x}^{(n)}) + B^{(n)} \Delta\mathbf{x}^{(n+1)} + \\ &\sum_{j=1}^{n_g} \nabla_x g_j(\mathbf{x}^{(n)}) \Delta\lambda_j^{(n+1)} + \sum_{i=1}^{n_h} \nabla_x h_i(\mathbf{x}^{(n)}) \Delta\mu_i^{(n+1)} = \mathbf{0} \end{aligned} \tag{2.138}$$

is derived by inserting (2.128) in (2.129) and introducing the abbreviation $B^{(n)}$ for the terms comprising the second derivative of $f(\mathbf{x})$ with respect to $\mathbf{x}$. The relations $\lambda_j^{(n+1)} = \lambda_j^{(n)} + \Delta\lambda_j^{(n+1)}$ and $\mu_j^{(n+1)} = \mu_j^{(n)} + \Delta\mu_j^{(n+1)}$allow to write (2.138) in the form given by

$$\nabla_x f(\mathbf{x}^n) + B^{(n)} \Delta\mathbf{x}^{(n+1)} + \sum_{j=1}^{n_g} \nabla_x g_j(\mathbf{x}^{(n)}) \lambda_j^{(n+1)} + \sum_{i=1}^{n_h} \nabla_x h_i(\mathbf{x}^{(n)}) \mu_i^{(n+1)} = \mathbf{0}. \tag{2.139}$$

For a better overview, the additional constraints (2.135) and the rearranged equations (2.139), (2.137) are summarized by

$$\begin{aligned} \lambda_i^{(n+1)} &\geq 0, \\ \lambda_j^{(n+1)} (g_j(\mathbf{x}^{(n)}) + \nabla_x g_j(\mathbf{x}^{(n)})^T \Delta\mathbf{x}^{(n+1)}) &= 0, \\ \nabla_x f(\mathbf{x}^n) + B^{(n)} \Delta\mathbf{x}^{(n+1)} + \sum_{j=1}^{n_g} \nabla_x g_j(\mathbf{x}^{(n)}) \lambda_j^{(n+1)} + \sum_{i=1}^{n_h} \nabla_x h_i(\mathbf{x}^{(n)}) \mu_i^{(n+1)} &= \mathbf{0}, \\ g_j(\mathbf{x}^{(n)}) + \nabla_x g_j(\mathbf{x}^{(n)})^T \Delta\mathbf{x}_j^{(n+1)} &\leq 0, \\ h_i(\mathbf{x}^{(n)}) + \nabla_x h_i(\mathbf{x}^{(n)})^T \Delta\mathbf{x}_i^{(n+1)} &= 0. \end{aligned} \tag{2.140}$$

Equation (2.131) is not affected by the additional constraints and is therefore repeated. Due to the linearization of the original problem and the introduced

additional constraints (2.135), the equations (2.140) describe the Kuhn-Tucker optimality conditions of a quadratic function as given by

$$\begin{aligned} \text{minimize:} \qquad & \nabla_x f(\mathbf{x}^n)^T \mathbf{s} + \frac{1}{2} \mathbf{s}^T B^{(n)} \mathbf{s}, \\ & g_j(\mathbf{x}^{(n)}) + \nabla_x g_j(\mathbf{x}^{(n)})^T \mathbf{s} \leq 0, \\ & h_i(\mathbf{x}^{(n)}) + \nabla_x h_i(\mathbf{x}^{(n)})^T \mathbf{s} = 0. \end{aligned} \tag{2.141}$$

The shown considerations allow formulating an optimization algorithm which is referred to as Sequential Quadratic Programming (SQP). Starting from a solution $\mathbf{x}^{(n)}$, it is possible to formulate an optimization problem on the basis of a quadratic function, which is also called quadratic program, for improving the solution $\mathbf{x}^{(n)}$. Thereby, each optimization step comprises the solution of a quadratic sub program. A drawback of the method is the determination of the Hessian matrix, which is computational expensive. Quasi-Newton methods give an approximation of the Hessian matrix by a reduced cost. The Broyden-Fletcher-Goldfarb-Shanno (BFGS) is a well known member of the class of the quasi-Newton methods. Thereby, [39] and [25] are given as references for this method. Provided the Hessian matrix $B^{(n)}$ is positive semidefinite $\Delta\mathbf{x}^T B^{(n)} \Delta\mathbf{x} \geq 0$, the quadratic problem (2.141) is convex and a solution, which complies the Kuhn-Tucker conditions is a global minimum. For this case efficient solution strategies, like the interior-point methods, exist, which are described in [25]. In order to enforce a positive semidefinite Hessian matrix, the BFGS method can be modified as suggested by Powell [25].

2.7 Summary

Generally, evolutionary strategies are characterized by low demands regarding the structure of the fitness landscape. These optimization procedures are able to search for an optimum based on zero-order information. As derivatives of the fitness function are not needed, evolutionary strategies are suitable for discontinuous optimization problems. The ability to overcome local minima is a further property of these optimization algorithms. For the analysis of the constitutive laws, real-valued as well as integer-valued parameters have to be considered. Therefore, for this task an evolutionary strategy comprising the introduced derandomized self adaptation is applied, as this algorithm is able to treat mixed-integer optimization problems. However, some investigations of this thesis are solely based on real-valued object variables. In these cases also the $(\mu/\mu, \lambda)$-CMA-ES, whose field of application is limited to real-valued object variables, is applied and compared with the $(1, \lambda)$-DR-ES. Provided the corresponding landscape of the optimization problem is unimodal, it is expected that the $(1 + 1)$-CMA-ES algorithm shows a better performance in comparison with the $(\mu/\mu, \lambda)$-CMA-ES [20]. This property

of the $(1+1)$-CMA-ES can give additional insight into the optimization task. As long as the search spaces of the optimization tasks are real-valued in this thesis, the performance of the evolutionary strategies is compared with the deterministic SQP algorithm.

Chapter 3

Production process of sheet metal parts

3.1 Introduction

The manufacturing of sheet metal parts for car bodies usually consists of several process steps. The original blank is transformed into the desired part shape by stamping, postforming, trimming and piercing operations. For each of these operations a part specific tool has to be designed. For the manufacturing of parts, the tools are mounted in a press line. Additional handling systems are necessary in order to transport the intermediate products from one press to the next one. The whole process runs usually fully automatic, which leads to high productivity. The design of the production process is determined by the producibility of the sheet metal part, the minimization of the sheet metal consumption, the robustness regarding scattering of the material behavior and the process conditions. Further aspects are the minimization of the investments for the tools, the required geometrical tolerances of the part and functionality demands like the mechanical strength of crash relevant parts.

3.2 The stamping operation

In the following chapter, production processes are discussed, which start with a stamping operation. The term stamping is used for describing the first shaping operation of the process and the term postforming is applied for the remaining shaping stages. The experiments of this thesis are based on stamping operations. Hence, in this thesis a detailed discussion of the design and the functionality of trimming and postforming operations is omitted. For a comprehensive description of stamping operations, a simplified example is introduced, as depicted in figure 3.1.

Figure 3.1: Example; The geometry of the part.

Figures 3.2 and 3.3 show a stamping operation, which is related to the mentioned example. The following section focuses on the description of the sequence of the stamping operation.

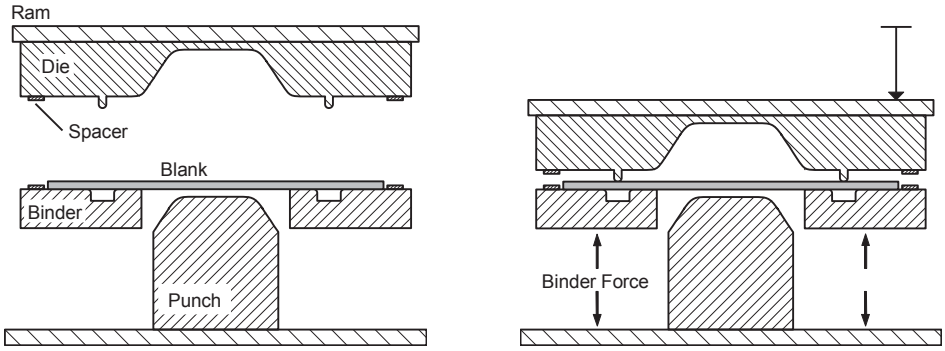

Figure 3.2: Example; Left: Initial position of the tool; Right: Illustration of the state, when the die, the blank and the binder are in contact.

The initial state of the press after inserting the blank into the tool is illustrated by figure 3.2 (left). During the first phase of the operation the press ram goes down. As soon as the die, the blank and the binder are in contact, the binder force begins to act against the die (figure 3.2 (right)). It has to be mentioned, that the binder force progression depends on the motion of the binder. For the built up of the desired binder force, a press specific level of binder movement is necessary. In the second phase of the operation, the drawbeads are formed, if existent, which completes the binder closing phase (figure 3.3 (left)). The functionality of drawbeads will be explained in the next section. Afterwards, the die goes down until the tool is closed and the material is formed according to the geometry of the die and the punch (figure 3.3 (right))[1]. During this phase, the material is plastically strained. The material flow in the binder zone strongly affects the result of the stamping operation. For controlling the material flow, there is a window of permissible levels of restraining forces. On the one hand, exceeding the upper limit of the restraining forces leads to an insufficient material flow, which causes material failure. On the other hand there is a tendency for wrinkles, if the material is not restrained enough [41].

[1] An introduction in press and tooling technology can be found in [40].

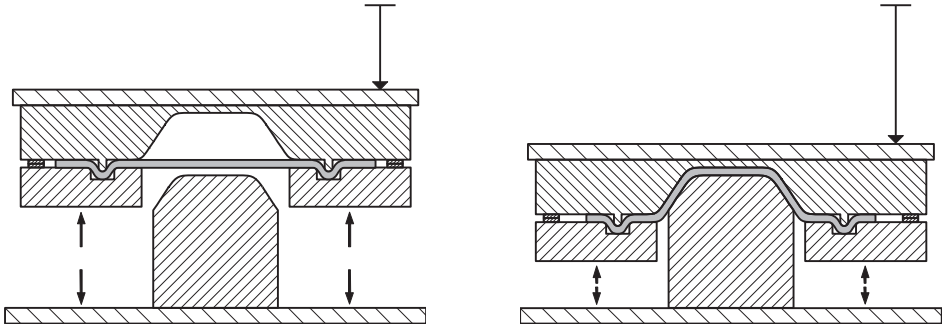

Figure 3.3: Example; Left: State of the tool after binder closing; Right: Final position of the tool after the forming operation.

The binder is connected with a hydraulic system, which is able to induce the desired binder force. The binder force causes a restraining force resulting from the frictional response between the binder, the blank and the die. This is one way to control the material flow of the sheet metal during the stamping operation. Another method for controlling the material flow are drawbeads, which are located perpendicular to the material flow in the binder region, as depicted in figure 3.5. While the material passes through the drawbead additional mechanical work needs to be done. This causes restraining forces acting in the opposite direction of the material flow. The mentioned solution can be applied locally in the binder zone. As opposed to the binder force, the drawbeads are more robust regarding scattering process conditions. The disadvantage of using drawbeads is the additional material consumption.

The edge contour of the formed material is a function of the restraining forces and the blank geometry. Figure 3.4 (right) shows the material flow of a stamping operation without a drawbead. The minimization of the material consumption implies that the edge of the blank moves close to the die radius during the stamping operation. If the edge of the sheet metal reaches the die radius zone, a discontinuity with respect to the restraining forces is caused, because the binder cannot control the material flow anymore. Such discontinuities can lead to process instabilities, which are usually omitted. In the case the operation contains drawbeads (figure 3.4(left)), the edge of the blank should not move into the drawbead, otherwise the continuity of the restraining forces is also disturbed. Figure 3.4 also demonstrates the fact, that drawbeads can increase the material consumption of the production process. Thereby, an equivalent strain field is assumed in the zones, which do not pass through the drawbead during the stamping operation.

Subsequently, the springback effect is introduced. In the closed state of the tool the contact forces between formed material and the die face are in equilibrium. When the tool opens, the mentioned forces cannot act anymore. The stamped part enters another equilibrium state, which is accompanied with a de-

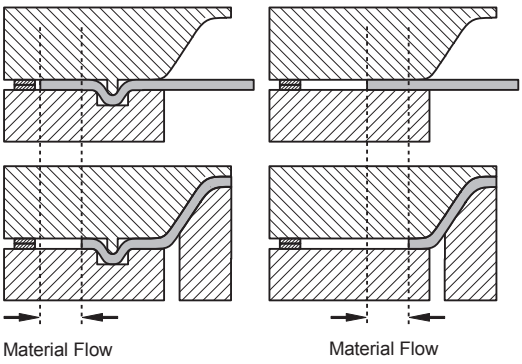

Figure 3.4: Comparison of the material flow with (left) and without (right) applying a drawbead.

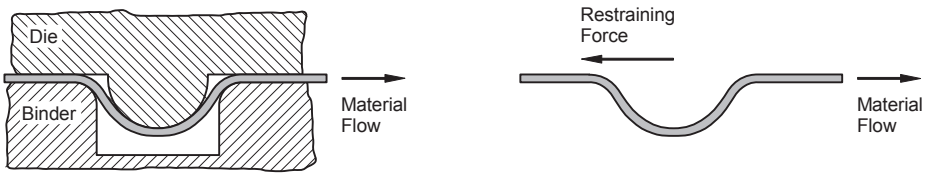

Figure 3.5: Drawbead; Left: Geometry of the drawbead; Right: The drawbead induces restraining forces, which act in the opposite direction of the material flow.

formation. This physical effect is called springback. In order to deal with this effect a tool modification, called springback compensation, is computed based on the deformation caused by the springback effect. The objective is to obtain the desired part geometry after it has reached the final equilibrium state. A description of the methods needed for a springback compensation is given in [42] and [43].

For the commissioning of the stamping tools the binder has to be touched up and the radii of the punch and die are polished. The above mentioned function of the binder regarding the control of the material flow requires a constant pressure distribution between the die, the blank and the binder.

Moreover, the system, consisting of the press, the tool and the sheet metal are slightly elastically deformed during the stamping operation [44],[45] and [46]. Therefore, it is necessary to modify the binder surface slightly, in order to obtain a constant pressure distribution. This modification has to be done manually in the tool shop. Spacers (figure 3.6), adjustable in height, between the binder and the die, give the operator of the production process in the press shop the chance to modify the above discussed pressure distribution locally. Such modifications are necessary to deal with scattering process conditions.

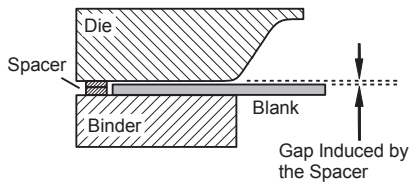

Figure 3.6: Illustration of a spacer.

3.3 Development of production processes

Usually the part geometry is given in the coordinate system of the product (global coordinate system of the car design). The first step of the production process development is the definition of the part alignment with respect to the direction of the press ram movement. A possible approach is to introduce an additional coordinate system, as depicted in figure 3.7, for the definition of this alignment. In the example of this thesis the z-coordinate is defined to be coincident with direction of the press ram movement. Regarding the stamping operation, the minimization of the sheet metal consumption, the consideration of the undercut condition and avoidance of wrinkles have to be taken into consideration. The term undercut is defined in the next section. Furthermore, subsequent operations in the direction of the press ram movement are preferred; otherwise an additional tool investment is necessary for the redirection of the press motion within the tool.

Therefore, for finding the best part alignment, all of the production operations have to be taken into consideration.

Figure 3.7: Definition of the drawing direction.

Any straight line parallel to the direction of the press ram movement, which causes two or more intersections with the part surface, defines points belonging to a region of undercut. Obviously, the regions of undercut change, if the part alignment with respect to the stamping direction changes (figure 3.8 (middle)). Aligned parts or intermediate geometries, which are produced by stamping operations, must not have any zone of undercut. If any alignment of the part violates the undercut condition, an intermediate shape has to be designed (figure 3.8 (right)). Such a geometry enables the engineer to remove the zones of undercut by splitting the shaping of the part in different operations. In this case at least one postforming operation is needed for the production of the desired part geometry.

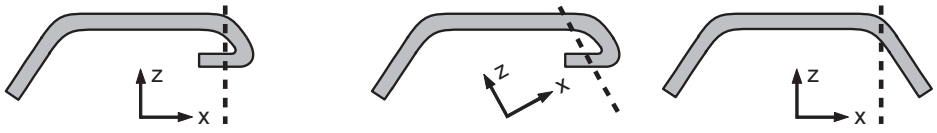

Figure 3.8: Example; Left: Analysis of the undercut of the part geometry with respect to direction 1. The part geometry possesses a zone of undercut with respect to the selected direction; Middle: Analysis of the undercut of the part geometry with respect to direction 2. The shown modification of the part alignment also leads to a zone of undercut; Right: Analysis of the undercut with respect to the intermediate geometry. This geometry in combination with the selected drawing direction does not show any undercut but needs an additional forming step.

As a next step the binder surface is designed. The main functionalities of the binder are the above mentioned material flow control and the avoidance of wrinkles. The second function cannot be explained by the example, depicted in figure 3.1. Especially for complex double-curved part geometries a non trivial binder geometry is necessary in order to deal with wrinkling effects. Wrinkles are caused by differences concerning the developed length of different cross sections of the same normal direction with respect to the die surface.

Finally the gap between the part geometry, respectively the intermediate shape and the binder has to be closed. This geometry is called addendum (figure 3.9 (left)). The geometry of the stamping operation is derived from the part or the

intermediate geometry and the binder and the addendum (figure 3.9 (right)). The subsequent operations are also designed at the same time.

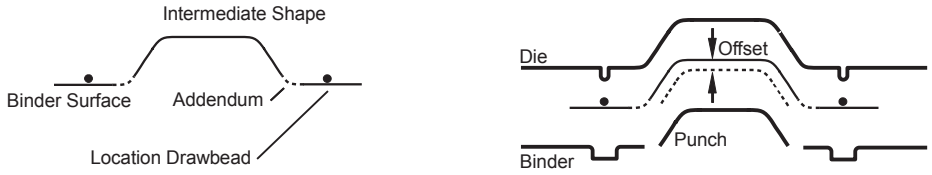

Figure 3.9: Example; Left: Illustration of a stamping operation based on the intermediate shape; Right: Derivation of the tool surfaces.

Today, the design of the production processes is supported by CAD systems. All process relevant surfaces and contours are described by a 3D model. Based on the process design the tool design is initiated and finite element analyses are performed. Such a simulation enables the design engineer to evaluate the stamping operation with respect to material failure and the development of wrinkles. As soon as a satisfying design has been found for the stamping operation, the subsequent operations are also analyzed based on a simulation. If the process has finally reached a mature state the springback is analyzed and, if necessary, compensated. For complex parts the design of a production process is a non trivial task. Usually, several optimization loops are necessary, to find the desired optimum regarding the mentioned conditions.

3.4 Example

By looking at the example, obviously, there is no part alignment, which does not violate the undercut condition figure 3.8 (left) and 3.8 (middle). Therefore, an intermediate shape is introduced as depicted in figure 3.8 (right). This geometry, in conjunction with the addendum and the binder, leads to the design of the stamping operation with respect to the tool surfaces (figure 3.9). The tool design is shown, schematically, by figures 3.2 and 3.3. As depicted in figure 3.10 the stamped material is trimmed in another operation and finally postformed in order to obtain the desired part geometry.

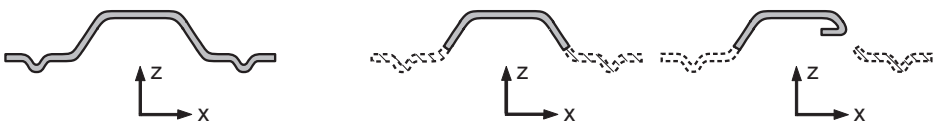

Figure 3.10: Example; Illustration of the production process; Left: Stamping operation; Middle: Trimming operation; Right: Postforming operation.

3.5 Industrial production process

As a further example the production stages of a side panel are given, which are illustrated by figure A.1. The process starts with a stamping operation (OP1) and is followed by two trimming operations (OP2, OP3). The remaining process steps (OP4, OP5, OP6) contain further trimming, piercing and postforming operations. Generally, car body shell parts like the side panel have to fulfill high requirements regarding the surface quality. Wrinkles, arising during stamping usually have a negative impact on the quality of the car body shell. Consequently, the stamping operation comprises a complex double-curved binder surface in order to minimize the development of wrinkles. The trimming of the part is distributed to several operations in order to enable an automatic disposal of the trimmed material.

Chapter 4

Steels for car bodies

4.1 The crystalline structure of metals

Metals, generally, consist of a crystalline structure. Technical metals are produced by a transformation from the liquid to the solid state. The growth of the metallic lattice starts locally at crystallization seeds. The crystals, resulting from different crystallization seeds, are called grains. In the final solid state of the metal the grain boundaries are in contact with each other [47]. In a perfect metal the electrons are not attached to a specific nucleus. This state of the electrons is called electron gas. Electrostatic forces are acting between the positively charged nuclei and the electron gas. Because of the nuclear structure of the metals it is possible for nuclei to change their position without affecting significantly the electrostatic equilibrium state [47].

4.2 The elastic behavior of metals

As long as a mechanical system returns to the initial state after load removal, the deformation is referred to as elastic. Loads applied to a structure consisting of metal atoms, cause a variation of the interatomic spacing of the nuclei. The atomic reaction is necessary in order to reach an equilibrium state with respect to the external load. After the load is removed, the nuclei return to their original position. Generally, elastic deformations change the volume of the metal. Provided, the metallic lattice is free of defects, the material will be deformed elastically until brittle fracture occurs [48].

4.3 The plastic behavior of metals

Plastic deformations are not reversible after load removal. The condition for the occurrence of a permanent deformation is the mentioned possibility of nuclei, to

change their position in a metallic lattice and the presence of defects that disturb the crystalline structure. Such defects usually occur in metals for technical applications during the growing phase of the crystalline structure. Typical defects are missing nuclei and foreign atoms, which are integrated in the crystalline structure. The mechanism of plastic deformation is based on the movement of dislocations, which are linear defects. Plastic yielding usually occurs in conjunction with an elastic deformation. At a low level of the external load, the material is deformed elastically, which generates the internal forces for the load balance. Higher load levels activate the movement of dislocations. In the simplest case the dislocations move along a line through the crystal, which is called slip line. Figure 4.1 illustrates the slip displacement of a dislocation [48]. For the movement of a dislocation from one lattice position to the next one, only the bonds in the vicinity have to be broken. Therefore the energy, necessary for the slip displacement, is relatively small [47] compared with breaking of the atomic bond. Since the movement of dislocation does not alter the crystal structure of the metal, the volume is not affected by this displacement mechanism [49]. The theory of plasticity assumes a macroscopically uniform strain distribution. However, as mentioned above, on microscopic scale the plastic deformation is confined to the slip of dislocations [50]. The force, necessary for the dislocation movement, is anisotropic with respect to the lattice axis. The lowest level of internal forces arises in planes with the highest density of nuclei. The lattice axes of the grains are randomly orientated in the metal. Statistically, the effect of the mentioned anisotropy disappears due to the high amount of grains. As the anisotropy does not affect the macroscopic behavior of the material, the metal properties are regarded as quasi isotropic [47]. Mechanical processes, such as cold rolling, can cause a preferred orientation of the grains, which leads to an anisotropy with respect to the plastic properties.

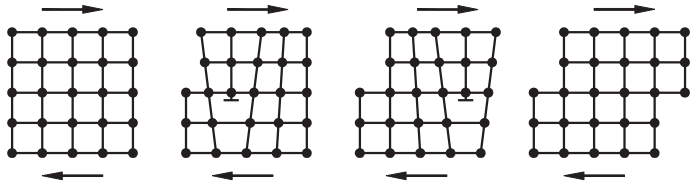

Figure 4.1: Slip displacement of a dislocation [48].

The strength of a metal is affected by several effects. With an increasing strain also the density of dislocations is increasing. In this case there is a need for a higher internal force level in order to move the dislocations, as the slip lines are blocking each other. This effect is called hardening. Provided the hardening effect would not exist, the maximum external force which could be applied to a structure would be determined by the force state initializing the dislocation movement. The

initial strength of a metal is also affected by the size of the grains and the presence of foreign atoms. Generally, the grain boundaries are obstructing the movement of the dislocations. The smaller the grains of a constant volume of metal are, the bigger the surface of the grain boundaries is. Therefore the size of the grains affect the slip displacement (Hall-Petch relation [51]). Additionally, the grain refinement also leads to an increased ductility of the material. Foreign atoms, dissolved in the metallic lattice, can also hinder the movement of the dislocations.

4.4 Metallurgy of steels

The remaining part of this chapter will be focused on steels. Iron carbon alloys, which can be forged without any additional treatment are called steels (concentration of carbon $< 2\%$ [52]). Even small variations of the carbon concentration can lead to remarkable changes of the steel characteristics. The crystalline structure of steels depends on the temperature. Some structures are just stable in a specific temperature range [53]. The lattice structures of steel are the cubic centered crystals of ferrite and the face centered crystals of austenite (figure 4.3). The iron-carbon phase diagram (figure 4.2) describes the crystalline structure in dependence on the carbon concentration and the temperature. The diagram is valid for very low cooling rates, which means the system is always in a thermodynamic equilibrium, and in the absence of other alloying elements. For example, if the melt with a carbon content in the range between 0.02% and 0.8% is cooled from 1600 degree Celsius to room temperature under the condition of the thermodynamic equilibrium, the austenite, which exists above $723°C$ [47] (figure 4.2), is transformed into a cubic centered lattice. The face centered crystals of austenite can dissolve more carbon atoms than the cubic centered ferrite. The carbon, which cannot be dissolved by the cubic centered lattice, precipitates as cementite and forms a lamellar structure with the ferrite. The characteristics of the ferrite phase are low hardness and high formability, whereas the cementite exhibits a high hardness and brittleness [47]. The phase, consisting of ferrite and cementite, is referred to as perlite. Provided, the cooling rate is violating the thermodynamic equilibrium, the diffusion of the carbon atoms is hinted. In this case a very fine distributed cementite phase is formed, which is also called bainite [52]. At high cooling rates the austenite transforms into a cubic centered lattice and the carbon atoms are trapped, which means they do not have enough time to diffuse out of the crystal structure. This leads to a distorted cubic centered lattice, which is called martensite. The formation of martensite causes a rising strength and mechanical hardness of steel. A side effect is the decreasing formability and the brittle material behavior [53]. In order to reduce the brittleness of martensitic steels, it is possible to perform a heat treatment, which is called tempering. This procedure enables the precipitation of iron carbides, which reduces the distortion of the cubic centered lattice. Finally a steel is obtained, which shows a compromise between a high hardness and an acceptable brittleness. Because of the high cooling rate, martensite is not shown in the iron-carbon phase diagram [54].

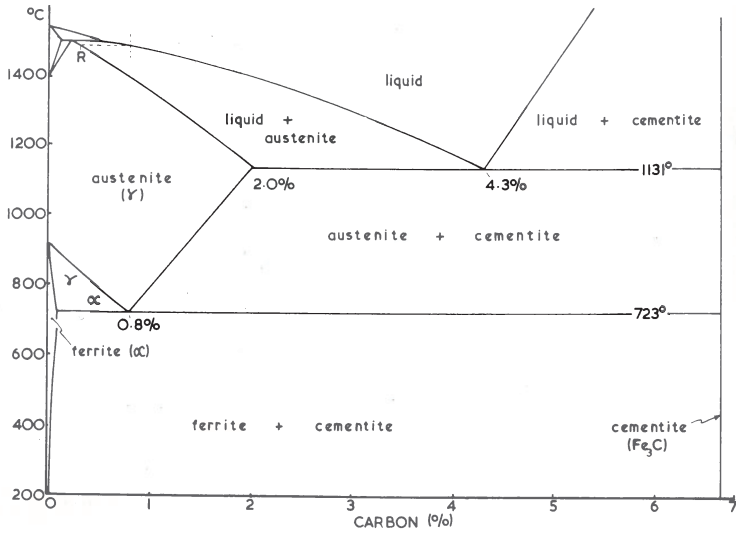

Figure 4.2: Illustration of an Iron-Carbon phase diagram [54].

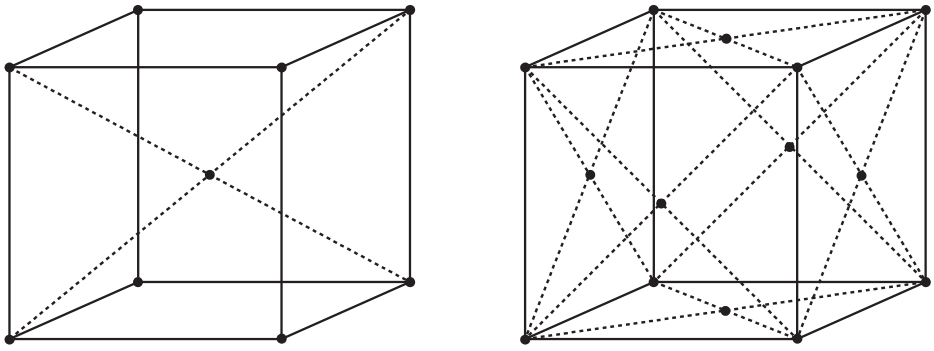

Figure 4.3: Left: Model of a cubic centered crystal.; Right: Model of a face centered crystal.

The diffusion rate of carbon can be decreased by adding additional alloying elements. As a consequence, the required cooling rate for obtaining martensite is reduced [47]. Alloying elements can also lead to the existence of austenite at ambient temperature and increase the strength of the steel based on finely dispersed carbides [52]. These carbides hinder the movement of the dislocations.

4.5 Steelmaking

The primary source material for the steel production is iron ore, lime and coke. Iron ore, occurring in the nature, is consisting of iron oxides and sulphides (Fe_3O_4;Fe_2O_3;$FeCO_3$;FeS_2), accompanied by other molecules like silicon oxides, manganese oxides and phosphorus oxides (SiO_2;Al_2O_3;CaO;MgO;P_2O_5) [55]. The conversion of iron ore to raw iron is performed in a furnace and is mainly consisting of the chemical reduction of iron oxides. The coke provides the carbon, which is necessary for the reduction process. Carbon has a higher affinity to oxygen than iron. Hence, the carbon removes the oxygen from the iron oxides. Additionally the silicon oxides, the manganese oxides and the phosphorus oxides are also reduced by the carbon. The sulphur is removed from the iron sulphides by the lime [55]. Finally raw iron is obtained from this process step. Raw iron is used for casting processes and for the steel production. The latter will be discussed in more detail in the next section.

For steelmaking, a converter is charged by hot raw iron. The task of the converter is to reduce the carbon concentration of the raw material. This is done by blowing oxygen into the converter, which leads to a chemical reaction between the oxygen and the carbon of the raw iron. The reaction product (CO) is gaseous and leaks out of the converter. The primary metallurgy ends with this process step. Other converters are used for the final composition of the alloying elements and for obtaining extremely low carbon contents, which is called secondary metallurgy. For the subsequent production steps the material is casted and transferred to the hot-rolling mill. If the production process is not immediately continued, slabs are cast.

In the case the hot-rolling process is run based on slabs, it is necessary to heat up the material again. In the hot-rolling mill the material is descaled, rolled for obtaining the desired sheet thickness, cooled and coiled. The result of this production step is referred to as hot-rolled strip. Additionally it is possible to produce hot-dip or electrolytically coated hot-rolled strips, if the material is not cold rolled. The production path of cold-rolled sheet comprises pickling, cold-rolling, annealing, cooling, temper-rolling and coiling. A hot-dip coated sheet is produced based on a modified annealing and cooling operation. Electrolytically coated cold-rolled sheets are made in a subsequent process step.

Hot-rolled strips are usually produced in thickness range of 1.6mm to 6 mm. Instead of cold-rolled sheets the hot-rolled strips tend to shrink and show less accuracy regarding the planarity and the thickness. The advantage of the latter mentioned type of sheet is the lower price as the cold-rolling process is not

required. Cold-rolled sheets are available with a thickness below than 1.6mm.

4.6 Steels for the automotive industry

In the following section, some cold-rolled steel types, for the application in the automotive industry, are discussed (for further details see [56]).

As mentioned above, carbon can be dissolved in the lattice structure of steels. This non stoichiometric compound between the iron and the carbon is referred to as interstitial bond. Steels, which consist of a ferrite structure without any dissolved carbon, are called interstitial free steels (IF-Steels). The structure of these steels comprises extremely small amounts of carbon. In order to remove the carbon from the ferrite structure the steel is alloyed with niobium or titanium. The alloying elements cause the formation of carbides and nitrides. The pure ferrite structure leads to an excellent formability and hardening properties. Furthermore such steels show a high resistance to aging [57]. These steels are applied for geometrical highly complex parts, as door inners or fenders.

In contrast to the IF-steels, the micro-alloyed steels show on the one hand a higher initial strength but on the other hand a lower formability. The reason for the mechanical characteristic of this steel type is the structure, consisting of fine grains and the finely dispersed carbides. Additionally, the amount of carbon is higher compared to IF-steels. The fine grains and the carbides hinder the movement of the dislocations, as discussed above, which finally increases the strengths of the steel. The carbides are formed by alloying the steel with niobium, titanium and vanadium. The fields of application of micro-alloyed steels are structural parts and crash relevant parts.

Lastly, dual-phase steels are discussed in this section, which consist of a martensite and a ferrite phase. Dual-phase steels show a relatively low initial strength, due to the ferrite, and a high tensile strength caused by the martensite. Another property of such steels is high energy absorption capacity, caused by the pronounced hardening effect. During the annealing process in the cold-rolling mill, the steel is partially transformed to austenite. The remaining non transformed phase is ferrite. Subsequently, the steel is fast cooled and the austenite transforms into martensite. Usually, dual-phase steels also contain very small amounts of retained austenite and bainite. Alloying elements like, manganese, chromium, molybdenum, silicon and vanadium are used in order to decrease the critical cooling temperature. The alloying concept has to be adapted to the possible cooling rates of the annealing line, which depends on the cooling facilities, the sheet thickness and the line speed. Hot dip galvanizing is performed during the annealing processes. As such production lines are characterized by a lower cooling rate, the amount of alloying elements has to be increased for suppressing the formation of bainite [58]. Dual-phase steels are used for geometrical complex structural parts and for crash relevant parts because of the high energy absorption capacity.

4.7 Summary

Today, the modeling of the elasto-plastic material behavior of sheet metals at the atomic level is computationally too expensive for industrial applications. Consequently, a suitable approximation of the microscopic level is needed to obtain applicable mathematical formulations for modeling the material response. Thereby, on the one hand a reduction of the complexity of the material behavior is necessary. On the other hand, the dominating characteristic of the material response needs to be reflected by such material models. An introduction of these models is given in chapter 5.2. The above mentioned anisotropy, which is induced by the cold rolling process, is a crucial material property of sheet metals, which are applied for car body parts. This effect also has to be considered by material models, which are used for forming simulations.

Chapter 5

Forming simulation

5.1 Continuum mechanics

5.1.1 Introduction

Mechanics is concerned with the investigation of the motion of material bodies under the influence of forces. In continuum mechanics the assumption is made, that the matter is continuously distributed in space [59]. The properties and the response of the matter are described by smooth scalar-, vector- or tensor-valued functions and the number of discontinuities is finite. Hence, microscopical inhomogeneities of the matter due to the molecular structure are ignored in continuum mechanics. An exception are constitutive models, which sometimes deal with the microscopical structure of the matter. But the response and the properties of such models are also assumed to be smooth and the number of discontinuities is again finite [60]. The notation, applied for the presentation of continuum mechanics, is taken from Haupt [59].

5.1.2 Kinematics

The kinematics describes the motion of a body. Figure 5.1 shows a material body B in the initial χ_{t_0} and in the deformed state χ_t. The latter mentioned state is called deformed or current configuration. The initial state is referred to as reference or undeformed configuration. The concept of different configurations is needed in order to measure the deformation of a body. The term initial configuration should be viewed as an idealization, because usually in reality such a state does not exist [60]. As the internal force state of solids depends on its deformation and the history of its deformation, a reference configuration is needed in order to label the material points. The vector variable $\mathbf{X}$, based on a Cartesian coordinate system, is defined on this configuration and does not change with time [60]. The components of the vector $\mathbf{X}$ are called material or Lagrangian coordinates. The

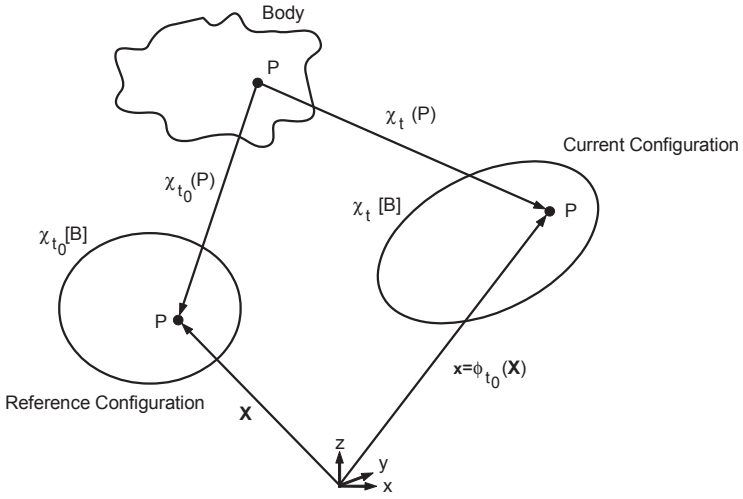

B: Body; $\mathbb{E}^3$: Euclidean Space; $\chi_{t_0}[B] \subset \mathbb{E}^3$; $\chi_t[B] \subset \mathbb{E}^3$

Figure 5.1: A reference and a deformed configuration [59].

relation between the deformed configuration χ_t and the reference configuration χ_{t_0} is described by the mapping function [61]:

$$\mathbf{x} = \phi_{t_0}(\mathbf{X}, t), \ \mathbf{X} \in \chi_{t_0}[B], \ \mathbf{x} \in \chi_t[B]. \tag{5.1}$$

As the current configuration is time-depended, the mapping is a function of time t. The coordinates of the vector $\mathbf{x}$, which give the position of the material point $\mathbf{X}$ at the time t, are called spatial or Eulerian coordinates.

A pure rigid motion, as formulated in (5.2), does not lead to any variation of the distance between material points:

$$\mathbf{x} = \mathbf{Q}(t)(\mathbf{X} - \mathbf{X}_o) + \mathbf{x}_0(t). \tag{5.2}$$

In this case the material is considered as unstrained. The rigid motion consists of a rotation about $\mathbf{X}_0$ defined by the orthogonal tensor $\mathbf{Q}(t)$ and a translation $\mathbf{x}_0(t)$. The rotation $\mathbf{Q}(t)$ has the following properties:

$$\mathbf{Q}^T = \mathbf{Q}^{-1}, \ \mathbf{Q}\mathbf{Q}^T = \mathbf{1}. \tag{5.3}$$

If the distance between material points changes, strains occur. In this case the motion deviates from a rigid body motion. Hence, a meaningful strain measure should filter out the rigid body motion [62]. For the characterization of the deformation the term deformation gradient is introduced:

$$\mathbf{F} = \frac{\partial \mathbf{x}}{\partial \mathbf{X}}. \tag{5.4}$$

Provided the motion is rigid, the deformation gradient gives the following result:

$$\mathbf{F} = \frac{\partial \left(\mathbf{Q}\left(t\right) \left(\mathbf{X} - \mathbf{X}_o \right) + \mathbf{x}_0 \left(t\right) \right)}{\partial \mathbf{X}} = \mathbf{Q}\left(t\right). \tag{5.5}$$

Obviously, the deformation gradient of a rigid body motion is identical with the associated rotation tensor. The tensor

$$\mathbf{E} = \frac{1}{2}\left(\mathbf{F}^T\mathbf{F} - \mathbf{1} \right) \tag{5.6}$$

represents a strain measure called Green strain tensor. Expression (5.7) shows the result of this tensor in the case of a rigid body motion:

$$\mathbf{E} = \frac{1}{2}\left(\mathbf{Q}^T\mathbf{Q} - \mathbf{1} \right) = \frac{1}{2}\left(\mathbf{1} - \mathbf{1} \right) = 0. \tag{5.7}$$

Consequently, this tensor is invariant regarding rigid body motions, which is the most important feature of strain measures. The Green strain tensor is not a unique measure for strains. There are many other strain measures, which are used in continuum mechanics. Subsequently, a strain rate measure, called rate-of-deformation, is introduced. For this tensor the definition of the velocity gradient is necessary

$$\begin{aligned} \mathbf{L} &= grad\mathbf{v} = \frac{\partial \mathbf{v}}{\partial \mathbf{x}} = \frac{\partial \mathbf{v}}{\partial \mathbf{X}} \frac{\partial \mathbf{X}}{\partial \mathbf{x}}, \\ \mathbf{F}^{-1} &= \frac{\partial \mathbf{X}}{\partial \mathbf{x}}, \\ \frac{\partial \mathbf{v}}{\partial \mathbf{X}} &= \frac{\partial}{\partial t}\frac{\partial \mathbf{x}}{\partial \mathbf{X}} = \frac{\partial}{\partial t}\mathbf{F} = \dot{\mathbf{F}}, \\ \mathbf{L} &= \dot{\mathbf{F}}\mathbf{F}^{-1}. \end{aligned} \tag{5.8}$$

The rate-of-deformation is defined by

$$\mathbf{D} = \mathrm{sym}\left(\mathrm{grad}\mathbf{v} \right) = \frac{1}{2}\left(\mathbf{L} + \mathbf{L}^T \right). \tag{5.9}$$

This tensor is also invariant with respect to rigid body motions. The proof can be found in [61].

5.1.3 Balance relations

This section deals with the balance relations for mass, linear momentum, rotational momentum and energy. These relations are considered to be universal laws of nature [59]. The free-body principle forms the foundation for the formulation of the balance relations. According to this principle, a slice of a body B in the

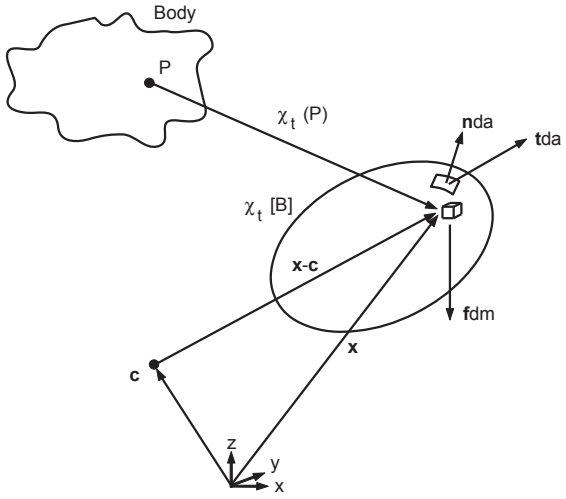

Figure 5.2: Force and torque [59].

current configuration χ_t with a finite volume and a piecewise smooth surface is imaginary cut out. The influence from the environment on this domain is substituted by physical quantities [59].

Figure 5.2 shows the physical quantities, which are involved in the momentum balance equations. The depicted slice is assumed to be in the current configuration. The physical quantities are divided into the external surface force density $\mathbf{t}$ (Cauchy stress vector) and the external volume force density per unit mass $\mathbf{f}$ (5.10), the external torque (5.11) with respect to the point $\mathbf{c}$, the linear momentum (5.12) and the rotational momentum (5.13):

$$\mathbf{F}(B,t) = \iint\limits_{\partial\chi_t(B)} \mathbf{t}\,\mathrm{d}a + \iiint\limits_{\chi_t(B)} \mathbf{f}\rho\,\mathrm{d}v, \tag{5.10}$$

$$\mathbf{M_C}(B,t) = \iint\limits_{\partial\chi_t(B)} (\mathbf{x}-\mathbf{c}) \times \mathbf{t}\,\mathrm{d}a + \iiint\limits_{\chi_t(B)} (\mathbf{x}-\mathbf{c}) \times \mathbf{f}\rho\,\mathrm{d}v, \tag{5.11}$$

$$\mathbf{I}(B,t) = \iiint\limits_{\chi_t(B)} \mathbf{v}\rho\,\mathrm{d}v, \tag{5.12}$$

$$\mathbf{D}_c(B,t) = \iiint\limits_{\chi_t(B)} (\mathbf{x}-\mathbf{c}) \times \mathbf{v}\rho\,\mathrm{d}v. \tag{5.13}$$

The balance equation of linear momentum (5.14) implies the equivalence of the external forces and the material time derivative of linear momentum:

$$\frac{\mathrm{d}}{\mathrm{d}t}\mathbf{I}\left(B,t\right)=\mathbf{F}\left(B,t\right). \tag{5.14}$$

As a consequence the material, belonging to the above mentioned domain, is accelerated if a resultant external force exists. In the case of static problems the material time derivative of linear momentum has to vanish. Hence, the resultant external force of the considered domain, has to be zero.

At this point, it should be mentioned, that the time derivative has to be performed with respect to a material point. As the material points are not fixed in space, the material time derivative has to take the material movement into account. The concept of the reference and the current configuration gives at any time a unique identification of material points for the computation of this derivative[1]. The material time derivative of a quantity is equal to the partial derivative with respect to time, if this quantity is represented by Lagrangian coordinates.

The balance equation of linear momentum does not take rotational movements into account. Therefore, equation (5.15) requires the equivalence of the change of the rotational momentum and the external torque, which is called balance of rotational momentum:

$$\frac{\mathrm{d}}{\mathrm{d}t}\mathbf{D}_c\left(B,t\right)=\mathbf{M}_c\left(B,t\right). \tag{5.15}$$

The balance of mass requires that the mass of any imaginary cut-out domain has to be constant. This means the matter does not pass the boundaries of the domain.

$$\frac{\mathrm{d}}{\mathrm{d}t}m\left(B,t\right)=0 \tag{5.16}$$

Finally, the balance of energy is presented by

$$\dot{K}\left(B,t\right)+\dot{E}\left(B,t\right)=L_e\left(B,t\right)+Q\left(B,t\right). \tag{5.17}$$

This equation contains the internal energy

$$E\left(B,t\right)=\iiint\limits_{\chi_t[B]} e\rho\mathrm{d}v, \tag{5.18}$$

the kinetic energy

$$K\left(B,t\right)=\frac{1}{2}\iiint\limits_{\chi_t[B]} \mathbf{v}^2\rho\mathrm{d}v, \tag{5.19}$$

the power of the external forces

[1] A comprehensive description of material time derivatives can be found in [60].

$$L_e\left(B,t\right) = \iint\limits_{\partial\chi_t[B]} \mathbf{t}\cdot\mathbf{v}\mathrm{d}a + \iiint\limits_{\chi_t[B]} \mathbf{f}\cdot\mathbf{v}\rho\mathrm{d}v, \tag{5.20}$$

and the resultant heat supply

$$Q\left(B,t\right) = \iint\limits_{\partial\chi_t[B]} q\mathrm{d}a + \iiint\limits_{\chi_t[B]} r\rho\mathrm{d}v. \tag{5.21}$$

The quantity e is called specific internal energy per unit mass. The heat flow density is described by q and r is referred to as heat supply per unit mass.

The presented formulation of the fundamental laws are valid for closed systems, i. e., an exchange of matter with the environment is not allowed. An extension of the presented fundamental laws for open systems can be found in [59].

5.1.4 Stress tensor

An important assumption in continuum mechanics is the linear dependence of the Cauchy stress vector $\mathbf{t}$ with respect to the surface normal $\mathbf{n}$ (5.22) of a cut-out domain [59]:

$$\mathbf{t}\left(\mathbf{x},t,\mathbf{n}\right) = \boldsymbol{\sigma}\left(\mathbf{x},t\right)\cdot\mathbf{n}. \tag{5.22}$$

The second-order tensor field $\boldsymbol{\sigma}(\mathbf{x},t)$ is called Cauchy stress. Based on this relation and the divergence theorem

$$\iint\limits_{a} \boldsymbol{\sigma}\cdot\mathbf{n}\mathrm{d}a = \iiint\limits_{v} \mathrm{div}\left(\boldsymbol{\sigma}\right)\mathrm{d}v, \tag{5.23}$$

the equation for the balance of linear momentum

$$\frac{\mathrm{d}}{\mathrm{d}t}\iiint\limits_{\chi_t[B]} \mathbf{v}\rho\mathrm{d}v - \iint\limits_{\partial\chi_t[B]} \mathbf{t}\mathrm{d}a - \iiint\limits_{\chi_t[B]} \mathbf{f}\rho\mathrm{d}v = \mathbf{0} \tag{5.24}$$

can be transformed into its local form by substituting the surface integral with a volume integral

$$\iiint\limits_{\chi_t[B]} \dot{\mathbf{v}}\rho - \mathrm{div}\boldsymbol{\sigma} - \mathbf{f}\rho\mathrm{d}v = \mathbf{0}. \tag{5.25}$$

As expression (5.25) has to be valid for any given volume of integration,

$$\dot{\mathbf{v}}\rho - \mathrm{div}\boldsymbol{\sigma} - \mathbf{f}\rho = \mathbf{0} \tag{5.26}$$

holds. The same transformation can be performed with the balance of rotational momentum. In [59] the derivation of the local form is described in detail. The local form of the balance of rotational momentum is given by

$$\boldsymbol{\sigma} = \boldsymbol{\sigma}^T. \tag{5.27}$$

As a consequence, the Cauchy stress tensor is symmetric, as long as the balance of rotational momentum is fulfilled.

The local form of energy balance equations is given by ($q = -\mathbf{qn}$)

$$\dot{e}\left(\mathbf{x}, t\right) = -\frac{1}{\rho}\mathrm{div}\mathbf{q} + r + \frac{1}{\rho}\boldsymbol{\sigma} : \mathrm{grad}\mathbf{v}. \tag{5.28}$$

The vector $\mathbf{q}$ is called Cauchy heat flux vector and is similarly derived as the Cauchy stress tensor. As long as the thermodynamical quantities $\mathbf{q}$ and r are not taken into account, the balance equation reduces to

$$\dot{e}\left(\mathbf{x}, t\right) = \frac{1}{\rho}\boldsymbol{\sigma} : \mathrm{grad}\mathbf{v}. \tag{5.29}$$

As the contraction of the tensorial product on two indices of a symmetric and a skew symmetric tensor is zero as shown by

$$\boldsymbol{\sigma} : \mathrm{grad}\mathbf{v} = \boldsymbol{\sigma} : \mathrm{sym}\left(\mathrm{grad}\mathbf{v}\right) = \boldsymbol{\sigma} : \mathbf{D}, \tag{5.30}$$

(5.29) can be expressed as given by

$$\dot{e}\left(\mathbf{x}, t\right) = \frac{1}{\rho}\boldsymbol{\sigma} : \mathbf{D}. \tag{5.31}$$

The physically significant product of the stress tensor and the strain rate tensor has to remain invariant. This connection between the mentioned tensors is also referred to as conjugation in power. As mentioned above, there are various definitions of strain rate tensors but the only one, which can be applied in conjunction with the Cauchy stress tensor, is the rate of deformation. For each type of strain rate tensor a stress tensor is necessary, which is conjugate in power. For example the conjugate stress tensor of the Green strain rate $\dot{\mathbf{E}}$ is the Second Piola-Kirchhoff stress tensor, as defined by

$$\mathbf{S} = \det\left(\mathbf{F}\right)\mathbf{F}^{-1}\boldsymbol{\sigma}\mathbf{F}^{-T}. \tag{5.32}$$

This symmetric stress tensor $\mathbf{S}$ refers to the reference configuration.

5.1.5 Initial and boundary conditions

The formulation of an initial-boundary-value problem consists of the balance equations, the constitutive laws and suitably defined initial and boundary conditions. Initial conditions are prescribed position or velocity distributions, defined at the beginning of the motion. Boundary conditions are either applied for stipulating a motion or a stress vector. The first mentioned case is referred to as geometric boundary condition. The prescription of stress vectors is called dynamic boundary condition [59].

5.2 Constitutive laws - stress-strain relation

5.2.1 Introduction

The relation between strains and stresses is formulated by the constitutive equations. Generally, constitutive laws are material specific relations between two physical quantities. In this work, constitutive laws for describing the stress-strain relation and the frictional response in a contact interface are discussed. As opposed to the introduced balance laws, the constitutive equations are non-universal in nature.

5.2.2 Formulation of constitutive laws

Truesdell [1] mentions three general principles for the design of constitutive laws:

- According to the principle of determinism, the current stress state of a material point is uniquely determined by the past history of the body's motion.
- Additionally the stress state is only affected by the history of motion of the point's environment. This principle is called local action. In this work only simple materials are discussed, in which the stress state of a material point is determined by the history of its deformation gradient.
- Finally, according to the principle of observer-invariance, the material response should remain unchanged under a superposed rigid body motion.

Materials can show a direction dependent material behavior. In other words, the change of the reference configuration can affect the material response. A symmetry group contains all possible changes of the reference configuration, which do not affect the material response. Expression (5.33) shows the associated mathematical representation of the constitutive functional based on the stress state

$$\boldsymbol{\sigma}(t) = \mathfrak{F}\left(\mathbf{F}(t)\right) = \mathfrak{F}\left(\mathbf{F}(t)\mathbf{H}\right). \tag{5.33}$$

Thereby, $\mathbf{H}$ is a time-independent tensor, belonging to the symmetry group and possessing the property $|\det(\mathbf{H})| = 1$ [59]. This property contains the assumption that any change of the volume should also alter the material response. The symmetry group of solids is a subset of the orthogonal tensors [62]. If the symmetry group is identical to the entire set of orthogonal tensors, the material is said to be isotropic.

Materials may show a disproportionally strong resistance to certain types of deformation. Kinematic conditions are introduced to model such material properties [59]. The plastic incompressibility, which will be discussed below, is an example for such a material behavior. Finally, the compliance of the principle of irreversibility has to be assured. However, today there is no generally valid and

universally acknowledged formulation of the principle of irreversibility. On the basis of experience, the Clausius-Duhem inequality proved its worth in continuum mechanics [59].

Subsequently, material models will be presented, which are applied for the description of the elasto-plastic material behavior of sheet metals. Furthermore, this chapter is focused on material models, which are suitable for forming simulations.

5.2.3 Split of the strain tensor

For modeling the elasto-plastic response of sheet metals, a domain is introduced, which defines the admissible stress states. The material response of a material point is elastic, if the associated stress state is not on the boundary of this domain. In this case only elastic strains occur. If the stress state is on the boundary of this domain, plastic yielding may occur. The strains related to plastic yielding are referred to as plastic strains. The total strains are a combination of elastic and plastic strains. A crucial issue of formulating elasto-plastic material models is the decomposition of the plastic and the elastic strains from the total strains. Two approaches are commonly used for forming simulations. Expression

$$\mathbf{D} = \mathbf{D}^e + \mathbf{D}^p \tag{5.34}$$

shows the additive split of the rate-of-deformation and

$$\mathbf{F} = \mathbf{F}^e \mathbf{F}^p \tag{5.35}$$

gives the multiplicative split of the deformation gradient. Especially, the multiplicative split leads to a very complicated representation of the constitutive law. In order to simplify the representations of the material model, infinitesimal deformations are assumed. Nevertheless, the presented elasto-plastic models can be extended for large deformations.

5.2.4 Infinitesimal deformations

In this section, the term infinitesimal deformation is defined and the consequences regarding continuum mechanics are discussed. The definition of infinitesimal deformations is taken from Haupt [59]. $\mathbf{u}(\mathbf{X}, t)$ is defined as the difference between the Eulerian and the Lagrangian coordinates:

$$\mathbf{u}(\mathbf{X}, t) = \mathbf{x} - \mathbf{X}. \tag{5.36}$$

Strains are considered to be small, if (5.37) and (5.38) are valid:

$$\|\mathbf{H}\| \ll 1, \ \|\mathbf{H}\| = \sqrt{\mathbf{H} : \mathbf{H}}, \tag{5.37}$$

$$|\mathbf{u}(\mathbf{X}, t)| \ll L_0. \tag{5.38}$$

L_0 is the characteristic length of the body. The definition of $\mathbf{H}$ is given by

$$\mathbf{H}(\mathbf{X},t) = \mathrm{Grad}\mathbf{u}(\mathbf{X},t). \tag{5.39}$$

For infinitesimal deformations, the difference between the reference and the current configuration is negligible, which implies expression

$$\mathbf{u}(\mathbf{X},t) \approx \mathbf{u}(\mathbf{x},t). \tag{5.40}$$

The assumption of infinitesimal deformations enables the linearization of the strain tensor

$$\boldsymbol{\epsilon} = \frac{1}{2}\left[\mathrm{grad}\mathbf{u}(\mathbf{x},t) + \mathrm{grad}\mathbf{u}(\mathbf{x},t)^T\right]. \tag{5.41}$$

For infinitesimal deformations, the additive split of the total strain is assumed

$$\boldsymbol{\epsilon} = \boldsymbol{\epsilon}^e + \boldsymbol{\epsilon}^p. \tag{5.42}$$

5.2.5 Elasticity

First of all, the modeling of an isotropic elastic material behavior is discussed in this section. Expression (5.43) shows an elastic constitutive law, which is applied for infinitesimal elastic strains:

$$\boldsymbol{\sigma} = \mathbf{C} : \boldsymbol{\epsilon}. \tag{5.43}$$

The relation between the stress state and the strain state is linear. Expression (5.44) shows a possible definition of the fourth order tensor $\mathbf{C}$ [61]:

$$\mathbf{C} = \lambda\mathbf{1}\otimes\mathbf{1} + 2\mu\mathbf{I}. \tag{5.44}$$

The material model contains the parameters λ and μ, which are called Lamé constants. For the expression (5.44) the second-order identity tensor $\mathbf{1}$ and the fourth-order symmetric identity tensor $\mathbf{I}$ is applied. A definition of these tensors is given in the appendix B. If the contraction of the tensorial product on two indices is performed, (5.44) can be written in the following form [48]:

$$\sigma_{ij} = \lambda\epsilon_{kk}\delta_{ij} + 2\mu\epsilon_{ij}. \tag{5.45}$$

The expressions (5.46) and (5.47) give the Young's modulus E and the Poisson ratio υ dependent on the Lamé constants:

$$E = \mu\frac{3\lambda + 2\mu}{\lambda + \mu}, \tag{5.46}$$

$$\upsilon = \frac{\lambda}{2(\lambda + \mu)}. \tag{5.47}$$

The elastic constitutive law may be derived from the potential:

$$\Psi = \frac{1}{2\rho}\boldsymbol{\epsilon} : \mathbf{C} : \boldsymbol{\epsilon}. \tag{5.48}$$

This approach will be useful for the derivation of the elasto-plastic constitutive law. The stress tensor is obtained from this potential as shown by

$$\boldsymbol{\sigma} = \rho\frac{\partial\Psi}{\partial\boldsymbol{\epsilon}} = \mathbf{C} : \boldsymbol{\epsilon}. \tag{5.49}$$

5.2.6 Plastic incompressibility

As mentioned in chapter 4, an elastic deformation of steel may be accompanied with a change of the volume. In contrast, the mechanism, causing plastic yielding, preserves the volume of the deformed material. This effect is termed hypothesis of plastic incompressibility [48]. In order to account for the incompressibility, the stress tensor is additively split into a hydrostatic and a deviatoric part

$$\mathrm{dev}\left(\boldsymbol{\sigma}\right) = \boldsymbol{\sigma} - \frac{1}{3}tr\left(\boldsymbol{\sigma}\right)\mathbf{1} = \mathbf{S}. \tag{5.50}$$

Only hydrostatic stresses can affect the volume of the material. Hence, the constitutive law for modeling plasticity only depends on the deviatoric part of the stress state.

5.2.7 Clausius-Duhem inequality

As opposed to the elastic response of the material, the plastic yielding is history dependent. The presented constitutive law is formulated on the basis of the internal variable concept. The internal variables are representing the deformation history of the material, like the hardening of the material. Plastic yielding is an irreversible material response, as the movement of the dislocations in the metal lattice, causing plastic yielding, cannot be reversed. For modeling the plastic material response, the compliance of this irreversibility is assured by the application of the Clausius-Duhem inequality:

$$\boldsymbol{\sigma} : \dot{\boldsymbol{\epsilon}} - \rho\left(\dot{\Psi} + s\dot{t}\right) - \mathbf{q}\cdot\frac{\mathrm{grad}\left(t\right)}{t} \geq 0. \tag{5.51}$$

The subsequent derivation of the mechanical dissipation is taken from Chaboche [48]. ρ is the density of the material, s the specific entropy, t the temperature and $\mathbf{q}$ the heat flux. The free energy is given by

$$\Psi = e - ts. \tag{5.52}$$

Under a constant ($\dot{t} = 0$) and uniform ($\mathrm{grad}\left(t\right) = 0$) temperature distribution, which is assumed in this thesis, the Clausius-Duhem inequality might be rewritten in the following form

$$\boldsymbol{\sigma} : \dot{\boldsymbol{\epsilon}} - \rho\dot{\Psi} \geq 0. \tag{5.53}$$

If the existence of a free energy potential, depending on the strain state and the internal variables, is assumed

$$\Psi\left(\boldsymbol{\epsilon}, \boldsymbol{\epsilon}^p, t, \boldsymbol{\alpha}_k\right), \tag{5.54}$$

the time derivative of the free energy can be expressed by

$$\dot{\Psi} = \frac{\partial \Psi}{\partial \boldsymbol{\epsilon}^e} : \dot{\boldsymbol{\epsilon}}^e + \frac{\partial \Psi}{\partial t}\dot{t} + \frac{\partial \Psi}{\partial \boldsymbol{\alpha}_k} * \dot{\boldsymbol{\alpha}}_k. \tag{5.55}$$

The symbol $*$ represents the suitable product, depending on the type of the internal variable (scalar, vector, tensor). As a constitutive law may consist of several internal variables, the index k is introduced. The derivation of (5.55) implies the assumption that Ψ is only affected by $\boldsymbol{\epsilon}^e$, which leads to a representation of the free energy, depending on the elastic strain, the temperature and the internal variables

$$\Psi\left(\boldsymbol{\epsilon}, \boldsymbol{\epsilon}^p, t, \boldsymbol{\alpha}_k\right) = \Psi\left(\left(\boldsymbol{\epsilon} - \boldsymbol{\epsilon}^p\right), t, \boldsymbol{\alpha}_k\right) = \Psi\left(\boldsymbol{\epsilon}^e, t, \boldsymbol{\alpha}_k\right). \tag{5.56}$$

Expression (5.57) shows the time derivative of the free energy ($\dot{t} = 0, \mathrm{grad}\,(t) = 0$):

$$\dot{\Psi} = \frac{\partial \Psi}{\partial \boldsymbol{\epsilon}^e} : \dot{\boldsymbol{\epsilon}}^e + \frac{\partial \Psi}{\partial \boldsymbol{\alpha}_k} * \dot{\boldsymbol{\alpha}}_k. \tag{5.57}$$

Expression (5.58) is obtained by inserting (5.57) into (5.53) and applying the additive split of the strain tensor for the stress power term $\boldsymbol{\sigma} : \dot{\boldsymbol{\epsilon}}$:

$$\boldsymbol{\sigma} : \dot{\boldsymbol{\epsilon}}^p + \boldsymbol{\sigma} : \dot{\boldsymbol{\epsilon}}^e - \rho\left(\frac{\partial \Psi}{\partial \boldsymbol{\epsilon}^e} : \dot{\boldsymbol{\epsilon}}^e + \frac{\partial \Psi}{\partial \boldsymbol{\alpha}_k} * \dot{\boldsymbol{\alpha}}_k\right) \geq 0. \tag{5.58}$$

The left hand side of (5.58) is termed as mechanical dissipation, which is the difference of the stress power $\boldsymbol{\sigma} : \dot{\boldsymbol{\epsilon}}$ and the change of the internal energy [61]. For an elastic deformation of a material, the dissipation is equal to zero. The forces, which are associated with the internal variables, are termed

$$\mathbf{q}_k = \rho\frac{\partial \Psi}{\partial \boldsymbol{\alpha}_k}. \tag{5.59}$$

If the constitutive law of elasticity (5.49) and (5.59) is inserted in (5.58), (5.60) is obtained

$$\boldsymbol{\sigma} : \dot{\boldsymbol{\epsilon}}^p - \mathbf{q}_k * \dot{\boldsymbol{\alpha}}_k \geq 0. \tag{5.60}$$

This form of the Clausius-Duhem inequality is subsequently applied for the derivation of the associative elasto-plastic constitutive law.

5.2.8 Elasto-plastic constitutive law

On the basis of the principle of maximum dissipation, which is often credited to von Mises [61], the associative elasto-plastic constitutive law is derived. As stated above, plastic yielding may occur, if the stress state is located on the boundary of the domain of the admissible stress states. Mathematically, the domain is described by a function f, which is termed as yield locus. f is a function of the stress state and the associated forces of the internal variables. $f = 0$ represents the boundary of the domain

$$f\left(\boldsymbol{\sigma}, \mathbf{q}_k\right) = 0. \tag{5.61}$$

Among the possible admissible states $\boldsymbol{\tau}$ and $\mathbf{p}$, $\boldsymbol{\sigma}$ and $\mathbf{q}$ is the actual state, which maximizes the dissipation (5.60)($\mathbb{S}$ $\in$space of the symmetric tensors):

$$D^p\left(\boldsymbol{\sigma}, \mathbf{q}_k, \dot{\boldsymbol{\epsilon}}^p \dot{\boldsymbol{\alpha}}_k\right) = \max_{\boldsymbol{\tau} \in \mathbb{E}_\sigma} \left(D^p\left(\boldsymbol{\tau}, \mathbf{p}_k, \dot{\boldsymbol{\epsilon}}^p, \dot{\boldsymbol{\alpha}}_k\right)\right), \; \mathbb{E}_\sigma = \left\{\boldsymbol{\tau} \in \mathbb{S} | f\left(\boldsymbol{\tau}, \mathbf{p}_k\right) \leq 0\right\}. \tag{5.62}$$

The maximization of the dissipation can be transformed into a minimization by introducing a negative sign. The dissipation is a linear function of the stress state and the internal variables. Therefore, this function is convex. Provided f is a strictly convex function, the maximization of the plastic dissipation is a convex optimization problem and a unique solution exists [26]. A sufficient regularity of the permissible states of the stress state and the internal variables is assumed. L^p is the Lagrange function of the optimization problem:

$$L^p\left(\boldsymbol{\sigma}, \mathbf{q}_k, \dot{\boldsymbol{\epsilon}}^p, \dot{\boldsymbol{\alpha}}\right) = -\boldsymbol{\sigma} : \dot{\boldsymbol{\epsilon}}^p + \mathbf{q}_k * \dot{\boldsymbol{\alpha}}_k + \lambda f\left(\boldsymbol{\sigma}, \mathbf{q}_k\right). \tag{5.63}$$

The expressions (5.64) and (5.65) show the stationary point of (5.63)

$$\frac{L^p\left(\boldsymbol{\sigma}, \mathbf{q}_k, \dot{\boldsymbol{\epsilon}}^p, \dot{\boldsymbol{\alpha}}\right)}{\partial \boldsymbol{\sigma}} = -\dot{\boldsymbol{\epsilon}}^p + \lambda \frac{\partial f\left(\boldsymbol{\sigma}, \mathbf{q}_k\right)}{\partial \boldsymbol{\sigma}} = 0, \; \dot{\boldsymbol{\epsilon}}^p = \lambda \frac{\partial f\left(\boldsymbol{\sigma}, \mathbf{q}_k\right)}{\partial \boldsymbol{\sigma}}, \tag{5.64}$$

$$\frac{L^p\left(\boldsymbol{\sigma}, \mathbf{q}_k, \dot{\boldsymbol{\epsilon}}^p, \dot{\boldsymbol{\alpha}}\right)}{\partial \mathbf{q}_k} = \dot{\boldsymbol{\alpha}}_k + \lambda \frac{\partial f\left(\boldsymbol{\sigma}, \mathbf{q}_k\right)}{\partial \mathbf{q}_k} = 0, \; \dot{\boldsymbol{\alpha}}_k = -\lambda \frac{\partial f\left(\boldsymbol{\sigma}, \mathbf{q}_k\right)}{\partial \mathbf{q}_k}. \tag{5.65}$$

The solution of the constraint optimization problem has to fulfill, as shown by (5.66), the local Kuhn-Tucker conditions:

$$\lambda \geq 0 \; , \; f\left(\boldsymbol{\sigma}, \mathbf{q}_k\right) \leq 0 \; , \; \lambda f\left(\boldsymbol{\sigma}, \mathbf{q}_k\right) = 0. \tag{5.66}$$

Expression (5.64) shows the evolution equation for the plastic strain and (5.65) the evolution of the internal variables. Plastic yielding occurs, if the yield locus is equal to zero and λ has a positive value. Expression (5.67) is obtained by inserting (5.64) and (5.65) into (5.60):

$$\lambda\boldsymbol{\sigma} : \frac{\partial f\left(\boldsymbol{\sigma}, \mathbf{q}_k\right)}{\partial \boldsymbol{\sigma}} + \lambda\mathbf{q}_k * \frac{\partial f\left(\boldsymbol{\sigma}, \mathbf{q}_k\right)}{\partial \mathbf{q}_k} \geq 0. \tag{5.67}$$

According to (5.67) the Clausius-Duhem inequality is a priori satisfied, if $f(\boldsymbol{\sigma}, \mathbf{q}_k)$ is convex, non-negative and zero-valued at the origin in the $\boldsymbol{\sigma}$ and $\mathbf{q}_k$ space. It is important to mention, that the convexity of f is not a consequence of the principle of irreversibility. However, it is convenient to formulate constitutive laws, which automatically comply the Clausius-Duhem inequality [62]. In associative plastic materials, the yield locus is used as a potential for the formulation of the evolution of the plastic strain and the internal variables. Expressions (5.68) and (5.69) show a generalized formulation of the evolution laws. In this case, the evolution of the plastic strain and the internal variables does not necessarily depend on the yield locus. The stress update algorithm, discussed in the next chapter, is presented on the basis of these equations:

$$\dot{\boldsymbol{\epsilon}}^p = \gamma \mathbf{r}\left(\boldsymbol{\sigma}, \mathbf{q}_k\right), \tag{5.68}$$

$$\dot{\mathbf{q}}_k = \gamma \mathbf{h}\left(\boldsymbol{\sigma}, \mathbf{q}_k\right). \tag{5.69}$$

However, for the investigations of this thesis only the flow rule according the expression (5.64) is applied. Therefore, subsequently the term yield locus also represents the flow rule.

5.2.9 Yield loci

Among a wide range of yield loci, three will be discussed in detail. The von Mises yield locus is suitable for materials, which show an isotropic inelastic material behavior. The Barlat ´89 [2] and the Barlat 2000 yield locus [3] [63] were designed for modeling the anisotropic plastic material behavior of sheet metals.

In order to simplify the formulation of the yield loci, a plastic material response without hardening effect is assumed (perfect plasticity). As a consequence, the yield loci do not contain any internal variables. In the section 5.2.10, the extension of the yield loci for modeling isotropic hardening is discussed.

For the derivation of the von Mises yield locus, a relation between the boundary of the elastic domain and the elastic shear energy [48] is assumed. Expression (5.70) shows the integration of the elastic shear energy w with respect to a material point up to the material response switches from an elastic to an inelastic behavior:

$$w = \int_0^{\boldsymbol{\epsilon}^e} \mathbf{S} : \mathrm{d}\mathbf{E}^e, \; dev(\boldsymbol{\epsilon}) = \mathbf{E}. \tag{5.70}$$

On the basis of the elastic constitutive law (5.44), a relation between the deviatoric strain and stress tensor can be derived [48]:

$$\mathrm{d}\mathbf{E}^e = \left(\frac{1}{2\mu}\right)\mathrm{d}\mathbf{S}. \tag{5.71}$$

The application of (5.71) enables the formulation of the shear energy for arbitrary stress states

$$w = \int_0^{\mathbf{s}} \frac{1}{2\mu}\mathbf{S} : \mathrm{d}\mathbf{S} = \frac{1}{4\mu}\mathbf{S} : \mathbf{S}. \tag{5.72}$$

According to the von Mises criterion, plastic yielding occurs at the same level of w independent of the loading path. Hence, it is sufficient to determine w on the basis of a single experiment. The beginning of plastic yielding for an arbitrary loading path can be predicted by comparing the elastic shear energy with the experimental determined value of w. Usually, w is determined by a tensile test (chapter 6). The stress state of this experiment is uniaxial

$$\boldsymbol{\sigma} = \begin{bmatrix} Y_0 & 0 & 0 \\ 0 & 0 & 0 \\ 0 & 0 & 0 \end{bmatrix}, \; \mathbf{S} = \begin{bmatrix} \frac{2}{3}Y_0 & 0 & 0 \\ 0 & -\frac{1}{3}Y_0 & 0 \\ 0 & 0 & -\frac{1}{3}Y_0 \end{bmatrix}. \tag{5.73}$$

Expression (5.74) shows the relation between the initial yield strength Y_0 and the shear energy, which is derived by inserting (5.73) in (5.72):

$$w = \left(\frac{1}{6}\mu\right) \cdot Y_0^2. \tag{5.74}$$

The given expressions (5.72),(5.74) enable to eliminate w

$$\frac{1}{4\mu}\mathbf{S} : \mathbf{S} = \frac{1}{6\mu}Y_0^2. \tag{5.75}$$

A rearrangement of (5.75) gives (5.76), which is referred to as von Mises yield locus:

$$f = \left(\frac{3}{2}\mathbf{S} : \mathbf{S}\right)^{\frac{1}{2}} - Y_0 = 0. \tag{5.76}$$

The introduction of the equivalent stress, shown by (5.77), will be useful for the definition of the hardening law (M: von Mises):

$$\overline{\sigma}^M = \left(\frac{3}{2}\mathbf{S} : \mathbf{S}\right)^{\frac{1}{2}}. \tag{5.77}$$

The yield locus gives negative values for stress states, which belong to the elastic domain, and is equal to zero for stress states on the boundary of the elastic domain. Hence, the function fulfills the above discussed requirements regarding a yield locus.

The rolling processes of the steel production causes an anisotropic material behavior (chapter 4), which is uniformly directed. Subsequently, two yield loci

are introduced, which are able to take this effect into account. The axes of anisotropy are coincident with the rolling direction, the transverse direction in the plane of the sheet and normal to this plane [8]. The shape of the boundary of the elastic domain will be referred to as yield locus shape in this work. The Barlat 2000 yield locus considers the direction dependent material behavior by a parameterized yield locus shape. This means, the onset of plastic yielding depends on the stress state. However, the values of the stress tensor depend on its basis. In order to obtain a unique description of the anisotropy, the basis of the stress tensor has to be coincident with the axes of anisotropy. Mathematically, the parameterization of the yield locus shape consists of two linear mappings of a given stress tensor, which can be controlled by the α_i values, and the yield locus exponent a:

$$\begin{bmatrix} L'_{11} \\ L'_{12} \\ L'_{21} \\ L'_{22} \\ L'_{66} \end{bmatrix} = \frac{1}{3} \begin{bmatrix} 2 & 0 & 0 \\ -1 & 0 & 0 \\ 0 & -1 & 0 \\ 0 & 2 & 0 \\ 0 & 0 & 3 \end{bmatrix} \begin{bmatrix} \alpha_1 \\ \alpha_2 \\ \alpha_7 \end{bmatrix}, \tag{5.78}$$

$$\begin{bmatrix} L''_{11} \\ L''_{12} \\ L''_{21} \\ L''_{22} \\ L''_{66} \end{bmatrix} = \frac{1}{9} \begin{bmatrix} -2 & 2 & 8 & -2 & 0 \\ 1 & -4 & -4 & 4 & 0 \\ 4 & -4 & -4 & 1 & 0 \\ -2 & 8 & 2 & -2 & 0 \\ 0 & 0 & 0 & 0 & 9 \end{bmatrix} \begin{bmatrix} \alpha_3 \\ \alpha_4 \\ \alpha_5 \\ \alpha_6 \\ \alpha_8 \end{bmatrix}, \tag{5.79}$$

$$\begin{bmatrix} X'_{11} \\ X'_{22} \\ X'_{12} \end{bmatrix} = \begin{bmatrix} L'_{11} & L'_{12} & 0 \\ L'_{21} & L'_{22} & 0 \\ 0 & 0 & L'_{66} \end{bmatrix} \begin{bmatrix} \sigma_{xx} \\ \sigma_{yy} \\ \sigma_{xy} \end{bmatrix}, \tag{5.80}$$

$$\begin{bmatrix} X''_{11} \\ X''_{22} \\ X''_{12} \end{bmatrix} = \begin{bmatrix} L''_{11} & L''_{12} & 0 \\ L''_{21} & L''_{22} & 0 \\ 0 & 0 & L''_{66} \end{bmatrix} \begin{bmatrix} \sigma_{xx} \\ \sigma_{yy} \\ \sigma_{xy} \end{bmatrix}, \tag{5.81}$$

$$\phi' = \left|X'_1 - X'_2\right|^a, \; \phi'' = \left|2X''_2 + X''_1\right|^a + \left|2X''_1 + X''_2\right|^a, \tag{5.82}$$

$$\phi = \phi' + \phi'' = 2\left(Y_0\right)^a. \tag{5.83}$$

The yield locus is formulated in the principal space of the mapped stress tensors $\left(\mathbf{X}', \mathbf{X}''\right)$. The parameters are obtained by the minimization of the difference between the measured stress states and strain rate ratios (R values) of different experiments (fundamental experiments, chapter 6) and the predictions of the yield locus. The Barlat 2000 yield locus is restricted to plane stress states. For mechanical systems, which are much thinner in one dimension than in the others and subjected to loads generating mainly stresses perpendicular to the direction of the thinnest dimension, the plane stress assumption is often made [62]. In this case, three components of the stress tensor are assumed to be zero as shown by

$$\boldsymbol{\sigma} = \begin{bmatrix} \sigma_{xx} & \sigma_{xy} & 0 \\ \sigma_{yx} & \sigma_{yy} & 0 \\ 0 & 0 & 0 \end{bmatrix}. \tag{5.84}$$

Forming simulations are often performed under the plane stress assumption. The convexity of the yield locus has been proven [3]. Expression (5.85) illustrates the Barlat2000 yield locus in the form as introduced for the von Mises yield locus:

$$f(\boldsymbol{\sigma}) = \overline{\sigma}^{B2000}(\boldsymbol{\sigma}) - Y_0 = \left(\frac{1}{2}\left(\boldsymbol{\phi}' + \boldsymbol{\phi}''\right)\right)^{\frac{1}{a}} - Y_0 = 0. \tag{5.85}$$

Expression

$$f = \left[\frac{1}{2}\phi\right]^{\frac{1}{a}} - Y_0 \tag{5.86}$$

gives the relation between these two formulations of the Barlat 2000 yield locus. Both versions are equivalent as shown by (5.87), which proves that the partial derivative with respect to the stress tensor is the same apart from the constant ψ. Hence, the relation between the stress state and the strain increment differs only by a factor:

$$\frac{\partial f}{\partial \sigma} = \frac{1}{2a}\left[\frac{\phi}{2}\right]^{\frac{(1-a)}{a}} \frac{\partial \phi}{\partial \sigma} = \psi \frac{\partial \phi}{\partial \sigma}. \tag{5.87}$$

From the perspective of the computational implementation, (5.85) should be preferred, because this formulation of the yield locus has the dimension of stress. As opposed to (5.85), (5.83) has the dimension of stress to the power of a. Especially for a large number of a, the evaluation of (5.83) could lead to computationally intractable numbers [62].

Finally, the Barlat ´89 yield locus is introduced, which is given by:

$$K_1 = \frac{\sigma_{xx} + h\sigma_{yy}}{2},\ K_2 = \sqrt{\left(\frac{\sigma_{xx} - h\sigma_{yy}}{2}\right)^2 + p^2\sigma_{xy}^2}, \tag{5.88}$$

$$f(\sigma) = \left(\frac{1}{2}\left[a\left|K_1 + K_2\right|^m + a\left|K_1 - K_2\right|^m + c\left|2K_2\right|^m\right]\right)^{\frac{1}{m}} - Y_0 = 0. \tag{5.89}$$

The Barlat ´89 yield locus reduces to the function proposed by Hill (1948) for the exponent of $m = 2$. The parameters a, c, h and p, which describe the anisotropy of the material, can be obtained from measured R values of tensile tests in three different directions. The parameters a and c are coupled, if a flow curve based on a tensile test in the rolling direction is applied. Another option is to compute the parameters by the minimization of the difference between the measured stress states and strain rate ratios (R values) of different experiments

(fundamental experiments, chapter 6) and the predictions of the yield locus. As the yield locus has a limited amount of parameters, it is necessary to make a compromise regarding the predictive capability with respect to the results of all the fundamental experiments.

5.2.10 Strain hardening

As mentioned above, the hardening effect of the material can be modeled by introducing internal variables. The further derivations are valid for the yield loci, which have been introduced. Subsequently, the hardening effect is assumed to be isotropic. Hence, a scalar internal variable and a scalar associate force are suitable for modeling the material hardening

$$\alpha = \epsilon^p. \tag{5.90}$$

As an internal variable the accumulated equivalent plastic strain is applied. Expression (5.91) shows the definition of the accumulated equivalent plastic strain:

$$\epsilon^p = \int \dot{\epsilon}^p \mathrm{dt},\ \dot{\epsilon}^p = \frac{\boldsymbol{\sigma} : \dot{\boldsymbol{\epsilon}}^p}{\overline{\sigma}}. \tag{5.91}$$

The equivalent plastic strain rate $\dot{\epsilon}^p$ is obtained by assuming the equivalence of the stress power given by the product of the equivalent quantities (equivalent plastic strain rate, equivalent stress) and the contraction of the tensorial quantities on two indices (plastic strain rate tensor, stress tensor). Expression (5.92) shows a postulated hardening law, depending on the internal variable, which is referred to as flow curve:

$$Y\left(\epsilon^p\right) = Y_0 + \kappa\left(\epsilon^p\right). \tag{5.92}$$

Y_0 represents the yield strength and κ is the associated force of the internal variable

$$q = \kappa. \tag{5.93}$$

Expression (5.94) shows the von Mises yield locus in consideration of the isotropic hardening law given by (5.92):

$$f\left(\boldsymbol{\sigma}, \kappa\right) = \left(\frac{3}{2}\mathrm{dev}\left(\boldsymbol{\sigma}\right) : \mathrm{dev}\left(\boldsymbol{\sigma}\right)\right)^{\frac{1}{2}} - \left(Y_0 + \kappa\right) = 0. \tag{5.94}$$

As opposed to expression (5.76) the elastic domain is not constant, if the hardening effect is considered (5.94). Thereby, the elastic domain is enlarged, independent of the loading path, by increasing values of κ. The partial derivative of (5.94) with respect to the associated force of the internal variables leads to

$$\frac{\partial f\left(\boldsymbol{\sigma}, \kappa\right)}{\partial \kappa} = \frac{\left(\partial\left(\frac{3}{2}\mathrm{dev}\left(\boldsymbol{\sigma}\right) : \mathrm{dev}\left(\boldsymbol{\sigma}\right)\right)^{\frac{1}{2}} - \left(Y_0 + \kappa\right)\right)}{\partial \kappa} = -1. \tag{5.95}$$

According to (5.96), the development of $\dot{\epsilon}^p$ is equal to the Lagrange multiplier λ:

$$\dot{\epsilon}^p = -\lambda \frac{\partial f(\boldsymbol{\sigma}, \kappa)}{\partial \kappa} = \lambda. \tag{5.96}$$

The expressions (5.97) summarize the associative elasto-plastic constitutive law for isotropic hardening and the assumption of infinitesimal strains on the basis of the von Mises yield locus:

$$\begin{aligned} \dot{\boldsymbol{\sigma}} &= \mathbf{C} : \dot{\boldsymbol{\epsilon}}, \\ \dot{\boldsymbol{\epsilon}}^p &= \lambda \frac{\partial f(\boldsymbol{\sigma}, \mathbf{q})}{\partial \boldsymbol{\sigma}}, \\ \dot{\epsilon}^p &= \lambda, \\ f(\boldsymbol{\sigma}, \kappa) &= \overline{\sigma}^M(\boldsymbol{\sigma}) - (Y_0 + \kappa(\epsilon^p)), \\ \lambda &\geq 0,\ f(\boldsymbol{\sigma}, \kappa) \leq 0,\ \lambda f(\boldsymbol{\sigma}, \kappa) = 0. \end{aligned} \tag{5.97}$$

5.2.11 Strain rate dependent hardening

The hardening effect can be influenced by the strain rate. A simple model to take this effect into account is the strain rate sensitivity m [64] [65]. Generally, the strain rate sensitivity can be formulated by different choices of the base of the logarithm [66]. In this thesis for the definition of the strain rate sensitivity the natural logarithm is taken and m is assumed to be independent of the strain history. Two tensile tests, performed under different rates (D, dynamic; S, static), are needed in order to identify the model parameter m

$$m = \frac{\ln\left(Y_D(\epsilon^p) / Y_S(\epsilon^p)\right)}{\ln\left(\dot{\epsilon}^p_D / \dot{\epsilon}^p_S\right)}. \tag{5.98}$$

Essentially, this approach modifies the flow curve dependent on the strain rate. Another approach for modeling the strain rate dependent hardening, comprising two model parameters, is the Cowper-Symonds model [67]. Finally also the Johnson-Cook model is mentioned, which is suitable for modeling the hardening behavior strain rate and temperature dependent [68].

5.2.12 The Bauschinger effect

Experimental observations based on uniaxial tests show that the hardening behavior of steel is affected by alternating tensile and compression loading (Bauschinger effect). Figure 5.3 shows a schematic visualization of the stress-strain relation of a specimen that firstly undergoes a uniaxial tensile loading up to point B is reached. Thereby, point A represents the initial yield strength. At point B a uniaxial compression load is induced, which leads to an elastic material response. Plastic

yielding under compression occurs at point C. Provided the absolute value of the uniaxial stress with respect to point C is lower than in point B, as shown by figure 5.3, a material softening occurs induced by the previous tensile loading.

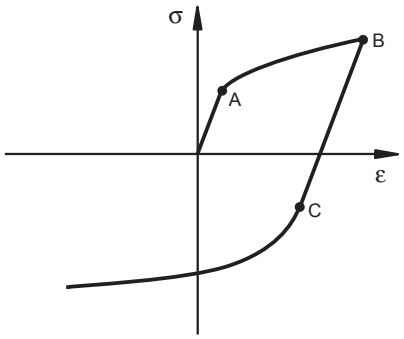

Figure 5.3: Example of the Bauschinger effect (Relation between the true stress σ and the true strain ϵ).

For considering the Bauschinger effect in the multiaxial case, the yield locus is extended by a kinetic stress tensor (back stress tensor) $\mathbf{X}$ as given by relation [7]

$$\bar{\sigma}(\boldsymbol{\sigma} - \mathbf{X}) - \kappa(\epsilon^p) - Y_0 \leq 0. \tag{5.99}$$

The kinematic stress tensor leads to a displacement of the yield locus in the stress space, which allows describing the Bauschinger effect. The evolution of the kinematic stress tensor is given by the non-linear kinematic hardening laws, which are introduced below. Subsequently, the Bauschinger effect is assumed to be isotropic. Consequently, the calibration of kinematic hardening models can be performed on the basis of uniaxial tension and compression tests.

Armstrong Federick law

Expression (5.100) illustrates the kinematic hardening law, suggested by Armstrong and Federick [69]:

$$d\mathbf{X} = C\left(\frac{2}{3}ad\boldsymbol{\epsilon}^p - \mathbf{X}d\epsilon^p\right). \tag{5.100}$$

The model parameters C and a can be calibrated based on an experimentally determined stress-strain relations obtained from uniaxial tension and compression tests. Under the assumption of a von Mises yield locus $f = \left[\frac{3}{2}dev\left(\boldsymbol{\sigma}\right) : dev\left(\boldsymbol{\sigma}\right)\right]^{\frac{1}{2}} - \kappa(\epsilon^p) - Y_0$ and the consideration of the relation (5.64) the following form of the Armstrong Federick law is obtained

$$d\mathbf{X} = C\left(a\frac{\mathbf{S}}{\bar{\sigma}_M} - \mathbf{X}\right)d\epsilon^p. \tag{5.101}$$

As the yield locus is independent of the hydrostatic stress state $f(\boldsymbol{\sigma} - \mathbf{X}) = f(\mathbf{S} - \mathbf{X})$ expression (5.101) can be written as given by

$$d\mathbf{X} = C\left(a\frac{\boldsymbol{\sigma}}{\bar{\sigma}_M} - \mathbf{X}\right)d\epsilon^p. \tag{5.102}$$

Under uniaxial tensile and compression test conditions, only the first eigenvalues of the stress and the kinematic stress tensor are non-zero. Consequently, (5.102) reduces to a scalar equation

$$\mathrm{d}X = C\,(a - X)\,\mathrm{d}\epsilon^p. \tag{5.103}$$

Furthermore, (5.103) comprises the identity $\overline{\sigma}_M = \sigma$. Thereby, σ represents the uniaxial stress and X the uniaxial kinematic stress. The solution of this differential equation is given by [7]

$$X(\epsilon^p) = \nu a + (X_0 - \nu a)e^{-\nu C(\epsilon^p - \epsilon_0^p)}. \tag{5.104}$$

If a specimen undergoes multiple cycles of tension and compression, the evolution of the kinematic stress has to be described by intervals. Each one represents a phase of tension or compression. The initial values X_0, ϵ_{p_0} are the values at the end of the previous phase. Depending on the plastic flow, ν is chosen to be either equal to 1 or -1.

In order to reflect the experimentally determined equivalent stress of this experiment, also the initial yield strength Y_0 and the strain hardening $\kappa(\epsilon_p)$ have to be taken into account as given by [7]

$$Y(\epsilon^p) = \nu a + (X_0 - \nu a)e^{-\nu C(\epsilon^p - \epsilon_0^p)} + \nu\left(\kappa(\epsilon^p) + Y_0\right). \tag{5.105}$$

The model parameters C and a can be calibrated by minimizing the deviation between the stress-strain relation of the model and the experimentally determined one. Thereby, multiple transitions between tension and compression and vice versa under different levels of accumulated plastic strain are necessary.

Chaboche Rousselier law

Chaboche and Rousselier suggest an extension of the Armstrong Federick law, which comprises multiple, additively aggregated, kinematic stress tensors $\mathbf{X} = \sum_{1=i}^{n}\mathbf{X}_i$. A comprehensive description of the Chaboche model can be found in [70]. For each kinematic stress tensor an evolution law is defined as given by

$$d\mathbf{X}_i = \frac{2}{3}C_i d\boldsymbol{\epsilon}^p - \gamma_i \mathbf{X}_i d\epsilon^p. \tag{5.106}$$

For the discussion of the Chaboche Rousselier Law, n is assumed to be equal to 1

$$d\mathbf{X} = \frac{2}{3} C d\boldsymbol{\epsilon}^p - \gamma \mathbf{X} d\epsilon^p. \tag{5.107}$$

The second sub-term on the right hand side limits the evolution of the kinematic stress increments. The maximum possible kinematic stress can be analyzed by determining the stationary point $d\mathbf{X} = 0$. As the strain increment $d\boldsymbol{\epsilon}^p$ is a deviatoric tensor, also $\mathbf{X} = dev(\mathbf{X})$ holds. This relation is only valid, if the initial value of the kinematic stress tensor is also deviatoric (for example $\mathbf{X}_0 = \mathbf{0}$). Consequently, the second invariant of the kinematic stress tensor can be computed by $J_2(\mathbf{X}) = (\frac{3}{2} dev(\mathbf{X}) : dev(\mathbf{X}))^{\frac{1}{2}} = (\frac{3}{2}\mathbf{X} : \mathbf{X})^{\frac{1}{2}}$. In [48] the limit case of the kinematic tensor is discussed on the basis of the second invariant of the kinematic stress tensor. By inserting $d\mathbf{X} = 0$ and $d\epsilon^p = \left[\frac{2}{3} d\boldsymbol{\epsilon}^p : d\boldsymbol{\epsilon}^p\right]^{\frac{1}{2}}$ in (5.107), the limit of the second invariant of the kinetic stress tensor is obtained

$$J_2(\mathbf{X}) \leq \frac{C}{\gamma}. \tag{5.108}$$

According to (5.108), the second invariant of the kinematic stress tensor is limited by a finite boundary. The relation (5.106) can be expressed as illustrated by

$$d\mathbf{X}_i = (C_i \frac{\boldsymbol{\sigma}}{\bar{\sigma}_M} - \gamma_i \mathbf{X}_i) d\epsilon^p, \tag{5.109}$$

which is derived in the same way as shown above on the basis of the Armstrong Federick law. The calibration of (5.109) can be performed as shown for the Armstrong Federick law. However, more model parameters are available for minimizing the deviation between the experimentally determined stress-strain relation and prediction of the model.

In this thesis, the law as given by (5.109) is applied. It has to be mentioned that this law is only equivalent to the Chaboche Rousselier model, if the plasticity model comprises a von Mises yield locus. The initial state of the kinematic tensor is assumed to be zero ($\mathbf{X}_0 = \mathbf{0}$).

5.3 Constitutive laws - friction

The contact of bodies can be accompanied with the transmission of forces between them. As long as the bodies cannot interpenetrate, forces can act in normal direction with respect to the contact interface. Additionally, most of the technical systems transmit non negligible forces in the corresponding tangent direction, induced by the frictional response. Provided the micromechanical behavior of the system in the contact area is neglected, the forces, acting in normal direction, can be treated by introducing a purely geometrical constraint. For modeling the friction, the derivation of a suitable constitutive law is necessary.

Generally, the frictional behavior is strongly affected by the presence of a lubricant. Thereby, the term dry friction describes the case without any lubricant in the contact interface. In this case, the frictional response is determined by the micromechanical behavior, which depends on the material properties of the bodies and their surface roughness [71]. However, technical systems usually comprise a lubricant in the contact zone. Therefore, dry friction has to be considered as a limit case. Provided, the bodies are not directly in contact due to a sufficient amount of lubricant, the frictional forces have to be transmitted solely by the lubricant. Under this condition, the frictional response is only determined by the hydrodynamic properties of the lubricant [72]. The frictional response, occurring in technical applications usually lies between the mentioned extreme cases.

Expression (5.110) shows the commonly applied friction model of Coulomb, which is based on the assumption of dry friction [73]:

$$\mathbf{t}_T(\mathbf{x},t) = -\mu\,|t_N(\mathbf{x},t)|\,\frac{\boldsymbol{\gamma}_T(\mathbf{x},t)}{\|\boldsymbol{\gamma}_T(\mathbf{x},t)\|},\ t_N = \mathbf{t}\cdot\mathbf{n},\ t_N \leq 0. \tag{5.110}$$

All the mentioned quantities refer to one of the two contact surfaces. Thereby, $\mathbf{n}$ describes the normal of the contact surface, $\mathbf{t}$ the surface traction and $\mathbf{t}_T$ the tangent force in the contact zone. $\boldsymbol{\gamma}_T(\mathbf{x},t)$ reflects the relative movement of the bodies in the contact interface in tangent direction. The negative sign is introduced, as the tangent force acts in the opposite direction of the relative movement $\boldsymbol{\gamma}_T$. According to the Coulomb model, the relation between the normal and the tangent force in the contact interface is linear. The model parameter μ is referred to as friction coefficient.

The dependency of the frictional response with respect to the relative velocity in the contact interface, the contact pressure and the temperature are not considered by the Coulomb model. However, it is possible to introduce a friction coefficient, which is a function of these quantities.

Generally, for the production of sheet metal parts in the press shop, lubricants are applied. Due to the contact pressure between the sheet and the tools, a direct contact between the sheet metal and the tool surface is expected. As specialized surface textures of the sheet metal are usually applied, the lubricant can still influence the frictional response in the contact interface [74]. Thereby, the texture partially retains the lubricant. Hence, in sheet metal forming an intermediate frictional behavior with respect to the above introduced extreme cases should occur. As mentioned above, the Coulomb model cannot consider the hydrodynamic frictional response, when a lubricant acts in the contact interface. Nevertheless, in this work, the Coulomb model is applied, which disregards the hydrodynamic effect of the lubricant (5.110).

It is assumed that the neglected effects can be considered, at least on average, by determining the friction coefficient inversely under forming conditions. Furthermore, micromechanical effects, induced by the normal forces, are ignored and therefore the contact in normal direction is represented by a geometrical constraint.

5.4 Failure criterion - Forming limit curve

5.4.1 Introduction

The most common failure mode in sheet metal forming is localized necking. For less ductile metals, fracture may occur without showing this failure mode. This case is not considered in this work. Before the onset of diffuse necking the material response is stable. Depending on the strain state, still additional external loading is possible without entering the localized necking state. The occurrence of localized necking requires a plane strain state. In the phase between the onset of diffuse and localized necking, the strain state is transformed, independent of the previous strain path to the plane strain state. According to Hora [75], this transition is accompanied with a hardening effect, which explains the additional forming capacity of the material. Obviously, in the case of a plane strain state, the material enters directly the localized necking mode, as the transition is unnecessary. Once the local necking zone is formed, the strain increments, caused by additional external loading, concentrate in this zone, whereas the material outside of the neck is marginally strained. Hence, in the state of instability a slight additional external loading leads to fracture. In order to obtain a stable production process of stamping parts in the press shop, the onset of localized necking is considered to be the failure limit and has to be avoided [76].

5.4.2 Prediction of localized necking

For the simulation based prediction of localized necking, the so called direct and indirect method can be applied [75]. For the first mentioned method a high resolution of the finite element mesh is needed, in order to predict the localized strain state directly, as the width of a localized neck is in the dimension of the sheet thickness [77]. Today, typically applied sizes of shell elements in industrial forming simulations are in the dimension of 1-2 times of the sheet thickness. Hence, the resolution of the discretization is insufficient for computing the strain state in the necking zone. Another approach, called indirect method, compares the computed strain and stress tensor fields with limit values.

The widely applied forming limit curve is one of the indirect methods for predicting the onset of localized necking, which is defined in the principal in-plane strain space and was originally introduced by Keeler [78] for $\alpha > 0$ and complemented by Goodwin [79] for $\alpha < 0$. The quantity α is given by expression

$$\alpha = \frac{\dot{\epsilon}_2}{\dot{\epsilon}_1}. \tag{5.111}$$

ϵ_1 and ϵ_2 are the first and second eigenvalues (principal values) of the in-plane strain tensor. Figure 5.4 shows an example of a forming limit curve.

For the evaluation of a forming simulation, the entire stain tensor field of the midsurface is visualized in combination with the forming limit curve (figure 5.5) in the eigenvalue space of the in-plane strain tensor. This diagram is referred to

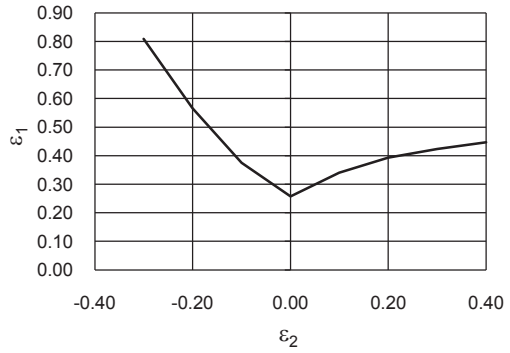

Figure 5.4: Example of a forming limit curve.

as forming limit diagram. A material point is considered to be safe in terms of localized necking under the condition that the associated strain state is located below the limit curve in the in-plane principal strain space.

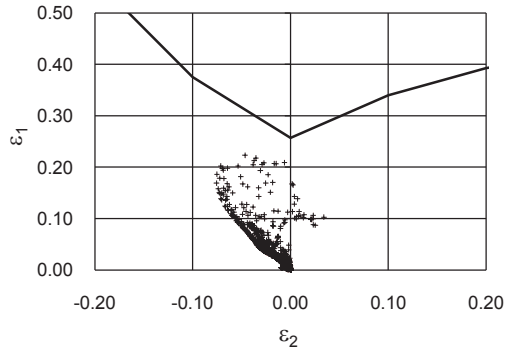

Figure 5.5: Example of a forming limit diagram.

The forming limit curve mainly depends on the hardening [80], the strain rate sensitivity [80] and the Bauschinger effect [77]. Additionally, the strain path affects the forming limit [81]. Generally, a forming limit curve is only valid for linear strain paths. A non-linear strain path can occur, if a part is produced by multiple forming operations.

In practice the forming limit curve is either determined experimentally or computationally. In chapter 6, the Nakajima experiment for the determination of the forming limit curve is introduced. In this work, only experimentally determined forming limit curves are applied. Hence, an introduction of procedures for the prediction of forming limits is omitted here. Approaches for the computation of

forming limits have been proposed for example by Marciniak and Kuczynski [82], Hora [75] and Gese [77].

5.5 Finite element method

5.5.1 Shape functions

The most common approach for computing numerical solutions of partial differential equations of engineering problems is the finite element method. The introduction of the finite element method, which is mainly based on [60] and [61], is focused on the field of solid mechanics. Furthermore, only purely mechanical problems are considered, which can be described without taking a heat flow and a heat supply into account.

The solution of the partial differential equations is approximated by shape functions. In order to obtain a good approximation of the solution, without formulating complex mathematical shape functions, the domain of the mechanical problem is geometrically subdivided, which is termed discretization. These sub domains are referred to as finite elements. The elements are described by a set of nodes. Each node contains its position in space. A set of elements and its nodes is called mesh.

Dependent on the mechanical problem, different types of meshes are applied in Finite-Element-Programs. For solid mechanics with a history dependent material behavior, Lagrange meshes are usually preferred. The nodes of this mesh type are coincident with the material points. Therefore, the nodes follow the motion of the material points. Subsequently, only Lagrangian meshes are discussed[2].

For the interpolation of the geometry and the field quantities within an element, usually the same shape functions are applied. Thereby, the interpolation is based on the corresponding coordinates and the values of the field quantities at the nodes. This approach is termed isoparametric concept [83]. Figure 5.6 illustrates as an example a velocity field in one dimension. The geometry $x(X)$ can be expressed by the given shape functions $N_1(X)$ and $N_2(X)$, dependent on the nodal coordinates x_1 and x_2. The same shape functions also provide a description of the velocity field $v(X)$, which depends on the nodal velocities v_1 and v_2. A detailed description of the shape functions, which are implemented in finite element programs, is given in [84].

5.5.2 Continuity of shape functions

On the basis of the fundamental theorem of calculus

[2] A comprehensive description of other mesh types like Eulerian or hybrid techniques, which combine the advantages of Eulerian and Lagrangian meshes, can be found in [60].

$$\int_a^b f_{,x}\,(x)\,\mathrm{dx} = f\,(b) - f\,(a)\,, \tag{5.112}$$

the continuity requirements for the shape functions between the element boundaries can be derived. $C^n(x)$ means that the nth derivative with respect to x of a function f is continuous [60]. According to (5.112), the definite integral can be computed, if f is $C^0(x)$.

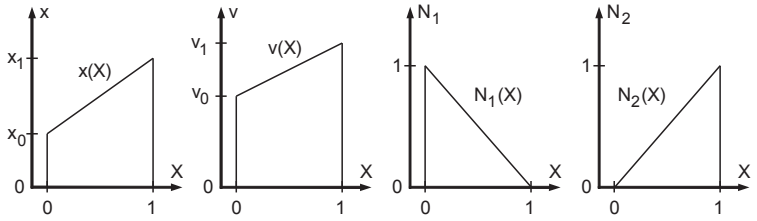

$$x(X) = N_1(X)x_0 + N_2(X)x_1$$
$$v(X) = N_1(X)v_0 + N_2(X)v_1$$
$$N_1(X) = 1 - X;\ N_2(X) = X$$

Figure 5.6: Example of shape functions.

Generally, the balance equations and the constitutive law can be formulated in different configurations. For the subsequent discussion, the updated Lagrange approach is selected, which implies a formulation of the continuum mechanical equations in the current configuration, as shown in the chapter 5.1. Expression (5.113) recalls the balance of momentum in the global formulation:

$$\iiint_{\chi_t[B]} \rho\dot{\mathbf{v}} - \mathrm{div}\boldsymbol{\sigma} - \rho\mathbf{f}\mathrm{d}v = \mathbf{0}. \tag{5.113}$$

The desired solution is the velocity field $\mathbf{v}$. This field is described by the same shape functions as the deformation field (figure 5.6). The constitutive law gives the dependency of stress state $\boldsymbol{\sigma}$ with respect to the rate of deformation $\mathbf{D}$. Hence, $\boldsymbol{\sigma}$ is a function of $\mathbf{D}$. $\mathbf{D}$ contains, as introduced above, the partial derivative of the velocity field $\mathbf{v}$ with respect to $\mathbf{x}$. Thus, the second derivative of the velocity field $\mathbf{v}$ is needed for the integration of (5.113). In consideration of (5.112), the required continuity of the shape functions, representing the velocity field $\mathbf{v}$, is $C^1(\mathbf{x})$. However, it is difficult to formulate shape functions, which show a $C^1(\mathbf{x})$ continuity between the element edges for two or three dimensions [60]. The continuity requirements concerning the shape function can be reduced by transforming the partial differential equation into the so-called weak form.

5.5.3 Weak form of the differential equations

According to the principle of d'Alembert, expression

$$\iiint_{\chi_t[B]} \mathbf{w}(\mathbf{x}) \cdot \boldsymbol{\eta}(\mathbf{x}) \, \mathrm{d}v = 0 \tag{5.114}$$

holds throughout the integration area χ_t for any test vector field $\boldsymbol{\eta}(\mathbf{x})$, if $\mathbf{w}(\mathbf{x}) = 0$ [59]. $\mathbf{w}$ is also a vector-valued function. Therefore (5.113) can be written in the given form by introducing the test function $\delta\mathbf{v}$:

$$\iiint_{\chi_t[B]} \delta\mathbf{v} \cdot \rho\dot{\mathbf{v}} - \delta\mathbf{v} \cdot \mathrm{div}\boldsymbol{\sigma} - \delta\mathbf{v} \cdot \rho\mathbf{f} \mathrm{d}v = 0. \tag{5.115}$$

The sub term, which contains the stress state $\boldsymbol{\sigma}$, can be reformulated by applying the product rule:

$$\iiint_{\chi_t[B]} \delta\mathbf{v} \cdot \mathrm{div}\boldsymbol{\sigma} \mathrm{d}v = \iiint_{\chi_t[B]} \mathrm{div}\left(\delta\mathbf{v} \cdot \boldsymbol{\sigma}\right) \mathrm{d}v - \iiint_{\chi_t[B]} \nabla\left(\delta\mathbf{v}\right) : \boldsymbol{\sigma} \mathrm{d}v. \tag{5.116}$$

Finally, the first summand on the right hand side of (5.116) is transformed into a surface integral (Gauss's theorem) and the result is inserted in (5.115):

$$\iiint_{\chi_t[B]} \delta\mathbf{v} \cdot \rho\dot{\mathbf{v}} \mathrm{d}v - \iint_{\partial\chi_t[B]} \delta\mathbf{v} \cdot \boldsymbol{\sigma} \cdot \mathbf{n} \mathrm{d}a + \iiint_{\chi_t[B]} \nabla\left(\delta\mathbf{v}\right) : \boldsymbol{\sigma} \mathrm{d}v - \iiint_{\chi_t[B]} \delta\mathbf{v} \cdot \rho\mathbf{f} \mathrm{d}v = 0. \tag{5.117}$$

Now, a continuity of $C^0(\mathbf{x})$ of the shape functions, representing the velocity field, is sufficient for the integration of the partial differential equation. For $\delta\mathbf{v}$ an arbitrary function can be applied. However the chosen function for $\delta\mathbf{v}$ has to meet the boundary conditions of the mechanical problem. Usually, the shape functions are also used for the formulation of $\delta\mathbf{v}$.

5.5.4 The discrete differential equations

Subsequently, the notation, given in [60], is applied. The element-wise integration of the partial differential equations on the basis of the shape functions leads to a discrete form of the problem. Expression

$$\mathbf{x}\left(\mathbf{X}, t\right) = \mathbf{x}_{\mathbf{I}}\left(t\right) N_{\mathbf{I}}\left(\mathbf{X}\right) \tag{5.118}$$

defines the approximation of the motion based on shape functions, which is applied for the discretization of the weak form of the introduced partial differential equation. The motion is described by the nodes, whose index is given by $\mathbf{I}$ and

its positions by $\mathbf{x_I}$. From the isoparametric concept follows expression (5.119), which gives an approximation of the displacement field:

$$\mathbf{u}\left(\mathbf{X},t\right)=\mathbf{u_I}\left(t\right)N_{\mathbf{I}}\left(\mathbf{X}\right). \tag{5.119}$$

The partial derivative of the displacement field with respect to the time, leads to the velocity field

$$\mathbf{v}\left(\mathbf{X},t\right)=\frac{\partial\mathbf{u}\left(\mathbf{X},t\right)}{\partial t}=\dot{\mathbf{u}}_{\mathbf{I}}\left(t\right)N_{\mathbf{I}}\left(\mathbf{X}\right). \tag{5.120}$$

As the shape functions do not depend on time, only the nodal velocities have to be considered. Consequently, the same shape functions can be applied as for the displacement field.

Expression

$$\frac{\partial\mathbf{v}}{\partial\mathbf{x}}=\mathbf{L}=L_{ij}=\mathbf{v}_{i\mathbf{I}}N_{\mathbf{I},j},\ \mathbf{D}=\frac{1}{2}\left(\mathbf{L}+\mathbf{L}^{T}\right), \tag{5.121}$$

shows the computation of the velocity gradient $\mathbf{L}$, which is needed for the determination of the rate of deformation $\mathbf{D}$. Subsequently, the index i refers to the components of vectors. For the derivation of the discrete form of the partial differential equation shown by (5.117), sub terms are introduced as shown by

$$\delta P^{\mathrm{int}}=\iiint\limits_{\chi_t[B]}\nabla\left(\delta\mathbf{v}\right):\boldsymbol{\sigma}\mathrm{d}v, \tag{5.122}$$

$$\delta P^{\mathrm{kin}}=\iiint\limits_{\chi_t[B]}\delta\mathbf{v}\cdot\rho\dot{\mathbf{v}}\mathrm{d}v \tag{5.123}$$

and

$$\delta P^{\mathrm{ext}}=\iint\limits_{\partial\chi_t[B]}\delta\mathbf{v}\cdot\boldsymbol{\sigma}\cdot\mathbf{n}\mathrm{d}v+\iiint\limits_{\chi_t[B]}\delta\mathbf{v}\cdot\rho\mathbf{f}\mathrm{d}v. \tag{5.124}$$

Thereby, the sub term δP^{int} is referred to as internal power, which is associated with the internal forces of the mechanical system. The external power δP^{ext} refers to the external forces and δP^{kin} corresponds to the kinetic forces. Expression (5.125) is an alternative form of (5.117), called principle of virtual power:

$$\delta P^{\mathrm{kin}}-\delta P^{\mathrm{ext}}+\delta P^{\mathrm{int}}=0. \tag{5.125}$$

As mentioned above, any test function, which fulfills the boundary conditions of the mechanical system can be applied as a test function. Commonly, the shape function is taken as a test function as shown by expression

$$\delta\mathbf{v}\left(\mathbf{X}\right)=\delta v_{i\mathbf{I}}N_{\mathbf{I}}\left(\mathbf{X}\right). \tag{5.126}$$

If (5.126) is inserted in (5.122),(5.123) and (5.124), the expressions

$$\delta P^{\mathrm{int}} = \delta v_{i\mathbf{I}} f_{i\mathbf{I}}^{\mathrm{int}} = \delta v_{i\mathbf{I}} \iiint\limits_{\chi_t[B]} \frac{\partial N_{\mathbf{I}}}{\partial x_j} \sigma_{ji} \mathrm{d}v, \tag{5.127}$$

$$\delta P^{\mathrm{kin}} = \delta v_{i\mathbf{I}} f_{i\mathbf{I}}^{\mathrm{kin}} = \delta v_{i\mathbf{I}} \iiint\limits_{\chi_t[B]} \rho N_{\mathbf{I}} \dot{v}_i \mathrm{d}v = \delta v_{i\mathbf{I}} \iiint\limits_{\chi_t[B]} \rho N_{\mathbf{I}} N_{\mathbf{J}} \mathrm{d}v \dot{v}_{i\mathbf{J}} = \delta v_{i\mathbf{I}} \mathbf{M}_{ij\mathbf{IJ}} \dot{v}_{j\mathbf{J}} \tag{5.128}$$

and

$$\delta P^{\mathrm{ext}} = \delta v_{i\mathbf{I}} f_{i\mathbf{I}}^{\mathrm{ext}} = \delta v_{i\mathbf{I}} \iint\limits_{\partial\chi_t[B]} N_{\mathbf{I}} n_j \sigma_{ji} \mathrm{d}a + \delta v_{i\mathbf{I}} \iiint\limits_{\chi_t[B]} N_{\mathbf{I}} \rho f_i \mathrm{d}v \tag{5.129}$$

are obtained. These expressions imply a summation over repeated indices. It is important to mention that the nodal velocities of the test functions can be placed in front of the integral. This property of the chosen test function leads to the so-called discrete momentum equations. Thereby, this equation comprises the entire set of nodes. For obtaining a compact notation, a vectorization according to the Voigt notation [60] of the nodal displacements $\mathbf{d}$, velocities $\mathbf{v}$, accelerations $\mathbf{a}$ and forces $\mathbf{f}$ is performed:

$$\mathbf{f} = f_a = f_{i\mathbf{I}},\ a = (\mathbf{I} - 1) n_{SD} + i. \tag{5.130}$$

The nodal forces $\mathbf{f}$ are taken as an example (n_{SD}: Number of space dimensions). The vector $\mathbf{f}^{ext}$ contains the external nodal forces and $\mathbf{f}^{int}$ the internal ones. Expression (5.131) shows (5.125) in the discrete form:

$$\delta v_{i\mathbf{I}} \left(M_{ij\mathbf{IJ}} \dot{v}_{j\mathbf{J}} + f_{i\mathbf{I}}^{int} - f_{i\mathbf{I}}^{ext} \right) = \delta \mathbf{v}^T \left(\mathbf{Ma} + \mathbf{f}^{int} - \mathbf{f}^{ext} \right) = 0. \tag{5.131}$$

The integrals of the equations (5.127),(5.128) and (5.129) are not determined in a closed form. A possible numerical solution of these integrals is the Gauss quadrature, which is shown by

$$\int_{-1}^{1}\int_{-1}^{1}\int_{-1}^{1} f(\boldsymbol{\xi}) \, \mathrm{d}\xi_1 \mathrm{d}\xi_2 \mathrm{d}\xi_3 = \sum_{Q_1=1}^{nQ_1} \sum_{Q_2=1}^{nQ_2} \sum_{Q_3=1}^{nQ_3} \omega_{Q_1} \omega_{Q_2} \omega_{Q_3} f\left(\xi_{1_{Q_1}}, \xi_{2_{Q_2}}, \xi_{3_{Q_3}} \right). \tag{5.132}$$

This quadrature procedure is based on a normalized cubic integration domain, whose extension in each dimension is given by the interval $[-1, 1]$. For the numerical integration, the function f needs to be evaluated at predefined positions in space - called integration points. The computed function values are finally

weighted and summed up as given by 5.132. The weights and the position of the integration points are given by tables. The number of integration points nQi (5.132) determines the degree of the polynomial, which is exactly integrated by the Gaussian quadrature. Further details regarding this numerical integration procedure can be found in [84].

In order to apply the numerical integration, the parental configuration is introduced. Figure (5.7) illustrates the mapping of the motion between the parent and the current configuration based on two dimensions.

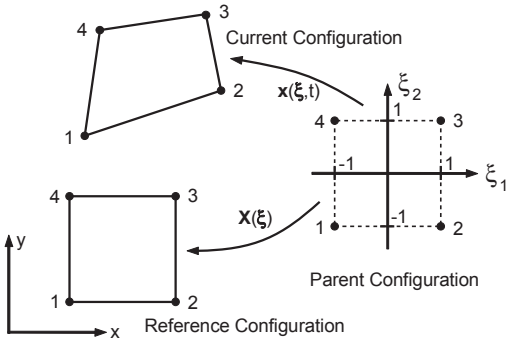

Figure 5.7: The parent configuration.

The motion, dependent on the coordinate system of the parent configuration is given by expression

$$\mathbf{x}\left(\boldsymbol{\xi},t\right)=\mathbf{x}_{\mathbf{I}}\left(t\right)N_{\mathbf{I}}\left(\boldsymbol{\xi}\right). \tag{5.133}$$

The displacement and velocity field can be expressed in the same manner. The numerical integration of the integrals (5.127),(5.128) and (5.129) is shown for the internal forces. The expression (5.134) refers to a single element and, therefore, the domain of the integration is described by the symbol E:

$$\delta P^{\text{int}}=\delta v_{i\mathbf{I}}f_{i\mathbf{I}}^{\text{int}}=\delta v_{i\mathbf{I}}\iiint\limits_{\chi_t[E]}\frac{\partial N_{\mathbf{I}}}{\partial x_j}\sigma_{ji}\mathrm{d}v. \tag{5.134}$$

For the application of the Gaussian numerical integration scheme, the domain of the parent configuration pc is applied for the integration

$$\delta P^{\text{int}}=\delta v_{i\mathbf{I}}\int\limits_{-1}^{1}\int\limits_{-1}^{1}\int\limits_{-1}^{1}\frac{\partial N_{\mathbf{I}}}{\partial x_j}\sigma_{ji}J_{\boldsymbol{\xi}}\mathrm{d}v_{pc}. \tag{5.135}$$

The computation of $J_{\boldsymbol{\xi}}$ is shown below. The partial derivative of the shape function with respect to $\mathbf{x}$ is performed on the basis of the coordinate system of the parent configuration

$$\delta P^{\text{int}} = \delta v_{i\mathbf{I}} \int_{-1}^{1}\int_{-1}^{1}\int_{-1}^{1} \frac{\partial N_{\mathbf{I}}}{\partial \xi_k}\frac{\partial \xi_k}{\partial x_j}\sigma_{ji} J_{\boldsymbol{\xi}} \mathrm{d}v_{pc} = \delta v_{i\mathbf{I}} \int_{-1}^{1}\int_{-1}^{1}\int_{-1}^{1} \frac{\partial N_{\mathbf{I}}}{\partial \xi_k} F^x_{kj}\sigma_{ji} J_{\boldsymbol{\xi}} \mathrm{d}v_{pc}. \tag{5.136}$$

For the computation of F^x_{kj}, the function $\boldsymbol{\xi}(\mathbf{x}, t)$ is needed, which cannot be written in a closed form. However, $F^{\xi}_{nm} = \partial x_n / \partial \xi_m$ can be computed. Expression (5.137) is obtained by inserting the inverse of F^{ξ}_{nm} in (5.136), which is equivalent to F^x_{kj}:

$$\delta P^{\text{int}} = \delta v_{i\mathbf{I}} \int_{-1}^{1}\int_{-1}^{1}\int_{-1}^{1} \frac{\partial N_{\mathbf{I}}}{\partial \xi_k}\left(F^{\xi}_{kj}\right)^{-1}\sigma_{ji} J_{\boldsymbol{\xi}} \mathrm{d}v_{pc},\ J_{\boldsymbol{\xi}} = det\left(\mathbf{F}^{\xi}\right). \tag{5.137}$$

Expression (5.137) shows the computation of the nodal forces on the basis of shape functions. The introduced scheme for determining the nodal forces is referred to as continuum element.

Finally, the element wise computed element nodal forces have to be combined to a vector, which describes all the nodal forces of the mechanical problem (global node force vector $\mathbf{f}^{int}$). This operation is referred to as scatter. Expression (5.138) shows the gather operation, which is applied to extract the displacement vectors of an element from the global displacement vector. The boolean matrix $\mathbf{L}_e$ is called connectivity matrix, which allows to extract element specific quantities from the associated global vector. Expression (5.138) shows the extraction of the element displacement vector $\mathbf{d}_e$ from the global displacement vector $\mathbf{d}$:

$$\mathbf{d}_e = \mathbf{L}_e \mathbf{d}. \tag{5.138}$$

The nodal forces are scattered by applying the transposed connectivity matrix. This procedure implies that the associated nodal forces of different elements, which refer to the same node, are summed up:

$$\mathbf{f}^{\text{int}} = \sum_e \mathbf{L}_e^T \mathbf{f}_e^{int}. \tag{5.139}$$

For solving of (5.131), a similar procedure needs to be performed for the external nodal forces $\mathbf{f}^{ext}$ and for the mass matrix $\mathbf{M}$.

5.5.5 Shell elements

The best accuracy of the numerical integration is obtained, if the domain of the continuum elements is similar to a cube in the current configuration. Large differences regarding the edge lengths of the elements lead to a reduction of the accuracy of the numerical integration [85]. Many technical applications like sheet

metal forming imply dealing with structures, which are very thin in one dimension compared with the other ones. Thereby, the thickness direction of formed sheet metal parts is in the dimension of millimeters and the remaining ones in the dimension of meters. According to Okan [86], at least 12 continuum elements in thickness direction are necessary in order to reflect the stress field of a bending operation accurately. The mentioned property of the numerical integration regarding the relation between the element edge lengths leads, in consideration of the findings reported by Okan [86], to a large amount of continuum elements and small element edge lengths. As shown below, the smaller the size of the elements, the larger the computational cost for solving the discrete partial differential equations based on an explicit integration scheme is. In case an implicit solution scheme is applied, the effort is rising by an increasing amount of elements. Hence, a reduction of the element size leads anyway to an increasing computational cost. Today, for industrial sheet metal forming simulations, the application of continuum elements is too expensive.

Subsequently, assumptions, verified by observations of the mechanical behavior of thin structures (shell structures), are introduced, which allow to reduce the effort for solving the discrete partial differential equations. These assumptions lead to another type of element, which is referred to as shell element[3]. For the development of shell elements, the kinematic of the structure is described on the basis of the deformation of a reference surface and additional assumptions. Commonly, however not necessarily, the midsurface is taken as such a reference. Figure 5.8 illustrates the kinematic assumptions of the Kirchhoff-Love and the Reissner-Mindlin theory on the basis of a shell, which is bent in one direction. According to the first mentioned theory, the normal to the midsurface remains straight and keeps normal. The latter mentioned one assumes that this normal remains only straight, however a rotation of it with respect to the midsurface is allowed. According to these theories, it is possible to describe the motion of an arbitrary material point by a relative rotation with respect to the motion of the midsurface (reference surface). As opposed to the Reissner-Mindlin assumption the Kirchhoff-Love assumption is limited to thin shells. Furthermore, the stress state normal to the midsurface is assumed to be negligible, which is referred to as plane stress condition.

In order to consider these assumptions, another weak form of the momentum balance needs to be derived. However, this procedure is very complex, especially if the elements have to be suitable for non-linear computations. Another approach is to apply continuum elements and to implement the kinematic assumptions by constraints on the motion of the corresponding nodes, which is referred to as continuum based shell theory. Additionally, the constitutive law needs to be adjusted in order to obtain a plane stress state. In this case it is sufficient to use only one element in thickness direction, which reduces the amount of elements, necessary for an accurate prediction of the stress and strain states enormously. Subsequently, only the latter mentioned theory is introduced.

[3] A comprehensive introduction in shell elements can be found in [87].

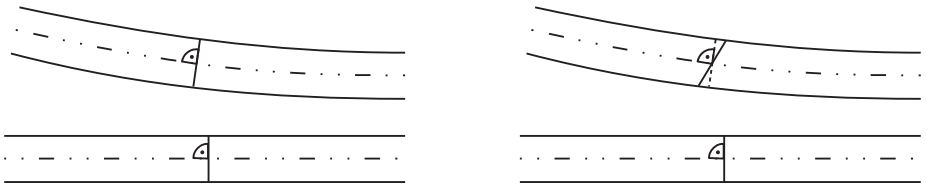

Figure 5.8: Kinematic assumptions; Left: Visualization of the Kirchhoff-Love assumption; Right: Visualization of the Reissner-Mindlin assumption.

Figure 5.9 illustrates the concept of the continuum-based shell elements, comprising a master slave node concept. The slave nodes are the nodes associated with the continuum element. The master nodes are located on the midsurface (reference surface). In order to formulate the relations between the master and slave nodes, a convention regarding the node numbering is introduced. The slave nodes on the top surface, which is the outer surface of the shell in the positive ξ_3-direction (local coordinate system of the element), are marked by $+$. The slave nodes on the opposite surface (bottom surface) are described by a $-$ sign. The correspondence between the master and the slave nodes is defined by coincident ξ_1 and ξ_2 coordinates. Each slave node possesses the same node number as the associated master node. Lines along constant ξ_1 and ξ_2 coordinates are called fibers and the unit vectors along them are referred to as directors $\mathbf{p_I}(\xi_1, \xi_2)$. Surfaces, defined by constant ξ_3 values are called lamina.

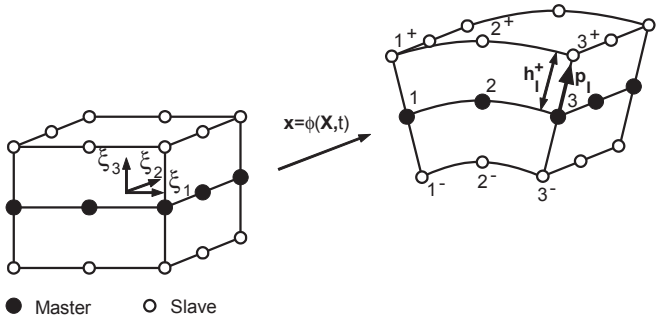

Figure 5.9: Example of a continuum-based shell element [60].

The Reissner-Mindlin kinematic assumption is reflected by requiring the fibers to remain straight. In order to obtain straight fibers, only two slave nodes are allowed to lie on a fiber. Additionally, the shape functions need to be linear.

As mentioned above, the kinematics of the shell is represented by rotations

with respect to the motion of the midsurface (reference surface) respectively the master nodes. The expressions (5.140) and (5.141) show the definition of the translational and rotational nodal velocities and the associated nodal forces and moments:

$$\dot{\mathbf{d}}_{\mathbf{I}} = \left[\begin{array}{cccccc} v_{x_{\mathbf{I}}} & v_{y_{\mathbf{I}}} & v_{z_{\mathbf{I}}} & \omega_{x_{\mathbf{I}}} & \omega_{y_{\mathbf{I}}} & \omega_{z_{\mathbf{I}}} \end{array} \right]^T, \tag{5.140}$$

$$\mathbf{f}_{\mathbf{I}} = \left[\begin{array}{cccccc} f_{x_{\mathbf{I}}} & f_{y_{\mathbf{I}}} & f_{z_{\mathbf{I}}} & m_{x_{\mathbf{I}}} & m_{y_{\mathbf{I}}} & m_{z_{\mathbf{I}}} \end{array} \right]^T. \tag{5.141}$$

The motion and the velocity field, depending on the local element coordinate system ξ_i, are given by the expressions (5.142) and (5.143) (nMN: Number of master nodes):

$$\mathbf{x}\left(\boldsymbol{\xi}, t\right) = \sum_{\mathbf{I}^-=1}^{nMN} \mathbf{x}_{\mathbf{I}^-}\left(t\right) N_{\mathbf{I}^-}\left(\boldsymbol{\xi}\right) + \sum_{\mathbf{I}^+=1}^{nMN} \mathbf{x}_{\mathbf{I}^+}\left(t\right) N_{\mathbf{I}^+}\left(\boldsymbol{\xi}\right), \tag{5.142}$$

$$\mathbf{v}\left(\boldsymbol{\xi}, t\right) = \sum_{\mathbf{I}^-=1}^{nMN} \mathbf{v}_{\mathbf{I}^-}\left(t\right) N_{\mathbf{I}^-}\left(\boldsymbol{\xi}\right) + \sum_{\mathbf{I}^+=1}^{nMN} \mathbf{v}_{\mathbf{I}^+}\left(t\right) N_{\mathbf{I}^+}\left(\boldsymbol{\xi}\right). \tag{5.143}$$

The kinematic condition is formulated by expressions (5.144) and (5.145):

$$\mathbf{v}_{\mathbf{I}^+} = \mathbf{v}_{\mathbf{I}}^M + h_{\mathbf{I}}^+ \boldsymbol{\omega}_{\mathbf{I}} \times \mathbf{p}_{\mathbf{I}}, \tag{5.144}$$

$$\mathbf{v}_{\mathbf{I}^-} = \mathbf{v}_{\mathbf{I}}^M - h_{\mathbf{I}}^- \boldsymbol{\omega}_{\mathbf{I}} \times \mathbf{p}_{\mathbf{I}}. \tag{5.145}$$

Thereby, h^+/h^- describe the initial distance between the midsurface and the top/bottom surface. The velocity of the master nodes is denoted by $\mathbf{v}_{\mathbf{I}}^M$. The continuum-based shell theory comprises the additional assumption that the balance of momentum in the direction of the fibers is not enforced, which allows treating the fibers as inextensible. As the fiber has to remain straight, the relative velocities of the slave nodes with respect to the corresponding master nodes can be computed by the cross product of the angular velocities and the director. The assumption of inextensible fibers enables to compute the velocities of the slave nodes by scaling the result of the cross product on the basis of the initial thickness.

For deriving a direct transformation between velocity vector of the master and the slave nodes (5.146), the cross product of (5.144) and (5.145) is rearranged as given by (5.147) and assembled to a transformation matrix $\mathbf{T}_{\mathbf{I}}$ as shown by (5.148):

$$\mathbf{T}_{\mathbf{I}} \dot{\mathbf{d}}_{\mathbf{I}} = \left[\begin{array}{c} \mathbf{v}_{\mathbf{I}^-} \\ \mathbf{v}_{\mathbf{I}^+} \end{array} \right], \tag{5.146}$$

$$h^+ \boldsymbol{\omega}_{\mathbf{I}} \times \mathbf{p}_{\mathbf{I}} = \boldsymbol{\Lambda}^+ \boldsymbol{\omega}_{\mathbf{I}},\ \Lambda_{ij}^+ = h^+ e_{ijk} p_k, \tag{5.147}$$

$$\mathbf{T_I} = \begin{bmatrix} \mathbf{I} & \mathbf{\Lambda}^- \\ \mathbf{I} & \mathbf{\Lambda}^+ \end{bmatrix}. \tag{5.148}$$

For enforcing the plane stress condition, the strain state, considered at each quadrature point, is transformed with respect to a coordinate system $(\widehat{\mathbf{e}}_x, \widehat{\mathbf{e}}_y, \widehat{\mathbf{e}}_z)$, whose z-direction is perpendicular to the lamina surfaces in the current configuration. Expression (5.149) shows the transformation of the rate of deformation to this coordinate system:

$$\widehat{\mathbf{D}} = \mathbf{R}_{\text{lam}}^T \mathbf{D} \mathbf{R}_{\text{lam}}, \; (R_{ij})_{\text{lam}} = \mathbf{e}_i \cdot \widehat{\mathbf{e}}_j. \tag{5.149}$$

Finally, the constitutive law is applied with respect to this coordinate system. The treatment of the plane stress assumption with respect to the constitutive law is given below in this chapter.

In consideration of the introduced constraints, the integration procedure of continuum elements can be applied for the computation of the nodal forces of the slave nodes. As a final step, the nodal forces of the master nodes are computed based on the transposed transformation matrix $\mathbf{T_I}$ and the forces of the slave nodes

$$\mathbf{f_I} = \mathbf{T_I}^T \begin{bmatrix} \mathbf{f_{I^-}} \\ \mathbf{f_{I^+}} \end{bmatrix}. \tag{5.150}$$

Apart from the internal forces also the external forces and the mass matrix have to be adjusted according to kinematic quantities given by (5.140). This leads to a discrete form of the partial differential equations.

Even though the strain field of the shell elements is linear in thickness direction, the corresponding stress state, which follows from the constitutive law of the material, is not necessarily linear. The elasto-plastic material model, which is investigated in this work, implies a non-linear relation between the strain and the stress state. In order to reflect this non-linearity, several quadrature points in thickness direction of the shell are needed.

The most significant drawbacks of the application of shell elements are the mentioned assumptions, which might limit the accuracy of the computation, and the occurrence of locking effects (shear, membrane and volume locking). Provided a shell is bent by moments acting on the edge of a structure and the resultant deformation is single curved, the transversal shear should vanish. However, shell elements can induce an undesired transversal shear under such a deformation mode. As the shear stiffness is larger than the bending stiffness, the split of the internal work with respect to the bending and shear, induced by the external loading and the dynamic forces, is shifted by the occurrence of this effect. Thereby, the corresponding internal work of the bending mode is reduced. Consequently, the bending stiffness is overestimated. This behavior of shell elements is referred to as shear locking. The above considered deformation mode is also inextensible in the tangent direction with respect to the reference surface. If the shell

element predicts an extension for such a case, again a shift of the internal work is induced, as the membrane stiffness is larger than the bending stiffness. This effect is referred to as membrane locking, which also leads to an overestimation of the bending stiffness. Provided, the material of a structure is incompressible, the violation of this constrained by an element is called volume locking. Procedures for circumventing these locking effects are the numerical underintegration, the application of high order shape functions or the so-called assumed strain methods[4]. In this thesis, an underintegrated 4-node quadrilateral shell element is applied, which is based on the first mentioned approach for avoiding the locking effects. This element comprises only one integration point with respect to the reference surface. In thickness direction the element contains several integration points for considering the non-linear relation between the strain and the stress state.

5.5.6 The explicit solution procedure

The introduced discrete partial differential equations are usually solved by explicit and implicit solution procedures. Among the explicit solution algorithms the central difference method on the basis of a diagonal mass matrix is the most applied one and therefore shown below. A rearrangement of (5.131) in consideration of ($\mathbf{C}_{damp}$: Damping matrix)

$$\mathbf{f}^n = \mathbf{f}^n_{ext} - \mathbf{f}^n_{int} \tag{5.151}$$

allows the computation of the nodal accelerations

$$\mathbf{a}^n = \mathbf{M}^{-1}\left(\mathbf{f}^n - \mathbf{C}_{damp}\mathbf{v}^{n-\frac{1}{2}}\right). \tag{5.152}$$

The accelerations referring to the time step n follow from the resultant global nodal forces of the same time step, which are defined by (5.151), and the nodal velocities of the point in time given by

$$t^{n-\frac{1}{2}} = \frac{1}{2}(t^n + t^{n-1}). \tag{5.153}$$

Provided, the mass matrix is diagonal, the computation of the nodal accelerations is a trivial task, which can be performed without solving an equation system. A diagonal mass matrix (lumped mass matrix) can be obtained by uniformly distributing the total mass of each element to its nodes.

The computed nodal accelerations allow determining the nodal velocities by an integration formula, which is derived by rearranging a difference formula, as shown by

$$\mathbf{v}^{n+\frac{1}{2}} = \mathbf{v}^n + (t^{n+\frac{1}{2}} - t^n)\mathbf{a}^n. \tag{5.154}$$

Thereby, the time increment is given by

[4] An introduction of this procedures is given in [60].

$$t^{n+1} = t^n + \Delta t^{n+\frac{1}{2}} \tag{5.155}$$

and the point in time for the integration of the nodal velocities is given by

$$t^{n+\frac{1}{2}} = \frac{1}{2}\left(t^{n+1} + t^n\right). \tag{5.156}$$

$\Delta t^{n+\frac{1}{2}}$ defines the time step. Finally, expression (5.157) shows the update of the nodal displacements:

$$\mathbf{d}^{n+1} = \mathbf{d}^n + \Delta t^{n+\frac{1}{2}} \mathbf{v}^{n+\frac{1}{2}}. \tag{5.157}$$

Consequently, the explicit solution procedure enables to accomplish the update of the nodal velocities and the displacements without solving any equations, which is the most important property of this method. Subsequently, the algorithm of the explicit method is introduced.

The procedure starts with the initialization of the nodal velocities, the stress state, the state variables of the material and the computation of the mass matrix. Furthermore the initial conditions of the mechanical problem are considered. As a next step, the global resultant nodal forces are determined by the subroutine *get force* (figure 5.11). Firstly, the global external forces are computed within this subroutine. Secondly, within a loop the internal forces of the elements are computed. Based on the connectivity matrix the nodal velocities of the considered element are extracted from the global velocity vector. A second loop is necessary to treat each integration point of each element, which comprises the computation of the strain measure, the update of the stress state according to the constitutive law and the numerical integration with respect to the considered element. The implementation of the stress update algorithm is shown below. For the calculation of the resultant nodal forces, the external nodal forces, related to the considered element are determined from the global external force vector by applying the connectivity matrix. Finally, the scatter operation is accomplished in order to complement the global resultant nodal force vector by the results, computed for each element. On the basis of the computed resultant nodal force vector, returned by the subroutine *get force*, the nodal accelerations are computed (5.152). As a next step, a loop is entered, which is stopped by reaching the termination time. The first operation within the loop is the update of the time, as shown by the expressions (5.155) and (5.156). According to (5.154), the nodal velocities are determined. For considering time dependent constraints, the prescribed nodal velocities are directly assigned to the global nodal velocity vector

$$v_{i\mathbf{I}}^{n+\frac{1}{2}} = \overline{v_i}(\mathbf{x_I}, t^{n+\frac{1}{2}}). \tag{5.158}$$

The nodal displacements are updated as given by expression (5.157). Generally, constraints can be also formulated in the same manner as shown above on the basis of displacements. Now, the subroutine *get force* is executed and the nodal accelerations are determined according to the time update, performed at

the beginning of the loop. Finally, also the nodal velocities are updated as shown by expression (5.159) and the algorithm is continued at the beginning of the loop:

$$\mathbf{v}^{n+1} = \mathbf{v}^{n+\frac{1}{2}} + (t^{n+1} - t^{n+\frac{1}{2}})\mathbf{a}^{n+1}. \tag{5.159}$$

Figure 5.10 summarizes the sequence of the explicit method, which is taken from [60]. The advantage of the explicit method is that it rarely fails by treating highly non-linear problems. However, the size of the time step has to be limited; otherwise the explicit method gives undesired solutions. A stable time step is given by

$$\Delta t = \alpha \Delta t_{crit},\ \Delta t_{crit} \leq \min \frac{l_e}{c_e}. \tag{5.160}$$

Thereby, l_e is the characteristic length of the element and c_e the wave speed, which depends on the material of the problem. This relation shows that a decreasing element size directly increases the amount of time steps needed for the solution of the problem. Consequently, the element length is one of the decisive factors influencing the total computation time. The parameter α is an additional safety factor, considering a possible destabilization of the solution procedure by the occurrence of nonlinearities and is recommended to be chosen between 0.8 and 0.98 [60].

1 Initialization, Consideration initial conditions
2 Call sub routine get force
3 Compute accelerations (5.152)
4 a) Time update (5.155) (5.156)
4 b) Partial update nodal velocities (5.154)
4 c) Consideration boundary conditions (5.158)
4 d) Update nodal displacements (5.157)
4 e) Call sub routine get force
4 f) Compute nodal accelerations $\mathbf{a}^{n+1}$ (5.152)
4 g) Second partial update nodal velocities (5.159)
4 h) Update Step $n = n + 1$
4 i) If t is not equal to the termination time goto $4a$)

Figure 5.10: Scheme of the explicit method [60].

5.5.7 The implicit solution procedure

The introduced implicit solution procedure can only treat static problems. This choice is made, as this restriction leads to a consistent derivation of the implicit solution originating from the potential energy. The solution of the mechanical problem, formulated by the potential energy, is found by determining the stationary point of expression

1 Initialization, $\mathbf{f}^n = 0$
2 Compute external nodal forces $\mathbf{f}^n_{ext}$
3 Loop, Elements
3 a) Perform gather operation (nodal displacements, nodal velocities)
3 b) Initialize $\mathbf{f}^n_{e_{int}} = 0$
3 c) Loop, Integration points
3 c) α) Compute strain measure
3 c) β) Stress update (see section 5.5.9)
3 c) γ) Compute internal forces $\mathbf{f}^n_{e_{int}}$
3 c) δ) End Loop
3 d) Compute external nodal forces with respect to the element
3 e) Compute resultant nodal forces with respect to the element $\mathbf{f}^n_e$
3 f) Determine resultant nodal forces (Perform scatter operation) $\mathbf{f}^n$
3 g) End Loop

Figure 5.11: The sub routine get force [60].

$$W(\mathbf{d}) = W_{int}(\mathbf{d}) - W_{ext}(\mathbf{d}) \tag{5.161}$$

in consideration of the constraints of the system. According to expression

$$0 = \mathbf{r} = \frac{\partial W}{\partial \mathbf{d}} = \frac{\partial W_{int}}{\partial \mathbf{d}} - \frac{\partial W_{\text{ext}}}{\partial \mathbf{d}} = \mathbf{f}^{int} - \mathbf{f}^{ext}, \tag{5.162}$$

the forces of conservative problems solely depend on the derivative of the associated potential. In the case of a static problem, the internal forces should be in equilibrium with the external forces and, consequently, the residuum $\mathbf{r}$ should be equal to zero. Commonly, this equation is solved by a Newton method. In order to apply this procedure, expression (5.162) is linearized as shown by

$$0 = \mathbf{r}(\mathbf{d}^\upsilon) + \frac{\partial \mathbf{r}(\mathbf{d}^\upsilon)}{\partial \mathbf{d}} \Delta \mathbf{d}. \tag{5.163}$$

Usually, multiple steps υ are necessary to determine the solution. Expression (5.164) illustrates the update of the displacement vector after each iteration:

$$\mathbf{d}^{\upsilon+1} = \mathbf{d}^\upsilon + \Delta \mathbf{d}. \tag{5.164}$$

The partial derivative of the residuum with respect to the displacement is the Hessian matrix of the potential energy

$$\mathbf{A} = \frac{\partial \mathbf{r}}{\partial \mathbf{d}} = \frac{\partial \mathbf{f}^{\text{int}}}{\partial \mathbf{d}} - \frac{\partial \mathbf{f}^{\text{ext}}}{\partial \mathbf{d}}. \tag{5.165}$$

The computation of the Hessian matrix implies a linearization of the constitutive law, the strain measure, the weak form of the balance equations and

deformation dependent loads [71]. The update of the displacement vector of each iteration is computed by solving the linear equation system given by

$$\mathbf{r} + \mathbf{A}\Delta\mathbf{d} = 0. \tag{5.166}$$

If the boundary condition just implies that a degree of freedom of a node is vanishing, it is sufficient to eliminate the corresponding equation from (5.166). Provided, a constraint depends on the displacement of the mechanical system, the Lagrange multiplier method can be deployed. Thereby, expression (5.161) is complemented by the constraint and the Lagrange multiplier. The solution is obtained by searching the stationary point of the Lagrange function

$$L = W + \boldsymbol{\lambda}^T\mathbf{g} = W + \lambda_{\mathbf{I}} g_{\mathbf{I}}. \tag{5.167}$$

The partial derivative of

$$\frac{\partial L}{\partial \mathbf{d}} = \frac{\partial W}{\partial \mathbf{d}} + \frac{\partial \mathbf{g}^T}{\partial \mathbf{d}}\boldsymbol{\lambda} \tag{5.168}$$

with respect to $\mathbf{d}$ is linearized for the application of the Newton method:

$$\frac{\partial W}{\partial \mathbf{d}} + \frac{\partial \mathbf{g}^T}{\partial \mathbf{d}}\boldsymbol{\lambda} + \frac{\partial^2 W}{\partial \mathbf{d}\partial \mathbf{d}}\Delta\mathbf{d} + \frac{\partial \mathbf{g}^T}{\partial \mathbf{d}}\Delta\boldsymbol{\lambda} + \lambda_{\mathbf{I}}\left[\frac{\partial^2 \mathbf{g}}{\partial \mathbf{d}\partial \mathbf{d}}\Delta\mathbf{d}\right]_{\mathbf{I}} = 0. \tag{5.169}$$

Additionally also the constrained function needs to be linearized as given by

$$\mathbf{g} + \frac{\partial \mathbf{g}}{\partial \mathbf{d}}\Delta\mathbf{d} = 0. \tag{5.170}$$

Expression (5.171) shows the resulting linear equation system, which has to be solved for each iteration:

$$\begin{bmatrix} \frac{\partial^2 W}{\partial \mathbf{d}\partial \mathbf{d}} + \lambda_{\mathbf{I}}\left[\frac{\partial^2 \mathbf{g}}{\partial \mathbf{d}\partial \mathbf{d}}\right]_{\mathbf{I}} & \frac{\partial \mathbf{g}^T}{\partial \mathbf{d}} \\ \frac{\partial \mathbf{g}}{\partial \mathbf{d}} & 0 \end{bmatrix} \begin{bmatrix} \Delta\mathbf{d} \\ \Delta\boldsymbol{\lambda} \end{bmatrix} = \begin{bmatrix} -\frac{\partial W}{\partial \mathbf{d}} - \frac{\partial \mathbf{g}^T}{\partial \mathbf{d}}\boldsymbol{\lambda} \\ -\mathbf{g} \end{bmatrix}. \tag{5.171}$$

Figure 5.12 summarizes the solution of a static problem based on the implicit method.

Subsequently, the solution of a static problem based on the implicit method is summarized. First of all, the initialization of the nodal displacements, the initial stress state and the state variables of the material need to be performed. Additionally the initial conditions are treated. Usually, the loads are increased incrementally, which leads to a better convergence of the implicit solution scheme. In this context, the term pseudo time is introduced, which is associated with the load increments. The pseudo time is only an artificial quantity, as in this section only static problems are considered. As a next step, the algorithm enters a loop, which is repeated until all the load increments are performed. Within this loop,

another loop is performed, which is terminated if the convergence criterion is met for the considered load increment. A typical convergence criteria is the comparison between the norm of the displacement increment and the total displacements

$$\|\Delta \mathbf{d}\| \leq \epsilon \|\mathbf{d}\| . \tag{5.172}$$

Other criteria are based on the residual and on the error energy, which are defined by the product of the displacement increment and the residual. Within the loop, the global resultant nodal forces are determined by the subroutine *get force*, which is identical to the one, introduced for the explicit method. Now, the Hessian matrix is computed and, if necessary, the constraints are considered. The linear equation system (5.166) or (5.171) is solved. Based on the solution, the trial displacement vector is updated. This procedure is repeated until the convergence criteria are met. After the inner loop is left, the computed trial displacement is considered to be the solution of the actual load increment and the load is increased.

1 Initialization, Consideration initial conditions
2 Newton iteration for load increment $n+1$
2 a) Call sub routine *get force* $\mathbf{f}\left(\mathbf{d}^{\upsilon}, t^{n+1}\right)$
2 b) Compute $A(\mathbf{d}^{\upsilon})$ (5.165)
2 c) Solve linear equation (5.166) or (5.171)
2 d) Update displacements (5.164)
2 e) Check convergence criterion (5.172), If not met then goto 2 a)
3 Update displacements $\mathbf{d}^{n+1} = \mathbf{d}^{\upsilon}$,
pseudo time $t = t + \Delta t$, step count $n = n + 1$
4 If t is not equal to the termination time goto 2

Figure 5.12: Scheme of the implicit method [60].

5.5.8 Discussion explicit, implicit methods

The simulation of a forming operation is a highly non-linear mechanical problem, which especially results from the material response and the contact constraints. The treatment of the contact constraints is not introduced in this thesis. A comprehensive description of computational contact mechanics can be found in [71]. The treatment of these nonlinearities is more difficult based on implicit methods than on the explicit ones. For example, the linearization of the constitutive law is not necessary, if the explicit method is applied. However, the implicit method needs less time steps for the computation of the solution. The drawback of implicit method with respect to the forming simulation is that the non-linearity, induced by the contact constraint, can cause the necessity of additional time steps. As the explicit method mainly comprises matrix multiplications, this method is more

suitable for distributing the computational tasks to different processors. Therefore, the disadvantage of the explicit method regarding the amount of time steps, needed for the computation of the solution, can be compensated by using multiple processors. Consequently, both methods can be advantageous concerning the needed time for computing the solution, depending on the available software and hardware resources. For the investigation and validation of the constitutive laws, the choice of the solution procedure should depend on the method applied in the serial operation. In this work the explicit method is chosen for the forming simulation. In the case of the springback simulation, the implicit method is advantageous. As this mechanical problem does not comprise strong nonlinearities, this method is able to give a solution within a few pseudo time steps. The application of the explicit method would imply the computation of much more time steps.

5.5.9 Stress update algorithm

Subsequently, the numerical implementation of the introduced elasto-plastic constitutive law is presented. The algorithm, shown below, is suitable for the explicit method. For the implicit solution procedure also a linearization of the elasto-plastic constitutive law is necessary.

Each time step implies a computation of the strain increment at the integration points of the elements. The constitutive law gives on the basis of this strain increment, the related stress update. The equations (5.173) recall the elasto-plastic constitutive law, which has been presented in chapter 5.2:

$$\begin{aligned} \dot{\boldsymbol{\sigma}} &= \mathbf{C} : (\dot{\boldsymbol{\epsilon}} - \dot{\boldsymbol{\epsilon}}^p), \\ \dot{\boldsymbol{\epsilon}}^p &= \dot{\lambda}\mathbf{r}, \\ \dot{\mathbf{q}} &= \dot{\lambda}\mathbf{h}, \\ \lambda &> 0,\ f \leq 0,\ \lambda f = 0. \end{aligned} \tag{5.173}$$

The elastic part of the constitutive law is written, as opposed to (5.49), in a rate form, which simplifies the numerical solution. First of all, under the assumption of an elastic material response the stress increment is computed:

$$\boldsymbol{\sigma}_{trial}^{n+1} = \boldsymbol{\sigma}^n + \mathbf{C} : \Delta\boldsymbol{\epsilon}. \tag{5.174}$$

As a next step, the material response is analyzed. If (5.175) is valid, the strain increment is elastic:

$$f\left(\boldsymbol{\sigma}_{trial}^{n+1}, \mathbf{q}^n\right) < 0. \tag{5.175}$$

In this case, the increment of the elastic strain is identical to the prescribed strain increment and (5.174) gives the stress update:

$$\boldsymbol{\sigma}^{n+1} = \boldsymbol{\sigma}_{trial}^{n+1},\ \mathbf{q}^{n+1} = \mathbf{q}^{n},\ \Delta\boldsymbol{\epsilon}^{e} = \Delta\boldsymbol{\epsilon}. \tag{5.176}$$

The treatment of the remaining cases

$$\begin{array}{lll} f\left(\boldsymbol{\sigma}^{n+1}, \mathbf{q}^{n}\right) = 0 & & \\ \dot{f} < 0 & & \text{elastic loading} \\ \dot{f} = 0 \quad \wedge & \lambda = 0 & \text{neutral loading} \\ \dot{f} = 0 \quad \wedge & \lambda > 0 & \text{plastic loading} \end{array} \tag{5.177}$$

will be shown below, which implies the computation of the solution of the differential equations (5.173). Simo and Hughes have summarized procedures for solving these equations. One of these procedures is the implicit Euler scheme. The expressions (5.178) summarize this scheme:

$$\begin{aligned} \dot{\mathbf{x}} &= f\left(t, \mathbf{x}\right), \\ t^{n} &= t^{0} + nh, \\ \mathbf{x}\left(t^{0}\right) &= \mathbf{x}^{0},\ \mathbf{x}\left(t^{n}\right) = \mathbf{x}^{n}, \\ \frac{\mathbf{x}^{n+1} - \mathbf{x}^{n}}{h} &\approx f\left(t^{n+1}, \mathbf{x}^{n+1}\right), \\ \mathbf{x}^{n+1} &\approx \mathbf{x}^{n} + hf\left(t^{n+1}, \mathbf{x}^{n+1}\right). \end{aligned} \tag{5.178}$$

The solution $\mathbf{x}^{n+1}$ can be computed based on the Newton method. The time discretization is defined by the increment h. Consequently, the application of the implicit Euler scheme leads to the expressions (5.179). The following notations have been taken from [60]:

$$\begin{aligned} \boldsymbol{\epsilon}^{n+1} &= \boldsymbol{\epsilon}^{n} + \Delta\boldsymbol{\epsilon}, \\ \boldsymbol{\epsilon}^{p^{n+1}} &= \boldsymbol{\epsilon}^{p^{n}} + \Delta\lambda^{n+1}\mathbf{r}^{n+1}\left(\boldsymbol{\sigma}^{n+1}, \mathbf{q}^{n+1}\right), \\ \mathbf{q}^{n+1} &= \mathbf{q}^{n} + \Delta\lambda^{n+1}\mathbf{h}^{n+1}\left(\boldsymbol{\sigma}^{n+1}, \mathbf{q}^{n+1}\right), \\ \boldsymbol{\sigma}^{n+1} &= \mathbf{C} : \left(\boldsymbol{\epsilon}^{n+1} - \boldsymbol{\epsilon}^{p^{n+1}}\right), \\ f^{n+1} &= f\left(\boldsymbol{\sigma}^{n+1}, \mathbf{q}^{n+1}\right) = 0. \end{aligned} \tag{5.179}$$

Subsequently, for all quantities, which refer to the time $n+1$, the subscript $n+1$ is omitted. Expression (5.180) shows the equations, suitable for a Newton method:

$$\begin{aligned} \mathbf{a} &= -\boldsymbol{\epsilon}^p + \boldsymbol{\epsilon}^{p^n} + \Delta\lambda\mathbf{r} = 0, \\ \mathbf{b} &= -\mathbf{q} + \mathbf{q}^n + \Delta\lambda\mathbf{h} = 0, \\ f &= f(\boldsymbol{\sigma}, \mathbf{q}) = 0. \end{aligned} \tag{5.180}$$

The linearization of $\boldsymbol{\sigma} = \mathbf{C} : (\boldsymbol{\epsilon} - \boldsymbol{\epsilon}^p)$ leads for the kth iteration step of the Newton method to expression (5.181), as $\boldsymbol{\epsilon}$ remains constant during the stress update [61] ($\Delta\boldsymbol{\epsilon}^p = \boldsymbol{\epsilon}^p - \boldsymbol{\epsilon}^{p^n}$; $\Delta\boldsymbol{\sigma} = \boldsymbol{\sigma} - \boldsymbol{\sigma}^n$):

$$\Delta\boldsymbol{\sigma} = -\mathbf{C} : \Delta\boldsymbol{\epsilon}^p. \tag{5.181}$$

This equation enables to perform the linearization of the first equation of (5.180) based on the stress state. The equations

$$\begin{aligned} \mathbf{a}^{(k)} + \frac{\partial \mathbf{a}^{(k)}}{\partial \boldsymbol{\sigma}^{(k)}} : \Delta\boldsymbol{\sigma}^{(k)} + \frac{\partial \mathbf{a}^{(k)}}{\partial \mathbf{q}^{(k)}} * \Delta\mathbf{q}^{(k)} + \frac{\partial \mathbf{a}^{(k)}}{\partial \Delta\lambda^{(k)}} \cdot \delta\lambda^{(k)} = 0, \\ \mathbf{b}^{(k)} + \frac{\partial \mathbf{b}^{(k)}}{\partial \boldsymbol{\sigma}^{(k)}} : \Delta\boldsymbol{\sigma}^{(k)} + \frac{\partial \mathbf{b}^{(k)}}{\partial \mathbf{q}^{(k)}} * \Delta\mathbf{q}^{(k)} + \frac{\partial \mathbf{b}^{(k)}}{\partial \Delta\lambda^{(k)}} \cdot \delta\lambda^{(k)} = 0, \\ f^{(k)} + \frac{\partial f^{(k)}}{\partial \boldsymbol{\sigma}^{(k)}} : \Delta\boldsymbol{\sigma}^{(k)} + \frac{\partial f^{(k)}}{\partial \mathbf{q}^{(k)}} * \mathbf{q}^{(k)} = 0 \end{aligned} \tag{5.182}$$

illustrate the linearization of (5.180) for the Newton iteration step k. The unknowns of the linearized equations are: $\Delta\boldsymbol{\sigma}^{(k)}$, $\Delta\mathbf{q}^{(k)}$ and $\Delta\lambda^{(k)}$. The linearization of these equations leads to (5.183), for the iteration step k of the Newton method:

$$\begin{aligned} f_A^{(k)} = \frac{\partial f^{(k)}}{\partial A},\ \mathbf{r}_A^{(k)} = \frac{\partial r^{(k)}}{\partial A},\ \mathbf{h}_A^{(k)} = \frac{\partial h^{(k)}}{\partial A}, \\ \Delta\mathbf{r}^{(k)} = \mathbf{r}_{\boldsymbol{\sigma}}^{(k)} : \Delta\boldsymbol{\sigma}^{(k)} + \mathbf{r}_{\mathbf{q}}^{(k)} * \Delta\mathbf{q}^{(k)}, \\ \Delta\mathbf{h}^{(k)} = \mathbf{h}_{\boldsymbol{\sigma}}^{(k)} : \Delta\boldsymbol{\sigma}^{(k)} + \mathbf{h}_{\mathbf{q}}^{(k)} * \Delta\mathbf{q}^{(k)}, \end{aligned}$$

$$\begin{aligned} \mathbf{a}^{(k)} + \mathbf{C}^{-1} : \Delta\boldsymbol{\sigma}^{(k)} + \Delta\lambda^{(k)}\Delta\mathbf{r}^{(k)} + \delta\lambda^{(k)}\mathbf{r}^{(k)} = 0, \\ \mathbf{b}^{(k)} - \Delta\mathbf{q}^{(k)} + \Delta\lambda^{(k)}\Delta\mathbf{h}^{(k)} + \delta\lambda^{(k)}\mathbf{h}^{(k)} = 0, \\ f^{(k)} + f_{\boldsymbol{\sigma}}^{(k)} : \Delta\boldsymbol{\sigma}^{(k)} + f_{\mathbf{q}}^{(k)} * \Delta\mathbf{q}^{(k)} = 0. \end{aligned} \tag{5.183}$$

The linear equation system is solved for the unknowns $\Delta\boldsymbol{\sigma}^{(k)}$,$\Delta\mathbf{q}^{(k)}$ and $\delta\lambda^{(k)}$. The expressions 5.184 show the update of $\boldsymbol{\epsilon}^{p^{(k+1)}}$, $\mathbf{q}^{(k+1)}$ and $\Delta\lambda^{(k+1)}$:

$$\begin{aligned} \boldsymbol{\epsilon}^{p(k+1)} &= \boldsymbol{\epsilon}^{p(k)} - \mathbf{C}^{-1} : \Delta\boldsymbol{\sigma}^{(k)}, \\ \mathbf{q}^{(k+1)} &= \mathbf{q}^{(k)} + \Delta\mathbf{q}^{(k)}, \\ \Delta\lambda^{(k+1)} &= \Delta\lambda^{(k)} + \delta\lambda^{(k)}. \end{aligned} \tag{5.184}$$

The procedure is repeated until convergence is obtained. Measures for the convergence are the residuals $\mathbf{a}^{(k)}$, $\mathbf{b}^{(k)}$ and $f^{(k)}$:

$$\mathbf{c}^{(k)} = \begin{bmatrix} \mathbf{a}^{(k)} \\ \mathbf{b}^{(k)} \end{bmatrix}, \ \left\|\mathbf{c}^{(k)}\right\| < Tolerance_1 \ \left|f^{(k)}\right| < Tolerance_2. \tag{5.185}$$

Finally, the converged solution gives the update values for $\boldsymbol{\sigma}^{n+1}$, $\mathbf{q}^{n+1}$ and $\boldsymbol{\epsilon}^{p^{n+1}}$.

5.5.10 Plane stress constraint

First of all, the elastic material response is discussed. Expression 5.186 shows an alternative form of (5.45):

$$\epsilon_{ij} = \frac{1+\upsilon}{E}\sigma_{ij} - \frac{\upsilon}{E}\sigma_{kk}\delta_{ij}. \tag{5.186}$$

Using the Voigt notation (definition see [60]), the strain and stress tensor can be represented by vectors. This allows a simpler representation of the fourth order elasticity tensor by a matrix:

$$\begin{bmatrix} \epsilon_{11} \\ \epsilon_{22} \\ \epsilon_{33} \\ \epsilon_{23} \\ \epsilon_{31} \\ \epsilon_{12} \end{bmatrix} = \begin{bmatrix} \frac{1}{E} & -\frac{\upsilon}{E} & -\frac{\upsilon}{E} & 0 & 0 & 0 \\ -\frac{\upsilon}{E} & \frac{1}{E} & -\frac{\upsilon}{E} & 0 & 0 & 0 \\ -\frac{\upsilon}{E} & -\frac{\upsilon}{E} & \frac{1}{E} & 0 & 0 & 0 \\ 0 & 0 & 0 & \frac{1+\upsilon}{E} & 0 & 0 \\ 0 & 0 & 0 & 0 & \frac{1+\upsilon}{E} & 0 \\ 0 & 0 & 0 & 0 & 0 & \frac{1+\upsilon}{E} \end{bmatrix} \begin{bmatrix} \sigma_{11} \\ \sigma_{22} \\ \sigma_{33} \\ \sigma_{23} \\ \sigma_{31} \\ \sigma_{12} \end{bmatrix}. \tag{5.187}$$

If the plane stress condition ($\sigma_{31} = 0$; $\sigma_{32} = 0$; $\sigma_{33} = 0$) is inserted in (5.187) the following relations are obtained:

$$\begin{aligned} \epsilon_{31} &= 0, \\ \epsilon_{32} &= 0, \\ \epsilon_{33} &= -\frac{\upsilon}{1-\upsilon}\left(\epsilon_{11} + \epsilon_{22}\right). \end{aligned} \tag{5.188}$$

Consequently, on the basis of the given in-plane strains $(\epsilon_{11}, \epsilon_{22}, \epsilon_{12})$, which result from the explicit solution procedure, the in-plane stress state $(\sigma_{11}, \sigma_{22}, \sigma_{12})$ can be computed. By enforcing the plane stress condition, the constitutive law also gives the out-of-plane strains based on a post-calculation (5.188).

In the case of a plastic material response, the stress update step can be complemented by the plane stress conditions [62]. Expression (5.189) shows the extended constitutive law:

$$\begin{aligned}
\boldsymbol{\epsilon}^{n+1} &= \boldsymbol{\epsilon}^{n} + \Delta\boldsymbol{\epsilon}, \\
\boldsymbol{\epsilon}^{p^{n+1}} &= \boldsymbol{\epsilon}^{p^{n}} + \Delta\lambda^{n+1} \cdot \mathbf{r}^{n+1}\left(\boldsymbol{\sigma}^{n+1}, \mathbf{q}^{n+1}\right), \\
\mathbf{q}^{n+1} &= \mathbf{q}^{n} + \Delta\lambda^{n+1} \cdot \mathbf{h}^{n+1}\left(\boldsymbol{\sigma}^{n+1}, \mathbf{q}^{n+1}\right), \\
\boldsymbol{\sigma}^{n+1} &= \mathbf{C} : \left(\boldsymbol{\epsilon}^{n+1} - \boldsymbol{\epsilon}^{p^{n+1}}\right), \\
f^{n+1} &= f\left(\boldsymbol{\sigma}^{n+1}, \mathbf{q}^{n+1}\right) = 0, \\
\sigma_{31} &= 0, \\
\sigma_{32} &= 0, \\
\sigma_{33} &= 0.
\end{aligned} \tag{5.189}$$

In [62] further methods are given for the consideration of the plane stress constraint.

5.6 Summary

The presentation of the theoretical background with respect to the forming simulation is aligned to the objectives of this thesis. Originating from continuum mechanics, the constitutive laws and the failure criterion are introduced, which are investigated in the subsequent chapters. The introduction of the finite element method is given, for the discussion of the results, obtained from forming simulations, and for the explanation of the post processing procedures, needed for the subsequently introduced optimizations.

Chapter 6

Experiments

The aim of this chapter is to introduce the experiments, which are needed for the identification and validation of the constitutive laws. The results of these experiments and a discussion of the experimental conditions are given in the subsequent chapters. For differentiating the functionality of the introduced experiments, three categories are defined:

- Fundamental experiments
- Complementary experiments
- Validation experiments

The fundamental experiments give the experimental input data for the calibration of the material model (see chapter 7) and the failure model according to the state of the art. In this work, the results and the evaluation procedure of these experiments are assumed to be reliable and therefore are not investigated.

The complementary experiments are introduced for generating additional input data for the material and the friction model calibration. An ideal complementary experiment shows a high sensitivity concerning one parameter of the material or friction model. As opposed to the fundamental experiments, the measured data of these experiments does not lead directly to the desired model parameter. For the parameter identification a comparison between the prediction of the simulation and the measured data is necessary. Suitable quantities are selected, which are sensitive with respect to the investigated model parameter. Finally a value for the model parameter is chosen, which gives the best prediction of the measured data on the basis of the selected quantities. This procedure is referred to as indirect method. The application of this method requires the determination of all the other model parameters in advance. Provided, the insensitivity of a model parameter with respect to the prediction of the measured quantities is proven, it is possible to apply the indirect method without knowing this parameter. This exception allows determining the unknown model parameters sequentially.

Finally additional validation experiments are proposed in order to validate the predictive capability of the material and friction models. Furthermore, these experiments are applied for the validation of the failure criteria. The results, obtained from these experiments are not taken into account for the model calibration.

One should consider that the introduced classification of the experiments (fundamental, complementary and validation experiments) generally depends on the applied constitutive laws. The classification, shown in this chapter, results from the constitutive laws, which are used in the subsequent chapters.

Generally, the usage of a standard set of complementary and validation experiments is recommended, which simplifies the material logistics, the execution of real and simulation based experiments and the postprocessing. In this paragraph, some key requirements for the design of these experiments are summarized.

- Deviations between the manufactured die face and the CAD data have to be avoided; otherwise the expressiveness of the experiments is reduced.
- The experiments should be suitable for all steel grades and aluminum alloys comprised in a car body.
- In order to minimize the computation time of forming simulations, a rigid tool behavior during the forming operation should be assumed. To avoid the violation of this assumption, an adequate tool stiffness has to be assured.
- The size of the specimen should be as small as possible in order to limit the expenses for purchasing material, logistics and measurements. Additionally, a small dimension of an experiment also has a positive effect regarding the computational cost of the related simulation based investigations.
- Today, shell elements are widely used for modeling the sheet metal of forming simulations. These elements can be applied, if the tool radius divided by the sheet thickness does not go below a value of 1.5 [88]. The tool design should consider this limitation. On the one hand, the applied sheet thickness should be minimal for avoiding the violation of shell element discretization restrictions. On the other hand, the availability of thin high strength steels could be limited.
- In order to avoid differences between the experiment and the simulation model, caused by touching up the binder zone, a material flow between the binder and the die should be avoided.

Consequently, tools which are applied for the series production of parts are not recommended for the identification and validation of constitutive laws, as the tryout of the tools and wear lead to deviations with respect to the CAD data. Furthermore, these tools are designed for a specific material and thickness.

An experiment is suitable for the identification or validation of material models, friction models and failure criteria, if and only if reproducible results are

obtained. It is recommended to use quantities for these investigations, which can be directly obtained from real experiments. Examples are material failure, the sheet thickness, the springback effect, the press force and the strain field on the part surface.

The reproducibility of the experiments has to be analyzed before comparing the results of the experiments with the simulation. It is recommended to perform at least three experiments under the same conditions and to select one of them as a reference for further investigations. The minimum deviation between the measured result and the mean of all experiments, which have been performed under the same conditions, is used as selection criteria. Applying mean values for the description of an experimental result could lead to non-physical states. This statement is of particular importance, if several quantities are measured based on a single experiment.

6.1 Fundamental experiments

6.1.1 Tensile test

The tensile test is a standardized experiment (EN ISO 6892-1) for the determination of the stress-strain relation under an uniaxial stress state. The specimen is loaded in direction of the tensile axis. Due to this load case, the corresponding eigenvalues of the stress state (principal stresses) within the specimen are zero, apart from the eigenvalue, associated with the tensile direction. Both, the applied tensile force and the elongation of the material are recorded while the experiment runs.

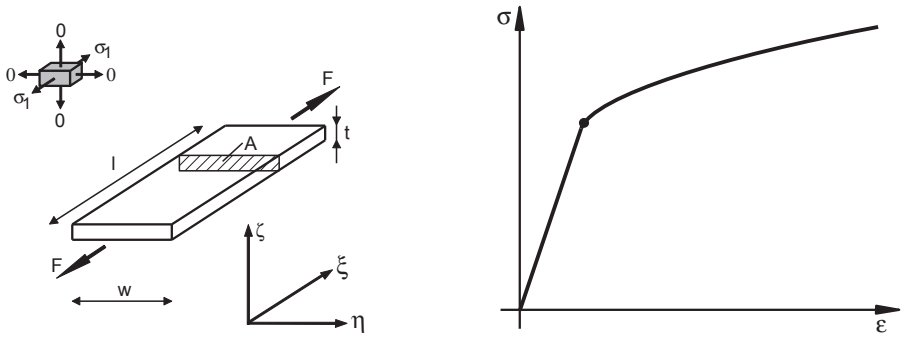

Figure 6.1: Tensile test; Left: Specimen of the experiment; Right: Schematic relation between the true stress σ and the true strain ϵ [80].

The stress state is computed in the current configuration, i. e., the Cauchy (or true) stress is identified. For the determination of the Cauchy stress from the tensile force and the measured elongation in tensile direction, plastic incompressibility is assumed $A_0 l_0 = A l$ ($A = wt$), which implies the preservation of the

volume. Expression (6.1) gives the relation between the Cauchy stress and the measured quantities:

$$\sigma = \frac{F}{A} = \frac{Fl}{A_0 l_0}. \tag{6.1}$$

The index 0 refers to the initial state. The corresponding logarithmic (or true) strain in direction of the tensile axis is shown by (6.2). In this case, the material time derivative of this strain measure is equal to the rate-of-deformation [60]:

$$\epsilon = \int_{l_0}^{l} \frac{\mathrm{d}l}{l}, \; \dot{\epsilon} = D. \tag{6.2}$$

Commonly, the plastic hardening (flow curve) is derived from the relation between the plastic strain and the stress state as shown by figure 6.1 (right). By a rising load, the specimen elongates uniformly. However, at a material specific strain level, diffuse necking occurs, which is accompanied with a non uniform elongation of the specimen. The above introduced expressions are only valid as long as the specimen is uniformly elongated. Unfortunately, due to this limitation, the maximum measurable equivalent plastic strain for the stress-strain relation is lower than that one occurring at industrial parts [89].

Additionally, the uniaxial stress states and R values (6.3) for the calibration of the yield locus are obtained from this experiment:

$$R = \frac{\dot{\epsilon}_{\eta\eta}}{\dot{\epsilon}_{\zeta\zeta}}. \tag{6.3}$$

On the basis of an uniaxial stress level below the yield strength, the Young's modulus and the Poisson's ratio can be determined.

6.1.2 Bulge test

A quadratic shaped specimen is clamped between the binder and the die (figure 6.3). The material flow in the binder zone has to be avoided, which is achieved by a sufficient binder force and a drawbead. These tool components are rotationally symmetric. Instead of a punch, oil is applied as a media for the forming process, which avoids the influence of friction apart from the die radius where the motion is negligible. The sheet metal is formed by an increasing level of oil pressure (figure 6.2)[89].

At the top of the dome, a biaxial stress state is induced. During the forming process, the deformation field in the region of the top of the dome and the oil pressure is recorded. Nowadays, optical measurement systems are available for the determination of a time dependent deformation field [90]. The exploitation of the measured data enables the computation of the associated strain field. If the ratio between the sheet metal thickness and the bulge diameter is small,

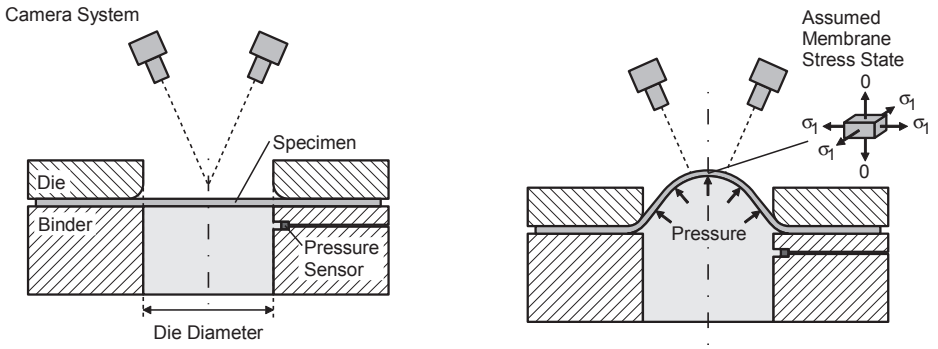

Figure 6.2: Bulge test; Left: State before performing the experiment; Right: State while performing the experiment.

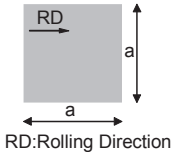

Figure 6.3: Specimen of the bulge test.

bending stresses can be neglected [91] and consequently, it is possible to deploy the membrane theory for the determination of the biaxial stress state

$$\sigma_b = \frac{pR}{2t}. \tag{6.4}$$

According to this relation, the biaxial stress state at the top of the dome depends on the oil pressure p, the curvature $\frac{1}{R}$ and the thickness t of the sheet metal at the corresponding location. Expression (6.4) is valid, if both principal stresses are assumed to be equivalent ($\sigma_b = \sigma_1 = \sigma_2$) [92]. Furthermore, the application of (6.4) implies the assumption that the shape of the dome in the pole zone is spherical. Originating from the assumption of plastic incompressibility, the strain in thickness direction is computed from principal strain values of the sheet surface (ϵ_1,ϵ_2):

$$t = t_0 e^{\epsilon_3},\ \epsilon_3 = -(\epsilon_1 + \epsilon_2). \tag{6.5}$$

The determination of the pole curvature is still a subject of research. One solution is to fit a sphere in the pole region for determining the curvature. Another solution is the application of a quadratic response surface instead of a sphere for the approximation of the pole surface [93]. On the basis of the bulge test a flow curve can be obtained, which does not show the limitation of the tensile test, as much higher strain levels can be reached before a material failure occurs. It has

to be mentioned that this flow curve refers to the biaxial stress state. Today, the biaxial flow curve is usually transformed to the space of the uniaxial flow curve. Finally, both flow curves are combined to a flow curve describing the hardening effect even for high strain levels. For this procedure an isotropic hardening of the material is assumed. An approach for this transformation is the application of the equivalent plastic work relation [94]. If the hardening behavior of the material depends on the stress state, the isotropic hardening assumption might not be suitable. In such a case, the biaxial flow curve serves a valuable contribution for the calibration of an anisotropic elasto-plastic hardening model. Finally, the bulge test gives a biaxial stress state and an additional R value (6.6) for the calibration of the yield locus[1]:

$$r_b = \frac{\dot{\epsilon}_{yy}}{\dot{\epsilon}_{xx}}. \tag{6.6}$$

6.1.3 Miyauchi test

For the generation of an approximately pure shear stress state, the Miyauchi test can be performed [96]. The definition of a pure shear stress state is given by [62]:

$$\sigma_1 = |\sigma_3|\,,\ \sigma_2 = 0,\ \sigma_1 > \sigma_2 > \sigma_3. \tag{6.7}$$

The eigenvalues σ_i of the stress tensor are assumed to be sorted ascending in expression (6.7). Figure 6.4 illustrates the specimen of the test, which is subdivided into the zones A,B,C for the explanation of the experiment.

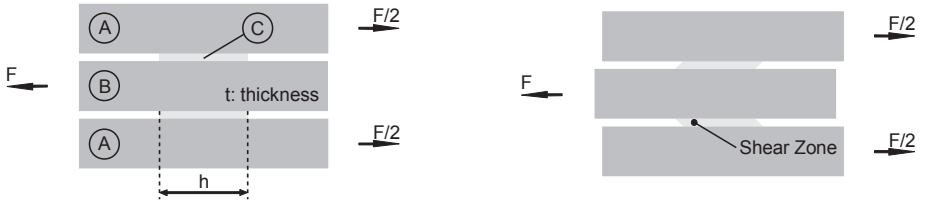

Figure 6.4: Miyauchi Test; Left: State before performing the experiment; Right: State after performing the experiment.

The external force F is acting, homogeneously distributed, in the zones A and B, causing a shear deformation in zone C. Figure 6.4 illustrates both, the initial state and the deformed state of the specimen. A fixture is needed, which is able to clamp the specimen sufficiently in these zones and enables to perform the test in a tensile testing machine. Optical measurement systems allow determining directly the time dependent deformation in zone C. On the basis of the measured deformation, the strain field is computed. The shear stress is obtained by applying

[1] Aretz shows in his work [95] that the Bulge test might not generally be suitable for the determination of the value of r_b.

$$\tau = \frac{F}{2ht}. \tag{6.8}$$

The evaluation of the experimental data leads to a flow curve with respect to the shear state and gives another stress state for the yield locus calibration. In case the material shows a pronounced anisotropic hardening, the experiment could be applied for the calibration of an elasto-plastic model, which takes this effect into account.

6.1.4 Nakajima test

The Nakajima test [81] is applied for the analysis of the onset of localized necking for different strain states. An alternative experiment has been proposed by Marciniak, which is not introduced here. Both experiments are standardized (ISO 12004-2).

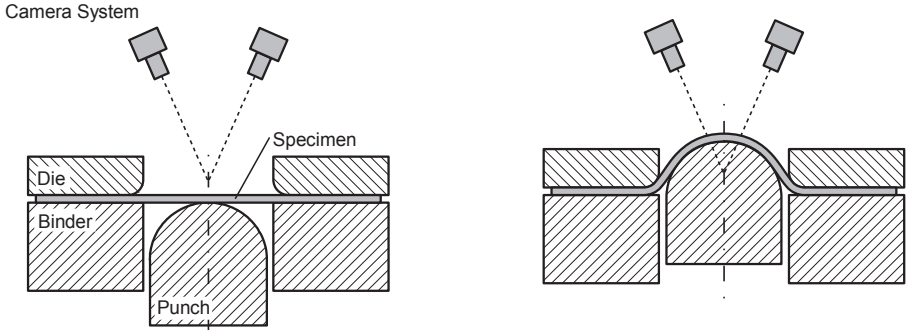

Figure 6.5: Nakajima Test; Left: State before performing the experiment; Right: State while performing the experiment.

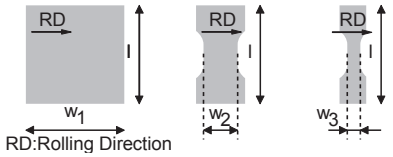

Figure 6.6: Nakajima Test; Specimen of the experiment.

The specimen is clamped between a rotationally symmetric binder and die. A material flow in the binder zone is avoided by a drawbead and a sufficient binder force. Usually, the Nakajima test is performed in specially designed testing machines. In this case, the forming operation can differ from the standard forming process (see chapter 3). Commonly, the binder and the die remain in a fixed position after the binder closing stage. The sheet metal is formed by a moving

spherical punch. Figure 6.5 illustrates the geometry of the tool and figure 6.6 the specimen. Different strain states are obtained by the variation of the specimen width w (figure 6.6). The deformation field is recorded during the forming process, which enables to compute a time-depended strain field on the surface. Friction affects the results of the Nakajima experiment. A suitable lubricant has to be deployed for reducing the effect of friction as much as possible [97]. For the determination of the limit strain before localized necking occurs, different methods have been proposed. Two of these methods are the position-dependent determination (ISO 12004-2) and time-dependent determination. Thereby, the time-dependent method proposed by Volk [98] is based on the thinning rate of the sheet metal in the necking zone. If localized necking occurs, the thinning rate in the necking zone increases significantly. This effect is taken as a criterion for the determination of the forming limit. The forming limit curve (FLC) is created on the basis of the determined forming limits with respect to different strain states.

6.2 Complementary experiments

6.2.1 YLIT-Experiments

The Yield Locus Identification Tools (YLIT) have been developed jointly by ThyssenKrupp Steel Europe and BMW. The YLIT-Experiments are performed to generate additional data for determining the best possible yield locus shape with respect to the considered steel grade. Two basic geometries are used:

- Spherical punch
- Cubic punch

All experiments consist of a rotationally symmetric die and binder. The YLIT-1-TKSE comprises a spherical punch and the YLIT-2-TKSE a cubical punch with fillets. The geometry of the YLIT-2-TKSE and YLIT-3-BMW is similar but different in dimension. The punch geometry of the YLIT-1-TKSE and the YLIT-4-BMW is identical; however the blank geometry is different. Additional information regarding the experiments is given in [99].

During the forming process, the specimen is clamped between the binder and the die. The forming process is identical to the standard process (chapter 3). However, these experiments can be performed in a testing machine for Nakajima experiments. In this case, the kinematical sequence of the tools can differ from the standard process (see section 6.1.4). While the specimen is formed, its deformation is recorded. On the basis of the deformation field, the strain field is computed a posteriori. For the investigation of the yield locus, the strain state of the material points are considered, which are finally located in the necking zone. Apart from the strain state, the maximum drawing depth according to the FLC is also determined. Both, the strain state and the drawing depth are compared with

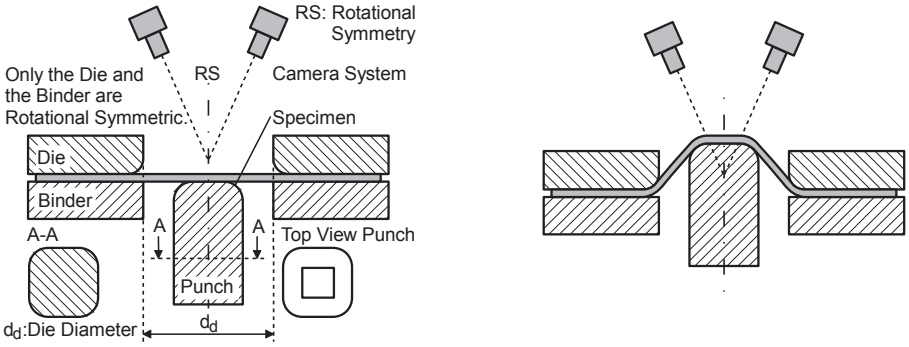

Figure 6.7: YLIT-3-BMW; Left: State before performing the experiment; Right: State while performing the experiment.

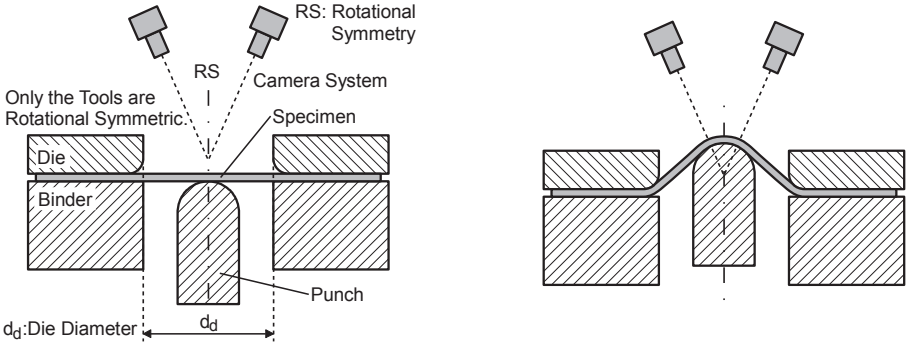

Figure 6.8: YLIT-4-BMW; Left: State before performing the experiment; Right: State while performing the experiment.

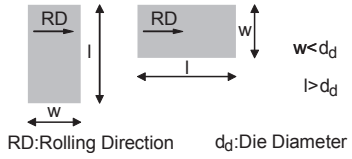

Figure 6.9: YLIT-Experiments; Specimens of the experiments.

the prediction of the simulation. The term drawing depth describes the maximum deformation of material points of the specimen with respect to the drawing direction at a given time during the forming operation. The maximum possible drawing depth is limited by the occurrence of a material failure (maximum drawing depth). The aim of this experiment is to search a yield locus shape, which leads to an accurate prediction of the measured quantities (indirect method). For obtaining the desired sensitivity of the yield locus shape on the prediction of the strain state and the drawing depth, the width of the rectangular specimen has to be optimized. As the measured data is determined before the elastic springback occurs, the measured strain field can be directly compared with the simulation result.

6.2.2 Bending experiment

For the investigation of the Young's modulus a bending test is proposed. A rectangular specimen is clamped between the binder and the die (figure 6.10). The specimen is bent by the punch movement. As long as the gap between the die and the punch is larger than the sheet thickness, the influence of friction is not expected to be significant.

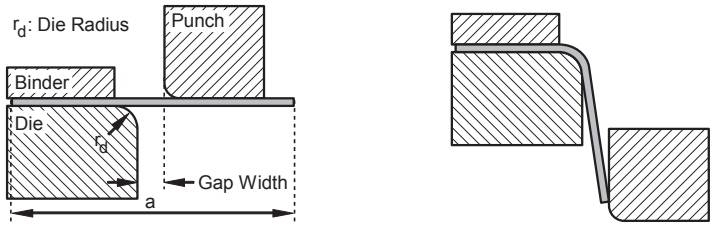

Figure 6.10: Bending experiment; Left: State before performing the experiment; Right: State after performing the experiment.

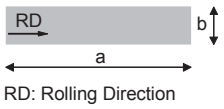

Figure 6.11: Bending experiment; Specimen of the experiment.

After the forming operation, before the punch is moved back to the initial position, the internal forces of the specimen are in equilibrium with the contact forces between the sheet and the tool surface. The movement of the punch to the initial position induces a new equilibrium state, which is accompanied with a deformation of the specimen (springback). The final geometry of the specimen is quantified by an angle α, as the zones A and C are not affected by the bending

operation (figure 6.12). Consequently, the angle α reflects the springback behavior of the specimen. The springback effect is directly proportional to the bending radius r_d [88]. Hence, for maximizing it and for minimizing the risk of reaching discretization limitations of shell elements, a high value for the bending radius is recommended [86]. Basically, an arbitrary alignment of the formed specimen is possible to evaluate the springback behavior. Most important is to choose an alignment, which allows a reproducible determination of the springback (angle α). In this thesis, the zone of the formed specimen, which is located between the binder and the die during forming, is clamped in the measuring fixture. Figure 6.12 illustrates the measuring fixture for the determination of the angle α. However, this type of alignment implies the influence of the gravity on the determined bending angle, which is expected to be small. The sensitivity of measured angle α with respect to the gravity depends on the stiffness of the formed specimen. Thereby, the stiffness is mainly affected by the initial thickness of the specimen. The thicker the material, the less influence is expected by gravity. Nevertheless, this effect should be investigated in advance before any comparison between measured and predicted angles.

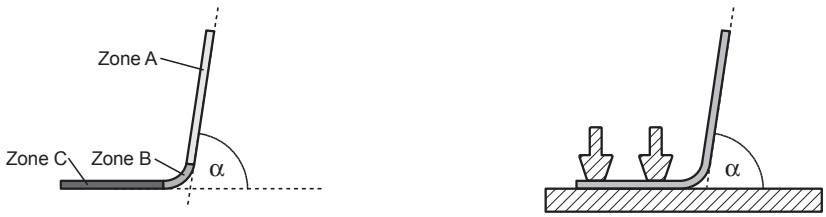

Figure 6.12: Bending experiment; Left: Definition of the angle α and the zones A, B and C; Right: The applied measuring fixture.

6.2.3 Friction experiment

For the investigation of the frictional behavior between, the sheet metal and the tools, it would be necessary to determine the stress distribution in the contact zone. Today, it is very difficult to measure the desired stress distribution during a forming process. Therefore, another approach is chosen in this work. The validity of the Coulomb friction model is assumed and the model parameter μ is determined by an inverse approach. The sensitivity of this experiment concerning the model parameters of the stress-strain relation will be shown in chapter 8. The dependency of the frictional behavior with respect to the contact pressure, the temperature and the relative velocity between the contact surfaces is neglected. Nevertheless, if a more advanced model for the description of the frictional behavior exists and its parameters are known, the proposed experiment could be applied for validation purpose. Figure 6.13 illustrates the proposed experiment. According to figure 6.14, the rolling direction of the specimen is chosen to be

perpendicular to the symmetry plane. The specimen is taken from the coil under preserving the as-delivered condition regarding the lubricant. Only in the center of the specimen the lubricant film is removed for inducing a grid for the strain measurement. However, this zone is not in contact with the tool surface and therefore the removal of the lubricant film does not affect the results of the experiment. During the forming process the specimen is clamped between the binder and the die. The sequence of the tool movement is identical to the standard forming process, which is shown in chapter 3. For the inverse determination of the model parameter μ, the strain state is measured at position P (figure 6.14) at the top surface. Thereby, the model parameter μ is adjusted in order to obtain a simulation based prediction of the strain state equal to the measured one. In order to maximize the dependency of the friction on the measured strain state, the relative movement between the sheet and the punch radius should be maximized. The desired property of the experiment is obtained by choosing R_p and d_{bp} (distance between the binder and the punch contour) sufficiently large. The experimental setup, used in this thesis, does not allow measuring the strain state during forming. Hence, the strain field is analyzed after tool opening. Under this condition, it is necessary to take the effect of the springback on the strain field into account. As a consequence, the forming simulation has to be complemented by a springback simulation in order to compare an equivalent mechanical state of the formed specimen.

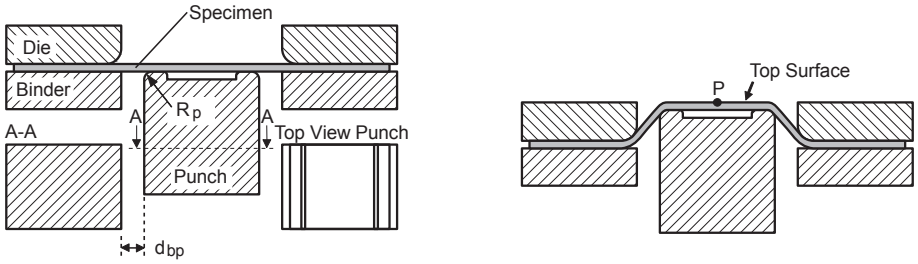

Figure 6.13: Friction experiment; Left: State before performing the experiment; Right: State after performing the experiment.

6.3 Validation experiments

6.3.1 U-Profile experiment

Generally, the deformation of car body parts, caused by the springback effect, is complex. It is a combination of side wall curl, torsion, flange and side wall rotations. The effect is mainly determined by the geometry, the material and production process of the part. Especially double-curved-part regions increase the geometrical stiffness and therefore reduce the springback effect.

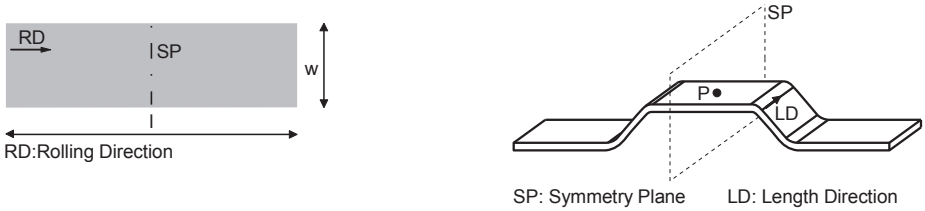

Figure 6.14: Friction experiment; Left: Specimen of the experiment; Right: Shape of the specimen after the forming operation.

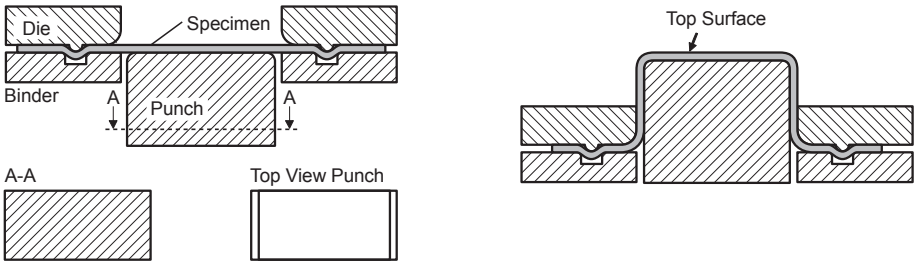

Figure 6.15: U-Profile experiment; Left: State before performing the experiment; Right: State after performing the experiment.

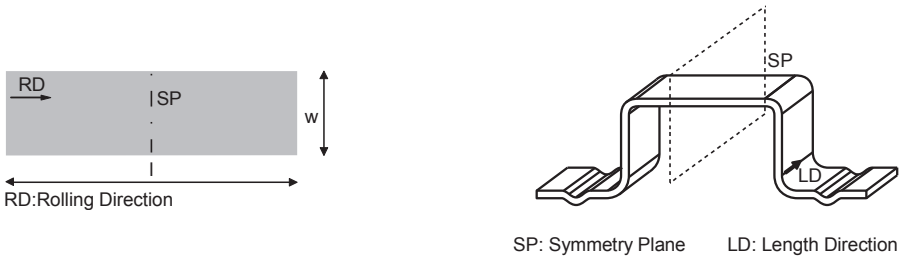

Figure 6.16: U-Profile experiment; Left: Specimen of the experiment; Right: Shape of the specimen after the forming operation.

For the validation of material and friction models based on the springback effect, a u-profile experiment is proposed (figure 6.15). The geometry of this experiment maximizes the springback effect because of the single-curved geometry and shows a complex deformation except from torsion. The forming process of this experiment comprises a binder closing and a stamping stage. A detailed description of the kinematical sequence of the tools is omitted here, as it is a standard forming process like introduced in chapter 3. In this work, the rolling direction of the specimen is chosen to be perpendicular to the symmetry plane (figure 6.16 (left)). Another orientation of the rolling direction with respect to the symmetry plane could give further information regarding the predictive capability of the material model. During forming, a relative movement between the sheet metal and the tool surface occurs. Hence, friction could affect the forming process. The equilibrium state of the formed sheet after tool opening will be referred to as actual geometry. If the material flow is homogeneous in length direction, the cross sections perpendicular to this direction with respect to the actual geometry are approximately identical. For obtaining the desired homogeneous material flow during the forming process, a drawbead is recommended, which is suitable for all considered materials. Without such a drawbead, slight disturbances of the lubricant distribution or geometrical defects, caused by the touch up procedure can lead to an inhomogeneous material flow. Consequently, it is sufficient to analyze a cross section for characterizing the actual geometry as shown by figure 6.17. For the analysis of the springback effect, the actual geometry has to be aligned. As the top surface (figure 6.15 (right)) can be approximately described by a plane, it is recommended to align the actual geometry with respect to this zone. In order to reduce the data, needed for quantifying the springback effect, the quantities side wall rotation, side wall curl and flange rotation are introduced (figure 6.17). The reference points A',B',C',D' and E' are derived under the assumption that the shrinking, caused by the springback effect, is negligible. If this assumption holds, the position of A' is determined by equating the developed length of SA and SA'. The remaining points B',C',D' and E' are identified in the same way.

The influence of the gravity on the actual geometry is minimized by aligning the length direction of the u-profile parallel with respect to the gravity acceleration. A comparison of the experimentally determined quantities with the prediction of the simulation enables to validate the applied material and friction model. A key requirement for comparing the simulation result with the measured data is the identity of the material flow. If deviations occur, the material flow of the simulation has to be adjusted according to the measured one.

6.3.2 Hole extrusion experiment

For the validation of the forming limit curve (FLC) with respect to low α values ($\alpha = \dot{\epsilon}_2/\dot{\epsilon}_1$), the hole extrusion experiment is proposed (figure 6.18). The specimen of the experiment comprises holes of different diameters d_i.

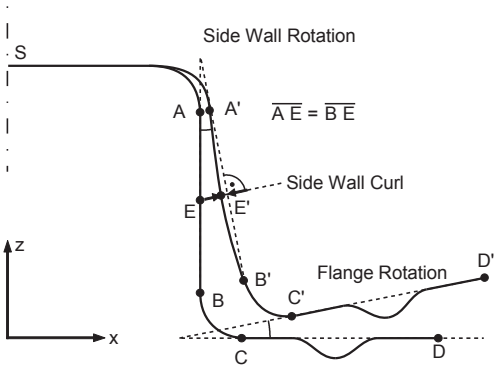

Figure 6.17: U-Profile experiment; Quantification of the springback effect.

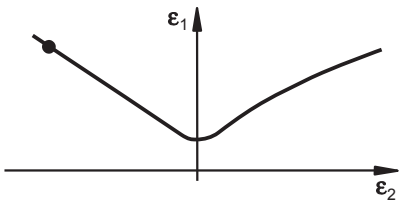

Figure 6.18: Hole extrusion experiment; Zone of the FLC validation.

The length direction of the specimen is, in this thesis, chosen to be parallel to the rolling direction. During the forming phase, the specimen is clamped between the binder and the die (figure 6.19 (left)). Subsequently, the hole is extruded by the punch (figure 6.19 (right)).

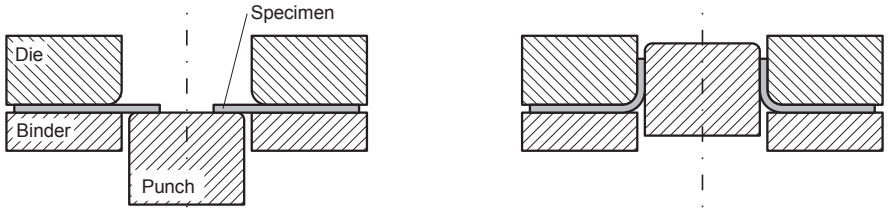

Figure 6.19: Hole extrusion experiment; Left: State before performing the experiment; Right: State after performing the experiment.

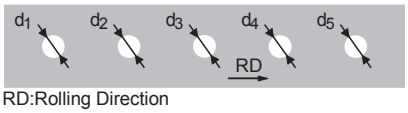

Figure 6.20: Hole extrusion experiment; Specimen of the experiment.

The center of the hole should lie on the rotational symmetry axis of the punch. In order to comply this condition, an additional fixture is needed, which supports the alignment of the specimen and clamps it during the binder closing phase. The kinematic sequence of the tools of this experiment is identical to the standard forming process, shown in chapter 3. The failure mode localized necking leads to a lower bound with respect to the hole diameter, which will be referred to as d_{min}. If the diameter d_i is chosen to be smaller than d_{min}, the hole extrusion will lead to localized necking. This diameter d_{min} is identified experimentally, by analyzing the onset of localized necking visually. It should be mentioned that depending on the investigated material this experiment can also lead to the failure mode fracture. However, in this thesis such materials are not treated. Subsequently, the hole diameter is varied in steps of 0.5mm. The manufacturing procedure of the hole can affect the onset of localized necking. A standard piercing operation leads to an additional material hardening of the sheet metal on the edge of the hole. The FLC is not suitable for the consideration of this effect. Hence, for the validation of the FLC another method for the manufacturing of the hole is needed. The mentioned hardening effect is avoided, if the hole is manufactured by a milling process. For the validation of the FLC, the diameter d_{min} is also determined based on the simulation. If the predicted value of d_{min} is coincident with experimentally identified value, the FLC is able to reflect the localized necking regarding the considered strain state. For this indirect validation of the FLC, the parameters

of the material and the friction model have to be determined in advance.

Nevertheless, if the hole is manufactured on the basis of a standard piercing process, the experimental result could be used for the validation of failure models, which takes the local hardening effects of trimming operations into account.

A similar experiment is described in the ISO/TS 16630. The objective of this experiment is to determine the limiting hole expansion ratio, which is given by

$$\lambda = \frac{D_h - D_0}{D_0}. \tag{6.9}$$

D_0 is defined as the initial hole diameter. In order to identify D_h, the specimen has to be observed during the forming process and the punch travel has to be stopped as soon as the material failure has extended through the thickness of the specimen. The advantage of the hole extrusion experiment, introduced in this thesis, is the possibility of evaluating the specimen a posteriori. Consequently, any observation of the specimen during the forming operation is not necessary, which simplifies the experimental setup.

6.3.3 Cylindrical deepening experiment

Finally, a validation experiment of the FLC regarding a strain state, which can be characterized by an α value slightly above 0 (figure 6.21), is introduced.

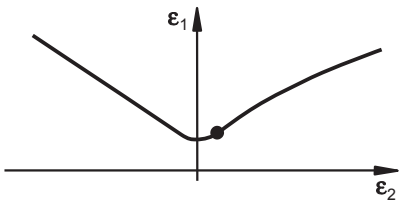

Figure 6.21: Cylindrical deepening experiment; Zone of the FLC validation.

Figure 6.22 shows the experimental setup of the experiment. During the forming process, the square shaped specimen is clamped between the binder and the die. The movement of the punch, the die and the binder is equal to the standard forming process described in chapter 3.

The objective of the experiment is to determine the maximum drawing depth limited by the onset of localized necking. Thereby, the movement of the press ram and the punch force are recorded. As the material flow between the binder and the die is prevented, the above mentioned strain state is induced in the side wall zone. Provided, a material failure occurs in this zone, the experiment can be applied for an indirect validation of the forming limit curve. The validation is performed by comparing the simulation based prediction of the maximum possible drawing depth with the experimentally determined maximum drawing depth. For this

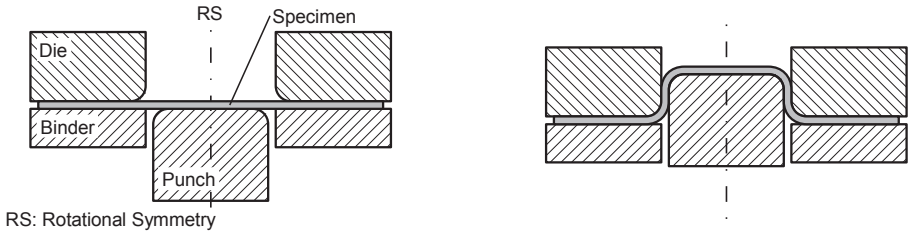

Figure 6.22: Cylindrical deepening experiment; Left: State before performing the experiment; Right: State while performing the experiment.

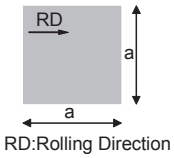

Figure 6.23: Cylindrical deepening experiment; Specimen of the experiment.

validation, the parameters of the material model and the friction model have to be identified in advance. As it is difficult to observe the development of localized necking during the forming process, the maximum drawing depth is determined indirectly.

The beginning t_0 of the forming operation is determined by the increasing punch force and the onset of localized necking t_1 is assumed to be coincident with the force maximum. The difference between the onset of localized necking and the fracture is assumed to be small in terms of the drawing depth[2]. As the progress of the ram movement is recorded, it is possible to derive the maximum drawing depths on the basis of t_0 and t_1.

[2]An investigation of the material response beyond the onset of localized necking is given in [100].

Chapter 7

Determination of the model parameters

This chapter treats the determination of the model parameters on the basis of the measured input data obtained from the fundamental experiments. The determination procedure of the model parameters depends on the selected material model. As mentioned in chapter 5.2 in this thesis elasto-plastic material models, under the assumption of an isotropic hardening behavior, are applied. Thereby, the yield loci Hill ´48, Barlat ´89 and Barlat 2000 are investigated. The Hill ´48 yield locus is obtained, if the exponent of the Barlat ´89 yield locus is chosen to be equal to 2. For the investigation of the Bauschinger effect, the applied material model is also complemented by the Chaboche-Rousselier kinematic hardening model. However, this thesis is not focused on this effect and therefore a description of the calibration procedure of this model is omitted. Table 7.1 shows the parameters, which can be directly identified from the results of the fundamental experiments. This table is only valid for the considered material models.

Table 7.1: Directly identified model parameters.

Elasticity	Yield Locus	Hardening
Young' Modulus Poisson Ratio	-	Flow Curve Strain Rate Sensitivity m

As a consequence, only a calibration procedure for identifying the model parameters of the yield locus is needed. As mentioned in chapter 5.2, the model parameters are obtained by the minimization of the difference between the measured stress states and strain rate ratios (R values) of different experiments (fundamental experiments, chapter 6) and the predictions of the yield locus. First of all, the computation of the stress states and strain rate ratios based on the yield

locus are introduced.

7.1 Tensile test

As mentioned in chapter 6, the tensile test is characterized by an uniaxial stress state. The direction of the induced force **F** defines the tensile axis of the experiment. α describes the angle between the tensile axis (coordinate system ξ, η, ζ) and the axes of anisotropy (coordinate system x,y,z). The x-axis of the latter mentioned coordinate system corresponds to the rolling direction.

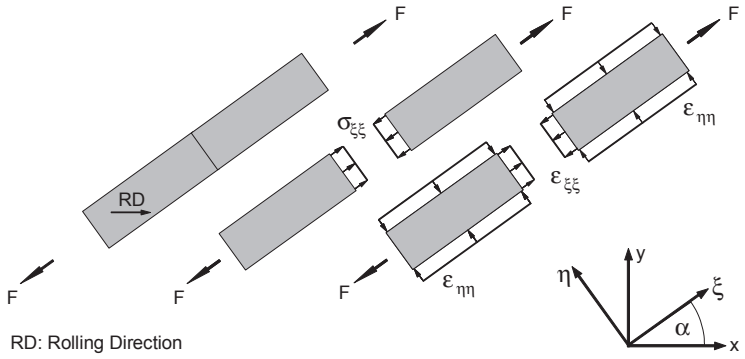

Figure 7.1: Tensile test; Stress state in the ξ, η-plane.

For the calibration of the yield locus, usually three types of specimens are investigated, differing regarding the angle (0°, 45° and 90°) between the tensile axis and the rolling direction. For each specimen the uniaxial stress and the R values are determined. The application of the yield locus requires a stress tensor representation, whose basis is coincident with the axes of anisotropy (chapter 5.2). The basis of the tensor $\boldsymbol{\sigma}$ (7.1) is coincident with the coordinate system ξ, η, ζ:

$$\boldsymbol{\sigma} = \begin{pmatrix} \sigma_{\xi\xi} & \sigma_{\xi\eta} \\ \sigma_{\eta\xi} & \sigma_{\eta\eta} \end{pmatrix}, \; \boldsymbol{\sigma}_* = \begin{pmatrix} \sigma_{xx} & \sigma_{xy} \\ \sigma_{yx} & \sigma_{yy} \end{pmatrix}. \tag{7.1}$$

The basis of the stress tensor $\boldsymbol{\sigma}_*$ (7.1) is identical with the axes of anisotropy. The relation between both representations $\boldsymbol{\sigma}$, $\boldsymbol{\sigma}_*$ of the uniaxial stress state is given by (7.2):

$$\boldsymbol{\sigma} = \mathbf{R}(\alpha)^T \boldsymbol{\sigma}_* \mathbf{R}(\alpha), \; \mathbf{R}(\alpha) = \begin{pmatrix} \cos\alpha & -\sin\alpha \\ \sin\alpha & \cos\alpha \end{pmatrix}. \tag{7.2}$$

Thereby, $\mathbf{R}(\alpha)$ is an orthogonal rotation tensor. Inserting $\boldsymbol{\sigma}_*$ into (7.2) gives the equations [50]:

$$\begin{aligned}
\sigma_{\xi\xi} &= \sigma_{xx}\cos^2\alpha + \sigma_{yy}\sin^2\alpha + \sigma_{xy}2\cos\alpha\sin\alpha, \\
\sigma_{\eta\eta} &= \sigma_{xx}\sin^2\alpha + \sigma_{yy}\cos^2\alpha - \sigma_{xy}2\cos\alpha\sin\alpha, \\
\sigma_{\xi\eta} &= -\left(\sigma_{xx} - \sigma_{yy}\right)\cos\alpha\sin\alpha + \sigma_{xy}\left(\cos^2\alpha - \sin^2\alpha\right).
\end{aligned} \tag{7.3}$$

As the ξ-axis of the coordinate system ξ,η,ζ is coincident with the tensile axis and the stress state is uniaxial, the first eigenvector of $\boldsymbol{\sigma}$ refers to the tensile axis. Therefore, $\sigma_{\xi\xi}$ is the principal value of the stress tensor and the remaining principal values are equal to 0.0. Consequently, a rearrangement of (7.3) in consideration of

$$\sigma_{u\alpha} = \sigma_{\xi\xi},\ \sigma_{\eta\eta} = 0,\ \sigma_{\xi\eta} = 0 \tag{7.4}$$

gives the stress tensor with respect to the axes of anisotropy

$$\begin{aligned}
\sigma_{xx} &= \sigma_{u\alpha}\cos^2\alpha, \\
\sigma_{yy} &= \sigma_{u\alpha}\sin^2\alpha, \\
\sigma_{xy} &= \sigma_{u\alpha}\cos\alpha\sin\alpha.
\end{aligned} \tag{7.5}$$

Finally, the associated equivalent stress of the yield locus, depending on the measured stress state of the tensile test and the model parameters, is computed. If the model parameters of the yield locus are calibrated in the desired way, the deviation between the computed equivalent stress and the stress value of the flow curve, regarding the equivalent hardening state $Y\left(\epsilon_{ref}\right)$, is small. The quantification of this deviation is shown below. Expression (7.6) introduces an abbreviation for the equivalent stress under an uniaxial stress state:

$$\overline{\sigma}_{u\alpha}\left(\mathbf{P}\right) = \overline{\sigma}\left(\boldsymbol{\sigma}_*\left(\sigma_{u\alpha}, \alpha\right), \mathbf{P}\right). \tag{7.6}$$

Thereby, $\overline{\sigma}$ is an equivalent stress, obtained from an arbitrary yield locus. The vector $\mathbf{P}$ comprises the parameters of the yield locus.

Apart from the equivalent stress, also the computation of the R_α value (7.7) [2] on the basis of the yield locus is introduced:

$$R_\alpha = \frac{\dot{\epsilon}_{\eta\eta}}{\dot{\epsilon}_{\zeta\zeta}}. \tag{7.7}$$

Figure 7.1 also illustrates the strain state of the tensile test in the ξ,η plane. Figure 7.2 complements the visualization of the strain state of 7.1 by the thickness direction.

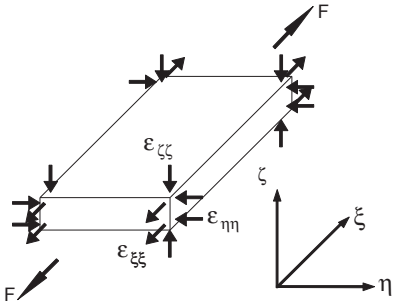

Figure 7.2: Tensile test; Visualization of the strain state.

For the computation of R_α the relation between the strain rate tensor $\dot{\boldsymbol{\epsilon}}$ and $\dot{\boldsymbol{\epsilon}}_*$

$$\dot{\boldsymbol{\epsilon}} = \begin{pmatrix} \epsilon_{\xi\xi} & \epsilon_{\xi\eta} \\ \epsilon_{\eta\xi} & \epsilon_{\eta\eta} \end{pmatrix}, \; \dot{\boldsymbol{\epsilon}}_* = \begin{pmatrix} \epsilon_{xx} & \epsilon_{xy} \\ \epsilon_{yx} & \epsilon_{yy} \end{pmatrix}, \tag{7.8}$$

is needed

$$\dot{\boldsymbol{\epsilon}} = \mathbf{R}(\alpha)^T \dot{\boldsymbol{\epsilon}}_* \mathbf{R}(\alpha), \; \mathbf{R}\,(\alpha) = \begin{pmatrix} \cos\alpha & -\sin\alpha \\ \sin\alpha & \cos\alpha \end{pmatrix}. \tag{7.9}$$

The basis of the strain rate tensor $\dot{\boldsymbol{\epsilon}}_*$ is the axes of anisotropy. The strain tensor $\dot{\boldsymbol{\epsilon}}$ refers to the coordinate system ξ,η,ζ. Inserting $\dot{\boldsymbol{\epsilon}}_*$ into 7.9 and applying $\mathbf{R}(\alpha)$ leads to

$$\begin{aligned} \dot{\epsilon}_{\xi\xi} &= \dot{\epsilon}_{xx}\cos^2\alpha + \dot{\epsilon}_{yy}\sin^2\alpha + \dot{\epsilon}_{xy} 2\cos\alpha\sin\alpha, \\ \dot{\epsilon}_{\eta\eta} &= \dot{\epsilon}_{xx}\sin^2\alpha + \dot{\epsilon}_{yy}\cos^2\alpha - \dot{\epsilon}_{xy} 2\cos\alpha\sin\alpha, \\ \dot{\epsilon}_{\xi\eta} &= -\left(\dot{\epsilon}_{xx} - \dot{\epsilon}_{yy}\right)\cos\alpha\sin\alpha + \dot{\epsilon}_{xy}\left(\cos^2\alpha - \sin^2\alpha\right). \end{aligned} \tag{7.10}$$

The strain rate $\dot{\boldsymbol{\epsilon}}_{\zeta\zeta}$ is not affected by the transformation of the basis of the strain rate tensor as the rotation is performed in the ξ,η plane. Provided the plastic incompressibility can be assumed, the expressions

$$\dot{\epsilon}_{\xi\xi} + \dot{\epsilon}_{\eta\eta} + \dot{\epsilon}_{\zeta\zeta} = 0 \tag{7.11}$$

and

$$\dot{\epsilon}_{xx} + \dot{\epsilon}_{yy} + \dot{\epsilon}_{zz} = 0 \tag{7.12}$$

hold. A rearrangement of 7.11, 7.12 and the equality $\dot{\epsilon}_{\zeta\zeta} = \dot{\epsilon}_{zz}$ leads to

$$\dot{\varepsilon}_{\zeta\zeta} = \dot{\varepsilon}_{zz} = -\left(\dot{\varepsilon}_{\xi\xi} + \dot{\varepsilon}_{\eta\eta}\right) = -\left(\dot{\varepsilon}_{xx} + \dot{\varepsilon}_{yy}\right). \tag{7.13}$$

Consequently, it is possible to formulate R_α depending on the strain rate tensor components of $\dot{\boldsymbol{\epsilon}}_*$:

$$R_\alpha = -\frac{\dot{\epsilon}_{xx}\sin^2\alpha + \dot{\epsilon}_{yy}\cos^2\alpha - 2\cos\alpha\sin\alpha\dot{\epsilon}_{xy}}{\dot{\epsilon_{xx}} + \dot{\epsilon_{yy}}}. \tag{7.14}$$

If the introduced relation between the strain rate tensor and the stress tensor is applied (Expression (5.64)),

$$\dot{\boldsymbol{\epsilon}}_* = \lambda\frac{\partial f}{\partial\sigma},\ \dot{\epsilon}_{xx} = \lambda\frac{\partial f}{\partial\sigma_{xx}},\ \dot{\epsilon}_{yy} = \lambda\frac{\partial f}{\partial\sigma_{yy}},\ \dot{\epsilon}_{xy} = \lambda\frac{\partial f}{\partial\sigma_{xy}}, \tag{7.15}$$

R_α can be expressed on the basis of the partial derivatives of the yield locus with respect to the stress tensor $\boldsymbol{\sigma}_*$ [4]:

$$R_\alpha\left(\boldsymbol{\sigma}_*\left(\sigma_\alpha,\alpha\right),\mathbf{P}\right) = -\left.\frac{\sin^2\alpha\frac{\partial f}{\partial\sigma_{xx}} + \cos^2\alpha\frac{\partial f}{\partial\sigma_{yy}} - \sin 2\alpha\frac{\partial f}{\partial\sigma_{xy}}}{\frac{\partial f}{\partial\sigma_{xx}} + \frac{\partial f}{\partial\sigma_{yy}}}\right|_{\boldsymbol{\sigma}_*(\sigma_{u\alpha},\alpha);\mathbf{P}}. \tag{7.16}$$

Expression (7.17) shows the application of a finite difference scheme for the numerical determination of the partial derivatives:

$$\begin{aligned}
\frac{\partial f}{\partial\sigma_{xx}} &\approx \frac{f\left(\sigma_{xx}+\Delta\sigma,\sigma_{yy},\sigma_{xy}\right) - f\left(\sigma_{xx}-\Delta\sigma,\sigma_{yy},\sigma_{xy}\right)}{2\Delta\sigma},\\
\frac{\partial f}{\partial\sigma_{yy}} &\approx \frac{f\left(\sigma_{xx},\sigma_{yy}+\Delta\sigma,\sigma_{xy}\right) - f\left(\sigma_{xx},\sigma_{yy}-\Delta\sigma,\sigma_{xy}\right)}{2\Delta\sigma},\\
\frac{\partial f}{\partial\sigma_{xy}} &\approx \frac{1}{2}\frac{f\left(\sigma_{xx},\sigma_{yy},\sigma_{xy}+\Delta\sigma\right) - f\left(\sigma_{xx},\sigma_{yy},\sigma_{xy}-\Delta\sigma\right)}{2\Delta\sigma}.
\end{aligned} \tag{7.17}$$

The partial derivative with respect to σ_{xy} implies the factor 0.5, as the yield locus f includes σ_{xy} and σ_{yx} [63]. For the comparison of the experimentally determined value and the computed R_α value the following abbreviation is introduced

$$R_\alpha\left(\mathbf{P}\right) = R_\alpha\left(\boldsymbol{\sigma}_*\left(\sigma_{u\alpha},\alpha\right),\mathbf{P}\right). \tag{7.18}$$

7.2 Bulge test

As mentioned in chapter 6, at the apex of the bulge specimen an equibiaxial stress state is generated. According to

$$\boldsymbol{\sigma} = \begin{pmatrix} \sigma_{\xi\xi} & \sigma_{\xi\eta} \\ \sigma_{\eta\xi} & \sigma_{\eta\eta} \end{pmatrix} = \begin{pmatrix} \sigma_b & 0 \\ 0 & \sigma_b \end{pmatrix} = \sigma_b \begin{pmatrix} 1 & 0 \\ 0 & 1 \end{pmatrix} \tag{7.19}$$

it is possible to extract the components σ_b from the stress tensor. As a result, the stress state is equivalently expressed by a multiplication of the scalar value σ_b and the identity tensor. As any vector remains unchanged by a multiplication with the identity tensor, every non-zero vector is an eigenvector of the identity matrix with eigenvalue of 1. Consequently, a transformation of the basis of the biaxial stress state does not affect the components of the stress tensor. Therefore, the biaxial stress state is directly inserted in the yield locus for the computation of the equivalent stress. Again, for the comparison of the obtained equivalent stress with the stress value of the flow curve, an abbreviation is introduced

$$\overline{\sigma}_b\left(\mathbf{P}\right) = \overline{\sigma}\left(\boldsymbol{\sigma}_*\left(\sigma_b\right), \mathbf{P}\right). \tag{7.20}$$

The measurement of the strain rate ratio

$$R_b = \frac{\dot{\varepsilon}_{yy}}{\dot{\varepsilon}_{xx}} \tag{7.21}$$

is an additional quantity for the calibration of the yield locus. Inserting (7.15) into (7.21) gives the R_b value in dependency of the partial derivatives of the yield locus with respect to the stress state $\boldsymbol{\sigma}_*$:

$$R_b\left(\boldsymbol{\sigma}_*\left(\sigma_b\right), \mathbf{P}\right) = \left.\frac{\frac{\partial f}{\partial \sigma_{yy}}}{\frac{\partial f}{\partial \sigma_{xx}}}\right|_{\boldsymbol{\sigma}_*(\sigma_b);\mathbf{P}}. \tag{7.22}$$

As opposed to the R_α value, the R_b value is defined for the strain state whose basis is identical with the axes of anisotropy. Expression (7.23) shows an abbreviation of the computed R_b value:

$$R_b\left(\mathbf{P}\right) = R_b\left(\boldsymbol{\sigma}_*\left(\sigma_b\right), \mathbf{P}\right). \tag{7.23}$$

7.3 Shear test

Depending on the angle α of the shear axes with respect to the axes of anisotropy, a transformation of the basis of the stress tensor $\boldsymbol{\sigma}$

$$\boldsymbol{\sigma} = \begin{pmatrix} 0 & \sigma_{\xi\eta} \\ \sigma_{\eta\xi} & 0 \end{pmatrix} = \begin{pmatrix} 0 & \sigma_s \\ \sigma_s & 0 \end{pmatrix} \tag{7.24}$$

has to be performed (figure 7.3). In consideration of an equivalent hardening state, the equivalent stress state is computed on the basis of the stress tensor, which is related to the axes of anisotropy. Expression (7.25) illustrates an abbreviation of the equivalent stress:

$$\overline{\sigma}_s\left(\mathbf{P}\right) = \overline{\sigma}\left(\boldsymbol{\sigma}_*\left(\sigma_s, \alpha\right), \mathbf{P}\right). \tag{7.25}$$

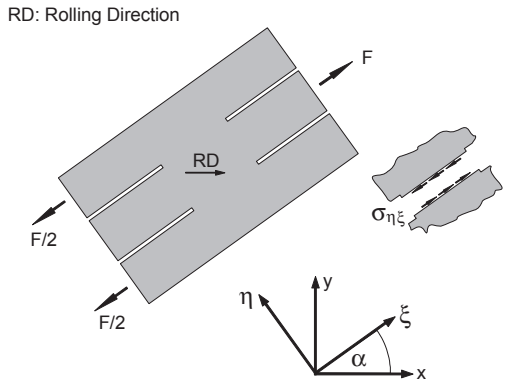

Figure 7.3: Shear test; Stress state in the ξ, η-plane.

7.4 Calibration of the Barlat 2000 yield locus

Usually, the flow curve for modeling the isotropic hardening is derived from a tensile test whose tensile axis is coincident with the rolling direction. The Barlat 2000 yield locus does not necessarily reproduce the flow curve exactly for this experiment. For example, if a calibration of the yield locus is performed based on an optimization by equally weighting the deviations between all the measured and predicted quantities, a difference between $\overline{\sigma}^{B2000}_{u0^\circ}\left(\boldsymbol{\sigma}_*, \boldsymbol{\alpha}, a\right)$ and $Y\left(\boldsymbol{\epsilon}_{ref}\right)$ is expected. Provided the hardening of the material can be assumed to be isotropic and an exact reproduction of the flow curve is desired, a scaling of the yield locus is applied:

$$f\left(\boldsymbol{\sigma}_*\right) = \gamma\overline{\sigma}^{B2000}\left(\boldsymbol{\sigma}_*, \boldsymbol{\alpha}, a\right) - Y\left(\boldsymbol{\epsilon}_{ref}\right) = 0. \tag{7.26}$$

The scaling factor γ is derived from equation

$$\gamma\overline{\sigma}^{B2000}_{u0^\circ}\left(\boldsymbol{\sigma}_*, \boldsymbol{\alpha}, a\right) = Y\left(\boldsymbol{\epsilon}_{ref}\right). \tag{7.27}$$

The vector $\boldsymbol{\alpha}$ contains the model parameters α_i of the Barlat 2000 yield locus. Subsequently, a multiplication of the model parameters α_i by the factor β is investigated. By inserting $\beta\boldsymbol{\alpha}$ into the Barlat 2000 yield locus, 7.28 can be derived:

$$\overline{\sigma}^{B2000}\left(\boldsymbol{\sigma}_*, \beta\boldsymbol{\alpha}, a\right) = \beta\overline{\sigma}^{B2000}\left(\boldsymbol{\sigma}_*, \boldsymbol{\alpha}, a\right). \tag{7.28}$$

Consequently, the multiplication of the vector $\boldsymbol{\alpha}$ by the scalar β is equal to a scaling of the yield yield locus. Therefore, provided the yield locus is scaled according to (7.26), its shape is not affected by the factor β. As a result, one of the α_i parameters can be prescribed without loss of generality. As a consequence, the space of the model parameter is reduced by one dimension.

7.4.1 Objective function

Firstly, a multiplicative aggregation on the basis of Harrington desirability functions is shown. Secondly, the objectives are additively combined to a single scalar objective value [4]. For a compact presentation of the objective functions, the sets A and B are introduced

$$\begin{aligned} A &= \{u0^\circ, u45^\circ, u90^\circ, b, s\}, \\ B &= \{0^\circ, 45^\circ, 90^\circ, b\}, \end{aligned} \tag{7.29}$$

and the domain of the parameter space α_i is given by

$$\alpha_i \in [L; U]. \tag{7.30}$$

7.4.2 Harrington desirability functions

By the application of the two-sided Harrington desirability function, the results of the equivalent stresses $\overline{\sigma}_I^{B2000}$ $(I \in A)$ and the R values R_J^{B2000} $(J \in B)$ are mapped onto an interval $[0, 1]$. For the formulation of the objective function, the results are multiplicatively aggregated as given by

$$d = \prod_{I \in A} d_2\left(\overline{\sigma}_I^{B2000}, U_I, L_I, n_I\right) \prod_{J \in B} d_2\left(R_J^{B2000}, U_J, L_J, n_J\right). \tag{7.31}$$

The choice of the Parameters U_I,L_I,n_I,U_J,L_J and n_J is discussed below. The value of the optimum is a priori known, as the target of the calibration procedure is the minimization of the deviation between predicted and measured stress states and strain rate ratios. In this case, the Harrington desirability functions are especially suitable, as only the location of the optimum in the model parameter space is unknown.

The domain of the model parameters α_i (7.30) can be considered by applying the one-sided Harrington desirability functions. Originating from the limits of the domain, the parameters of the desirability functions are derived

$$L \rightarrow b_{0_L}, b_{1_L},\ U \rightarrow b_{0_U}, b_{1_U}. \tag{7.32}$$

The parameter b_1 defines the slope within the gray zone between the states 0.0 and 1.0. Depending on the choice of b_1 the parameter b_0 determines the position

of the gray zone. As the domain of the model parameter space is a hypercube, for each dimension of the model parameter space two one-sided Harrington desirability functions have to be defined.

Expression (7.33) gives the desirability functions for the domain of the model parameter space:

$$g = \prod_{i=1}^{7} d_1\left(\alpha_i, b_{0_L}, b_{1_L}\right) \prod_{i=1}^{7} d_1\left(\alpha_i, b_{0_U}, b_{1_U}\right). \tag{7.33}$$

The objective function is given by

$$F = 1 - dg. \tag{7.34}$$

Subsequently, the term MAHDF (Multiplicative Aggregation based on Harrington Desirability Functions) is applied in order to refer to the presented aggregation of the objectives and the treatment of the constraints.

7.4.3 Additive aggregation of the objectives

Subsequently, another formulation of the objective function is discussed, without applying the Harrington desirability functions. Expression (7.35) shows an additive aggregation of the objectives to a single scalar value f:

$$f = \sum_{I \in A} \gamma_I \left(\frac{\overline{\sigma}_I^{B2000} - Y\left(\epsilon_{ref}\right)}{Y\left(\epsilon_{ref}\right)} \right)^2 + \sum_{J \in B} \gamma_J \left(\frac{R_J^{B2000} - R_J^{ed}}{R_J^{ed}} \right)^2. \tag{7.35}$$

Thereby, each measured quantity is compared with the prediction of the model and the result is normalized by the measured quantity. Finally, the normalized result is squared in order to penalize larger deviations disproportionate (ed: experimentally determined). In this case, the boundary condition with respect to the α_i values is considered by a penalty function as given by

$$\begin{aligned} g_U\left(x\right) &= \begin{cases} \left(1 + |x - U|^{n_U} k_U\right) & if \quad x > U \\ 1 & if \quad x \leq U \end{cases}, \\ g_L\left(x\right) &= \begin{cases} \left(1 + |x - L|^{n_L} k_L\right) & if \quad x < L \\ 1 & if \quad x \geq L \end{cases}. \end{aligned} \tag{7.36}$$

Thereby, for both, the lower g_L and the upper bound g_U, a penalty function is defined. The penalty functions (7.36) are multiplicatively aggregated as given by expression

$$g = \prod_{i=1}^{7} g_U\left(\alpha_i\right) g_L\left(\alpha_i\right). \tag{7.37}$$

Finally, the additively aggregated objectives and the penalty functions are combined multiplicatively to a single scalar objective value

$$F = fg. \tag{7.38}$$

For this type of aggregation the term AAOMAC (Additive Aggregation of the Objectives and Multiplicative Aggregation of the Constraints) is introduced.

7.4.4 Termination of the optimization

The termination criterion for the application of the evolutionary strategies is twofold. On the one hand, the maximum number of objective function evaluations is limited by the parameter n_{max}. On the other hand, a criterion based on the model parameter space is applied. For the latter mentioned criterion, the difference between the α_i values of current and the previous fitness function evaluation is computed for each dimension

$$\Delta\alpha_i^{n+1} = \left|\alpha_i^{n+1} - \alpha_i^n\right|. \tag{7.39}$$

The obtained value $\Delta\alpha_i^{n+1}$ is accumulated according to

$$\Delta\beta_i^{n+1} = \Delta\beta_i^n\,(1-c) + \Delta\alpha_i^{n+1}c. \tag{7.40}$$

The accumulation concept is taken from [33]. The significance, defined by c, of the previous $\Delta\alpha_i^{(n+1)}$ values decreases exponentially. If the accumulated value $\Delta\beta_i^{n+1}$ of all i is smaller than the threshold ϵ, the optimization is aborted:

$$\left(\forall\, i \in \{1,\ldots,7\} : \Delta\beta_i^{(n+1)} < \epsilon\right) \vee n > n_{\max}. \tag{7.41}$$

In this thesis, c is chosen to be equal to 0.8 and for ϵ a value of 0.0001 is applied.

7.4.5 Weighting of the objectives

Basically, the yield locus should give a good prediction of the stress states and the strain rate ratios of the fundamental experiments. However, over-fitting effects have to be definitely avoided. Oscillations of the yield locus shape could lead to a non-physical response of the material model, as the Clausius-Duhem inequality might be violated (chapter 5.2). Considering the Barlat 2000 yield locus, the anisotropy of the sheet metal is introduced by two linear transformations, which avoids oscillations and the yield locus is even convex. However, depending on the material, the Barlat 2000 yield locus might not be able to predict all the measured results of the fundamental experiments in the same quality. Therefore, the calibration procedure has to deal with the definition of compromises. For a high quality of the prediction of some stress states and strain rate ratios, a worse representation of the remaining states has to be accepted. In this chapter, the

underlying prioritization is performed based on experience. The lowest priority for the calibration of the investigated DX54 steel grade is given to the shear stress. All the subsequent analyses are performed on the basis of this steel grade.

The expressions (7.42) give the relation between the parameters of the desirability functions and the constants, defined in table 7.2:

$$\begin{aligned} U_I &= Y(\epsilon_{ref}) + Y(\epsilon_{ref})\, c_I,\ I \in A, \\ L_I &= Y(\epsilon_{ref}) - Y(\epsilon_{ref})\, c_I, \\ U_J &= R_J^{ed} + R_J^{ed} c_J,\ J \in B, \\ L_J &= R_J^{ed} - R_J^{ed} c_J. \end{aligned} \tag{7.42}$$

The priority of a stress state or a strain rate ratio can be increased by choosing a lower value of the exponent n. Also the parameters U and L can be modified in order to change the priority of an objective. For the subsequent investigations, only the exponent of the shear stress is increased in order to reduce its priority in comparison to the other objectives.

Table 7.2: Weights of the multiplicative aggregation.

$c_I = 2$
$c_J = 2$
$n_{u0^\circ} = n_{u45^\circ} = n_{u90^\circ} = n_b = 3;\ n_s = 10$
$n_J = 3$
$I \in A,\ J \in B$

Table 7.3 summarizes the weights, applied for the additive aggregation of the objectives. Again, the priority of the objective related to the shear stress is reduced. In this case, the weight γ_s is decreased. The other objectives are equally weighted. Furthermore, the choice of the parameters regarding the penalty function are given by table 7.3.

Table 7.3: Weights of the additive aggregation and the parameters of the penalty functions.

$\gamma_{u0^\circ} = \gamma_{u45^\circ} = \gamma_{u90^\circ} = \gamma_b = 1;\ \gamma_s = 0.01$
$\gamma_J = 1$
$n_U = n_L = 5$
$k_U = k_L = 5$
$J \in B$

7.4.6 Investigation of the calibration procedure

In this section, the calibration of the Barlat 2000 yield locus on the basis of different optimization algorithms ($(\mu/\mu, \lambda)$-CMA-ES, $(1+1)$-CMA-ES, $(1, \lambda)$-DR-ES and SQP) is investigated. Additionally, the introduced procedures for aggregating the objectives are compared. In this section, the exponent of the Barlat 2000 yield locus is chosen to be equal to 5.0. It is assumed that the subsequently presented results are invariant with respect to the choice of this exponent.

Generally, calibration problems can be multimodal [13]. Therefore, a global optimization algorithm could be advantageous for the calibration of the yield locus. For the subsequent investigation, the initial values of the parameters α_i are chosen to be equal to 1, as recommended in [3]. The domain of the parameter space is given by

$$\alpha_i \in [0; 2]\,. \tag{7.43}$$

Firstly, the results of a yield locus calibration resulting from a standard $(\mu/\mu, \lambda)$-CMA-ES and an additive aggregation ($AAOMAC$) are presented. The performance of evolutionary strategies can differ between optimizations of the same problem, as these algorithms are based on statistical methods. As a consequence, the calibrations of the yield locus are repeated 100 times in order to evaluate the performance of the optimization. Figure 7.4 (left) shows the number of objective function evaluations, needed for finding an optimum for each optimization. The $(\mu/\mu, \lambda)$-CMA-ES algorithm in combination with the mentioned aggregation of the objectives is able to find the optimum within 1500 and 3000 computations of the objective function value. The mean value of the needed objective function evaluations is 2398.

For the analysis of the progression of the objective function value, optimization 21 is chosen (figure 7.4 (right)), which represents the mean in terms of the needed objective function values for finding the optimum. Figure 7.4 (right) is based on a logarithmic scale. This figure confirms the above suggested stopping criterion.

Figure 7.5 shows the results of optimizations, performed under the application of a $(\mu/\mu, \lambda)$-CMA-ES in combination with a multiplicative aggregation ($MAHDF$). The results are evaluated in the same way as described above. The analysis of the results show that the $MAHDF$ is advantageous regarding the convergence.

Apart from the $(\mu/\mu, \lambda)$-CMA-ES also a $(1+1)$-CMA-ES is analyzed. Igel [20] reported a better performance of the $(1+1)$-CMA-ES in the case of a unimodal optimization problem. According to figure 7.6 (left), the performance of the $(1+1)$-CMA-ES is better than the standard $(\mu/\mu, \lambda)$-CMA-ES. This result indicates a possible unimodality of the Barlat 2000 yield locus calibration problem.

By applying the MAHDF approach in combination with the CMA-ES-(1+1) the performance of the optimization improves (figure 7.7 (left)).

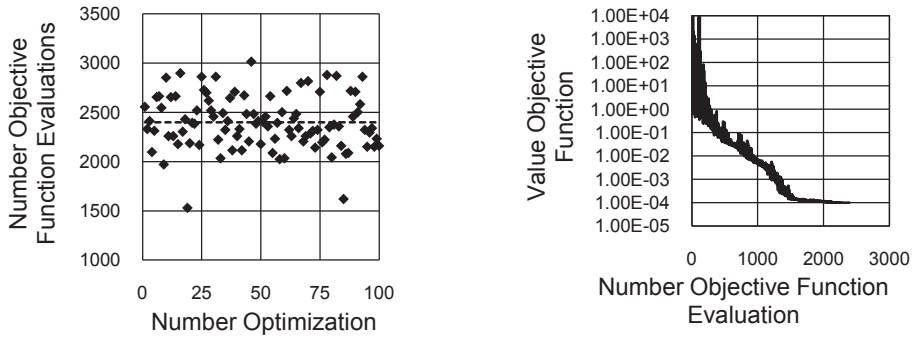

Figure 7.4: This investigation is based on the $(\mu/\mu, \lambda)$-CMA-ES algorithm and the AAOMAC is applied; Left: Analysis of the number of the needed objective function evaluations for finding the optimum; Right: Propagation of a single optimization (Optimization 21).

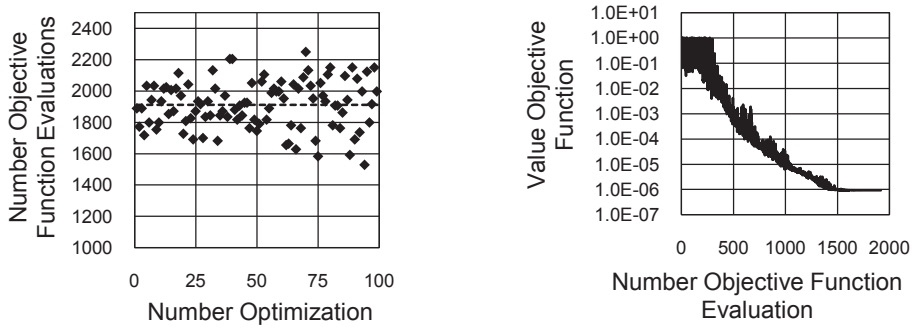

Figure 7.5: This investigation is based on the $(\mu/\mu, \lambda)$-CMA-ES algorithm and the MAHDF is applied; Left: Analysis of the number of the needed objective function evaluations for finding the optimum; Right: Propagation of a single optimization (Optimization 27).

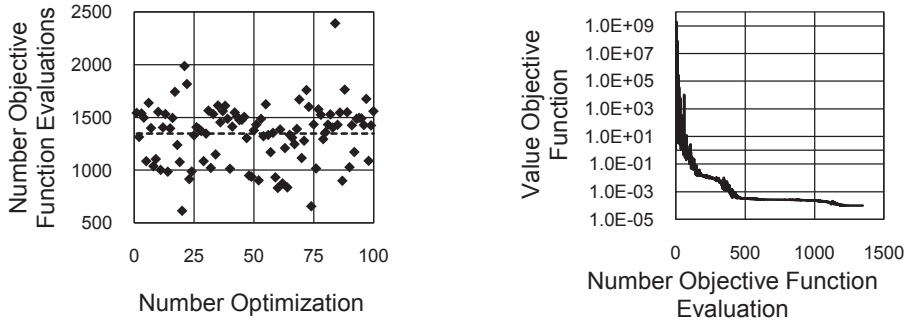

Figure 7.6: This investigation is based on the $(1 + 1)$-CMA-ES algorithm and the AAOMAC is applied; Left: Analysis of the number of the needed objective function evaluations for finding the optimum; Right: Propagation of a single optimization (Optimization 30).

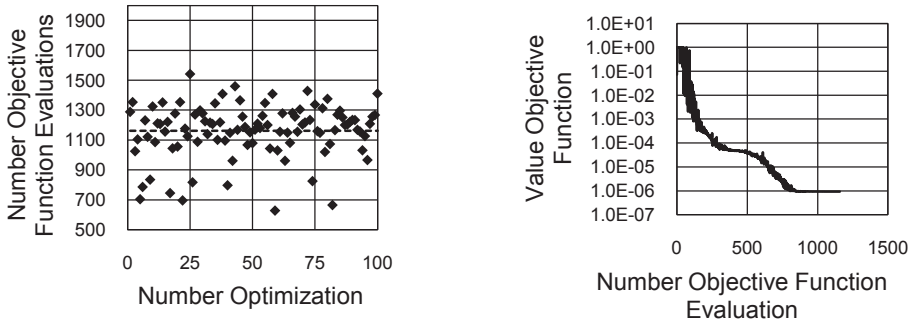

Figure 7.7: This investigation is based on the $(1 + 1)$-CMA-ES algorithm and the MAHDF is applied; Left: Analysis of the number of the needed objective function evaluations for finding the optimum; Right: Propagation of a single optimization (Optimization 93).

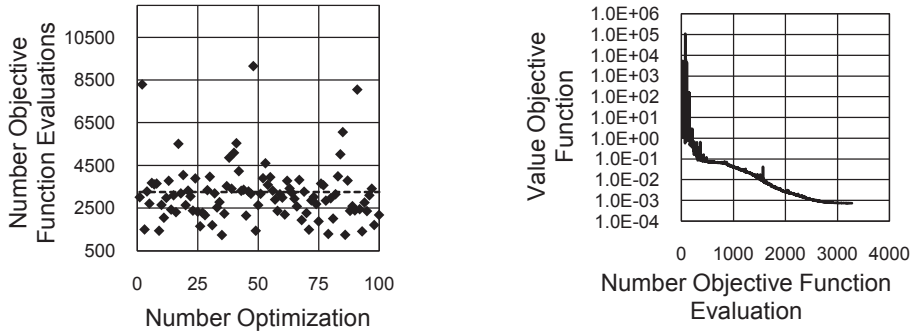

Figure 7.8: This investigation is based on the $(1, \lambda)$-DR-ES algorithm and the AAOMAC is applied; Left: Analysis of the number of the needed objective function evaluations for finding the optimum; Right: Propagation of a single optimization (Optimization 4).

The $(1, \lambda)$-DR-ES shows a worse performance as the $(\mu/\mu, \lambda)$-CMA-ES algorithms (figures 7.8, 7.9) and in this case, the $AAOMAC$ is advantageous in comparison with the $MAHDF$.

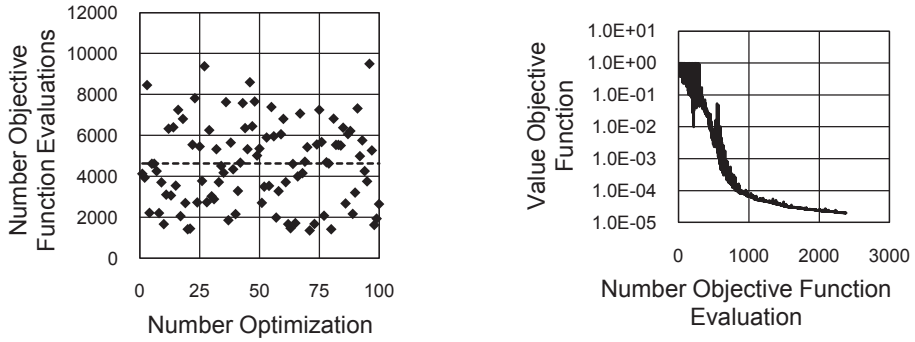

Figure 7.9: This investigation is based on the $(1, \lambda)$-DR-ES algorithm and the MAHDF is applied; Left: Analysis of the number of the needed objective function evaluations for finding the optimum; Right: Propagation of a single optimization (Optimization 79).

Finally, the SQP algorithm in combination with the AAOMAC shows the best performance (figure 7.10). This result is again an indication that the investigated problem could be, at least within the investigated domain, unimodal. Both optimizations based on the SQP algorithm are stopped, when the same value of the objective function is reached as obtained by applying the $(\mu/\mu, \lambda)$-CMA-ES.

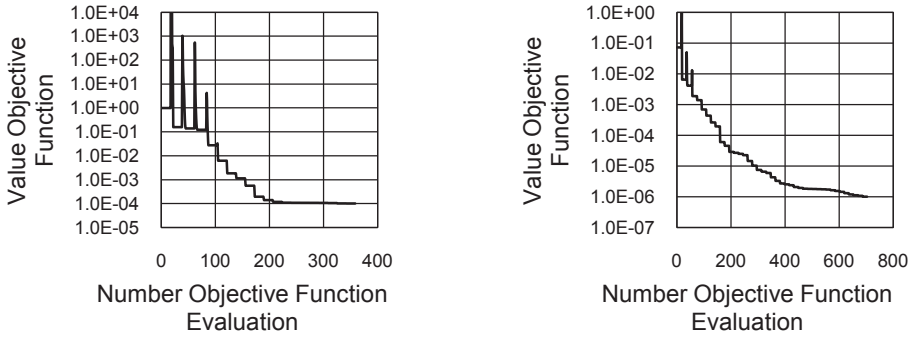

Figure 7.10: This investigation is based on the SQP algorithm; Left: Propagation of the optimization using the $AAOMAC$; Right: Propagation of the optimization using the $MAHDF$.

Table 7.4: Calibration of the Barlat 2000 yield locus using the AAOMAC.

Quantity	ED	$(\mu/\mu, \lambda)$ -CMA-ES	$(1+1)$ -CMA-ES	$(1, \lambda)$ -DR-ES	SQP
$\sigma^N_{u0^\circ}$	1.000000	1.000000	1.000000	1.000000	1.000000
$\sigma^N_{u45^\circ}$	1.032511	1.000002	0.999951	0.998167	0.999970
$\sigma^N_{u90^\circ}$	0.996696	1.000506	1.000513	1.025667	1.000575
σ^N_b	1.164572	1.164636	1.164670	1.165610	1.164549
σ^N_s	0.585851	0.532718	0.532719	0.538683	0.532729
$R^N_{0^\circ}$	1.000000	1.000000	1.000000	1.000000	1.000000
$R^N_{45^\circ}$	0.780172	0.780297	0.780203	0.777518	0.780189
$R^N_{90^\circ}$	1.271552	1.271703	1.271600	1.263591	1.271696
R^N_b	0.431034	0.431082	0.431052	0.428901	0.431043
F		9.98E-05	9.98E-05	7.29E-04	1.00E-04

The tables 7.4 and 7.5 summarize the predictions of the Barlat 2000 yield locus depending on the used optimization algorithm for the calibration of the model parameters (ED: experimentally determined). The depicted stress states are normalized with respect to the stress state of the tensile test, whose tensile axis is coincident with the rolling direction (N: Normalized):

$$\sigma^N_I = \frac{\sigma_I}{\sigma_{u0^\circ}},\ I \in A. \tag{7.44}$$

Also the strain rate ratios are transformed as given by

$$R^N_J = \frac{R_J}{R_{0^\circ}},\ J \in B. \tag{7.45}$$

The algorithms $(\mu/\mu, \lambda)$-CMA-ES, $(1+1)$-CMA-ES and SQP lead to similar results independent of the applied method for the aggregation of the objectives. The $(1, \lambda)$-DR-ES algorithm does not reach the same level regarding the quality of the calibration. Neither the AAOMAC nor the MAHDF approach generally leads to a better performance of the optimization. For the industrial application, the SQP algorithm combined with the AAOMAC seems to be a good choice.

Table 7.5: Calibration of the Barlat 2000 yield locus using the MAHDF.

Quantity	$(\mu/\mu, \lambda)$ -CMA-ES	$(1+1)$ -CMA-ES	$(1, \lambda)$ -DR-ES	SQP
$\sigma^N_{u0^\circ}$	1.000000	1.000000	1.000000	1.000000
$\sigma^N_{u45^\circ}$	1.000339	1.000366	0.995789	1.000884
$\sigma^N_{u90^\circ}$	1.001821	1.001835	0.986455	1.003796
σ^N_b	1.161177	1.161204	1.168191	1.160623
σ^N_s	0.532888	0.532892	0.529737	0.533360
$R^N_{0^\circ}$	1.000000	1.000000	1.000000	1.000000
$R^N_{45^\circ}$	0.777034	0.777314	0.792740	0.774955
$R^N_{90^\circ}$	1.261597	1.261531	1.307770	1.258105
R^N_b	0.427429	0.427425	0.442515	0.429197
F	9.16E-07	9.16E-07	7.75E-06	1.00E-06

7.5 Calibration of the Barlat ´89 yield locus

For the identification of the parameters a,c,h and p of the Barlat ´89 yield locus, the same procedure based on the minimization of the introduced objective functions could be applied. However, another approach exists for the determination of the Barlat ´89 yield locus parameter, which has been suggested by Barlat and is shown below [2].

Provided the flow curve is derived from a tensile test, whose tensile axis is coincident with the rolling direction, the parameters a and c are coupled:

$$a = 2 - c. \tag{7.46}$$

This relation is derived by inserting this stress state $\sigma_{xx} = Y(\epsilon_{ref})$;$\sigma_{yy} = 0$; $\sigma_{xy} = 0$ into the Barlat ´89 yield locus. Expression

$$\sigma_{yy} h = Y(\epsilon_{ref}) \tag{7.47}$$

is derived by inserting the stress state of an tensile test, whose tensile axis is perpendicular to the rolling direction $\sigma_{xx} = 0$ $\sigma_{xy} = 0$. The formulation of the

Barlat ´89 yield locus enables the analytical determination of R_α, as an analytical solution of the derivative of f with respect to $\boldsymbol{\sigma}_*$ exists [2]:

$$\begin{aligned}\dot{\epsilon}_{xx} = \dot{\lambda}\frac{\partial f}{\partial \sigma_{xx}} = \dot{\lambda} m \Big\{ & a\left(K_1 - K_2\right)\left|K_1 - K_2\right|^{m-2}\left(\frac{1}{2} - \frac{\sigma_{xx} - h\sigma_{yy}}{4K_2}\right) \\ & + a\left(K_1 + K_2\right)\left|K_1 + K_2\right|^{m-2}\left(\frac{1}{2} + \frac{\sigma_{xx} - h\sigma_{yy}}{4K_2}\right) \\ & + 2^m c K_2^{m-1}\frac{\sigma_{xx} - h\sigma_{yy}}{4K_2}\Big\},\end{aligned} \tag{7.48}$$

$$\begin{aligned}\dot{\epsilon}_{yy} = \dot{\lambda}\frac{\partial f}{\partial \sigma_{yy}} = \dot{\lambda} m \Big\{ & a\left(K_1 - K_2\right)\left|K_1 - K_2\right|^{m-2}\left(\frac{h}{2} + h\frac{\sigma_{xx} - h\sigma_{yy}}{4K_2}\right) \\ & + a\left(K_1 + K_2\right)\left|K_1 + K_2\right|^{m-2}\left(\frac{h}{2} - h\frac{\sigma_{xx} - h\sigma_{yy}}{4K_2}\right) \\ & - 2^m c K_2^{m-1} h\frac{\sigma_{xx} - h\sigma_{yy}}{4K_2}\Big\},\end{aligned} \tag{7.49}$$

$$\begin{aligned}\dot{\epsilon}_{xy} = \dot{\lambda}\frac{\partial f}{\partial \sigma_{xy}} = \dot{\lambda} m \Big\{ & a\left(K_1 + K_2\right)\left|K_1 + K_2\right|^{m-2} \\ & - a\left(K_1 - K_2\right)\left|K_1 - K_2\right|^{m-2} \\ & + 2^m c K_2^{m-1}\Big\} p^2 \frac{\sigma_{xy}}{2K_2}.\end{aligned} \tag{7.50}$$

For this yield locus Barlat derived an alternative expression for the computation of R_α:

$$R_\alpha(a, c, h, p) = \frac{2mY\left(\epsilon_{ref}\right)^m}{\left(\frac{\partial f}{\partial \sigma_{xx}} + \frac{\partial f}{\partial \sigma_{yy}}\right)\sigma_{u\alpha}} - 1. \tag{7.51}$$

If R_{00° and R_{90° are represented under the application of (7.48),(7.49) and (7.51), two expressions are obtained depending on c and h. Both expressions are independent of p as the shear stress σ_{xy} vanishes by transforming the related uniaxial stress tensors of R_{00° and R_{90° to the axes of anisotropy. A rearrangement of the obtained relations leads to the expressions

$$a = 2 - c = 2 - 2\sqrt{\frac{R_{0^\circ}}{1 + R_{0^\circ}}\frac{R_{90^\circ}}{1 + R_{90^\circ}}} \tag{7.52}$$

and

$$h = \sqrt{\frac{R_{0^\circ}}{1 + R_{0^\circ}} \frac{1 + R_{90^\circ}}{R_{90^\circ}}}. \tag{7.53}$$

Finally, p can be numerically determined by equating the experimentally determined $R^{ed}_{45^\circ}$ value with the computed $R^{B89}_{45^\circ}(a, c, h, p)$ value according to

$$R^{B89}_{45^\circ}(a, c, h, p) = R^{ed}_{45^\circ}. \tag{7.54}$$

7.6 Summary

In this chapter, calibrations of the yield loci are introduced, which are applied in the subsequent sections. Within the domain of the investigated parameter space, the calibration of the Barlat 2000 yield locus seems to be an unimodal problem. Therefore, a SQP algorithm in combination with an additive aggregation of the deviations between the predictions of the model and the measured quantities is recommended for this task.

Chapter 8

Calibration of the constitutive laws

8.1 Introduction

The examinations, presented in this and the following chapters, are based on the interstitial free mild steel DX54 and all simulations are performed with the simulation system LS-Dyna. In order to obtain comparable simulation results, each simulation is performed by the same choice of the numerical parameters, as given in the appendix D. The investigation of the procedures for the evaluation of the fundamental experiments are not subject of this work and therefore the stress states and the strain rate ratios, obtained from these experiments, are assumed to be suitable for the calibration of a material model.

The von Mises yield locus, which is not able to reflect the anisotropy of sheet metals, is not considered in the subsequent investigations and is only presented in chapter 5.2 for the introduction of the Barlat ´89 and the Barlat 2000 yield locus. A commonly applied yield locus in the industrial environment is the Hill ´48. The Barlat ´89 yield locus reduces to the Hill ´48, if its exponent is chosen to be equal to 2. The calibration of the Hill ´48 yield locus is simple, provided the same calibration procedure is applied as shown for the Barlat ´89 yield locus (see chapter 7), which is based on three R values, obtained from three tensile tests. As the exponent of the Barlat ´89 yield locus is predefined ($m = 2$), only the parameters a,c,h and p have to be calibrated. Nevertheless, the calibration of the Hill ´48 yield locus could be also performed by taking additional fundamental experiments into account. However, in this work the calibration of the Hill ´48 yield locus is limited to the procedure, shown in chapter 7.

As opposed to the Hill ´48, the Barlat ´89 offers more flexibility to control its shape, as this formulation comprises the exponent as an additional parameter. Again, various calibration procedures exist to determine the model parameters of this yield locus. For the further investigations, the exponent is treated indepen-

dent of the determination of the model parameters a,c and h, which are identified in the same way as shown in chapter 7. However, one has to bear in mind that for the calibration of the parameter p, the value of the exponent has to be known in advance. The exponent is identified by an inverse method, which is introduced below.

The Barlat 2000 yield locus needs further fundamental experiments for the calibration of its eight parameters α_i and the exponent a. In this work, the calibration of the Barlat 2000 yield locus is performed on the basis of tensile, bulge and Miyauchi tests. Thereby, three tensile tests are performed as described above, which give the R values $R_{0^\circ} = R_{00}$, $R_{45^\circ} = R_{45}$ and $R_{90^\circ} = R_{90}$ and the uniaxial stress states $\sigma_{u0^\circ} = \sigma_{00}$, $\sigma_{u45^\circ} = \sigma_{45}$ and $\sigma_{u90^\circ} = \sigma_{90}$. From the Bulge test a biaxial stress state and from the Miyauchy test a shear stress state are obtained. All of the experimentally determined stress states have to be identified under an equal state of hardening $Y(\epsilon_{ref})$. The parameters α_i are obtained by the minimization of the difference between predicted and measured stress states and strain rate ratios (see chapter 7).

Figure 8.1 illustrates a calibration of the Barlat 2000 yield locus for the material DX54. For the calibration of the yield locus parameters, the R_b value is assumed to be equal to 1. For each measured stress state and strain rate ratio the same weight is applied as given in table 7.2. The yield locus Barlat 2000 reflects the stress states of the fundamental experiments sufficiently (figure 8.1/figure 8.2). An exception is the shear stress, which is less accurately predicted by this model calibration. If other weights are used for the calibration of the yield locus, the model value of the shear stress might show less deviation with respect to the experimentally determined one. If the exponent is chosen to be equal to 2, the biaxial stress state is not predicted well compared with the other exponents.

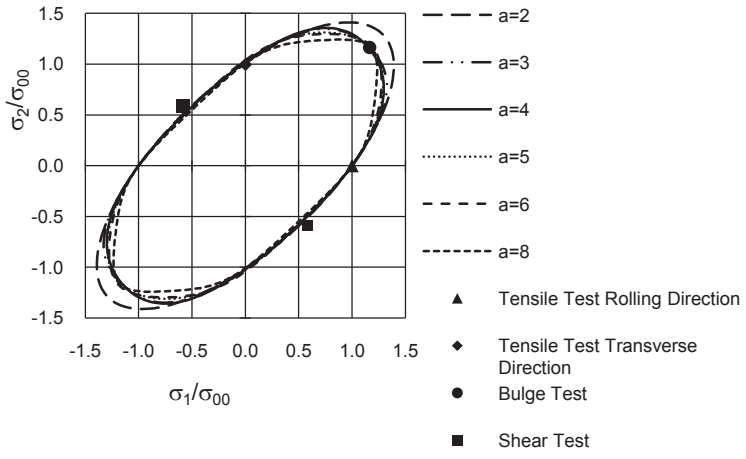

Figure 8.1: Barlat 2000 yield locus; Comparison between the measured and the predicted stress states.

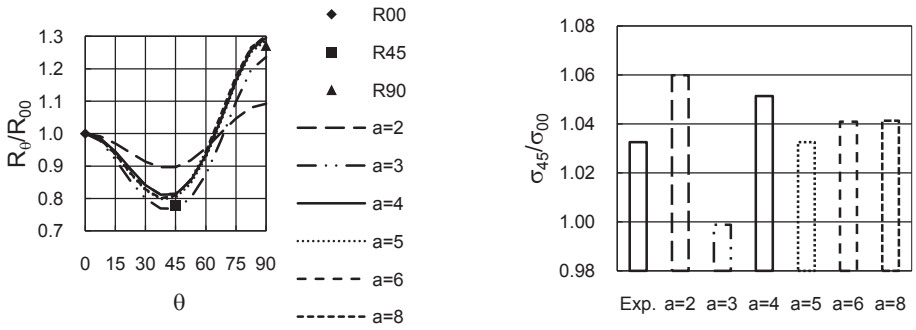

Figure 8.2: Barlat 2000 yield locus; Left: Comparison between the measured and the predicted R values; Right: Comparison between the measured and the predicted σ_{u45° value.

Figure 8.2 (left) illustrates the prediction of the R values. Apart from $a = 2$, slight deviations between the measured and the computed R values on the basis of the yield locus Barlat 2000 are recognizable (R_{45}, R_{90}). The stress state σ_{u45° of the tensile test, whose angle between the tensile axis and the rolling direction is 45°, is also well reflected by the yield locus. As mentioned above, the application of the yield locus requires a stress tensor representation, whose basis is coincident with the axes of anisotropy. Commonly, the yield locus is visualized in the eigenvalue space of the stress tensor. Consequently, the experimentally determined stress state can only be visualized in this space, if the associated transformation of the basis with respect to the axes of anisotropy leads to a tensor belonging to the eigenvalue space. Therefore, the uniaxial stress state σ_{u45° cannot be visualized in the eigenvalue space, as the mentioned transformation induces a σ_{xy} value unequal to zero. Therefore, the diagram 8.2 (right) is introduced.

The stress states, which are related to plane strain states, obviously differ, if different exponents are applied. Unfortunately, the experimental data does not give an indication regarding the selection of the exponent.

According to

$$\frac{max[\sigma_1(a=4)] - max[\sigma_1(a=6)]}{\sigma_{u0^\circ}} \sim 0.02, \tag{8.1}$$

it seems to be difficult to identify the exponent on the basis of a plane strain experiment. This is because, a highly accurate measurement of the stress state with respect to the plane strain state is necessary in order to determine the exponent. Provided such an experiment exists, it is necessary to bear in mind that the identification of the exponent would strongly depend on the measurement accuracy of the fundamental experiments. For example, a slight deviation of the biaxial stress state from the true value, in combination with the result of the plane strain experiment, would lead to a different exponent. Therefore, an additional type of identification experiments is necessary in order to determine the yield

locus exponent.

Obviously, the question regarding the yield locus exponent is avoided if the Hill ´48 yield locus is applied. However, as shown by figure 8.3 the Hill ´48 (Barlat ´89 yield locus; $m = 2$) is not able to reflect the experimentally determined stress states (fundamental experiments) in the same way as the Barlat 2000 yield locus. The biaxial stress state and σ_{u45° are poorly reflected by the yield locus Hill ´48 (figure 8.3, 8.4 (right)).

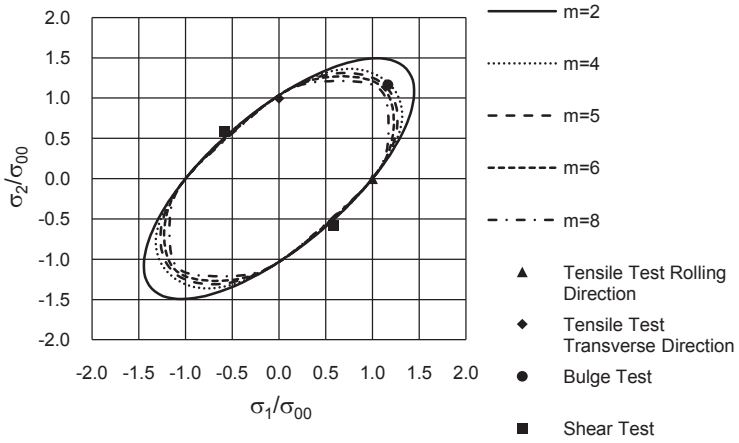

Figure 8.3: Barlat ´89 yield locus; Comparison between the measured and the predicted stress states.

However, the R values are exactly predicted, as the calibration procedure of this yield locus is solely based on them (figure 8.4 (left)). Also the Barlat ´89 cannot reach the same level of accuracy regarding the prediction of the measured data obtained from the calibration experiments in comparison with the Barlat 2000 yield locus. According to the figures 8.3 and 8.4 (right), the prediction of the biaxial stress state and σ_{u45° depends on the exponent. On the one hand, the larger the exponent is chosen, the better the Barlat ´89 yield locus reflects the stress state σ_{u45°. On the other hand, the best representation of the stress state σ_b is given for exponents between 4.0 and 5.0 (figure 8.3). Within the investigated range of exponents, there is none, which leads to an accurate prediction of all the considered stress states. The representation of the R values is of same quality, independent of the choice of the exponent, which results from the chosen calibration procedure. Consequently, the Barlat 2000 yield locus might able to predict arbitrary stress states better than the Hill ´48 and Barlat ´89 yield locus, provided the identified exponent reflects the material behavior. Therefore, it seems to be reasonable to focus the subsequent investigations on the Barlat 2000 yield locus.

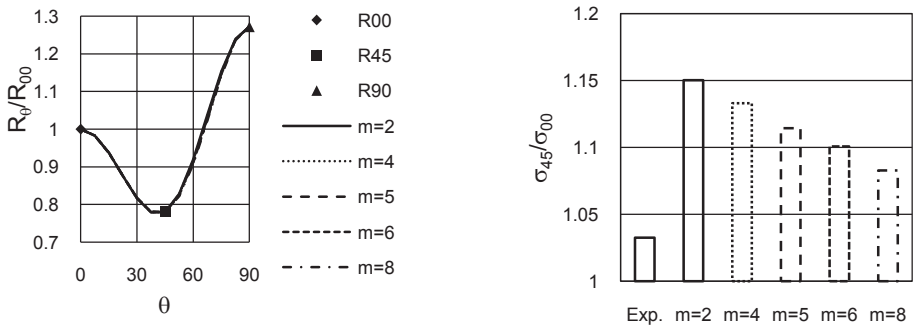

Figure 8.4: Barlat ´89 yield locus; Left: Comparison between the measured and the predicted R values; Right: Comparison between the measured and the predicted σ_{u45° value.

Other yield loci like Banabic 2005 [4] or Dell 2006 [101] have the same potential of reflecting the measured data of the fundamental results on a same quality level as the Barlat 2000 model. In this context, it is assumed that the Barlat 2000 yield locus represents this class of yield loci, which allows focusing the further investigations on this model.

In recent years, yield loci like the CPB06ex3 [5] have been proposed comprising more model parameters. On the one hand, these yield loci offer an accurate prediction of the experimentally determined stress states and strain rate ratios. On the other hand, the increased amount of model parameters is accompanied with the need for additional fundamental experiments. For example, for the application of the yield locus CPB06ex3 21 model parameters have to be identified for a plane stress problem. Today, it seems to be difficult to conduct all these fundamental experiments for industrial applications.

Finally, the question arises, whether the differences with respect to the yield locus shape are relevant for forming simulations. Figure 8.5 illustrates the specimen of the YLIT-3-BMW experiment and three simulation results, based on different yield locus setups. The location of the predicted necking remarkably depends on the choice of the yield locus and the exponent. This example underlines the need for choosing an appropriate yield locus and, if necessary, its exponent.

Another aspect of the material model is the hardening effect. In industrial practice, the material hardening is usually assumed to be isotropic and is described by the flow curve, which is obtained from a tensile test in the rolling direction. Under uniaxial stress conditions, the maximum measurable equivalent plastic strain is lower than that one occurring at industrial parts. On the one hand, an appropriate extrapolation of the measured data, obtained from the tensile test, could be performed. On the other hand, further experiments are available (for example: Bulge test) to complement the uniaxial flow curve that do not have the same limitation as the tensile test.

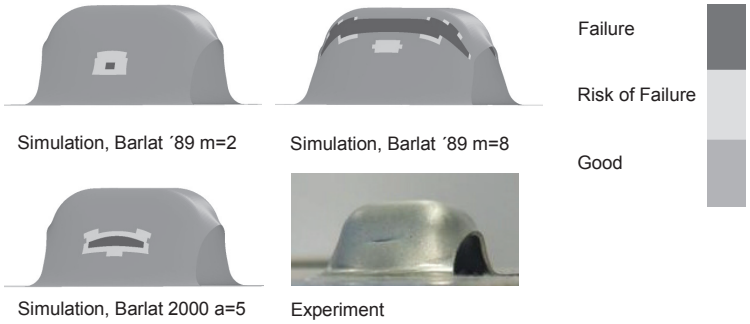

Figure 8.5: YLIT-3-BMW; Locations of the occurrence of localized necking, depending on the choice of the yield locus and its exponent [99].

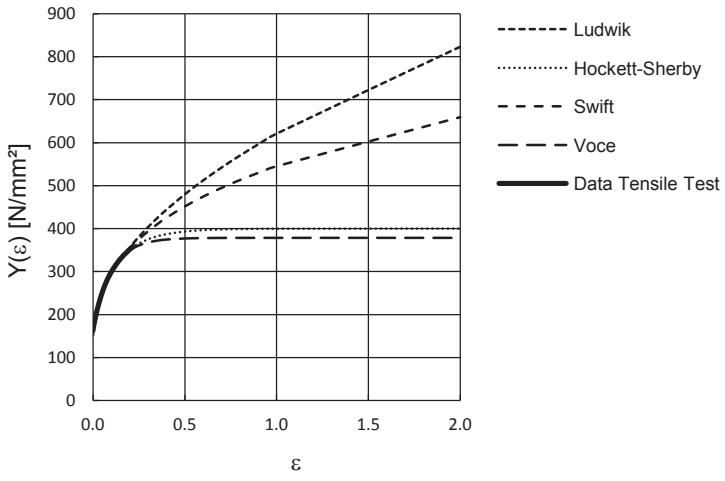

Figure 8.6: Flow curves using different extrapolation methods; Ludwik [102], Hockett-Sherby [103], Swift [104] and Voce [105].

For the first mentioned approach experience is needed, in order to choose a suitable extrapolation. Figure 8.6 shows the result of standard extrapolation methods. Depending on the choice of the extrapolation method, a remarkably different hardening behavior is assumed. Additionally, arbitrary linear combinations based on the shown extrapolation methods can be generated for modeling the hardening effect. In this work, the flow curve is derived from the experimental data of tensile and bulge tests, as this approach is less dependent on experience and should allow a more realistic representation of the hardening effect. Nevertheless, the subsequently presented results depend on the chosen way of the description of the hardening effect.

Sheet metals also show a strain rate dependent hardening behavior. It is still an open question whether this effect has to be taken into account for industrial forming simulations.

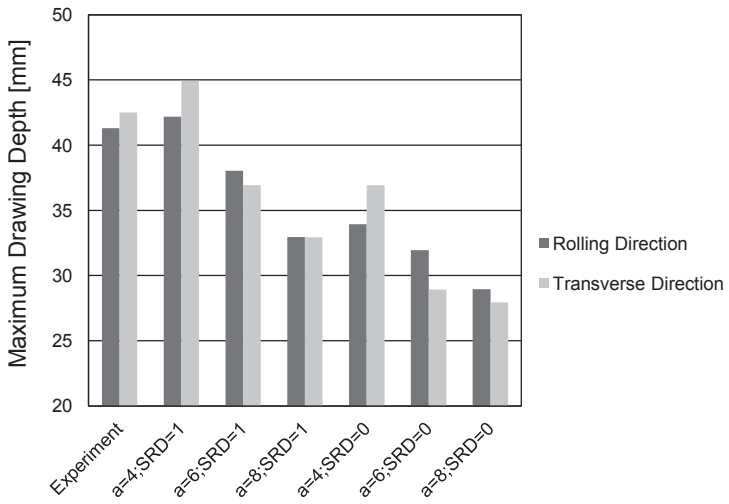

Figure 8.7: Influence of the strain rate dependency of the hardening effect (SRD=1: The strain rate dependency is considered; SRD=0: The strain rate dependency is not considered).

Figure 8.7 summarizes simulation based predictions of the maximum drawing depth under variation of the Barlat 2000 yield locus exponent regarding the YLIT-4-BMW. Furthermore, both cases are considered, with ($SRD = 1$) and without ($SRD = 0$) taking the strain rate dependency of the material hardening effect into account. Additionally, the experimentally determined maximum drawing depth is also given in figure 8.7. A significant dependency of the consideration of the strain rate effect on the prediction of the drawing depth is recognizable. These results indicate the necessity for analyzing the strain rate dependency of the hardening effect. These results confirm the findings reported in [99].

As mentioned in chapter 5.2, the elastic material model comprises the model parameters Young's modulus and Poisson ratio. For the prediction of the springback effect both model parameters play a crucial role, as the part deforms elastically in order to reach another equilibrium state after tool opening. Usually the Young's modulus is assumed to be independent of the strain state. Commonly, for modeling the elastic behavior of steel, it is recommended to choose the Young's modulus equal to $210000 N/mm^2$. For example, this value can be found in [106]. However, the investigations of Doege et al. show an influence of the deformation on the value of the Young's modulus (figure 8.8). Other authors like Thibaud et al. [107] and Yoshiha et al. [6] also report a dependency of the Young's modulus with respect to plastic yielding.

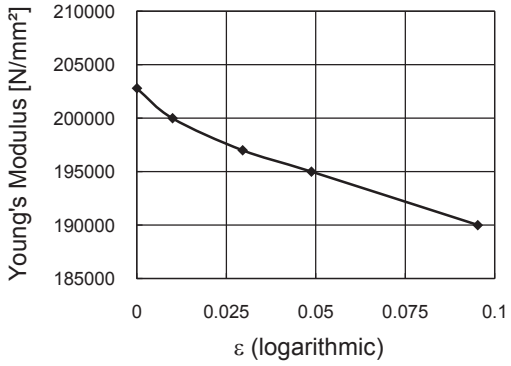

Figure 8.8: Strain dependency of the Young's modulus; DC06 [12].

Even at low strain levels, the Young's modulus is below the common literature values. For an equivalent strain of 10%, the Young's modulus decreases to a value of $190000 N/mm^2$. It has to be mentioned, that the results of figure 8.8 are obtained from the material DC06. However, in this chapter the material DX54 is investigated. It is assumed that the DX54 will also show a strain dependent Young's modulus of the same magnitude, as both materials differ only slightly regarding the tolerances of the yield strength and the coating (DX54 hot-dip coated, DC06 electrolytically coated). Industrial parts can show equivalent strain levels on such a scale and therefore this effect should be investigated for obtaining the best possible springback prediction. In order to be able to apply a standard material model, comprising a Young's modulus, which is independent of the strain history, a simplified approach is chosen for taking the observations of Doege et al. into account. Thereby, it is assumed to be sufficient to apply a reduced Young's modulus. The Poisson ratio is considered to be independent of the strain history and is directly determined from the tensile test.

Furthermore, cyclic loading of metals affects the material response, which is referred to as Bauschinger effect. The complementary and validation experiments are not expected to be strongly sensitive with respect to this effect. However, the

Chaboche-Rousselier kinematic hardening model [7] will be deployed in order to confirm this expectation.

The measured data, obtained from the investigated experiments, might depend on friction between the tool surface and the specimen. In order to determine a description of the friction, the Coulomb model is applied and its model parameter μ is inversely calibrated.

For the subsequent investigations, a material model comprising an elastic model, the Barlat 2000 yield locus and an isotropic hardening model is deployed. The exponent of the yield locus, the need for the consideration of the strain state dependency of the Young's modulus, the friction coefficient and the necessity of considering the strain rate dependent hardening and the Bauschinger effect cannot be determined by the fundamental experiments. It is proposed to identify these unknown model parameters inversely by complementary experiments. Thereby, the consideration of the strain rate dependency of the hardening effect and the Bauschinger effect is treated as unknown model parameter.

In an ideal case, the results of each complementary experiment are exactly sensitive with respect to one of the unknown parameters. Provided, for each unknown parameter such an experiment would exist, the identification procedure could be performed in an arbitrary order. However, the complementary experiments might be sensitive with respect to more than one unknown. Under these circumstances, it can still be possible to determine the values of the investigated parameters. However, the order of determining the unknowns is not arbitrary any more. The knowledge regarding the sensitivities allows investigating whether the determination of the desired parameter is possible on the basis of a given set of experiments. Furthermore, if necessary, an order for evaluating the experiments can be derived. Finally, it is necessary to know, whether any combination of the unknown parameters exists, which leads to a sufficient accurate prediction of the measured data.

For the analysis of the sensitivities, a formulation of an optimization problem is recommended. The objective function, which has to be minimized, is the difference of the results obtained from the simulation and the measured data [108]. The parameters of the optimization are the above mentioned unknown parameters of the material and friction model. The time consumption for the optimization is determined by the computation time of an objective function evaluation, which lies in this case between an hour and a few hours, and the soft- and hardware resources. Therefore, an optimization strategy is preferred, which gives the desired result with a minimum of objective function evaluations. Additionally, an optimization strategy is needed, which allows sensitivity analyses, supports the treatment of discrete parameters and is able to overcome local minima. Grid and gradient methods are, therefore, not recommended. It is proposed to use evolutionary strategies for performing the optimization. An evolutionary strategy implying a derandomized self adaptation [35] ($(1, \lambda)$-DR-ES) meets the mentioned demands and shows a high robustness regarding nonlinearities. Hence, this approach seems to be a good compromise in comparison to a sampling, which can be

more computationally expensive, and does not focus on the interesting parameter space regions. In other words, the application of an optimization based approach enables to use the knowledge of the optimum, given by the measured data. Because of the computational cost of the objective function evaluations, the number of simulation runs is limited to 100. Therefore, the presented optimization results are not expected to reflect the best possible optimum, as more objective function evaluations would be desirable. The chosen limit is a compromise in order to obtain the desired information by investing an affordable computational effort. The contribution of the optimization regarding the choice of the unknown parameters is threefold. Firstly, the sensitivities of the investigated parameters with respect to the deviation between the simulation results and the measured data are given. Secondly, depending on the sensitivities, the optimization allows the identification of the unknowns. Thirdly, the investigation based on the optimization assures that interrelations between the unknown parameters are considered.

The range of the parameter space is derived from investigations or defined on the basis of experience. According to the findings, summarized in figure 8.1, the lower limit of the Barlat 2000 yield locus exponent is chosen to be equal to 2.5. This investigation shows a loss of the flexibility of the Barlat 2000 yield, if the yield locus exponent is selected from an interval between 2.0 and 3.0. But it has to be mentioned that this interval is only valid for the investigated material. The upper limit is set based on experience equal to 8. The range of the Young's modulus is derived from the lowest value reported by the investigations of Doege and the common literature value ($210000 N/mm^2$). Finally, the range of the friction model parameter is chosen according to experience. A summary of the parameters, discussed in this section, is given by table 8.1.

Table 8.1: Summary of the unknown model parameters.

Parameter
Strain Rate Dependency of the Hardening Effect
Exponent Barlat 2000
Kinematic Hardening
Young's Modulus
Friction Coefficient

8.2 YLIT-Experiments

As mentioned in chapter 6, the YLIT-Experiments are performed to generate additional data for determining the best possible yield locus shape with respect to the considered sheet metal. According to the figures 8.1 and 8.3 the shape of the yield locus of the investigated material is asymmetric in the principal stress space. In order to take this property into account and to maximize the benefit

of the YLIT-Experiments two specimens are considered, as introduced in [99]. Thereby, the specimens differ in the angle between their length direction and the axes of anisotropy. For the subsequent investigations this angle is chosen to be equal to 0° (rolling direction RD) and 90° (transverse direction TD).

Figure 8.9 illustrates the scheme of the optimization for the investigation of the YLIT-Experiments. As depicted, each optimization step comprises a calibration of the yield locus parameter α_i depending on the selected yield locus exponent a. The parameters α_i are computed as given in chapter 7. After the yield locus parameters are determined, the input files for the simulation are generated, the forming simulation is performed and the results are evaluated. Thereby, both specimens are considered simultaneously within a simulation run. Subsequently, the simulation results are prepared for the comparison with the measured data. Finally the value of the objective function is computed.

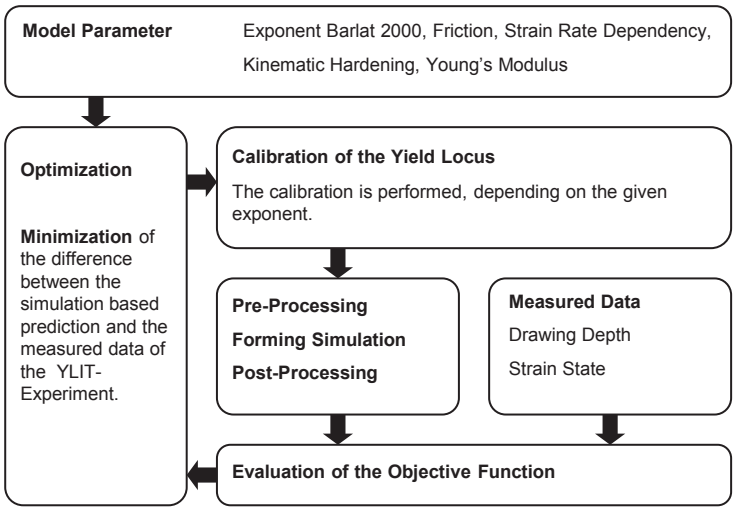

Figure 8.9: YLIT-4-BMW; Sequence of the Optimization.

The quality of the material model is measured on the basis of the comparison between the predicted and the experimentally determined maximum drawing depth. Beyond this limit value, the experiments of the investigated material DX54 show the failure mode localized necking (figure A.2). Therefore, the forming limit curve is applied for the evaluation of the state of the material concerning the occurrence of failure. The experimental determination of the maximum drawing depth is difficult, as the onset of localized necking is a question of interpretation. Differences regarding philosophy of the identification of localized necking between the YLIT-Experiments and the Nakajima experiment should be avoided (see chapter 6). Otherwise, a consistent comparison regarding the predicted and the experimentally determined maximum drawing depth is not possible. In order

to avoid these difficulties, in [109] it is suggested to derive the experimentally determined maximum drawing depth based on measured strain fields and the forming limit curve. Generally, for the application of the forming limit curve, a strain field describing the midsurface of the sheet with respect to the thickness direction is needed. However, the measured strain field corresponds to the surface of the sheet. The deviation of the strain fields belonging to the surface and the midsurface is assumed to be negligible in the necking zone.

Table 8.2: YLIT-4-BMW; Measured results.

Experiment	ϵ_1	ϵ_2	d_{MDD} [mm]
$1(RD)$	0.402	-0.141	41.9
$2(RD)$	0.397	-0.145	41.3
$3(RD)$	0.384	-0.138	40.9
			41.4 (Mean RD)
$4(TD)$	0.423	-0.164	42.3
$5(TD)$	0.429	-0.164	42.5
$6(TD)$	0.421	-0.169	42.7
			42.5 (Mean TD)

Additionally, the prediction of the strain state in the necking zone is taken into account. Thereby, the strain state of a material point is taken, which is located within the necking zone. However, the measured strain state of this material point refers to a drawing depth, which does not show localized necking.

The analysis of the failure limit and the strain state is performed subsequent to the simulation. As today's available storage media do not allow storing the simulation results of each computed time step (explicit method), the export of the needed data has to be predefined at given points in time. Consequently, the quality of the simulation based prediction in terms of the maximum drawing depth depends on the choice of the points in time which define the export of the results. It seems to be reasonable to consider the quality, regarding the predicted material failure, with respect to the drawing depth. Therefore, a set D of drawing depths is introduced, which defines the export of the simulation results. The choice of the size of this set is a compromise between the time consumption of the data export and the resolution of the predicted maximum drawing depth. In this work, the size of the set D is chosen to be 27. The mean value of the experimentally determined maximum drawing depth of the specimens in rolling direction and in transverse direction is referred to as reference drawing depth. This reference value is included to the set D. Originating from the reference, 13 ascending and also 13 descending drawing depths are included to this set as shown by table 8.3. The values, given in this table, refer to the reference drawing depth. According to table 8.3 the resolution of the data export is chosen to be dependent on the deviation between the predicted and the experimentally determined forming limit.

The resolution is maximized in the range of the reference drawing depth.

Table 8.3: YLIT-4-BMW; Definition of the export of the simulation results with respect to the reference drawing depth.

Index Plot State	1	2;3	4;5	6;7	8;9
Drawing Depth $[mm]$	± 0.00	± 0.25	± 0.50	± 0.75	± 1.00
Index Plot State	10;11	12;13	14;15	16;17	18;19
Drawing Depth $[mm]$	± 1.25	± 1.50	± 1.75	± 2.00	± 2.50
Index Plot State	20;21	22;23	24;25	26;27	
Drawing Depth $[mm]$	± 3.00	± 4.00	± 5.00	± 6.00	

Table 8.4: YLIT-4-BMW; The chosen values of the parameters of the Harrington desirability functions.

Parameter	Drawing Depth; d^a_{MDD}	Strain State; ϵ_1, ϵ_2
U	4	0.5
L	-4	-0.5
n	2	2

In consideration of the forming velocity, the set D is mapped on a set of points in time. According to the latter mentioned set, the results of the simulation are exported. Consequently, 27 strain fields are obtained, referring each to a known drawing depth. Finally, the maximum drawing depth is identified for both specimens, whose associated strain field does not contain any points in the principal strain space lying above the forming limit curve. Additionally, as two specimens are investigated, two further strain fields are exported, applied for the analysis of the strain states referring to the above mentioned material points in the necking zone.

For the formulation of an optimization problem, three objectives per specimen have to be treated. The first objective is the difference between the measured and the predicted maximum drawing depth. The second and the third objective result from the deviation between the measured and predicted first ϵ_1 and second principal ϵ_2 in-plane strain, regarding the considered material point. The expressions (8.2) summarize the computation of the mentioned objectives ($S = \{RD, TD\}$; sim: simulation; ed: experimentally determined; d_{MDD}: Displacement of the material points with respect to the drawing direction, which define the maximum drawing depth):

$$f^a_{d_{MDD}} = d^a_{MDDsim} - d^a_{MDDed},\ f^a_{\epsilon_1} = \epsilon^a_{1_{sim}} - \epsilon^a_{1_{ed}},\ f^a_{\epsilon_2} = \epsilon^a_{2_{sim}} - \epsilon^a_{2_{ed}},\ a \in S. \quad (8.2)$$

For treating this multiple objective problem desirability functions are applied, as no conflict between the objectives is expected. In this case, a prior knowledge regarding the link between the objectives is necessary.

Table 8.4 summarizes the parameters of the Harrington desirability function, which are applied for linking the objectives ($O = \{d_{MDD}, \epsilon_1, \epsilon_2\}$). The values for the parameters are chosen based on experience.

For the drawing depth and for both principal values of the considered strain state a desirability function is defined. On the basis of this set of desirability functions for each specimen (in and perpendicular to the rolling direction) a minimization problem is formulated as shown by

$$f = 1 - \prod_{Q \in O} \prod_{a \in S} d_2(f^a_Q, U_Q, L_Q, n_Q). \quad (8.3)$$

Table 8.5: YLIT-4-BMW; Domain of the parameter space.

Parameter	Domain	Type
Strain Rate Dependency (SRD) (0 =off; 1 =on)	$0-1$	Discrete
Exponent Barlat 2000	$4-8$	Continuous
Kinematic Hardening (KH) (0 =off; 1 =on)	$0-1$	Discrete
Young's Modulus	$190000N/mm^2$ $-\ 210000N/mm^2$	Continuous
Friction Coefficient	$0.08-0.12$	Continuous

Table 8.5 shows the domain of the parameter space. For the optimization, the experiments 2 and 5 are taken as a reference (table 8.2). The selection of the reference is based on the maximum drawing depth. These experiments show the least deviation with respect to the mean value.

The subsequent optimization results are based on the experiment YLIT-4-BMW. The punch shape of this experiment is identical to the YLIT-1-TKSE, however, the shape of the blank and the process conditions are different. According to figure 8.10 (left), satisfying results are only obtained in consideration of the strain rate dependency of the hardening effect. The best prediction of the strain state and the drawing depth is obtained by choosing the exponent between 4.9 and 5.3. This range is derived from figure 8.11 by considering both, the best and the worst fitness value related to each yield locus exponent. Figure 8.11 (right) results from figure 8.11 (left) by hiding all simulation runs, which are performed without taking the strain rate dependency of the hardening into account.

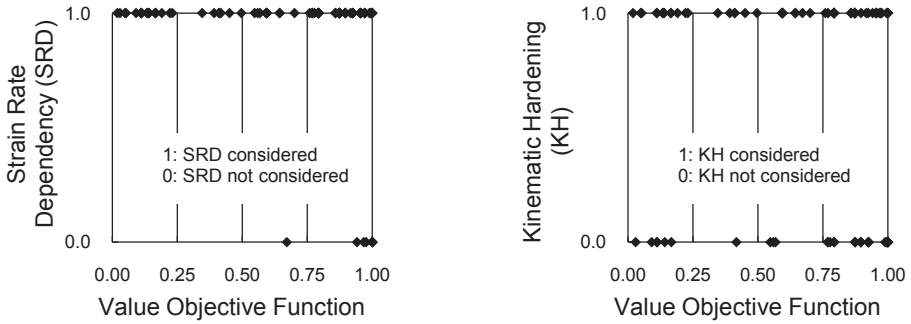

Figure 8.10: YLIT-4-BMW; Left: Relation between the strain rate dependency of the hardening effect and the objective function; Right: Relation between the consideration of the kinematic hardening model and the objective function.

In [110] the same batch of the material DX54 is investigated. However, the experiment is performed in the laboratory of ThyssenKrupp Steel Europe (YLIT-1-TKSE). The presented results in this thesis are based on the experiment YLIT-4-BMW, which is performed in the laboratory of BMW. The measured data of both laboratories lead in combination with the inverse determination of the Barlat 2000 yield locus exponent to similar conclusions. According to the optimization results, shown in [110], a yield locus exponent between 4.7 and 5.0 can be recommended for the considered steel grade, which is in a good accordance with the investigation shown above. If the exponent is chosen to be equal to 5.0, the measured data of both laboratories can be well predicted by the simulation. Both the results shown in [110] and in this work are based on the same forming limit diagram.

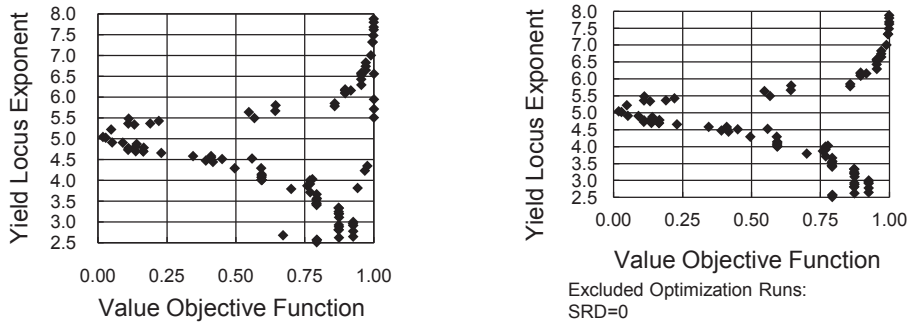

Figure 8.11: YLIT-4-BMW; Analysis of the influence of the yield locus exponent on the value of the objective function; Left: All experiments are taken into account; Right: Only objective function evaluations are visualized, which consider the strain rate dependency of the hardening.

According to figure 8.12 (right), friction does not play a crucial role for the prediction of the measured quantities of the investigated YLIT-Experiment, as objective function values close to the optimum are obtained for friction coefficients between 0.09 and 0.12. Additionally, with and without taking the kinematic hardening model into account (figure 8.10 (right)), the same minimum value of the objective function is obtained. As the blank of the YLIT-Experiment does not contain any zone, whose related stress state undergoes changes between tension and compression during forming, the measured quantities should not be affected by the Bauschinger effect. This theoretical consideration is in accordance with the optimization result. From the optimization results follows that the optimum is independent of the choice of the Young's modulus. The Young's modulus only influences the elastic part of the strain state. As $\epsilon^e \ll \epsilon^p$ (ϵ^e accumulated equivalent elastic strain; ϵ^p accumulated equivalent plastic strain) holds for this experiment, the influence of the Young's modulus should be small. Low objective function values are obtained independent of the choice of the Young's modulus (figure 8.12 (left)).

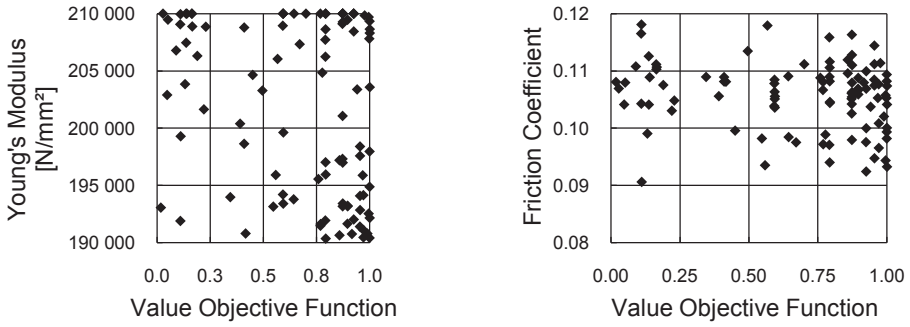

Figure 8.12: YLIT-4-BMW; Left: Relation between the Young's modulus and the objective function; Right: Relation between the friction coefficient and the objective function.

8.2.1 Barlat 2000 yield locus; A generalized parameter identification

The above presented investigations are performed by a variation of the yield locus shape, which only depends on the yield locus exponent. Thereby, the R_b value and the weights of the input data, obtained from the fundamental results, are kept constant. Subsequently, the variation of the yield locus shape is complemented by adding the R_b value and the weights as additional parameters.

In order to investigate the effect of these additional parameters on the predictive capability of the simulation, another optimization on the basis of the YLIT-4-BMW experiment is performed. The above identified dependences of

the Young's modulus, the friction coefficient, the strain rate dependency of the hardening effect and the kinematic hardening are assumed to be valid independent of the parameterization of the yield locus shape and the mentioned weights. Therefore, these parameters are excluded from this analysis. Because of their marginal sensitivity, the values of the Young's modulus and the friction coefficient are chosen based on experience and the kinematic hardening model is not applied. The strain rate dependency of the material is considered. Consequently, the optimization comprises

- the yield locus exponent,
- the R_b value and
- eight weighting factors.

Generally, a small deviation between the stress and the strain rate ratios of the fundamental experiments and the prediction of the yield locus is desired. Therefore, the multiplicative aggregation on the basis of the Harrington desirability function is preferred for this investigation, as this approach penalizes deviations of a single quantity between the input data and the prediction of the model strongly. Basically, also the additive aggregation, as introduced in chapter 7 could be applied. This solution would lead in combination with the SQP Algorithm to a better performance regarding the calibration of the yield locus parameters α_i. However, the difference regarding the computational effort is negligible in comparison to a single forming simulation.

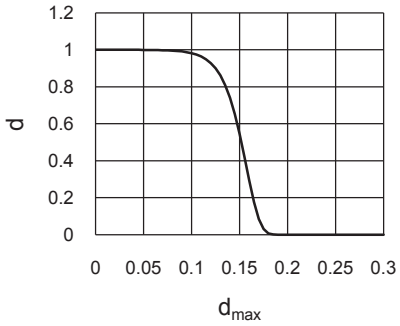

Figure 8.13: YLIT-4-BMW; Penalization of large values of d_{max} by applying a one-sided Harrington desirability function.

Preliminary investigations showed that depending on the choice of the weights, even under the application of the Harrington desirability functions, large deviations between the input data and the prediction of the model can occur. In order to avoid gaining wrong conclusions, such undesired calibrations are considered by penalizing the value of the objective function of the optimization. Thereby,

the objective function (8.3) is complemented (8.4) by an one-sided Harrington desirability function, which maps the maximum deviation d_{max} (8.5) between the input data and the model prediction to an interval between $[0;1]$:

$$f = 1 - \left[\prod_{Q \in O} \prod_{a \in S} d_2(f_Q^a, U_Q, L_Q, n_Q) \right] d_1(d_{max}, b_0, b_1), \tag{8.4}$$

$$\begin{aligned} d_\sigma &= \max_{I \in A} \left\{ |(\overline{\sigma}_I - Y(\epsilon_{ref}))/Y(\epsilon_{ref})| \right\}, \\ d_R &= \max_{J \in B} \left\{ \left| (R_J - R_J^{ed})/R_J^{ed} \right| \right\}, \\ d_{max} &= \max \left\{ d_\sigma; d_R \right\}. \end{aligned} \tag{8.5}$$

The parameters of the one-sided Harrington desirability function are experience based chosen ($b_0 = 11; b_1 = -77$). Figure 8.13 shows a visualization of the corresponding desirability function. The choice of parameters b_0 and b_1 lead to a significant penalization of the objective function, if d_{max} is greater than 0.1.

The parameter space of the optimization is summarized by table 8.6. The application of the Harrington desirability functions for the calibration of the yield locus leads to three weights for each quantity of the input data. For reducing the dimension of the problem, the parameters U, L and n of the desirability function are coupled as given by

$$\begin{aligned} U_I &= Y(\epsilon_{ref}) + Y(\epsilon_{ref})\, w_I,\ I \in A, \\ L_I &= Y(\epsilon_{ref}) - Y(\epsilon_{ref})\, w_I, \\ U_J &= R_J^{ed} + R_J^{ed} w_J,\ J \in B, \\ L_J &= R_J^{ed} - R_J^{ed} w_J, \\ n_I &= w_I, \\ n_J &= w_J, \\ w_I &> 0, \\ w_J &> 0. \end{aligned} \tag{8.6}$$

As the parameter space contains only real valued parameters, the optimization can be realized by all the introduced optimization algorithms. The budget of objective function evaluations is limited to 150 for each optimization. Subsequently, the results of the optimizations based on the $(1, \lambda)$-DR-ES, the $(\mu/\mu, \lambda)$-CMA-ES, the $(1+1)$-CMA-ES and the SQP are compared.

Table 8.6: YLIT-4-BMW; Domain of the parameter space.

Parameter	Domain	Type
Exponent Barlat 2000	$2.5 - 8$	Continuous
R_b	$0.5 - 1.5$	Continuous
$w_I,\ I \in A$	$1.0 - 3.0$	Continuous
$w_J,\ J \in B$	$1.0 - 3.0$	Continuous

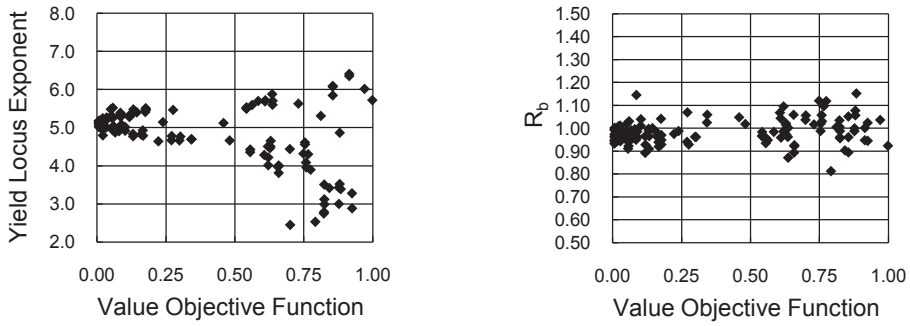

Figure 8.14: YLIT-4-BMW; $(1, \lambda)$-DR-ES; Left: Relation between the yield locus exponent and the objective function; Right: Relation between the R_b value and the objective function.

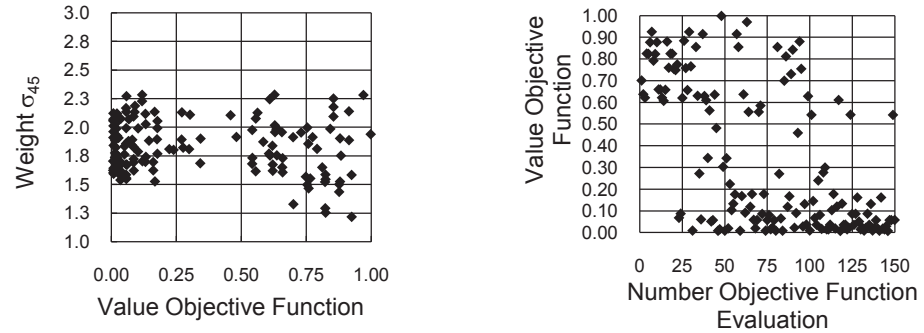

Figure 8.15: YLIT-4-BMW; $(1, \lambda)$-DR-ES; Left: Relation between the weight of the σ_{u45° value and the objective function; Right: Propagation of the optimization.

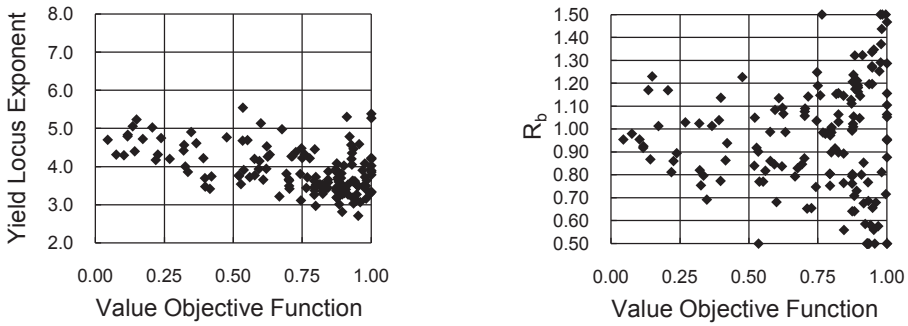

Figure 8.16: YLIT-4-BMW; $(\mu/\mu, \lambda)$-CMA-ES; Left: Relation between the yield locus exponent and the objective function value; Right: Relation between the R_b value and the objective function.

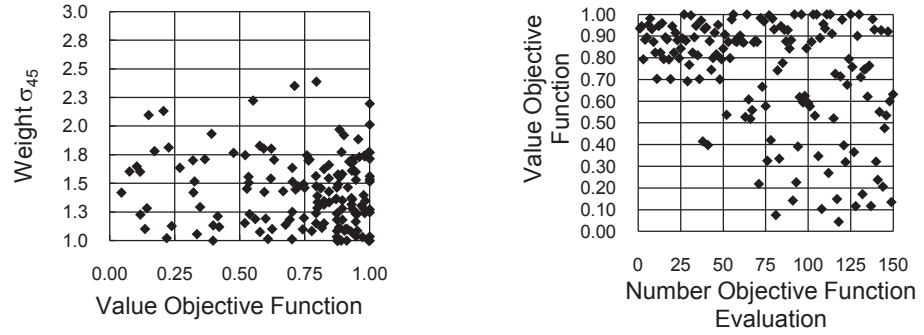

Figure 8.17: YLIT-4-BMW; $(\mu/\mu, \lambda)$-CMA-ES; Left: Relation between the weight of the σ_{u45° value and the objective function; Right: Propagation of the optimization.

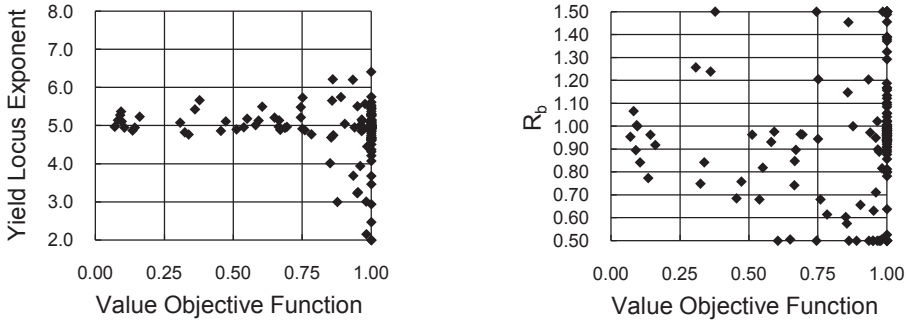

Figure 8.18: YLIT-4-BMW; $(1 + 1)$-CMA-ES; Left: Relation between the yield locus exponent and the objective function; Right: Relation between R_b value and the objective function.

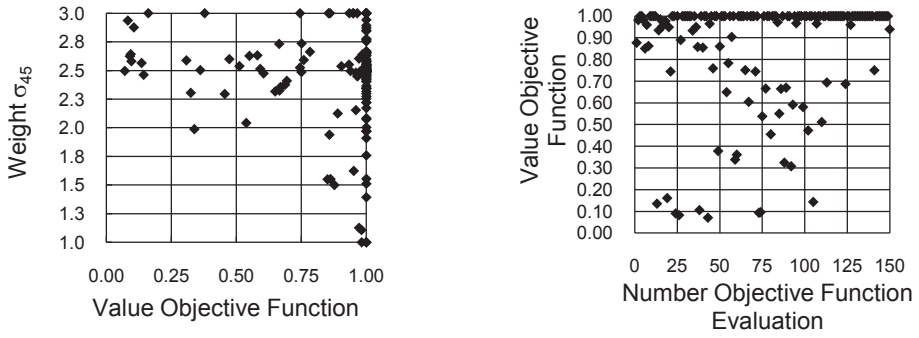

Figure 8.19: YLIT-4-BMW; $(1+1)$-CMA-ES; Left: Relation between the weight of the σ_{u45° value and the objective function; Right: Propagation of the optimization.

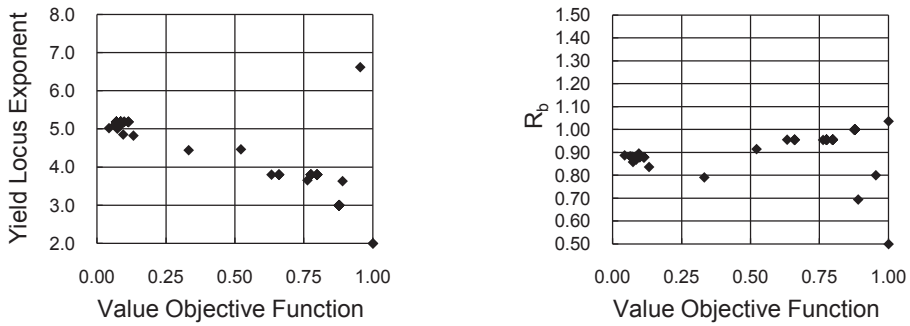

Figure 8.20: YLIT-4-BMW; SQP; Left: Relation between the yield locus exponent and the objective function; Right: Relation between the R_b value and the objective function.

Table 8.7: YLIT-4-BMW; Summary of the computed optimums.

Parameter	$(1,\lambda)$ -DR-ES	$(\mu/\mu,\lambda)$ -CMA-ES	$(1+1)$ -CMA-ES	SQP
Lowest Objective Function value	0.0068	0.0442	0.0707	0.0432
Yield locus exponent	5.1754	4.6987	4.9718	5.0202
R_b	0.9632	0.9545	0.9540	0.8874
Weight σ_{u45°	1.7033	1.4191	2.4965	1.1196
Weight σ_{u90°	1.1274	1.7036	1.0000	1.1821
Weight σ_b	1.1310	2.2178	1.0450	1.6630
Weight σ_s	1.0485	2.8588	3.0000	1.6566
Weight R_{0°	1.7244	1.2382	1.1826	1.7289
Weight R_{45°	2.1859	1.8121	1.0000	2.0320
Weight R_{90°	1.777	2.1172	2.9971	2.0412
Weight R_b	1.7497	2.1143	3.0000	2.4764

By summarizing the results of the optimizations, the best prediction of the measured data is obtained by choosing the yield locus exponent between 4.7 and 5.2 (figures 8.14, 8.16, 8.18, 8.20 (left)), which is in accordance with the previous investigations. The sensitivity of the yield locus exponent with respect to the quality of the simulation result is shown by each optimizer. Above, the value of the R_b value is assumed to be equal to 1.0. The optimization results confirm this assumption. Apart from the $(1,\lambda)$-DR-ES all the investigated optimizers indicate a dependency of the R_b value with respect to the predictive capability of the simulation (figures 8.14, 8.16, 8.18, 8.20; (right)).

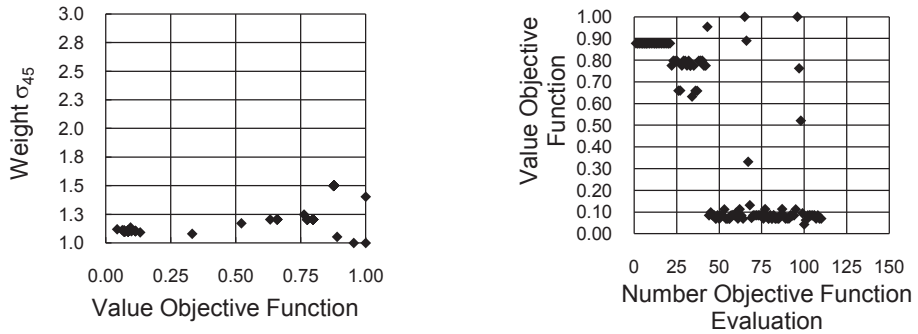

Figure 8.21: YLIT-4-BMW; SQP; Left: Relation between the weight of the σ_{u45° value and the objective function; Right: Propagation of the optimization.

The $(\mu/\mu, \lambda)$-CMA-ES needs the most objective function evaluations for reaching low objective function values. On the basis of the budget of 150 objective function evaluations, the (1 + 1)-CMA-ES gives the worst result regarding the objective function (table 8.7). Both, the SQP and the $(1, \lambda)$-DR-ES converge fast. However, the $(1, \lambda)$-DR-ES gives lower objective function values within the considered budget of objective function evaluations.

Generally, the yield locus should reflect each input data set with a high accuracy. Therefore, difference of the weights should be as small as possible. According to Table 8.7 the lowest objective function value, identified by the $(1, \lambda)$-DR-ES algorithm, is associated with the smallest differences of the weights in comparison to the other algorithms. Table 8.8 illustrates the input data and the prediction of the yield locus on the basis of the best simulation run of the $(1, \lambda)$-DR-ES optimization. The given stress states and strain rate ratios are normalized as introduced in chapter 7.

The optimizations show the possibility of determining the best possible weights, the yield locus exponent and the R_b value automatically. According to the presented examinations, the $(1, \lambda)$-DR-ES should be preferred for this task.

Table 8.8: Comparison between the input data and the prediction of the model based on the optimum obtained from the $(1, \lambda)$-DR-ES.

Quantity	Input Data	Model Prediction
σ_{u0°	1.000000	1.000000
σ_{u45°	1.032511	1.000032
σ_{u90°	0.996696	1.001763
σ_b	1.164572	1.164573
σ_s	0.585851	0.532380
R_{0°	1.000000	1.000000
R_{45°	0.780172	0.785487
R_{90°	1.271552	1.273829
R_b	0.415170	0.418341

8.2.2 Barlat ´89 yield locus

Apart from the Barlat 2000 model also the Barlat ´89 yield locus is investigated by an additional optimization. For the calibration of the yield locus parameter a,c,h and p, the procedure, described in chapter 7, is utilized. The parameter space is chosen to be identical to the one, defined by table 8.5. Regarding the consideration of the strain rate dependency of the hardening effect, the optimization exhibits the same correlation between the measured data and the simulation results in comparison with the Barlat 2000 model (figure 8.23). Consequently, only when

the strain rate dependent hardening is taken into account, it is possible to predict the measured data accurately. The best possible prediction of the experimentally determined drawing depth and strain state is achieved by selecting the yield locus exponent in the range between 3.7 and 4.0 (figure 8.22).

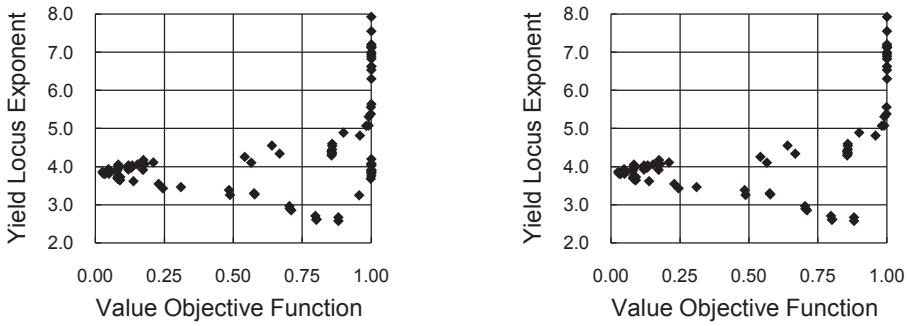

Figure 8.22: YLIT-4-BMW; Barlat ´89; Left: Relation between the yield locus exponent and the objective function; Right: Relation between the yield locus exponent and the objective function. However, only the objective function evaluations are visualized, which are performed in consideration of the strain rate dependency of the hardening effect.

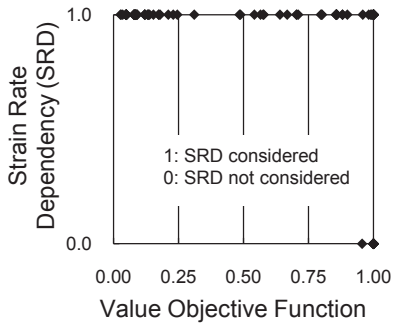

Figure 8.23: YLIT-4-BMW; Barlat ´89; Relation between the consideration of the strain rate dependency of the hardening and the objective function.

8.2.3 Discussion of the results

According to table 8.9, both yield loci lead to an accurate prediction of the measured quantities. As the Barlat 2000 yield locus reflects the measured quantities of the fundamental results more accurately than the Barlat ´89 yield locus, the prediction of arbitrary stress states should be better. Therefore, the Barlat 2000

yield locus is preferred in this work. The commonly applied Hill ´48 does not give the best possible prediction of the measured quantities. The consideration of the strain rate dependency of the hardening effect leads in combination with the Hill ´48 yield locus to a remarkable overestimation of the forming limit. Consequently, the consideration of the strain rate dependency of the hardening effect does not necessarily lead to an improvement of the stress-strain relation. Additionally, an increasing accuracy by applying a complex yield locus should not be taken for granted. Hence, for the inverse identification of a complex yield locus, the strain rate dependency of the hardening effect should be taken into consideration. More generally, it can be concluded, that a calibration of a yield locus should not be performed without carefully considering the material hardening.

Table 8.9: YLIT-4-BMW; Investigations of the Barlat ´89 and Barlat 2000 yield locus.

Experiment	Type	Investigated Quantities				Value Objective Function
YLIT-4-BMW		RD/TD	ϵ_1	ϵ_2	d_{MDD} $[mm]$	
	Simulation Barlat ´89 m=2 SRD=off	RD	0.493	-0.237	42.7	0.4030
		TD	0.512	-0.259	42.4	
	Simulation Barlat ´89 m=2 SRD=on	RD	0.457	-0.222	47.0	0.9807
		TD	0.463	-0.240	47.9	
	Simulation Barlat ´89 m=3.9 SRD=on	RD	0.411	-0.165	42.2	0.0562
		TD	0.404	-0.170	42.2	
	Simulation Barlat 2000 $a = 5.12$ SRD=on	RD	0.415	-0.159	41.2	0.0173
		TD	0.403	-0.173	42.4	
	Measured Data	RD	0.397	-0.145	41.3	
		TD	0.429	-0.164	42.5	

In [99] the YLIT-2-TKSE and the YLIT-3-BMW are applied for the validation of the determined exponent. Table 8.10 shows the published results, which confirm the above presented findings. It should be mentioned that the examinations of [99] and of this thesis are performed under the application of the same batch of

the DX54. The Barlat 2000 in combination with an exponent equal to 5.0 leads to satisfying results with respect to the investigated YLIT-Experiments. The predicted strain state of the YLIT-2-TKSE and the YLIT-3-BMW underlines that Barlat 2000 yield locus is advantageous in comparison with the Hill ´48 model, concerning the investigated DX54 steel grade.

Table 8.10: Results obtained from the experiments YLIT-2-TKSE and YLIT-3-BMW [99].

Source Data	YLIT-2-TKSE		YLIT-3-BMW	
	ϵ_1, RD	ϵ_2, RD	ϵ_1, TD	ϵ_2, TD
Measured Data	0.41	-0.14	0.36	-0.14
Simulation Barlat 2000, a=5.0 SRD=on	0.40	-0.17	0.36	-0.15
Simulation Barlat ´89, m=2 SRD=on	0.47	-0.25	0.36	-0.19
Simulation Barlat ´89, m=2 SRD=off	Mesh Instability	Mesh Instability	0.40	-0.20

Provided the Barlat 2000 or the Barlat ´89 yield locus and the same approach for modeling the hardening effect is applied, the optimization shows a need for taking the strain rate sensitivity into account. Furthermore, as the predicted quantities of the YLIT-4-BMW are insensitive with respect to the Young's modulus, the friction and the Bauschinger effect, it is possible to determine the exponent of the yield locus indirectly from this experiment. Nevertheless, for the investigation of the remaining complementary experiments, the same parameter set is applied in order to analyze whether a mandatory order of the evaluation of these experiments exists.

8.3 Bending experiment

As opposed to the investigations of the YLIT-Experiments, the yield locus exponent is subsequently reduced to discrete values. As a consequence, the calibration of the α_i values of each exponent can be done in advance. For the calibration of the yield locus parameter, the R_b value is assumed to be 1.0 and the weights, regarding the results of the fundamental experiments, of the multi-objective calibration procedure are chosen as given in table 7.3. The optimization process is illustrated by figure 8.24.

The parameter space of the optimization is complemented by the Poisson ratio. This parameter can be identified by evaluating a tensile test. The Poisson

ratio is included in the subsequent optimization in order to analyze, whether it is necessary to determine this parameter experimentally. Alternatively, it could be sufficient to take a literature value $v = 0.30$ [111] for this parameter. The domain of the optimization parameters are given by table 8.11.

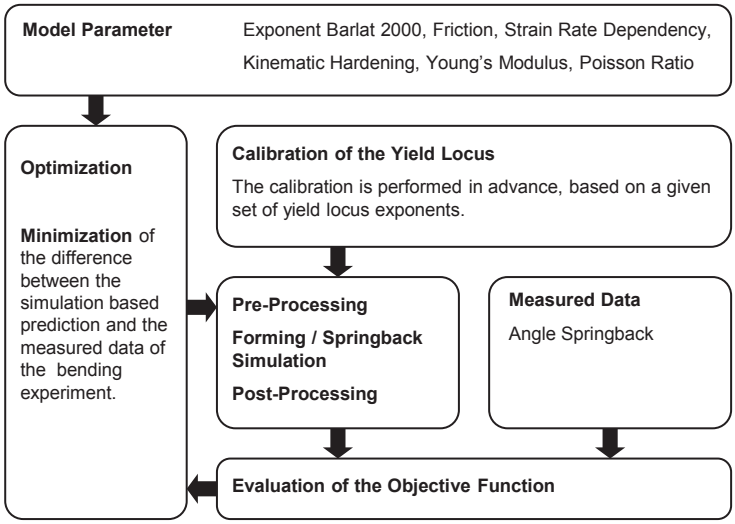

Figure 8.24: Bending experiment; Sequence of the optimization.

Table 8.11: Bending experiment; Domain of the parameter space.

Parameter	Domain	Type
Strain Rate Dependency (SRD) (0 =off; 1 =on)	$0-1$	Discrete
Exponent Barlat 2000	$4-8$	Discrete
Kinematic Hardening (KH) (0 =off; 1 =on)	$0-1$	Discrete
Young's Modulus	$190000N/mm^2$ $-\ 210000N/mm^2$	Continuous
Poisson Ratio	$0.24-0.30$	Continuous
Friction Coefficient	$0.08-0.12$	Continuous

For the quantification of the deviation between the real experiment and the prediction of the simulation, the difference of the angle α is computed. This quantity is defined as given by figure 6.12 and is directly used for the formulation of the objective function:

Table 8.12: Bending experiment; Measured results.

Experiment	Angle (α)[°]
1	82.43
2	82.57
3	82.93
Mean	82.64

$$f_{BE1} = |\alpha_{sim} - \alpha_{ed}| \,. \tag{8.7}$$

The application of the norm leads to a minimization problem (BE: Bending experiment).

Table 8.12 shows the experimentally determined angles α. As a reference for the optimization experiment 2 is taken, as it shows the least deviation with respect to the mean value. According to figure 8.25, the deviation between the measured and the predicted springback angle depends on both, the consideration of the strain rate effect of the material hardening and the yield locus exponent.

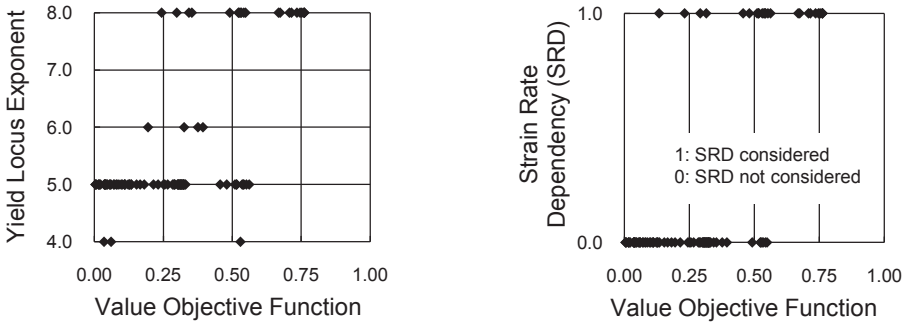

Figure 8.25: Bending experiment; Left: Relation between the yield locus exponent and the objective function; Right: Relation between the strain rate dependency of the hardening effect and the objective function.

According to 8.26 (right), a slight influence of the Poisson ratio with respect to the quality of the springback prediction is recognizable. The Young's modulus shows a stronger sensitivity regarding the conformity of the simulation and the measured data (figure 8.26 (left)). The figures 8.27 illustrate a visualization of the optimization results, obtained on the basis of an exponent equal to 5. This sub space shows the sensitivity of the Young's modulus clearer. The elastic springback behavior is mainly determined by the stress state after tool closing and the elastic material response. Consequently, the parameters of the elastic material model

play a more important role as for the prediction of the strain field, which is confirmed by this sensitivity analysis.

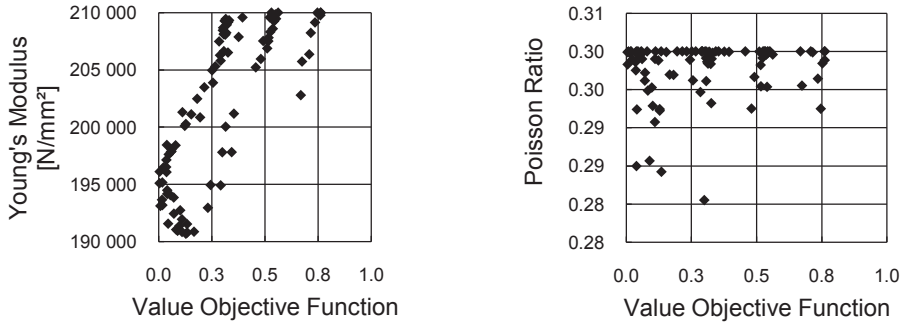

Figure 8.26: Bending experiment; Left: Relation between the Young's modulus and the objective function; Right: Relation between the Poisson ratio and the objective function.

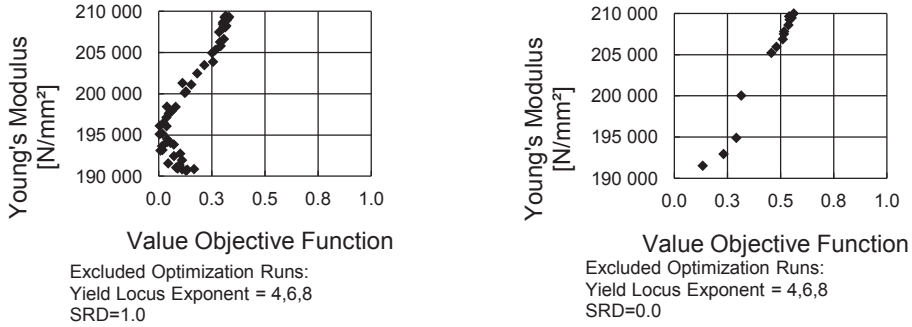

Figure 8.27: Bending experiment; Analysis of the Young's modulus based on a yield locus exponent equal to 5; Left: Objective function evaluations without consideration of the strain rate dependency of the hardening effect; Right: Objective function evaluations with consideration of the strain rate dependency of the hardening effect.

Finally the effect of the friction and the Bauschinger effect on the objective function is investigated. The parameter of the friction model does not show a sensitivity (figure 8.28). This result can be explained by the contact pressure between the punch and the blank, which should be small in comparison with industrial parts. Hence, a significant shear stress in the contact zone, induced by the friction, should not occur.

Furthermore, an influence of the Bauschinger effect on the predicted springback is not expected, as a transition between tension and compression should not

occur at any material point. This assessment is confirmed by the optimization result.

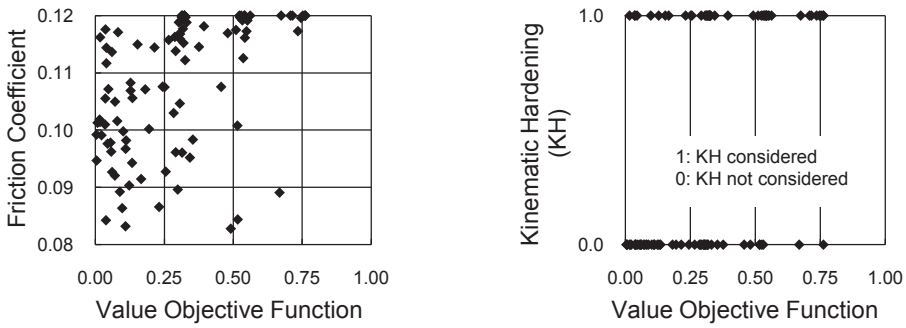

Figure 8.28: Bending experiment; Left: Relation between the friction coefficient and the objective function; Right: Relation between the consideration of the kinematic hardening model and the objective function.

By considering figure 8.25 (right) it has to be concluded that better results are obtained by ignoring the strain rate dependency of the material, which is a contradiction with respect to the results of the YLIT-Experiments. However, this experiment shows a strong linear sensitivity concerning the Young's modulus. According to figures 8.27 (left) and 8.27 (right) a prediction of the measured data should be possible either with our without taking the strain rate dependency into account. Consequently, at least two solutions of the optimization exist and, therefore, it is not possible to derive inversely values of the unknowns from this experiment. This also explains the above mentioned contradiction regarding the strain rate sensitivity. For the procedure of determining the unknown model parameters, this experiment can give a contribution. However, apart from one, all the sensitive unknown parameters have to be identified in advance. As this experiment is highly sensitive regarding the Young's modulus, this model parameter is determined by the bending experiment.

8.4 Friction experiment

For the friction experiment the optimization procedure is given by figure 8.29 and the domain of the parameter space is shown by table 8.13.

Table 8.14 shows the measurement data, obtained from the friction experiment. The experiments 1 and 4 show the least deviation from the mean values and are therefore chosen as a reference for the optimization. The position P of the considered strain state is defined in chapter 6. The predicted strain state is derived from the integration point, representing the position P at the top surface.

For measuring the deviation between the simulation based prediction and the measured data on the basis of the strain state, the distance of both results in

Table 8.13: Friction experiment; Domain of the parameter space.

Parameter	Domain	Type
Strain Rate Dependency (SRD) (0 =off; 1 =on)	$0-1$	Discrete
Exponent Barlat 2000	$4-8$	Discrete
Kinematic Hardening (KH) (0 =off; 1 =on)	$0-1$	Discrete
Young's Modulus	$190000N/mm^2$ $-\ 210000N/mm^2$	Continuous
Friction Coefficient	$0.08-0.12$	Continuous

Table 8.14: Friction experiment; Measured results.

Experiment	ϵ_1	ϵ_2
1	0.130	-0.088
2	0.132	-0.088
3	0.128	-0.082
4	0.130	-0.088
Mean	0.130	-0.087

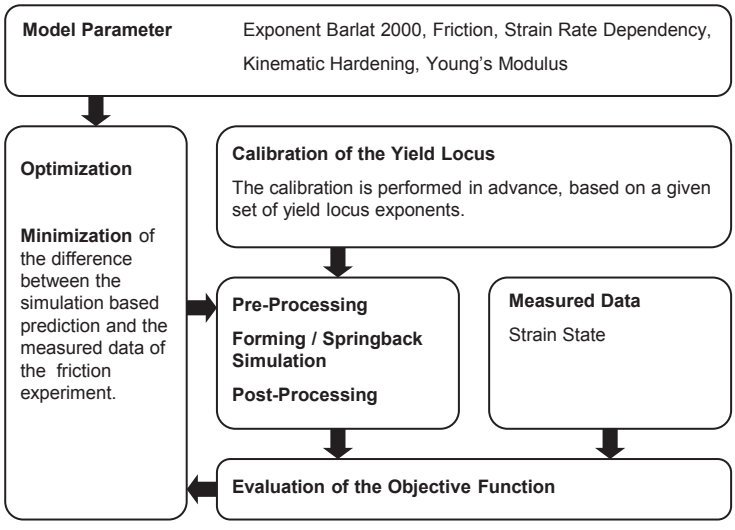

Figure 8.29: Friction experiment; Sequence of the optimization.

the eigenvector space (principal in-plane strain space) is computed (FE: Friction experiment):

$$f_{FE} = \sqrt{(\epsilon_{1_{sim}} - \epsilon_{1_{ed}})^2 + (\epsilon_{2_{sim}} - \epsilon_{2_{ed}})^2}. \tag{8.8}$$

According to figure 8.30 (right), the deviation of the strain state between the measured data and the prediction of the simulation depends on the consideration of the strain rate effect of the material hardening. The yield locus exponent shows only a slight sensitivity (figure 8.30 (left)). However, for a best possible inverse identification of the friction model parameter, the yield locus exponent should be determined in advance.

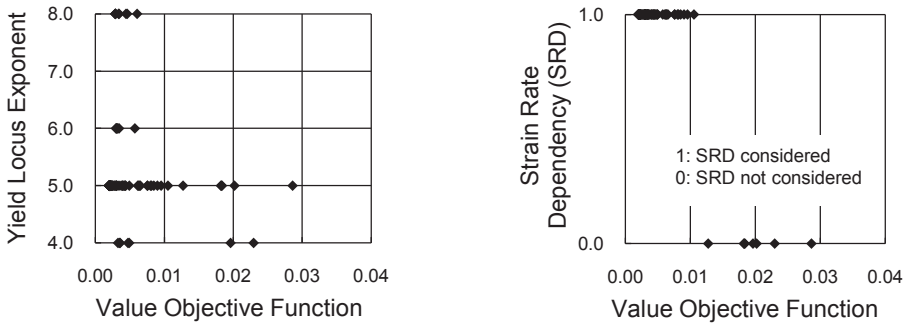

Figure 8.30: Friction experiment; Left: Relation between the yield locus exponent and the objective function; Right: Relation between the consideration of the strain rate dependency of the hardening effect and the objective function.

Furthermore, the optimization results (figure 8.31) do not indicate a sensitivity of the difference between the predicted and the measured strain state with respect to the choice of the Young's modulus and the Bauschinger effect. The elastic part of the strain state is small in comparison with the plastic one. Consequently, the sensitivity of the Young's modulus on the prediction of the strain state, which only affects the elastic part of the strain state, should be small. The optimization result confirms this assumption. None of the material points undergo a change between tension and compression during the forming operation. Therefore, the mechanical behavior of this experiment should not be affected by the Bauschinger effect, which is also in accordance with the presented results.

A strong correlation between the parameter of the friction model and the quality of the predicted strain state at the considered position is shown by the optimization (figure 8.32). According to this result, it is possible to determine the friction coefficient inversely.

The optimization on the basis of the friction experiment shows a sensitivity of the objective function with respect to the consideration of the strain rate dependency of the hardening effect and the friction. In consideration of the YLIT-Experiments only the friction model parameter remains unknown. A satisfying

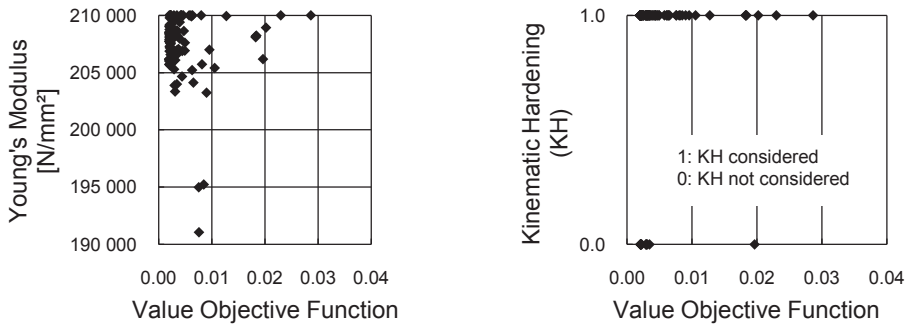

Figure 8.31: Friction experiment; Left: Relation between the Young's modulus and the objective function; Right: Relation between the consideration of the kinematic hardening model and the objective function.

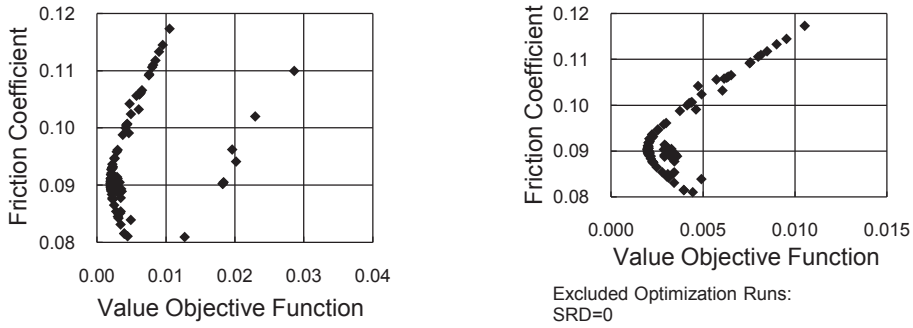

Figure 8.32: Friction experiment; Left: Relation between the friction coefficient and the objective function; Right: Relation between the friction coefficient and the objective function in consideration of the strain rate dependency of the hardening effect.

prediction of the strain state is obtained by taking the strain rate sensitivity into account, which is in accordance with the findings based on the YLIT-Experiments.

8.5 Discussion of the results of the sensitivity analysis

According to the above presented findings, the yield locus identification tools (YLIT) are suitable for indirectly determining both, the necessity for the consideration of the strain rate dependency of the hardening effect and the choice of the yield locus exponent. The optimization based on the bending experiment shows a sensitivity of the yield locus exponent, the strain rate dependency of the material hardening and the Young's modulus with respect to the predicted springback. In the case of the friction experiment, the consideration of the strain rate dependency of the hardening effect and the friction coefficient play a crucial role for the prediction of the measured data. Provided, the examination of the YLIT-Experiments is performed in advance, the bending and friction experiments allow determining the Young's modulus and the friction coefficient separately. The discussion of this section shows the necessity of evaluating the complementary experiments in a pre-defined order. As expected, all the investigated experiments are insensitive with respect to the Bauschinger effect. Generally, the applied evolutionary strategy supports the analysis of the experiments, which are performed for the inverse determination of model parameters. Even the limited number of objective function evaluations is sufficient for the computation of the desired sensitivities of the unknown model parameters with respect to the measured data.

8.6 Determination of the unknown model parameters

For the investigated material the shown optimization results of the YLIT-4-BMW are sufficient for the determination of the yield locus exponent. As mentioned above, the amount of objective function evaluations is limited, because of the computational cost. In order to analyze the best possible value of the exponent the golden section interval division is deployed (see 2.2.2). Thereby, the strain rate sensitivity of the hardening effect is taken into account and for the remaining unknowns values are selected based on experience (Young's modulus= $190000 N/mm^2$; $\mu = 0.10$; the kinematic hardening model is not considered). Figure 8.33 comprises the results of the search of the yield locus exponent. The results refer to the experiment YLIT-4-BMW. The domain of the yield locus exponent is chosen to be $[2; 8]$.

The search for the yield locus exponent is assumed to be converged after 7 objective function evaluations. Table 8.15 shows a comparison between the simulation runs 7 and 9, which does not show a significant difference. However,

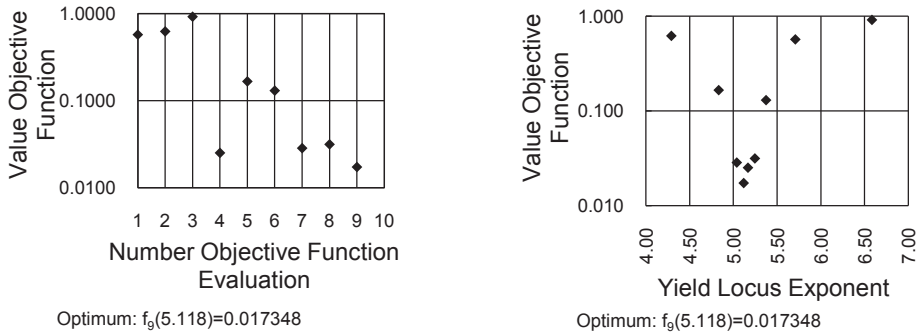

Figure 8.33: YLIT-4-BMW; Golden section interval division; Left: Propagation of the optimization; Right: Relation between the yield locus exponent and the objective function.

between simulation run 6 and 7 an improvement regarding the drawing depth is recognizable.

Table 8.15: YLIT-4-BMW; Analysis of the golden section interval devision.

Evaluation Objective Function	Exponent	RD/TD	ϵ_1	ϵ_2	d_{MDD} $[mm]$	Value Objective Function
6	5.374	RD	0.418	-0.156	40.2	0.1302
		TD	0.403	-0.169	41.7	
7	5.039	RD	0.414	-0.159	41.4	0.0285
		TD	0.404	-0.175	42.9	
9	5.118	RD	0.415	-0.159	41.2	0.0173
		TD	0.403	-0.173	42.4	

The shown results confirm the findings of section 8.2. Furthermore, the golden section interval division enables to determine the yield locus exponent within a few objective function evaluations. For the investigation of another material, the golden section interval division can be directly applied, if the following conditions are fulfilled:

- The weights for taking the fundamental experiments regarding the yield locus calibration into account are known.
- An appropriate value of R_b is known.

Thereby, it is assumed that the results regarding the strain rate dependency of the hardening effect are generally valid, provided the same strategy for determining the flow curve is applied.

Table 8.16: YLIT-4-BMW; Analysis of the yield locus exponent.

Type	Exponent	RD/TD	ϵ_1	ϵ_2	d_{MDD} $[mm]$	Value Objective Function
Simulation	5.00	RD	0.409	-0.159	41.9	0.1033
		TD	0.400	-0.175	43.7	
Simulation	5.12	RD	0.415	-0.159	41.2	0.0173
		TD	0.403	-0.173	42.4	
Measured Data		RD	0.397	-0.145	41.3	
		TD	0.429	-0.164	42.5	

Even though the best prediction of the measured quantities is obtained based on selecting the yield locus exponent equal to 5.12 (table 8.16), for the further investigations this parameter is chosen to be equal to 5.0. This choice results from the comparison between the investigations on the basis of the YLIT-1-TKSE and the YLIT-4-BMW. Choosing the Barlat 2000 yield locus exponent equal to 5.0 leads to an adequate prediction of the measured quantities with respect to both experiments.

As discussed, it is recommended to identify the friction coefficient inversely, in consideration of the identified yield locus exponent and the necessity of taking the strain rate sensitivity of the material hardening into account. Consequently, only one unknown sensitive parameter remains. For the inverse determination of the parameter of the friction model, a uniformly distributed sampling of an one dimensional set of friction coefficients could be applied. For each member of this set a simulation is performed and the same objective function is evaluated as for the above introduced optimization. The best choice of the friction coefficient corresponds to the lowest computed value of the objective function. The advantage of this approach is that the simulations can be performed simultaneously. However, for the identification of the material model parameters, it is sufficient to perform the simulations sequentially, which offers the chance to take the intermediate results into account for defining the next optimization steps [24]. For the determination of the friction coefficient two sequential methods are investigated. Figure 8.35 shows the results of the golden section interval division. After five simulation runs the optimization is assumed to have converged, as the value of the objective function only changes marginal between the friction coefficients 0.0894 and 0.0917 (see table 8.17 and figure 8.35). According to Figure 8.34, the correlation between the friction coefficient and the value of the objective function is similar to a second degree polynom. Hence, also a Lagrangian interpolation is applied for the determination of the minimum, comprising a second degree polynom. Figure 8.36 illustrates the results of this procedure. The Lagrangian interpolation is slightly advantageous in comparison to the other methods, as four objective function evaluations are sufficient to compute a friction coefficient lying

in the interval between 0.0894 and 0.0917.

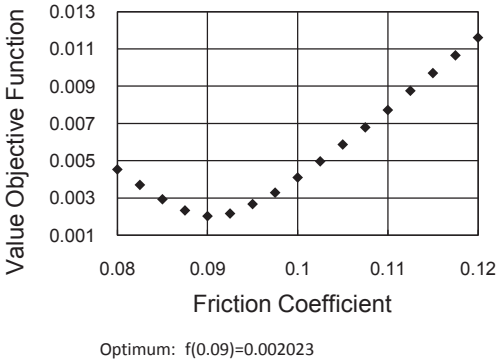

Figure 8.34: Friction experiment; Uniform sampling; Relation between the friction coefficient and the objective function.

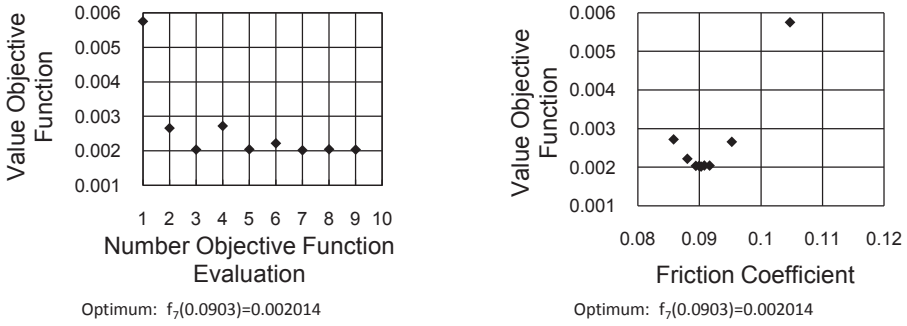

Figure 8.35: Friction experiment; Golden section interval division; Left: Propagation of the optimization; Right: Relation between the friction coefficient and the objective function.

Table 8.17: Friction experiment; Summary of the results of the golden section interval division.

Number Objective Function Evaluation	Friction Coefficient	Value Objective Function
1	0.104721	0.005754
2	0.095279	0.002656
3	0.089443	0.002033
4	0.085836	0.002719
5	0.091672	0.002040
6	0.088065	0.002216
7	0.090294	0.002014
8	0.090820	0.002042
9	0.089969	0.002032

Table 8.18: Friction experiment; Summary of the results of the Lagrange interpolation method.

Number Objective Function Evaluation	Friction Coefficient	Value Objective Function
1	0.080000	0.004532
2	0.100000	0.004099
3	0.120000	0.011614
4	0.091089	0.001997
5	0.090466	0.002038
6	0.091824	0.002094
7	0.091004	0.002013
8	0.091290	0.002032
9	0.091122	0.001989

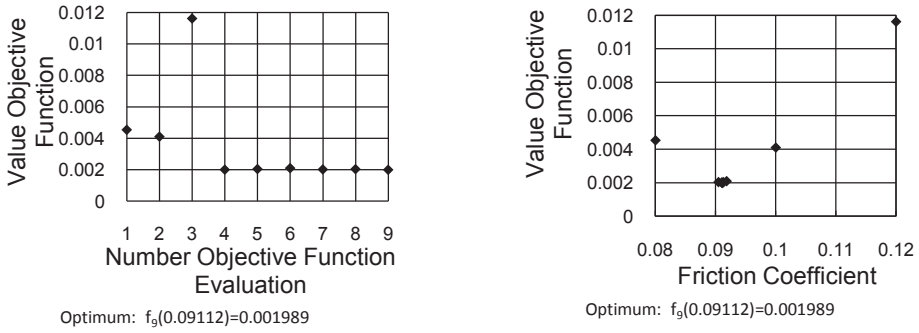

Figure 8.36: Friction experiment; Lagrange interpolation; Left: Propagation of the optimization; Right: Relation between the friction coefficient and the objective function.

Finally, the remaining unknown - the Young's modulus is investigated by one dimensional strategies on the basis of the bending experiment. The application of the inverse method is possible, if the yield locus and the necessity of the consideration of the strain rate dependency of the material hardening are determined in advance. Only one unknown remains, which can be searched by a one-dimensional procedure. In consideration of the fluctuations of the experiment (table 8.12), a maximum deviation between the predicted and the measured angle α of ± 0.05 seems to be sufficient for the inverse identification of the Young's modulus. The result of the inverse determination of the Young's modulus, based on a uniform sampling, is given by figure 8.37. Additionally, the results of the golden section interval division are shown by figure 8.38. According to 8.37, the correlation between the Young's modulus and the objective function is quasi linear. Therefore, the interpolation method Regula Falsi iteration is also analyzed. For the application of this method, the objective function is modified as given by expression (BE: Bending experiment):

$$f_{BE2} = \alpha_{sim} - \alpha_{ed}. \tag{8.9}$$

The result of this method is, as illustrated by 8.39, slightly better than the golden section interval division in consideration of the needed accuracy.

Figure A.5 shows the accumulated plastic strain of the upper surface after the forming operation. As the maximum accumulated plastic strain of the bending experiment is within the range of Doege's investigations (see figure 8.8), also an extended elasticity model is applied. This model is able to take the dependency of the Young's modulus with respect to the accumulated equivalent plastic strain into account. The same values of the remaining unknowns are chosen as for the inverse determination of the Young's modulus. This extended elasticity model leads to an objective function value of 0.32. This result is worse than the one obtained by the optimization. However, the result is better than choosing the common literature value of the Young's modulus ($210000 N/mm^2$), which leads

to an objective function value of 0.49 (see figure 8.37). One has to bear in mind that Doege investigated the steel grade DC06. Provided the relation between the Young's modulus and the accumulated plastic strain would be known for the investigated material, the prediction of the extended model could be better and the bending experiment could be applied for validation purposes. In this thesis the bending experiment is applied as a complementary experiment and the inversely determined Young's modulus is investigated based on the validation experiments.

Depending on the considered experiment, the interpolation methods show a slight advantage. If, a general method is preferred for the determination of the unknowns, the golden section interval division is recommended.

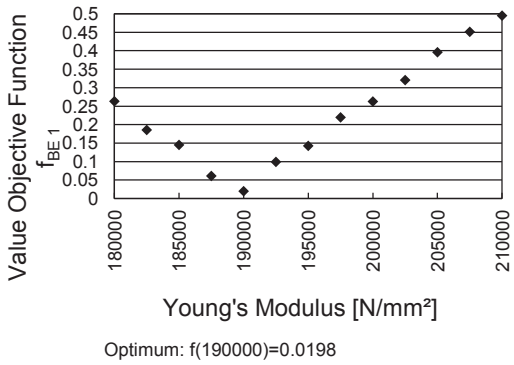

Figure 8.37: Bending experiment; Uniform sampling; Relation between the Young's modulus and the objective function.

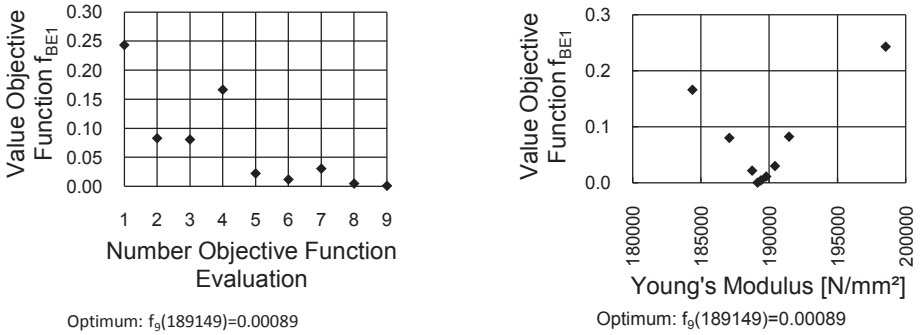

Figure 8.38: Bending experiment; Golden section interval division; Left: Propagation of the optimization; Right: Relation between the Young's modulus and the objective function.

For the final material and friction model calibration, a unique set of parameters has to be identified, which leads for each experiment to a satisfying prediction of

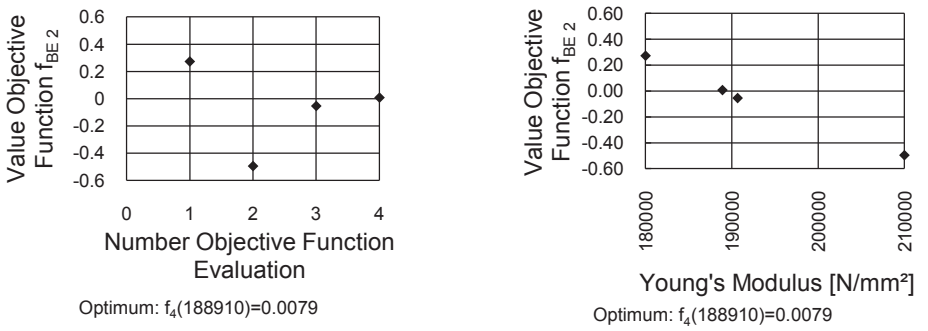

Figure 8.39: Bending experiment; Regula Falsi iteration; Left: Propagation of the optimization; Right: Relation between the Young's modulus and the objective function.

the measured data. This condition is complied by the identified model parameters (table 8.19), as shown by table 8.20.

Table 8.19: Summary of the inverse parameter identification.

Parameter	Value
Yield Locus Exponent	5.0
Friction Coefficient	0.091
Strain Rate Dependency	Considered
Kinematic Hardening	Not Considered
Young's Modulus	$189000 N/mm^2$

For the chosen material and friction model, the fundamental and the complementary experiments are sufficient for determining the unknown parameters. However, additional complementary experiments might be needed, if more complex models need to be calibrated. Even the investigated sequence of evaluating the complementary experiments might depend on the type of material and friction model. Consequently, the introduced procedure of determining the unknowns is only suitable for a material model comprising the assumption of isotropic hardening and a Barlat 2000 yield locus. Other yield loci, comprising less or an equal amount of model parameters like the Barlat ´89 can be also treated by the introduced procedure.

Table 8.20: Verification of the identified unknowns (table 8.19).

Experiment	Type	Investigated Quantities				Value Objective Function
YLIT-4-BMW		RD/TD	ϵ_1	ϵ_2	d_{MDD} $[mm]$	
	Simulation	RD	0.409	-0.159	41.9	0.1033
		TD	0.400	-0.175	43.7	
	Measured Data	RD	0.397	-0.145	41.3	
		TD	0.429	-0.164	42.5	
Bending Experiment		Angle $\alpha[^\circ]$				
	Simulation	82.56				0.0066
	Measured Data	82.57				
Friction Experiment		ϵ_1	ϵ_2			
	Simulation	0.129	-0.089			0.00202
	Measured Data	0.130	-0.088			

8.7 Noise in numerical solutions

The above shown sensitivity analyses do not indicate a strong effect of numerical noise on the computed quantities. In this context, noise is defined as the variation of the results induced by repeating the numerical solution of a mechanical problem. In order to investigate the noise, each complementary experiment is performed multiple times under the same parameter configuration. This investigation allows deciding, whether additional methods are necessary for treating noise. The unknowns are chosen according to the results of the identification procedure, as given by table 8.19. For analyzing the results, the same objective functions are applied as for the sensitivity analyses. Additionally, for each simulation the calibration of the yield locus is repeated. Consequently, both, the stability of the simulation and the calibration procedure are investigated. The maximum deviation of the objective function value between two simulation based predictions is below $1.0 \cdot 10^{-6}$ for each complementary experiment. In consideration of the above presented results, the numerical solution of the mechanical problem is stable and additional methods for treating noise are not necessary.

8.8 Discussion of the complementary experiments

This section is devoted to the discussion of the most important issues regarding the measurement methodology, the treatment of the simulation results and numerical settings. For the shown investigations, the above identified unknowns are applied (table 8.19).

8.8.1 YLIT-Experiments

The strain fields, resulting from the measured data and the simulation, are discrete. Generally, each strain state of the discrete fields refers to a location in space. Thereby, the associated locations of the strain states, resulting from the simulation, are not coincident with those, obtained from the measured data. As a consequence, an interpolation of the discrete strain fields is necessary in order to compare the strain states at defined reference locations. In order to avoid performing such an interpolation for both discrete strain fields, the reference locations are taken from the measured data. Therefore, it is sufficient to compute the strain states at the reference locations on the basis of the simulation result.

Expression (8.10) shows the applied interpolation formula [112], which weights the contribution of a quantity in consideration of the associated distance with respect to the reference location:

$$Z = \frac{\left(\sum_{i=1}^{N-1} \frac{Z_i}{R_i^2}\right) + \frac{C\widehat{Z}}{\widehat{R}^2}}{\left(\sum_{i=1}^{N-1} \frac{1}{R_i^2}\right) + \frac{C}{\widehat{R}^2}}. \tag{8.10}$$

This distance is also applied for the selection of the N nearest quantities, taken into account for the interpolation. Figure 8.40 illustrates the interpolation scheme. In this work, N is chosen to be equal to 10. The quantity, whose position is the closest one to the preference location, is especially weighed by the constant C. The value of C=1.5 is taken according to the recommendation of [113]. R_i defines the distance of the point i to the reference location. Z_i represents the value of the quantity, which is interpolated, at the point i. The variables denoted by "ˆ" refer to the point, which is located closest to the reference location.

The first and second in-plane principal strains are interpolated independently from each other by the introduced scheme. The corresponding positions of the strain state, which are taken into account for the interpolation, are coincident with the integration points belonging to the element. In this thesis only shell elements are considered. On the basis of the shape functions, the locations of the integration points in the midsurface are determined. As a next step, the normal direction of the element is computed according to the definition of the applied FEM-System. In conjunction with the normal direction, the position of each integration point can be computed. The applied under-integrated element type comprises only one integration point in the midsurface. All the integration points in thickness direction lie on the same fiber. For the interpolation of the

strain state, only the outer integration point, corresponding to the surface of the measured strain field, is taken into account.

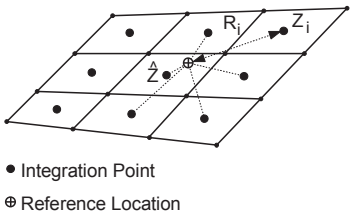

Figure 8.40: YLIT-4-BMW; Interpolation of the quantities referring to integration points of the elements.

Because of the applied Gaussian integration in thickness direction, none of the integration points are directly located at the top surface. The applied element would also support a Simpson integration scheme in thickness direction, which implies integration points directly located on the surface. However, as mentioned above, all the experiments of this work should be computed with the same numerical configuration. As the Gaussian integration scheme is advantageous for computing bending stresses under the same computational effort, this scheme is applied in this work. As a consequence, for the comparison of the computed and the measured strain field, the integration points are considered, which are closest to the optically measured surface. The deviation between the strain states, related to these integration points, and the associated surface strain states are assumed to be negligible. This simplification is possible, as the considered location for the comparison between the measured and the computed strain state is not subject to bending effects.

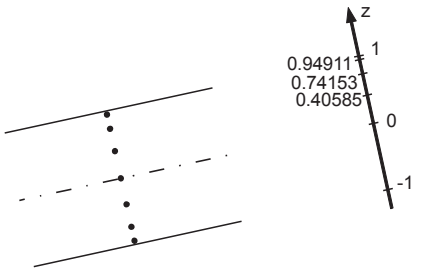

$z_* = 0.94911$
$z_0 = 0.0$

$\epsilon_1(z_0) = 0.40013$
$\epsilon_1(z_*) = 0.40690$

$\Delta\epsilon = \epsilon_1(z_0) - \epsilon_1(z_*) = -0.00677$

Figure 8.41: YLIT-4-BMW; First principal strain; Left: Geometrical conditions of the considered element; Right: Computed strain states.

The strain state, shown by figure 8.41, is taken from a simulation, which is

based on the identified unknown parameters (table 8.19). Thereby, only the specimen is considered, whose length direction is parallel to the transverse direction.

The difference between the given first principal strains is small (figure 8.41). Additionally, the local z-coordinate of the outer integration point is 0.94911, as the applied Gaussian integration comprises 7 integration points through the thickness. As the Reissner-Mindlin shell elements are applied, the strain distribution in thickness direction is linear. Therefore, the difference between $\epsilon_1(z_*)$ and $\epsilon_1(z = 1)$ is marginal in consideration of the depicted geometrical conditions. Consequently, for the discussed application, it is not necessary to distinguish between the strain state of the outer integration point and the surface.

8.8.2 Bending experiment

The prediction of the springback behavior strongly depends on the computed stress state after the forming operation. For an accurate prediction of the stress state an appropriate choice of the element size is necessary. If the element size is chosen to be too large, the bending stresses are not reflected well by the simulation model. The larger the bending radius, the larger the element size can be chosen.

In the thesis of Okan [86] an edge length of shell elements between $0.5mm$ and $2.0mm$ is investigated on the basis of a rotational bending operation and a bending radius of 3mm. Okan [86] recommends an alignment of the mesh of the specimen as shown by figure 8.42. Provided this alignment is performed, the prediction of the springback is invariant with respect to the investigated range of the element length. In this thesis, the bending radius is chosen to be equal to $10mm$. An element edge length of $1.0mm$ is selected, which should give in consideration of the investigations of Okan, an accurate prediction of the stress state.

Figure 8.42: Bending experiment; Left: For the generation of the mesh of the specimen, the depicted nodes are assumed to be extruded in y-direction. An alignment of the mesh in x-direction leads to equal x-coordinates of the nodes N_i and the point A; Right: Definition of the gap width.

Generally, deviations between the tool geometry in the laboratory and the simulation model can affect the conclusions, if model parameters are inversely determined. In this context, it is most difficult to provide the desired gap width (figure 8.42 (right)), as this quantity depends on the manufacturing tolerances of

the die and the punch. Furthermore, the gap width also depends on the assembly accuracy of the tool and the design of the guides, which assure a reproducible alignment between the die and the punch. Therefore, the effect of the gap width on the springback behavior is investigated based on simulations.

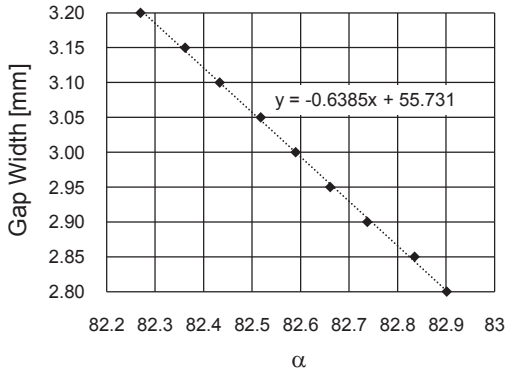

Figure 8.43: Bending experiment; Analysis of the influence of the gap width on the prediction of the springback.

The correlation between the gap width and the predicted springback angle is approximately linear. Hence, figure 8.43 also comprises a regression of a linear function. From the given slope follows that a deviation between the experiment and the simulation model of $0.0063mm$ leads to an error of $0.01°$. Consequently, the gap width of the tool and the simulation model has to match very accurately. As it is difficult to adjust the gap width of the tool according to the design value in consideration of the needed accuracy, it is recommended to measure it by applying a gauge block and to adapt the simulation model according to the measured result. At this point it has to be mentioned that the gap width might alter due to the elastic deformation of the press and the tool. Consequently, this effect has to be minimized by assuring a sufficient stiffness of the tool in the design phase of the experiment.

The alignment of the formed specimen, for measuring the springback, is introduced in chapter 6. For the prediction of the springback, boundary conditions have to be introduced, which reflect the alignment induced by the measurement fixture. Figure 8.44 shows the applied statically determined support conditions.

As mentioned in chapter 6, the measured springback is expected to be slightly affected by the gravity effect. A simulation based investigation showed that the angle α is $0.05°$ smaller, if the springback simulation is complemented by the consideration of the gravity effect. The direction of the gravity field is coincident with the positive z-coordinate, as given in figure 8.44. Even though the influence of the gravity effect is rather small, it is still considered by the investigations of this thesis. However, the effect of the gravity on the measured springback depends on the sheet thickness. Therefore, the given result is only valid for the

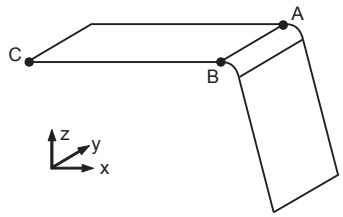

Locked degrees of freedom:
A:x,y,z
B:x,z
C:z

Figure 8.44: Bending experiment; Support conditions for the springback simulation.

investigated steel DX54, whose sheet metal thickness is $1.0mm$.

8.8.3 Friction experiment

The comparison between the predicted and the measured strain state is limited to a single point P. The applied simulation model considers the double symmetry of the mechanical problem. Subsequently, only the computed quarter of the formed specimen is considered. The evaluated strain states are given by the integration points of the elements, which are closest to the top surface (definition top surface, see chapter 6). For the further discussion a set Q is defined, which contains these integration points. The integration points of the midsurface of the applied element type are located between the element nodes.

As a consequence of the considered symmetry, the point P is located at the intersection of the symmetry planes. Hence, a strain state will never be available at this location, as the symmetry condition is defined by the element nodes. Consequently, the question arises, whether an extrapolation is necessary, in order to obtain a suitable prediction at the point P.

Figure 8.46 shows the strain states of the integration points, on the top surface in the neighborhood of the point P in the principal in-plane strain space. As mentioned above, the applied element type possesses only one integration point, which corresponds to the top surface. Therefore, the evaluation of 16 elements leads to 16 computed strain states. The size of the evaluated zone is $16mm \times 16mm$ in the original state before forming. According to figure 8.46, the investigated zone of the strain field can be regarded as constant, if the maximum measurement accuracy of 0.001 with respect to the principal strain values is taken into consideration.

Consequently, a significant difference of the strain state at the intersection of the symmetry planes (point P) and the related closest integration point, belonging to Q, is not expected. Therefore the strain state, related to this integration point, is considered to be the desired prediction with respect to the point P.

As mentioned in chapter experiments, the strain field is measured after tool opening. In order to obtain the mechanical state of the specimen after tool opening, the consideration of the elastic springback is necessary, which might significantly affect the prediction of the strain field. Figure 8.46 shows the first and

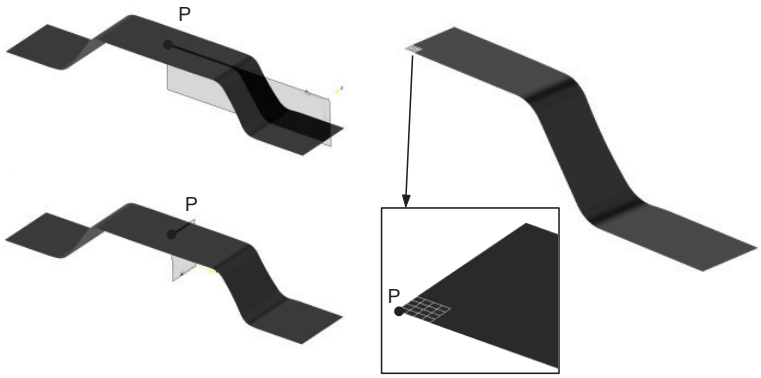

Figure 8.45: Friction experiment; Definition of the symmetry planes.

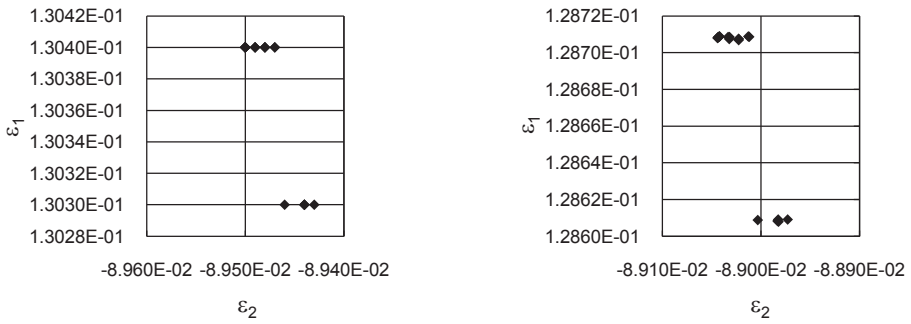

Figure 8.46: Friction experiment; Strain state of the set Q; Left: In the closed state of the tool; Right: After the springback of the specimen.

second principal strain field, with and without consideration of the springback effect in the neighborhood of the point P. Thereby, the depicted strain states result from the integration points belonging to the set Q. Obviously, the springback effect should be taken into consideration, as the strain state is affected in the dimension of the measurement accuracy. A comparison of the figures 8.46 and 8.47 shows that the difference between the corresponding strain states of the integration points, belonging to the set Q and the midsurface, is marginal. Hence, the strain states of the outer integration points can be considered to be equivalent to the ones at the surface.

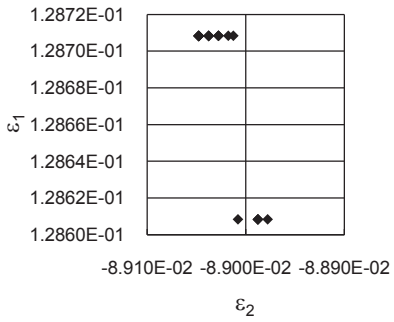

Figure 8.47: Friction experiment; Strain state of the integration points on the midsurface, which lie on the same fiber as the integration points of the set Q (after the springback of the specimen).

Chapter 9

Validation experiments

9.1 Introduction

The validity with respect to the scope of application is the most important property of a calibrated material and friction model. In other words, the calibrated model, derived from a few selected experimentally determined quantities, has to be able to treat arbitrary stress states, occurring in industrial forming simulations. Unfortunately, it is impossible to verify all possible stress states by comparing simulation based predictions with measured data. For the industrial application, it seems to be reasonable to limit the validation to some selected experiments. However, one has to bear in mind, that such a validation cannot be regarded as a proof of the general predictive capability of the investigated material model.

In order to obtain the best possible quality of the validation, the same batch of sheet metal should be applied for the fundamental, the complementary and the validation experiments. Regarding the subsequent investigations, this recommendation is complied. All the experimentally determined data is based on the interstitial free steel DX54. According to the findings of the chapter 8, which refer to the investigated steel DX54, the Barlat 2000 yield locus in combination with an isotropic hardening leads to a satisfying prediction of the measured quantities concerning the YLIT-Experiments. Additionally, the strain rate dependency of the hardening effect should be considered, if the flow curve is derived from the tensile and the bulge tests. Finally, the chapter 8 also comprises an inverse determination of the Young's modulus and the friction coefficient.

Subsequently, each experiment is analyzed by an optimization, whose parameter space contains the yield locus exponent, the consideration of the strain rate dependency of the hardening effect, the consideration of the kinematic hardening model, the Young's modulus and the friction coefficient. These optimizations are performed in order to investigate whether it is possible to predict the measured data by a variation of these parameters. Furthermore, an analysis regarding the sensitivities of the parameters with respect to the accuracy of the simulation

model is needed. These sensitivities indicate, which parameters are validated by the considered experiment. Each optimization is performed on the basis of the same parameter space, as defined by table 9.1, and an evolutionary strategy is applied, comprising a derandomized self adaptation [35] ($(1, \lambda)$-DR-ES).

Table 9.1: Domain of the parameter space.

Parameter	Domain	Type
Strain Rate Dependency (SRD) (0 =off; 1 =on)	$0 - 1$	Discrete
Exponent Barlat 2000	$4 - 8$	Discrete
Kinematic Hardening (KH) (0 =off; 1 =on)	$0 - 1$	Discrete
Young's Modulus	$190000 N/mm^2$ $- 210000 N/mm^2$	Continuous
Friction Coefficient	$0.08 - 0.12$	Continuous

Additionally, the prediction of the simulation on the basis of the selected models and their parameters (table 8.19) is investigated. This chapter comprises the investigation of the u-profile, the cylindrical deepening and the hole extrusion experiment. A description of the experimental setup, the measured quantities and the related evaluation procedure is given in chapter 6.

9.2 U-Profile experiment

The u-profile experiment is performed in order to validate the considered material and friction model on the basis of the springback effect. As opposed to all of the other experiments, discussed in this thesis, the specimen of the u-profile experiment is not clamped between the die and the binder. Under ideal conditions, the springback effect is large compared with the measurement accuracy. Consequently, the springback effect should be maximized. The larger the drawing depth the larger the side wall curl and the flange rotation are. Provided, the specimen is clamped in the binder zone, the attainable drawing depth is mainly determined by the forming limit of the material. Higher levels of drawing depth are possible, if a material flow between the binder and the die occurs. Hence, a relative movement in the interface between the specimen and the tool surface in the binder zone is desired (figure 9.1 (left)). In order to analyze the effect of the investigated parameters on the quality of the springback prediction, the material flow in the binder zone should be adapted according to the experimentally determined one. Subsequently the material flow is quantified by a scalar value, representing the distance between the edge of the specimen and the center of the drawbead (figure 9.1 (right)). The material flow along the length direction of the formed specimen (definition see figure 6.16) is assumed to be constant.

Figure 9.1: U-Profile experiment; Left: Definition of the binder zone; Right: Definition of the d_{ESCD}.

For the description of the material flow, the quantity d_{ESCD} is introduced (distance between the edge of the specimen and the center of the drawbead). Provided a deviation between the predicted and the measured material flow occurs, additional restraining forces are defined in the simulation model. This procedure only works, if the d_{ESCD} of the simulation is smaller than the experimentally determined one. However, without any artificial restraining force, none of the performed simulations showed the opposite case. Hence, the treatment of this event is not considered in this thesis. As spacers are applied between the binder and the die, the material flow is mainly affected by the geometry of the drawbead, the friction and the additional restraining forces. Figure 9.2 shows the sequence of the optimization, which also comprises the adaption of the d_{ESCD}. A description of the algorithm, applied for the adjustment of the material flow is given below.

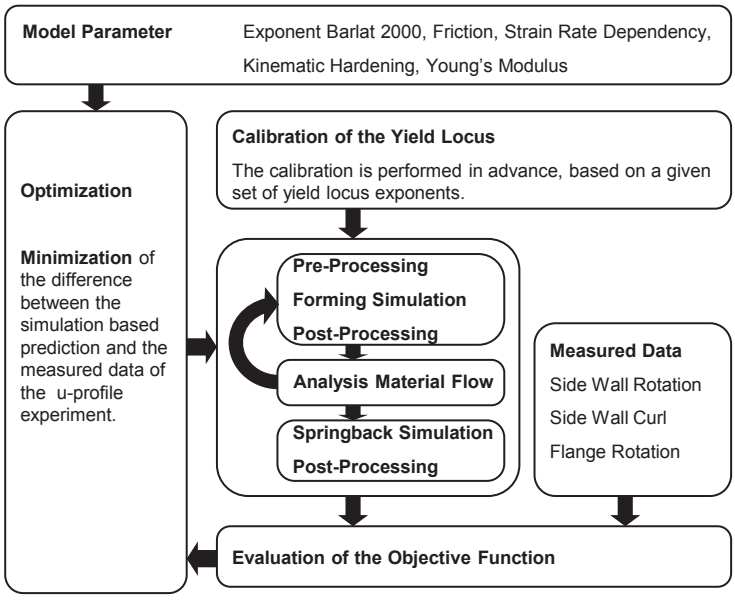

Figure 9.2: U-Profile experiment; Sequence of the optimization.

The springback behavior of the specimen is quantified by the scalar values side

wall rotation α_{SWR}, side wall curl d_{SWC} and flange rotation α_{FR}. Consequently, for the comparison between the predicted and the measured data these quantities need to be combined to a single scalar objective value. The aggregation of the objectives is performed by applying the two-sided Harrington desirability function [22]. The desirability values are aggregated multiplicatively as given by

$$\begin{aligned} f_{\alpha_{SWR}} &= \alpha_{SWR_{sim}} - \alpha_{SWR_{ed}}, \\ f_{d_{SWC}} &= d_{SWC_{sim}} - d_{SWC_{ed}}, \\ f_{\alpha_{FR}} &= \alpha_{FR_{sim}} - \alpha_{FR_{ed}}, \end{aligned} \tag{9.1}$$

$$f = 1 - \prod_{Q \in W} d_2(f_Q, U_Q, L_Q, n_Q),\ W = \{\alpha_{SWR}, d_{SWC}, \alpha_{FR}\}\,. \tag{9.2}$$

This expression also comprises the formulation of a minimization problem. Table 9.2 summarizes the parameters, which are chosen based on experience for the definition of the desirability functions.

Table 9.2: U-Profile experiment; The chosen values of the parameters of the Harrington desirability functions.

Parameter	α_{SWR}	d_{SWC}	α_{FR}
U	4	1	4
L	-4	-1	-4
n	2	2	2

Table 9.4 shows the estimated measurement accuracy of the applied evaluation procedure, which is derived from the measurement procedure and the measurement equipment. The values of the measured quantities (table 9.3) do not reflect the fluctuations of the experimental results, as each experiment leads to the same result. It is assumed that the interval defined by the measurement accuracy contains the fluctuations of the corresponding real values.

Table 9.3: U-Profile experiment; Measured results.

Experiment	α_{SWR}	d_{SWC}	α_{FR}
1	2.5	9.0°	12.0°
2	2.5	9.0°	12.0°
3	2.5	9.0°	12.0°

Table 9.4: U-Profile experiment; Estimated measurement accuracy.

α_{SWR}	d_{SWC}	α_{FR}
$\pm 0.25°$	$\pm 0.25mm$	$\pm 0.25°$

The figures 9.3, 9.4, 9.5, 9.6 and 9.7 summarize the results of the optimization. According to figure 9.3 (left), the springback of the u-profile does not depend on the choice of the yield locus exponent. The accordance between the predicted and the experimentally determined springback is affected by considering the strain rate dependency of the hardening effect. Both, the friction coefficient and the Young's modulus might influence the conformity between the simulation result and the measured data (figure 9.4).

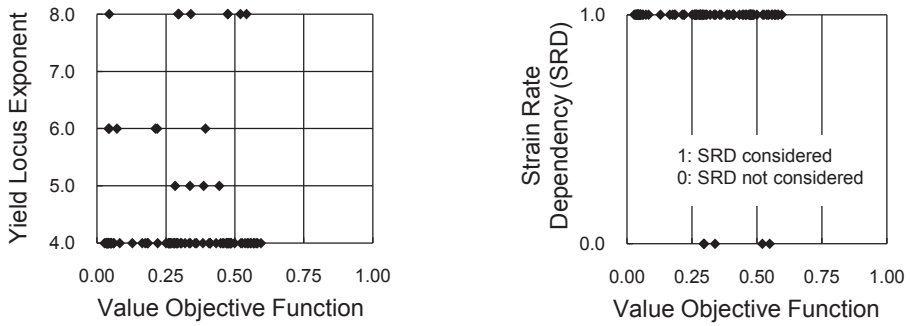

Figure 9.3: U-Profile experiment; Left: Relation between the yield locus exponent and the objective function; Right: Relation between the consideration of the strain rate dependency of the hardening effect and the objective function.

In this context the question arises, whether it is sufficient to reduce either the Young's modulus or the friction coefficient in order to obtain low objective function values. However, it could be also possible that both parameters need to be reduced. In order to answer this question, the parameter space is subdivided. Figure 9.5 (left) illustrates the correlation between the friction coefficient and the objective function value. Thereby, only objective function evaluations are considered, which comprise values of the Young's modulus greater than $200000N/mm^2$. According to this figure, a dependency between the friction coefficient and the objective function is not recognizable. Based on the same procedure also the Young's modulus is analyzed. In this case, only simulation runs are considered, which comprise friction coefficients greater than 0.09. The best objective function values can be obtained by values of the Young's modulus close to the lower bound of the object variable space. According to figure 9.5 (right), an approximately linear correlation between the Young's modulus and the objective function exists.

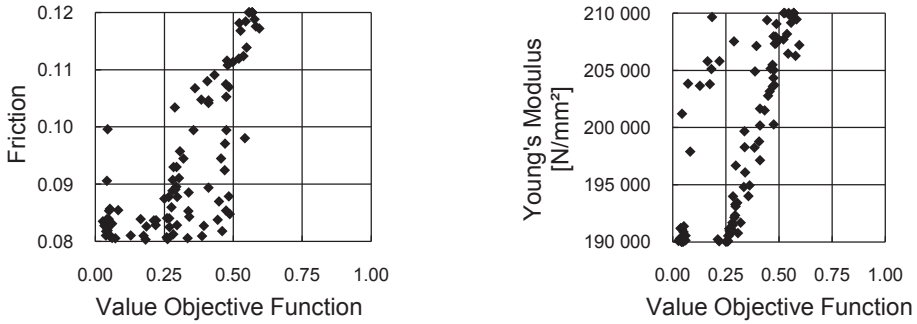

Figure 9.4: U-Profile experiment; Left: Relation between the friction coefficient and the objective function; Right: Relation between the Young's modulus and the objective function.

Figure 9.6 is obtained by excluding additionally all the simulation runs, which are performed with and without consideration of the kinematic hardening effect. According to this figure, independent of the consideration of the kinematic hardening model, an approximately linear correlation between the Young's modulus and the objective function exists.

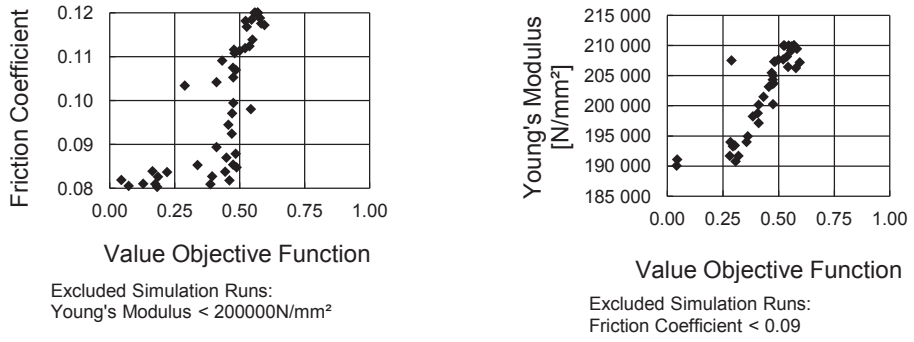

Figure 9.5: U-Profile experiment; This figure shows subspaces of the optimization results; Left: Relation between the friction coefficient and the objective function value; Right: Relation between the Young's modulus and the objective function value.

Finally, the Bauschinger effect is investigated. According to figure 9.7, the kinematic hardening model should not be applied.

Figure 9.8 visualizes the geometry of the specimen before and after springback (Choice parameters: Table 9.5 second line). Table 9.5 summarizes some additional investigations regarding the consideration of the Bauschinger effect. The best prediction is obtained, if the kinematic hardening model is not applied. Provided the

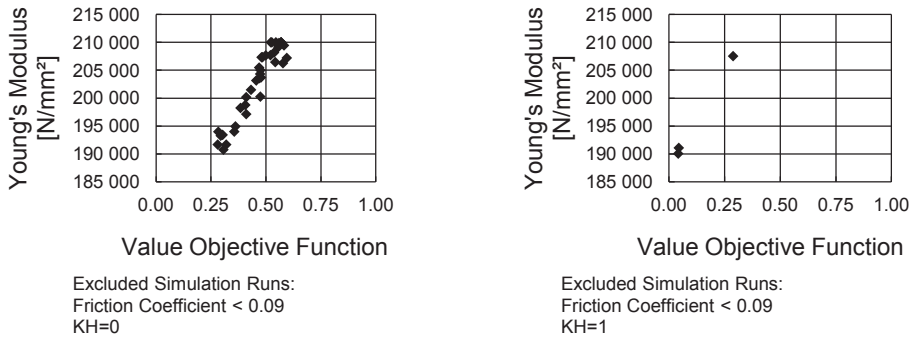

Figure 9.6: U-Profile experiment; This figure shows the relation between the Young's modulus and the objective function value of two different subspaces of the optimization.

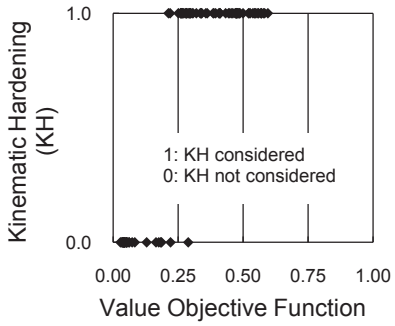

Figure 9.7: U-Profile experiment; Relation between the consideration of the kinematic hardening model and the objective function.

kinematic hardening model is applied, the quality of the simulation based prediction can be improved by decreasing the Young's modulus. However, such a modification of the Young's modulus would be problem specific. Therefore, table 9.5 contains another simulation based on an extended elasticity model, which is able to take the dependency of the Young's modulus with respect to the accumulated equivalent plastic strain into account. This model disregards any effect of the prestrain path, as the Young's modulus depends on the accumulated equivalent plastic strain. According to figure A.6, the maximum accumulated equivalent plastic strain exceeds the domain of Doege's investigations. Therefore the relation between the accumulated plastic strain and the Young's modulus is linearly extrapolated for this examination. Thereby, a better prediction of the springback is obtained. In consideration of the uncertainties with respect to the mentioned extrapolation it can be concluded that the application of the kinematic hardening model should be complemented by a suitable description of the dependency of the Young's modulus regarding plastic yielding. Unsatisfying results are obtained, if the kinematic hardening model is applied in combination with a Young's modulus of $210000 N/mm^2$. The determination of a reduced Young's modulus based on the bending experiment, offers the chance to improve the springback prediction. However, if the accumulated equivalent plastic strain differs significantly in different regions of an industrial part, it is recommended to apply an extended elasticity model as mentioned above. The results show the need for another validation experiment, which is especially designed for being highly sensitive with respect to the Bauschinger effect.

Finally, the results, obtained from the u-profile experiment confirm the choice of the unknown parameters, identified by the complementary experiments.

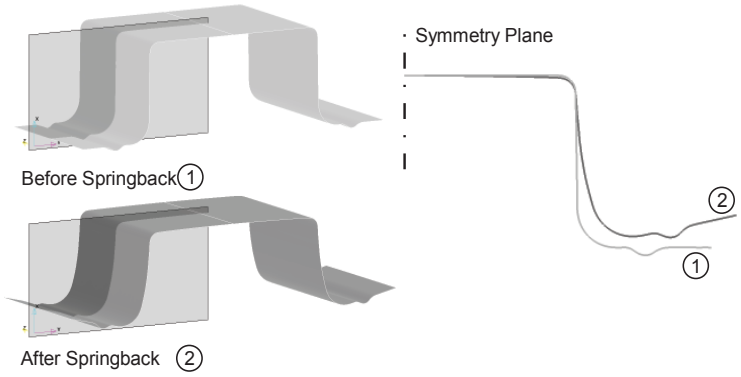

Figure 9.8: U-Profile experiment; Geometry of the specimen before and after springback.

Table 9.5: U-Profile experiment; Investigation of the kinematic hardening model (SRD= *on*, Yield locus exponent= 5, $\mu = 0.091$).

Type	Investigated Quantities			Value Objective Function
	α_{SWR} [°]	d_{SWC} [mm]	α_{FR} [°]	
Simulation Young's Modulus= $189000 N/mm^2$ KH= *on*	9.49	2.06	11.85	0.1894
Simulation Young's Modulus= $189000 N/mm^2$ KH= *off*	9.02	2.52	12.35	0.0080
Simulation Young's Modulus= $210000 N/mm^2$ KH= *on*	8.01	1.80	10.58	0.4920
Simulation Young's Modulus= $210000 N/mm^2$ KH= *off*	8.57	2.09	11.08	0.2075
Simulation Young's Modulus= $174000 N/mm^2$ KH= *on*	9.61	2.32	11.93	0.0544
Simulation Young's Modulus Strain Dependent KH= *on*	9.01	2.43	10.95	0.0715
Measured Data	9.0	2.5	12.0	

9.3 Cylindrical deepening experiment

The objective of this experiment is the validation of the forming limit curve (FLC) (see chapter 6), which requires the occurrence of the failure mode localized necking. The investigated material DX54 showed this failure mode in combination with this experiment. The derivation of the maximum drawing depth (d_{MDD}) from the measured data is given in chapter 6. Table 9.6 shows the results referring to the investigated steel DX54. The first experiment, given by this table, shows the smallest deviation with respect to the mean value and, therefore, is taken as a reference drawing depth for the optimization.

Table 9.6: Cylindrical deepening experiment; Measured results.

Experiment	d_{MDD} [mm]
1	23.0
2	23.1
3	22.6
Mean Value	22.9

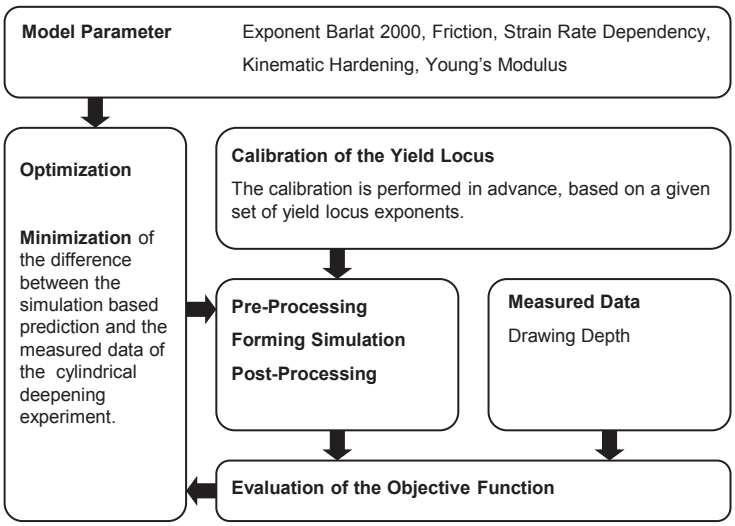

Figure 9.9: Cylindrical deepening experiment; Sequence of the optimization.

For the evaluation of the FLC, the simulation based prediction of the maximum drawing depth is compared with the experimentally determined one. The predicted maximum drawing depth is obtained by the same procedure, as introduced for the YLIT-Experiments. Based on a predefined set of drawing depths,

the associated strain fields are evaluated in terms of the FLC. This leads to a relation between the drawing depth and the predicted occurrence of localized necking. Table 9.7 shows the investigated drawing depths of the simulation, which are given with respect to the reference drawing depth.

Table 9.7: Cylindrical deepening experiment; Evaluated drawing depths concerning the simulation.

Index Plot State	1	2;3	4;5	6;7	8;9	10;11	12;13
Drawing Depth $[mm]$	± 0.00	± 0.10	± 0.20	± 0.30	± 0.40	± 0.50	± 0.60
Index Plot State	14;15	16;17	18;19	20;21	22;23	24;25	26;27
Drawing Depth $[mm]$	± 0.70	± 0.80	± 0.90	± 1.00	± 1.25	± 1.50	± 2.00

The objective function is defined by (CDE: Cylindrical deepening experiment)

$$f_{CDE} = |d_{MDD_{sim}} - d_{MDD_{ed}}| \,. \tag{9.3}$$

Thereby, the difference between the experimentally determined maximum drawing depth and the predicted one is computed. The application of the norm leads to a minimization problem.

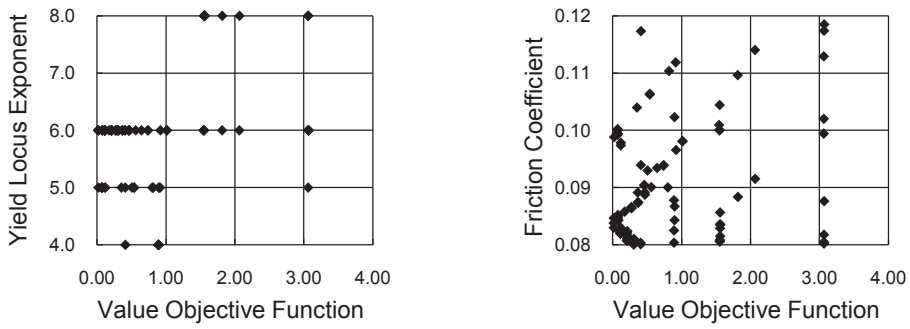

Figure 9.10: Cylindrical deepening experiment; Left: Relation between the yield locus exponent and the objective function; Right: Relation between the friction coefficient and the objective function.

The scheme of the optimization sequence is given by figure 9.9. Figure 9.10 (left) shows a correlation between the yield locus exponent and the objective function. Also the consideration of the strain rate dependency of the hardening effect affects the accuracy of the simulation based prediction (figure 9.11 (left)). If the objective function evaluations, comprising a yield locus exponent equal to 4.0, are excluded from the evaluation of the optimization results, satisfying objective

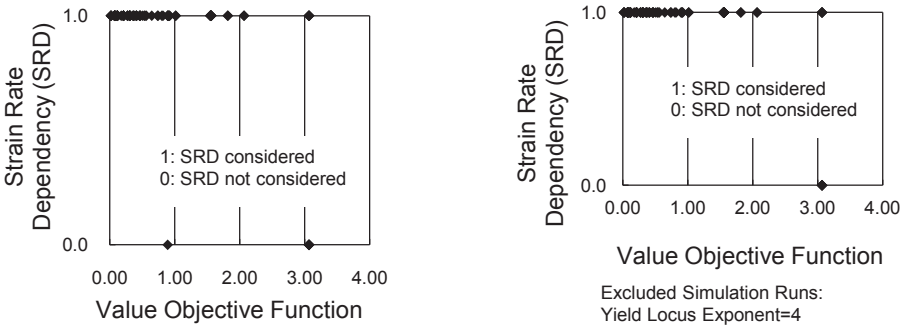

Figure 9.11: Cylindrical deepening experiment; Left: Relation between the consideration of the strain rate dependency of the hardening effect and the objective function; Right: Relation between the consideration of the strain rate dependency of the hardening effect by excluding the objective function evaluations, which are based on a yield locus exponent equal to 4.

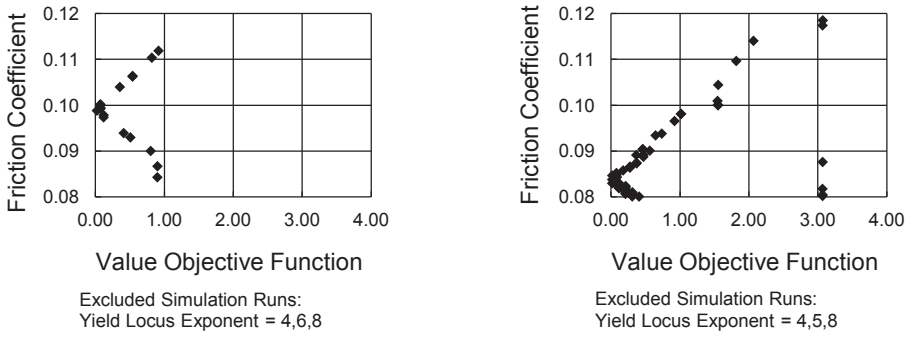

Figure 9.12: Cylindrical deepening experiment; Relation between the friction coefficient and the objective function; Left: The yield locus exponent is chosen to be equal to 5; Right: The yield locus exponent is chosen to be equal to 6.

function values are only obtained in consideration of the strain rate dependency of the hardening effect. A low yield locus exponent seems to stabilize the material response.

Also the choice of the friction coefficient influences the conformity between the simulation and the experiment (figure 9.10(right)). A better visualization of the correlation between the friction coefficient and the objective function is obtained by excluding the objective function evaluations based on selected yield locus exponents. According to figure 9.12, more than one optimum exists, depending on the choice of the yield locus exponent. In such a case the validation is successful, if one of the optimums corresponds to the identified unknown model parameters.

The optimization results show that the prediction of the drawing depth does not depend on the choice of the Young's modulus (figure 9.13 (left)). As the elastic strains are very small compared with the plastic ones, the influence of the Young's modulus should be small, which is confirmed by the optimization result. Furthermore, the consideration of the kinematic hardening model does not affect the prediction of the maximum drawing depth. This result is expected, as none of the material points undergo a change between tension and compression during the forming operation.

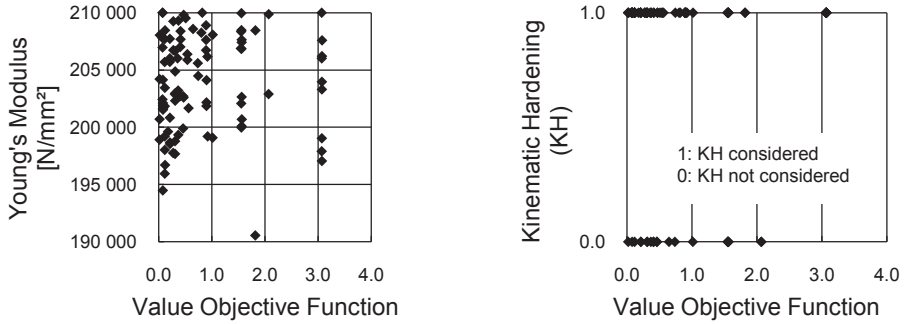

Figure 9.13: Cylindrical deepening experiment; Left: Relation between the Young's modulus and the objective function; Right: Relation between the consideration of the kinematic hardening model and the objective function.

The discussion of the results shows that a validation of the forming limit curve is only possible, if the material and the friction model is well calibrated.

Table 9.8 shows the prediction of the simulation on the basis of the model calibration of chapter 8. In comparison with the experimentally determined maximum drawing depth the simulation result is slightly optimistic. Under the assumption that the calibration of the material and friction model is reliable, this result indicates, that the forming limit is reflected too optimistic by the FLC in the investigated zone. However, the identified accuracy of this FLC in combination with the calibrated material and friction model should be still suitable for tool shop and press shop applications.

Table 9.8: Cylindrical deepening experiment; Validation of the identified unknowns (table 8.19).

Type	d_{MDD}[mm]	Value Objective Function
Simulation	23.8	0.8
Measured Data	23.0	

9.4 Hole extrusion experiment

The objective of the hole extrusion experiment is the validation of the forming limit curve (see section 5.4). Thereby, the smallest possible hole diameter (d_{min}) is identified, which does not lead to localized necking during forming. The investigation of the unknown parameters (table 9.1) on the basis of an optimization, which gives the best possible prediction of d_{min}, would imply a determination of d_{min} for each parameter configuration. Generally, the simulation based determination of d_{min} for a given parameter configuration comprises several simulations, as each one gives the prediction of the occurrence of localized necking with respect to only one hole diameter. In order to avoid such a computational expensive procedure, the hole diameter is kept constant. This diameter, which will be referred to as reference diameter, is chosen to be equal to the smallest possible value according to an experimental study (table 9.9). A conservative interpretation of the results of table 9.9 leads to the conclusion that a hole diameter of $d = 10.5mm$ should generally not lead to localized necking.

Table 9.9: Hole extrusion experiment; Summary of the experimental results (LN: Localized necking; WN: Without localized necking).

Hole Diameter [mm]	Stripe 1	Stripe 2	Stripe 3	Stripe 4
9.0	LN	LN	LN	LN
9.5	LN	LN	LN	LN
10.0	WN	WN	WN	LN
10.5	WN	WN	WN	WN
11.0	WN	WN	WN	WN

Based on the chosen reference diameter $d = 10.5mm$ a point in the search space (table 9.1) is searched, which gives the most pessimistic prediction in terms of localized necking. Consequently, this optimization does not contain a comparison with measured data, as the reference diameter represents the experimental observation. This modified optimization sequence is visualized by figure 9.15. The quantification of this objective is realized by determining the maximum of d_{FLC_i} as defined by figure 9.14 (HEE: Hole extrusion experiment)

$$f_{HEE} = -\max(d_{FLC_i}). \tag{9.4}$$

The negative sign is introduced to transform the $\max(d_{FLC_i})$ to a minimization problem. Provided, the strain path is linear, this approach gives a reasonable estimation of the remaining forming potential. If d_{FLC_i} is equal to 1.0, the strain state s_i lies on the forming limit curve. For strain states, which are located above the forming limit curve, the corresponding d_{FLC_i} value is greater than 1.0.

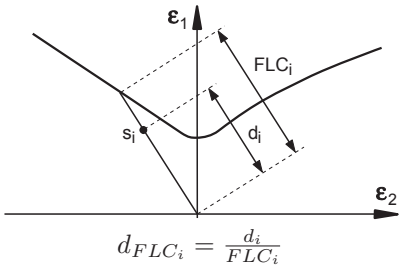

Figure 9.14: Hole extrusion experiment; Definition of d_{FLC_i}.

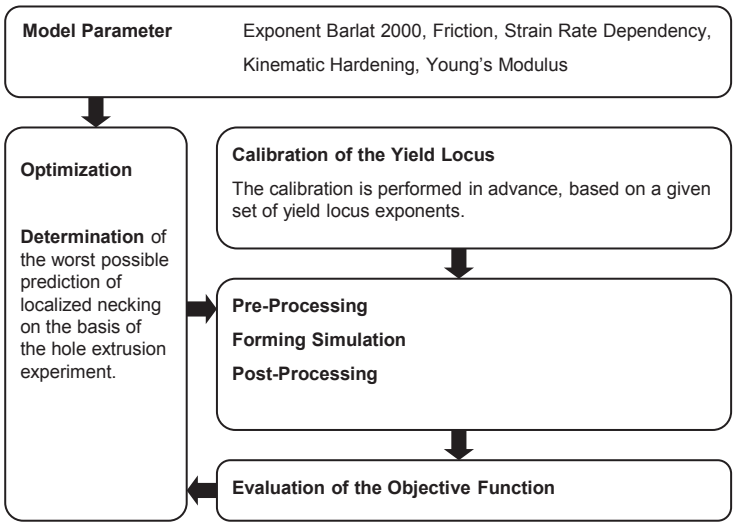

Figure 9.15: Hole extrusion experiment; Sequence of the optimization.

Figure 9.16 (left) illustrates that a choice of the yield locus exponent equal to 8.0 leads to the prediction of localized necking on the basis of the reference hole diameter. The objective function evaluations, resulting from the other yield locus exponents, do not lead to the prediction of a material failure. All the objective

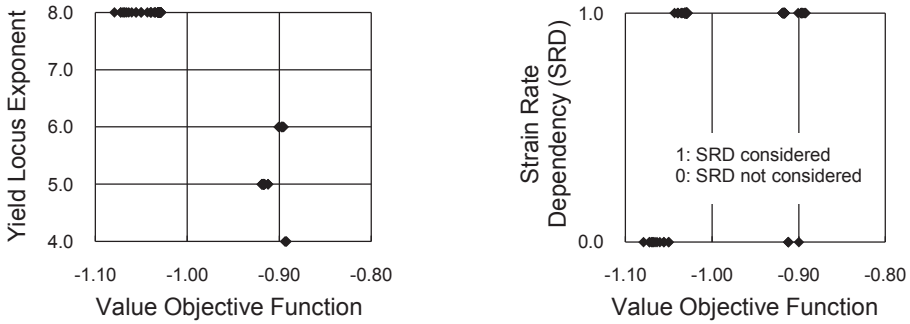

Figure 9.16: Hole extrusion experiment; Left: Relation between the yield locus exponent and the objective function; Right: Relation between the consideration of the strain rate dependency of the hardening effect and the objective function.

function evaluations, which show an objective function value below -1.0 correspond to a yield locus exponent of 8.0. Figure 9.16 (right) shows the analysis of the strain rate dependent hardening effect. Provided only the objective function values below -1.0 are considered, the stabilization effect of the strain rate dependent hardening is recognizable. For the objective function evaluations, which lead to an objective function value above -1.0, the consideration of the strain rate dependent hardening marginally affects the distance of the most critical point ($\max(d_{FLC_i})$) to the forming limit curve.

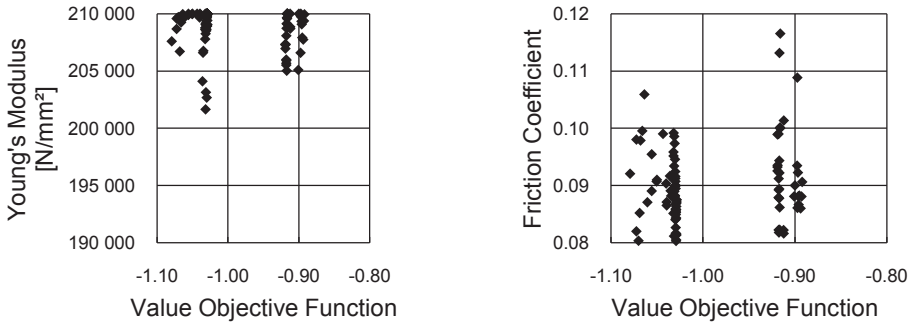

Figure 9.17: Hole extrusion experiment; Left: Relation between the Young's modulus and the objective function; Right: Relation between the friction coefficient and the objective function.

According to figure 9.17 (left), the choice of the Young's modulus does not affect the failure prediction. As the elastic strains are very small compared with the plastic ones, the elastic material behavior influences the total strain state only slightly, which explains the result of 9.17 (left). Also the friction coefficient

does not affect the prediction of the localized necking. A correlation between the objective function and the consideration of the kinematic hardening model is not recognizable (figure 9.18). This result is expected, as none of the material points undergo a change between tension and compression during the forming operation.

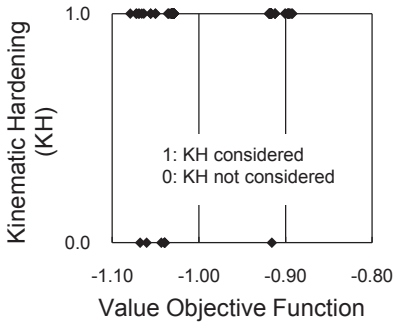

Figure 9.18: Hole extrusion experiment; Relation between the consideration of the kinematic hardening model and the objective function.

Due to the presented results, associated with the yield locus exponent equal to 8.0, a carefully identified material model is needed, in advance of the evaluation of this experiment.

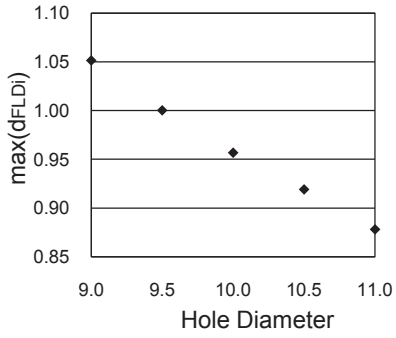

Figure 9.19: Hole extrusion experiment; Verification of the identified unknowns (table 8.19).

Figure 9.19 shows the prediction of the simulation on the basis of the identified unknown parameters as given by table 8.19. In comparison to the experimental study, the prediction of the simulation is slightly to optimistic. Consequently, the investigated FLC leads to a slight overestimation of the forming limit with respect to the investigated strain state, provided the constitutive laws reflect the material and frictional response well.

9.5 Discussion of the results

The results of the optimizations, shown in this chapter, confirm the choice of the unknown parameters, identified by the complementary experiments. The exponent of the yield locus and the friction coefficient have a negligible effect on the value of the objective function of the u-profile experiment. However, the consideration of the strain rate dependency of the hardening effect, the Bauschinger effect and the Young's modulus affect the prediction of the springback of this experiment. The investigations also show that the application of the analyzed kinematic hardening model should be complemented by a suitable model for considering the dependency of the Young's modulus with respect the plastic yielding. According to the above presented findings, the objective function of the cylindrical deepening experiment is sensitive concerning the yield locus exponent, the consideration of the strain rate dependency of the hardening effect and the friction coefficient. The consideration of the Bauschinger effect and the Young's modulus does not influence the predicted maximum drawing depth. The results of this experiment also show that such optimizations are not necessarily unimodal. The prediction of the smallest possible hole diameter of the hole extrusion experiment is primarily affected by the choice of the yield locus exponent.

9.6 Noise in numerical solutions

The u-profile, the cylindrical deepening and the hole extrusion experiment are investigated with respect to noise of the computed quantities, caused by the FEM simulation. The analysis is performed in the same way as introduced in chapter 8. None of the experiments shows remarkable fluctuations of the value of the introduced objective function values due to numerical noise.

9.7 Discussion of the experiments

9.7.1 U-Profile experiment

As mentioned above, the material flow of the simulation is adapted according to the experimentally determined one. The adaptation of the material flow is performed by applying artificial restraining forces. Based on experience, the correlation between the restraining force and the material flow in the binder zone is assumed to be linear. Therefore a Regula Falsi iteration is deployed for the determination of the restraining force, provided the d_{ESCD} deviates from the measured value. In consideration of the experimental conditions, it seems to be reasonable to allow deviations between the experimentally determined and the predicted d_{ESCD} of $\pm 0.5mm$. For example, even under laboratory conditions it is difficult to trim and to align the specimen with respect to the binder surface within the tolerance of $\pm 0.5mm$.

For the first simulation run, a value of the artificial restraining force has to be specified. Furthermore, for the adaption of the material flow, a tolerance regarding the d_{ESCD} needs to be defined and two trial restraining force values (upper and lower bound) have to be given. The choices of the mentioned quantities, applied in this thesis, are summarized in table 9.10.

Table 9.10: U-Profile experiment; Parameters of the material flow adjustment.

Lower Limit	$0.0N/mm$
Upper Limit	$20.0N/mm$
Tolerance d_{ESCE}	$\pm 0.5mm$

Provided, the first simulation run leads to a d_{ESCD} which is smaller than the experimentally determined one, another forming simulation is induced. In order to adjust the material flow a higher level of restraining force is needed. Consequently, the upper bound is taken as a trial. Originating from the d_{ESCD}, obtained from the second simulation, and the d_{ESCD} of the previous simulation an adjustment of the artificial restraining force is computed on the basis of Regula Falsi iteration. In the case the computed restraining force does not lead to the desired material flow, further adaptations of the restraining force can be computed by the Regula Falsi iteration. In the regular case, the upper value should lead to a d_{ESCD}, which is larger than the one of the experiment. Consequently, the Regula Falsi iteration can be applied for the determination of the root of the function f_{MFA} (MFA: Material flow adjustment), as given by

$$f_{MFA} = d_{ESCD_{ed}} - d_{ESCD_{sim}}. \tag{9.5}$$

Provided, the upper trial value is still not sufficient to obtain a larger d_{ESCD} as the experimentally determined one, the upper value is multiplicatively enlarged.

The trial value for the subsequent objective function evaluations is derived from the mean values of the previously applied artificial restraining forces. This procedure can be regarded as a simple learning strategy in order to avoid computing at least three forming simulations for each objective function evaluation. Figure 9.20 shows a comparison of the trial and the needed artificial restraining forces. Only 26% of the objective function evaluations are associated with an adjustment of the trial restraining force. Provided an optimization needs to be performed under the application of a similar material, the initial restraining force should be increased, according to the results shown by figure 9.20. The experimentally determined value of the d_{ESCD} is $43.0mm$. According to figure 9.21 (left), all the associated forming simulations of the objective function evaluations comply the above given tolerance. Figure 9.21 (right) summarizes the objective function evaluations, whose corresponding artificial restraining force is adjusted by the application of the Regula Falsi iteration. Without exception, the difference

between the d_{ESCD} value obtained from the forming simulation and the desired one is very small. Additionally, the adaption of the trial restraining force converged without investing more than three forming simulations (figure 9.22). The assumed linear relation between the material flow and the artificial restraining force is confirmed by this result. However, one has to bear in mind, that this linear relation is only valid for small changes of the restraining forces.

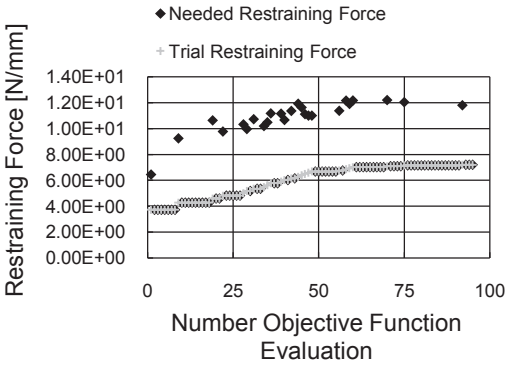

Figure 9.20: U-Profile experiment; Applied artificial restraining forces for the adjustment of the material flow.

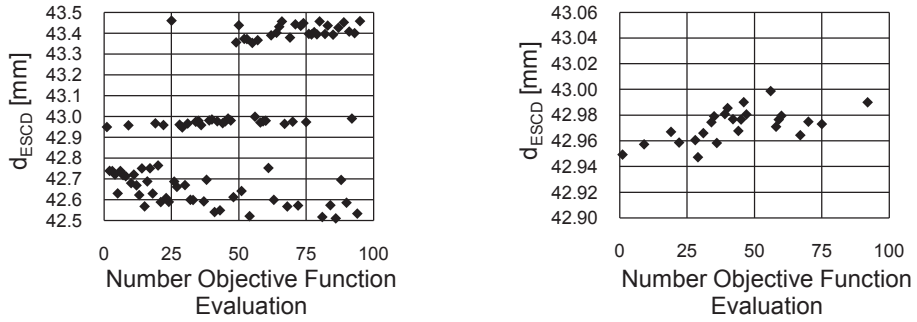

Figure 9.21: U-Profile experiment; Left: The corresponding value of the d_{ESCD} of each objective function evaluation; Right: Value of the d_{ESCD} of objective function evaluations comprising an adjustment of the artificial restraining force.

9.7.2 Cylindrical deepening experiment

Provided, the specimen is not clamped in the binder zone, the maximum drawing depth depends on the material flow in the binder zone. In this case the material flow of each objective function evaluation has to be adjusted to the experimentally

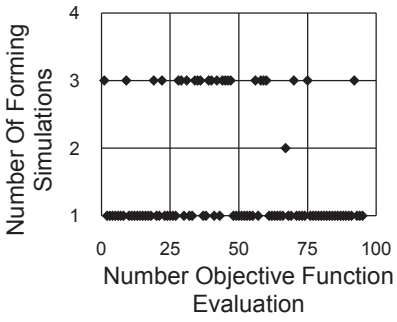

Figure 9.22: U-Profile experiment; Number of forming simulations per objective function evaluation.

determined one, as performed for the u-profile experiment. Additionally, the material flow also depends on the touching up procedure, which is very difficult to consider in the simulation model. For the u-profile experiment, spacers have been applied to avoid this effect. However, in this case spacers would cause strong wrinkles, which leads to unstable experimental data. Therefore, as mentioned in chapter 6, the specimen is clamped between the binder and the die. Consequently, the maximum drawing depth depends mainly on the formability of the material. However, as shown by the optimization, the friction, occurring in the interface between the specimen and the tool, affects the maximum possible drawing depth.

9.7.3 Hole extrusion experiment

Optical measurement systems enable to compute the strain field on the surface of the specimen based on the deformation of the measurement grid. The applied experimental equipment does not support an online measurement of the deformation. Therefore, only the strain field, associated with the state of the specimen after tool opening, can be considered. In this context the question arises, whether it would be possible to validate the forming limit curve directly by the strain field, derived from the optical measurement system. However, for the application of the forming limit curve, the strain field needs to be known at the midsurface, which cannot be determined without additional mechanical assumptions. Furthermore, the applied laser technology for inducing the measurement grid on the surface of the specimen leads to imperfections on the sheet metal surface, which affects the onset of localized necking.

For the comparison of the measured and the predicted strain state, localized necking should be avoided. An experimental analysis showed that the occurrence of localized necking can be avoided by choosing the hole diameter $d \geq 11mm$ (material: DX54).

Therefore, in this thesis the results of the optical measurement system are

only applied for the validation of the predicted strain field. The strain difference between the outer Gaussian integration point and the surface is neglected.

For obtaining an equivalent mechanical state of the specimen compared with the experiment, the forming simulation is complemented by a springback simulation. Figure A.7 shows the difference between the first and second principal strains. The prediction of the simulation is in good accordance with the experimentally determined strain field. However, deviations are visible in the highlighted zones. These deviations can be explained by the analysis of the measurement grid. The accuracy of the computed strain field is interfered in the highlighted zones, as the grid points are strongly distorted there. Therefore, the mentioned deviation should be an artifact.

Chapter 10

Uncertainties in the input data

For the investigations of the previous chapters, the quantities, derived from the fundamental experiments, are assumed to be given. These quantities will be referred to as input data in this chapter. However, their true values are unknown. In this context the question arises, whether the conclusions of the inverse determination regarding the yield locus parameters, the Young's modulus and the friction coefficient depend on the uncertainties of the input data. Additionally, the conformity between the simulation based predictions and the measured data of the validation experiments might also be affected by these uncertainties. Unfortunately, the determination of the confidence interval of the input data is very costly. Hence, the interval of the uncertainty is estimated on the basis of experience and the mean is assumed to be coincident with the measured values.

A possible solution for investigating this question could be a design of experiments (DOE) of the input data in the estimated range of their uncertainty. Thereby, for each variation of the input data, the unknowns (Young's modulus, yield locus parameters, friction coefficient) are inversely determined according to the introduced one-dimensional methods. For the identification of the yield locus parameters, the one-dimensional method might not be sufficient for other materials. Provided for the calibration of the yield locus an inverse identification of the yield locus exponent, the R_b value and the weighting of the input data are necessary, a multidimensional optimization needs to be performed. Such a procedure based on a design of experiments gives the sensitivity of the input data with respect to the inversely identified unknowns. These sensitivities allow evaluating the reliability of the inverse parameter identification. Provided, this evaluation leads to satisfying results, the validation experiments could be analyzed in the same way by computing the sensitivity of the uncertain input data with respect to the accordance between the simulation and experiment. For the treatment of the validation experiments, it seems to be reasonable to keep the inversely deter-

mined model parameters fixed, as this study is focused on the investigation of the uncertainty with respect to the input data. On the basis of such an investigation it can be assured, that the conclusions, derived from the validation experiments, do not strongly depend on the uncertainty of the input data. The needed input data depends on the choice of the material and friction model and its calibration procedure. Subsequently, the applied material model comprises a model for elasticity, the Barlat 2000 yield locus, an isotropic hardening and the consideration of the strain rate dependency of the hardening effect. The considered Coulomb friction law implies only one model parameter - the friction coefficient. This parameter is determined inversely by the friction experiment and, therefore, the input data does not contain any quantity regarding the friction model. The calibration of the Barlat 2000 yield locus is performed as given in chapter 7. From the chosen models and the calibration procedure of the yield locus follows a thirteen dimensional parameter space for the mentioned investigations (see table 10.1). In consideration of the commonly available hardware resources in an industrial environment and the chosen material model, such a procedure would be too expensive. If a material model and its calibration procedure needs less input quantities, the discussed approach could be affordable in terms of computational effort.

10.1 An optimization based approach

However, in this thesis, an approach is preferred, which is able to cope with all common material models and calibration procedures applied in the field of sheet metal forming simulations. Hence, another procedure is suggested. Instead of performing a design of experiment, an optimization problem can be formulated.

Table 10.1: Assumed tolerances of the input data.

Parameter	Tolerance	Parameter	Tolerance
σ_{u0°	$\pm 1\%$	m value	$\pm 2\%$
σ_{u45°	$\pm 1\%$	$\Delta\kappa(1.5)$ (Scaling Flow Curve)	$\pm 1\%$ w.r.t. $\kappa(1.5)$
σ_{u90°	$\pm 1\%$	ΔY (Shift Flow Curve)	$\pm 1\%$ w.r.t. Y_0
σ_b	$\pm 1\%$	υ (Poisson ratio)	$\pm 5\%$
σ_s	$\pm 1\%$	t_b (Blank Thickness)	$\pm 1\%$
R_{0°	$\pm 5\%$		
R_{45°	$\pm 5\%$		
R_{90°	$\pm 5\%$		

The parameter space of the optimization follows from the input data and the assumed uncertainties. The objective is to find a vector in the search space, which maximizes the deviation between the simulation result and the measured data of the considered experiments. The objective function, introduced for each experiment in the previous chapters, can be also applied for this optimization by

transforming the minimization into a maximization problem (see chapter 2). As a result, the worst case regarding the influence of the uncertainty of the input data on the conformity between the investigated experiment and the simulation based prediction is obtained. This approach is a compromise in order to analyze the quality of the inverse determined parameters by investing a minimum of computational effort.

For the validation experiments less computational effort is needed to analyze the sensitivity of the uncertainties with respect to the conformity between the simulation result and the measured data, as for each point in the parameter space only one simulation run is needed for obtaining the objective function value. However, today, the application of a DOE is in this case still too expensive and therefore also the same optimization based approach is applied for the validation experiments.

10.2 Treatment of the modified input data

Table 10.1 summarizes the input data, needed for the calibration of the chosen constitutive laws. Furthermore, this table shows the assumed uncertainties regarding the input data. The definition of β and ΔY is given below. The parameters of the yield locus are calibrated for each computation of the objective function before the forming simulation is performed. Consequently, any change of the input data concerning the calibration of the yield locus parameters is considered. The hardening effect is in this work described by a flow curve, which is given by discrete supporting points. It does not seem to be reasonable to include each point of the flow curve to the set of the input data. The corresponding dimension of the search space would grow enormously, depending on the amount of supporting points, which is usually greater than 10. Consequently, the flow curve is assumed to be given and the uncertainty with respect to the true value of the flow curve is reflected by two mapping operations, as given below. The first mapping, shown by

$$Y_{SHFC}(\epsilon^p, \Delta Y) = Y_0 + \Delta Y + \kappa\left(\epsilon^p\right), \tag{10.1}$$

is a shift of the flow curve ΔY parallel to the axis of the equivalent stress. This shift of the flow curve is introduced for modeling the uncertainty with respect to the determination of the yield strength (SHFC: Shift flow curve). The second mapping reflects the uncertainty regarding the slope of the experimentally determined flow curve. According to

$$Y_{SCFC}(\epsilon^p, \beta) = Y_0 + \beta\kappa\left(\epsilon^p\right),\ \beta = 1 + \frac{\Delta\kappa\left(\epsilon_r^p\right)}{\kappa\left(\epsilon_r^p\right)}, \tag{10.2}$$

the scaling operation is independent of the yield strength Y_0. Hence, both mapping operations are independent of each other. The scaling factor β is derived

from a given variation $\Delta\kappa$, which is defined with respect to a given equivalent plastic strain ϵ_r^p (SCFC: Scaling flow curve).

On the basis of the modified static flow curve, a set of flow curves representing each a specific strain rate is computed by applying the strain rate sensitivity model. As the m value is a parameter of the strain rate sensitivity model, the value of this parameter follows directly from the modified input data. Also the blank thickness t_b and the Poisson Ratio υ possess the same property. In this thesis, the uncertainty of the input data, needed for the identification of the model parameters of the kinematic hardening model, is not considered.

10.3 Investigation of the optimization algorithm

For performing the mentioned investigations, a suitable optimization algorithm needs to be chosen. Subsequently, the performance of the $(1, \lambda)$-DR-ES, the $(\mu/\mu, \lambda)$-CMA-ES, the $(1 + 1)$-CMA-ES and the SQP is compared on the basis of the YLIT-4-BMW experiment. It is assumed that the obtained findings are representative for this optimization task. Therefore, the chosen optimization algorithm is applied for the investigation of the other experiments. For the mentioned investigation, the unknown parameters of the friction and material model are chosen as given by table 8.19. Figure 10.1 shows the sequence of the optimizations.

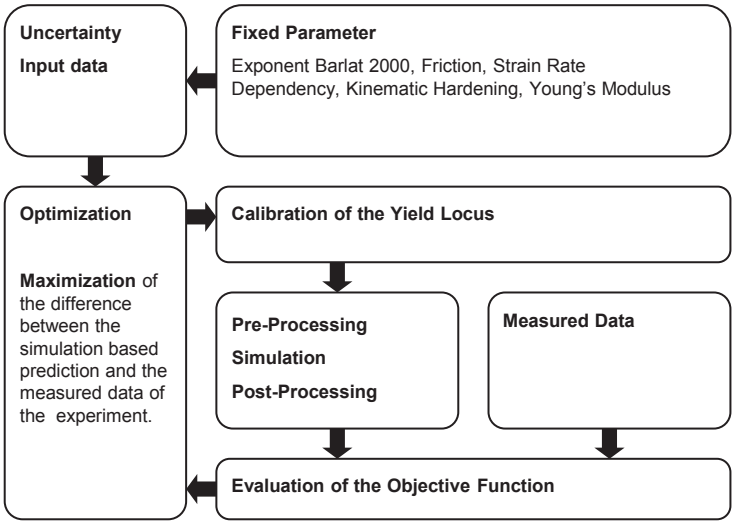

Figure 10.1: Sequence of the optimizations.

The figures 10.2 and 10.3 show the performance of the investigated optimization algorithms based on the YLIT-4-BMW experiment. Bearing in mind the

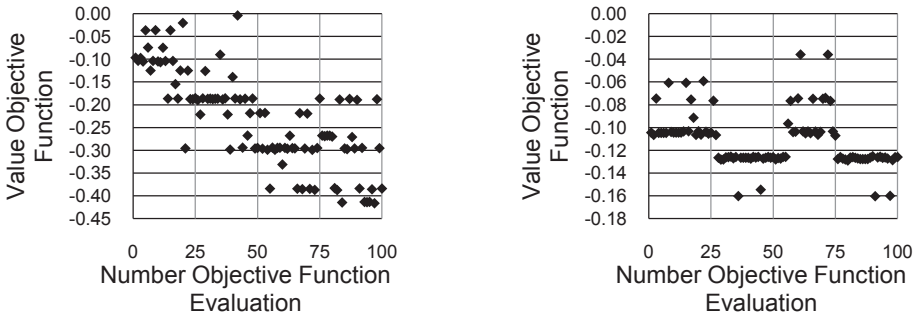

Figure 10.2: YLIT-4-BMW; Progression of the optimization; Left: Application of the $(1, \lambda)$-DR-ES algorithm; Right: Application of the SQP algorithm.

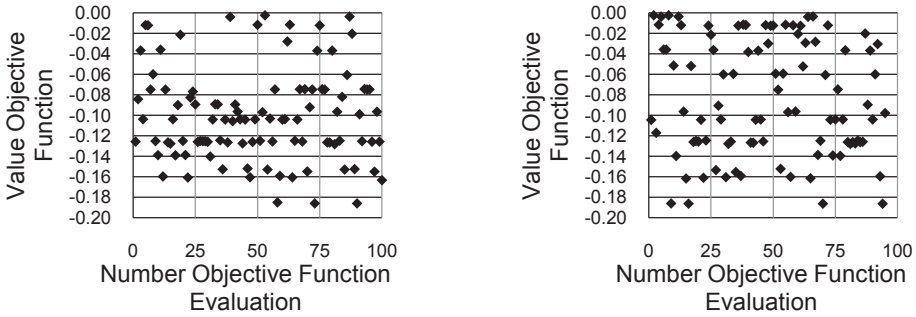

Figure 10.3: YLIT-4-BMW; Progression of the optimization; Left: Application of the $(\mu/\mu, \lambda)$-CMA-ES algorithm; Right: Application of the $(1 + 1)$-CMA-ES algorithm.

limited budget of 100 objective function evaluations, the $(1, \lambda)$-DR-ES is the best suitable procedure for this optimization task.

10.4 Experiments

For each experiment, the worst case, identified by this optimization approach, is compared with the prediction of the simulation implying the standard material and friction model calibration (table 10.2). In table 10.2 the absolute values of the objective function evaluations are given. As mentioned above, the uncertainty of the measured quantities has been assumed. Hence, a wider range of interval of the uncertainty could lead to worse results. The figures 10.2, 10.3, 10.4, 10.5 and 10.6 show the progression of the optimizations of the experiments. According to these figures, the computed worst case regarding the prediction of the measured data of each experiment should be reliable.

10.4.1 YLIT-4-BMW

Even with the worst possible set of measured quantities, obtained from the fundamental experiments, the results of the YLIT-4-BMW are predicted well (table 10.2). Consequently, the identified yield locus exponent gives satisfying results in the domain of the uncertainty of the fundamental experiments. A similar result is reported in [110], which is based on the experiment YLIT-1-TKSE.

10.4.2 Bending experiment

As shown by table 10.2, the prediction of springback is affected by the uncertainty of the input data. In addition, the springback of the specimen is also strongly affected by the gap width, as mentioned in chapter 9. Consequently, this experiment has to be performed very carefully, in order to exclude all known negative effects. However, this investigation shows, that the inverse determination of the Young's modulus cannot be performed highly accurate, as the difference between choosing the Young's modulus equal to $190000 N/mm^2$ and $210000 N/mm^2$ is $0.5°$ (see figure 8.37). Nevertheless, it seems to be better to derive a reduction of the Young's modulus based on the bending experiment than using the standard literature value of the Young's modulus. If the relation between the Young's modulus and the accumulated plastic strain is given, the bending experiment can serve as a validation experiment.

10.4.3 Friction experiment

The analysis of the friction experiment does not show a strong dependence of the uncertainty concerning the input data on prediction of the strain state at the reference position P. Therefore, according to this examination, this experiment is suitable for an inverse determination of the friction coefficient. But it has to

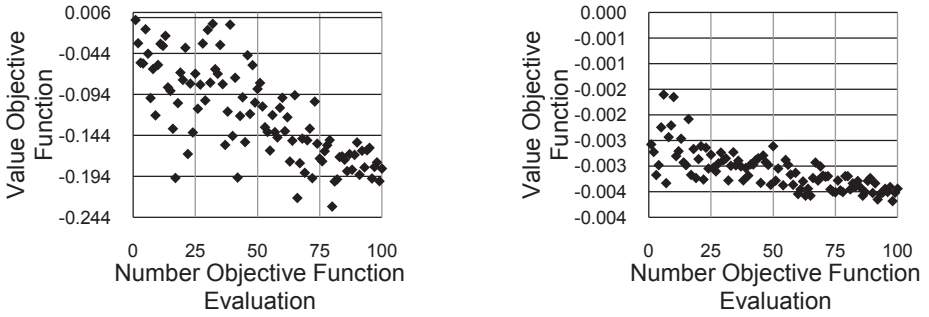

Figure 10.4: Progression of the optimization; Left: Investigation based on the bending experiment; Right: Investigation based on the friction experiment.

be mentioned that the objective of the friction experiment is not to calibrate the Coulomb model for press shop conditions. The friction coefficient is only needed for the simulation of the presented experiments.

10.4.4 U-Profile experiment

Table 10.2 does not show a strong effect of the uncertainty of the input data with respect to the predicted side wall curl. The deviation of the side wall rotation and the flange rotation between the standard model calibration and the worst case is larger. Consequently, a validation based on this experiment should take these uncertainties, induced by the input data, into account. This optimization is performed by the selection of the parameters as given by table 8.19. Consequently, the optimization is performed without taking the kinematic hardening effect into account. However, a similar result is expected if the stress-strain relation comprises the kinematic hardening model and the extrapolated relation between the accumulated plastic strain and the Young's modulus.

10.4.5 Cylindrical deepening experiment

As shown in table 10.2, the maximum deviation between the experimentally determined drawing depth and the predicted one is slightly higher than the one obtained from identified material model (see table 8.19). The optimization results show (figure 10.5 (right)) the existence of choices of the input data, belonging to the domain of uncertainty, which lead to a precise prediction of the drawing depth.

10.4.6 Hole extrusion experiment

The value of the objective function represents the distance (see chapter 9) of the most critical point in the principal in-plane strain space with respect to forming

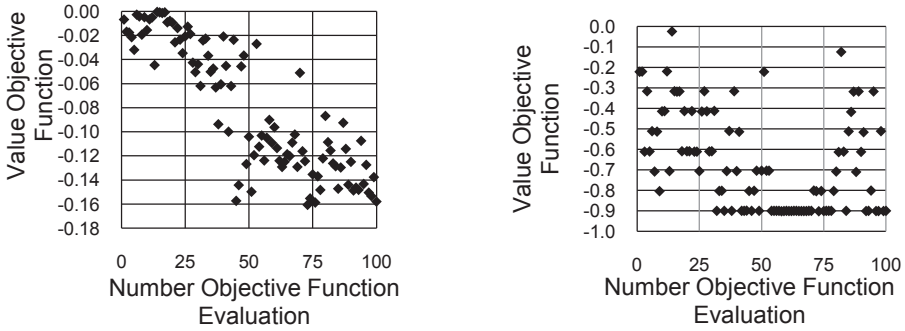

Figure 10.5: Progression of the optimization; Left: Investigation based on the u-profile experiment; Right: Investigation based on the cylindrical deepening experiment.

limit curve. According to table 10.2, the dependency of the objective function value with respect to the uncertainty of the input data is marginal.

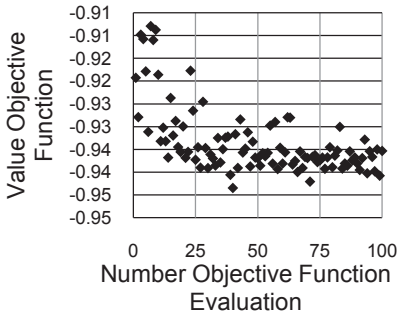

Figure 10.6: Progression of the optimization; Investigation of the hole extrusion experiment.

10.5 Summary

Generally, for the inverse determination of the unknown model parameters and the validation of constitutive laws the effect of the uncertainty with respect to the input data should be taken into consideration. Otherwise, the reliability of the investigations remains unknown. The prediction of the quantities, which are related to the springback effect shows the strongest sensitivity regarding the uncertainties of the input data (u-profile experiment, bending experiment). In consideration of the limited budget of objective function evaluations for the proposed optimization task the application of the $(1, \lambda)$-DR-ES is recommended.

Table 10.2: Summary of the investigations regarding the uncertainties of the input data.

Experiment	Type	Investigated Quantities				Value Objective Function
YLIT-4-BMW		RD/TD	ϵ_1	ϵ_2	d_{MDD} $[mm]$	
	Simulation	RD	0.409	-0.159	41.9	0.1033
		TD	0.400	-0.175	43.7	
	Simulation Worst Case	RD	0.411	-0.165	42.9	0.4169
		TD	0.402	-0.184	44.9	
	Measured Data	RD	0.397	-0.145	41.3	
		TD	0.429	-0.164	42.5	
Bending Experiment		Angle $\alpha[^\circ]$				
	Simulation	82.56				0.0066
	Simulation Worst Case	82.80				0.2309
	Measured Data	82.57				
Friction Experiment		ϵ_1	ϵ_2			
	Simulation	0.129	-0.089			0.00202
	Simulation Worst Case	0.129	-0.091			0.00369
	Measured Data	0.130	-0.088			
U-Profile Experiment		$\alpha_{SWR}[^\circ]$	$\alpha_{FR}[^\circ]$	$d_{SWC}[mm]$		
	Simulation	8.9	2.54	12.2		0.00548
	Simulation Worst Case	9.7	2.69	13.3		0.16055
	Measured Data	9	2.5	12		
Cylindrical Deepening Experiment		d_{MDD}[mm]				
	Simulation	23.8				0.8
	Simulation Worst Case	23.9				0.9
	Measured Data	23.0				
Hole Extrusion Experiment		$max\left(d_{FLC_i}\right)$				
	Simulation	0.919				0.919
	Simulation Worst Case	0.943				0.943

Chapter 11

Summary and outlook

This thesis is focused on constitutive laws, which are suitable for forming simulations in an industrial environment. For modeling the elasto-plastic material response, an elasticity model, a yield locus and a hardening model needs to be chosen. Additionally, the Bauschinger effect, the strain rate dependency of the hardening effect and the dependency of the Young's modulus with respect to plastic yielding might need to be taken into consideration. The completion of the material model by the consideration of the Bauschinger effect or the strain rate dependent hardening is interpreted as a boolean model parameter and is considered to be unknown. For reflecting the dependency of the Young's modulus with respect to plastic yielding, this model parameter is also treated as unknown. The frictional response between the sheet metal and the tool surface is described by the Coulomb model, which comprises one model parameter - the friction coefficient. In this context, this parameter is also assumed to be unknown.

For the identification of potentials regarding the improvement of the predictive capabilities of the forming simulation, additional experiments are necessary. The examination of these experiments can be performed by formulating optimization problems, which comprise an objective function quantifying the deviation between the simulation based prediction and the measured data. The task of the optimization is to search for a choice of the unknown model parameters, which leads to the best possible prediction of the measured data. The result of such an optimization is twofold: Firstly, the best possible predictive capability of the simulation based on the selected material model (elasticity model, yield locus and hardening law) is known by the variation of the unknown model parameters. Secondly, information regarding the sensitivity of the unknown model parameters with respect to the simulation based prediction is obtained. Thereby, the optimization based procedure assures the consideration of the interactions between the unknown model parameters. For this task, a $(1, \lambda)$-DR-ES is applied, which belongs to the group of evolutionary strategies. This algorithm allows treating integer-valued and real-valued object variables. Additionally, as this algorithm is based

on statistical methods, the $(1, \lambda)$-DR-ES allows combining the task of searching for an optimum and deriving information regarding the sensitivities of the object variables within a single optimization. Subsequently, the findings, obtained from this procedure are discussed.

The presented investigations based on the YLIT-Experiments show that the Barlat 2000 yield locus is advantageous compared with the widely applied Hill ´48 or Barlat ´89 yield locus for modeling the material response of the steel grade DX54. Unfortunately, the choice of the exponent of the Barlat 2000 model cannot be determined by the considered fundamental experiments. A disadvantageous choice of this exponent can lead to worse simulation based predictions than applying a simpler model like the Hill ´48. Therefore, a carefully performed validation has to precede the application of a complex yield locus like the Barlat 2000 for the forming simulation. A general ranking of the suitability with respect to industrial applications cannot be given, as other steel grades or aluminum alloys might be sufficiently described by a model comprising less model parameters like the Hill ´48. Basically, the Barlat ´89 also enables a satisfactory modeling of the material response in terms of the YLIT-Experiments. However, this yield locus does not reach the same level of quality concerning the reproduction of the measured stress and strain rate ratios, derived from the fundamental experiments, like the Barlat 2000 yield locus. Therefore, in this thesis the Barlat 2000 yield locus is preferred, as this model should give a better prediction of the material response for arbitrary stress states.

The analysis shows the need for taking the strain rate dependency of material hardening into account, if the Barlat 2000 yield locus is applied and the flow curve is entirely derived from the fundamental experiments. Otherwise, the simulations of the YLIT-Experiments show unsatisfactory predictions of the measured data. The investigation also shows the connection between modeling the material hardening and the yield locus. If the strain rate dependency of the material hardening is taken into account and the Hill ´48 yield locus is applied, the maximum drawing depth is overestimated. The yield locus Hill ´48 leads to better predictions concerning the YLIT-Experiments, if the strain rate dependency of the material hardening is not taken into account. However, one has to bear in mind that these findings are only valid for the chosen way of deriving the flow curve. The industrial relevance of the examinations based on the YLIT-Experiments is shown in [114] based on an industrial part (body side). This publication comprises an investigation of the influence of the choice of the yield locus, its exponent and the consideration of the strain rate dependency of the hardening on the prediction of the material thinning. Essentially, the findings derived from the YLIT-Experiments are confirmed by this study. For example the application of the Barlat 2000 yield locus without consideration of the strain rate dependency of the hardening effect leads to an unrealistic prediction of the material thinning.

Another effect, investigated in this thesis, is the dependency of the Young's modulus with respect to plastic yielding. Based on the bending experiment, the observations of Doege et al. can be confirmed. The bending experiment enables

to estimate a reduction of the Young's modulus with respect to the dimension of equivalent plastic strain induced by this experiment. The examination of the u-profile experiment showed, that this approach leads to an improved prediction of the springback. Using this reduced Young's modulus, the consideration of the Bauschinger effect worsens the prediction of the springback behavior of the u-profile. However, if a model is applied, which considers the non-linear dependency of the Young's modulus with respect to plastic yielding and the Bauschinger effect, a satisfying prediction of the springback of the u-profile can be obtained. Thereby, the relation between the Young's modulus and the accumulated plastic strain, which is taken from Doege et al., is extrapolated. For getting more insight into this issue, the determination of the Young's modulus with respect to the maximum expected level of accumulated plastic strain, occurring in industrial forming simulations, is necessary. However, this effect of the material response needs to be analyzed on the basis of another experiment. The inverse determination of the reduced Young's modulus based on the bending experiment, is only a simplified approach in order to improve the springback prediction. Furthermore, an experiment is needed, which shows a stronger sensitivity with respect to the Bauschinger effect.

For the description of the frictional response between the sheet metal and the tool surface, the Coulomb model is applied. The examination of this model is performed in order to describe the frictional response concerning the experimental conditions of the introduced experiments. Thereby, the friction coefficient is determined inversely based on the friction experiment. For an improved prediction of the frictional response under the press shop conditions, the applied model should take the temperature, the pressure and the relative velocities between the tool and the sheet metal in the contact interface into consideration. If such a model and its calibration is available, the introduced friction experiment can be applied for validation purpose.

The strain state, induced by the hole extrusion experiment cannot be easily obtained from the Nakajima test. However, a tensile test enables to create such a strain state. Therefore, the hole extrusion test can be performed to validate a forming limit curve, derived from the results of the Nakajima and the tensile test. This validation assures the right choice of the slope of the forming limit curve with respect to its left branch. The validation of the prediction of localized necking with respect to the plane strain state is of special importance as most of the industrial deep drawing parts fail by this strain state. Therefore, the validation of the predictive capability of the forming simulation is complemented by the cylindrical deepening experiment. The analysis of this thesis shows that the applied forming limit curve is able to reflect the failure mode localized necking sufficiently accurate with respect to the investigated strain states using the identified constitutive laws and their parameters. In other words, the prediction of the simulation is in accordance with the experimental observations concerning the onset of localized necking.

The sensitivities, obtained from the optimization based investigations, allow formulating a simplified inverse determination of the yield locus exponent of the Barlat 2000 yield locus, the reduction of the Young's modulus and the identification of the friction coefficient of the Coulomb model. Thereby, the determination of the yield locus exponent has to precede the identification of the Young's modulus and the friction coefficient. Provided the R_b value and the weighting of the stress and strain rate ratios, obtained from the fundamental experiments, are known, the search for the yield locus exponent is one dimensional. By applying the golden section interval division, within 7 objective function evaluations, a satisfying value of the yield locus exponent can be computed for the investigated material. The YLIT-Experiments also allow to determine the weighting of the input data and the R_b value. In this case the object variable space is 10 dimensional, if the Barlat 2000 yield locus is calibrated. As this search space is solely real valued, the $(1, \lambda)$-DR-ES, the $(\mu/\mu, \lambda)$-CMA-ES, the $(1+1)$-CMA-ES and the SQP algorithm are investigated. The best performance is obtained by applying the $(1, \lambda)$-DR-ES.

The inverse determination of the friction coefficient and the reduction of the Young's modulus can be performed simultaneously. In both cases, the dimension of the parameter space is one-dimensional. The best of the investigated methods for finding the friction coefficient is the Lagrange interpolation. The reduction of the Young's modulus can be efficiently determined by applying the Regula Falsi iteration. However, the friction coefficient as well as the reduction of the Young's modulus can be also efficiently determined by applying the golden section interval division. Generally, the result of the inverse determination of unknown parameters depends on the formulation of the universal and non-universal laws of nature and their numerical solution. Therefore, if possible, direct methods should be preferred. Provided, direct methods for the determination of the yield locus exponent, the Young's modulus and the friction coefficient are available, the introduced complementary experiments can serve as validation experiments.

The inversely identified unknown parameters should lead to the desired predictive capability of the constitutive laws. In order to analyze the quality of the chosen way of modeling the material and the frictional response, the predictions of the simulation and the measured data are compared on the basis of the validation experiments. Obviously, the calibrated constitutive laws are only satisfying, if they lead to a successful prediction of the measured data of all the validation experiments. As the amount of validation experiments is limited, the underlying validation should be interpreted as an indication of the predictive capability of the forming simulation. However, this procedure should not be regarded as proof of the general validity of the chosen constitutive laws, their calibration, the applied universal laws of nature and the associated numerical solution.

The measured data, obtained from the fundamental experiments is expected to deviate from the true values. For the investigation of the related consequences concerning the inverse determination of the discussed model parameters and the performed validations, an optimization based approach is suggested. Thereby, the

space of the object variables comprises all the measured data, obtained from the fundamental experiments. The objective of the optimization is to determine the worst possible simulation based prediction by considering the uncertainty with respect to results obtained from the fundamental experiments. For this investigation, the inversely determined unknowns are excluded from the search space. Provided, the worst possible prediction of the simulation still gives acceptable results, the influence of this uncertainty is assumed to be small. In this context, a general valid definition for the distinction between acceptable and unacceptable results cannot be given, as such a classification depends on the needed predictive capabilities of the forming simulation. As the associated search space of this optimization is real-valued, the performance of different optimization algorithms is compared. The best performance is obtained by applying the $(1, \lambda)$-DR-ES algorithm. Apart from the experiments related to the springback effect, none of the investigated experiments show a strong influence of the uncertainty of the input data with respect to the accordance between the simulation and the measured data, which confirms their desired field of application. However, the bending experiment can only give an estimation of the reduction of the Young's modulus in order to capture its dependency with respect to plastic yielding.

The presented results confirm that a stress-strain relation, consisting of a complex material model, does not necessarily lead to an improved accuracy of the forming simulation. All the known effects of the material response need to be analyzed in order to obtain the desired benefits from a complex model. Additionally, an extensive validation procedure is necessary in order to assure the functionality of the applied stress-strain relation. The $(1, \lambda)$-DR-ES shows the best performance with respect to the optimization tasks, presented in this thesis, among the investigated algorithms. An exception is the calibration of the Barlat 2000 yield locus, which seems to be an unimodal optimization problem within the investigated search space. Therefore, the application of the SQP in combination with an additive aggregation of the objectives is recommended for this task.

In this thesis, potentials and a procedure for the identification and validation of material models are shown, in order to maximize the benefit of the forming simulation. Additionally a method, for taking the uncertainties of the input data for the identification and validation of material models into account, is suggested.

11.1 Outlook

The most limiting factor for the presented investigations is the computational cost of the FEM simulations. In chapter 10 the effect of the uncertainty with respect to the input data on the identification and the validation of material models is examined. For this task the budget of 100 objective function evaluations is rather small. More objective function evaluations would be desirable in order to obtain a more reliable assessment of this issue.

The investigations of this thesis are limited to a single batch of the considered material. However, different batches of the same material might show scattering

material properties, which can for instance affect the feasibility of the parts and their springback behavior. For the consideration of fluctuating material properties in an industrial environment, a suitable compromise between the benefit of modeling this effect and the related additional cost has to be found, since it seems to be too expensive to perform the presented investigations for different batches of the same material.

The assumption of an isotropic hardening behavior might not be suitable for all steel grads and aluminum alloys, applied for a car body. Consequently the information regarding the material hardening with respect to different stress states obtained from the fundamental experiments, could be utilized for the calibration of enhanced material models. As a consequence, the shape of the yield locus changes depending on the material hardening. As the shape of the yield locus has a significant influence on the predicted strain and stress states, such a model needs to be validated very carefully. The findings, which result from the YLIT-Experiments, show that slight modifications of the yield locus shape can cause significant changes of the predicted strain state. The challenge of deploying a yield locus, which is able to consider the anisotropic hardening behavior, is to assure for any deformation history a meaningful response of the model. Possible mathematical models for taking an anisotropic hardening into account can be found in [115] and [101]. At this point one should also think of a non-associative flow rule, which would allow combining a simple flow potential with a complex yield locus. Such a model allows avoiding any negative side effects of a changing yield locus surface, caused by an anisotropic hardening law.

None of the presented experiments is highly sensitive with respect to the Bauschinger effect. Therefore, an additional experiment for the validation of a kinematic hardening model is required. Such a validation should also take into account that the Bauschinger effect especially affects the material response of material points, which undergo a non-linear strain path.

High strength steels can show apart from localized necking the failure modes shear and normal fracture. For the prediction of such failure modes the forming limit curve is not suitable. Hence, other failure criteria have to be deployed and the validation process has to be complemented by further experiments for assuring their predictive capability.

Today, theoretical physics is the best known method for predicting the behavior of the nature on the basis of few experimental observations. Nevertheless, the laws, given by theoretical physics are not equivalent to reality. Thereby, in the future, theoretical physics will only improve but will never be able to describe nature exactly. As the forming simulation is embedded in this theoretical frame work, one should never expect exact predictions from it.

Appendix A

Additional figures

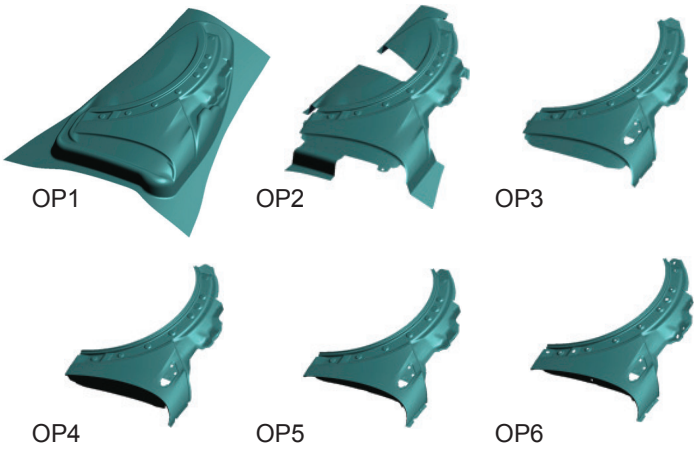

Figure A.1: Production process of a side panel.

Figure A.2: YLIT-Experiments; Left: Shape of the specimen of the YLIT-3-BMW after forming; Right: Shape of the specimen of the YLIT-4-BMW after forming.

Figure A.3: Bending experiment; The shape of the specimen after the bending operation.

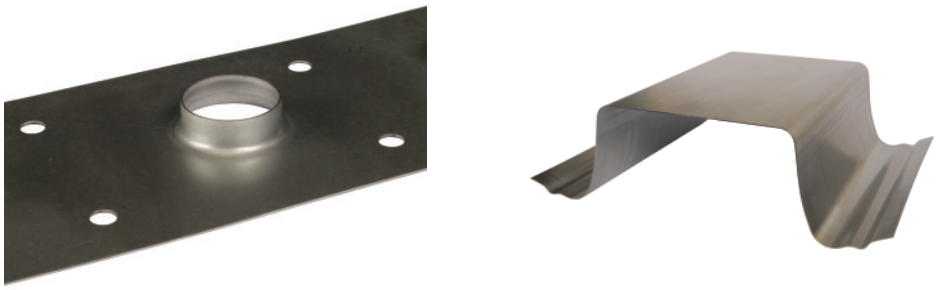

Figure A.4: Left: Hole extrusion experiment; The shape of the specimen after the forming operation; Right: U-Profile experiment; The shape of the specimen after the forming operation.

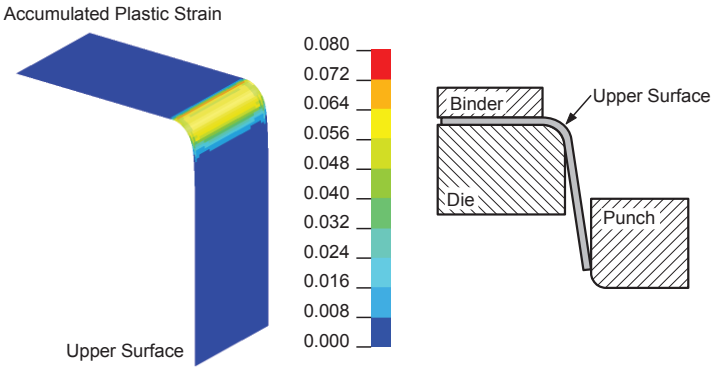

Figure A.5: Bending experiment; Field of the accumulated plastic strain on the upper surface.

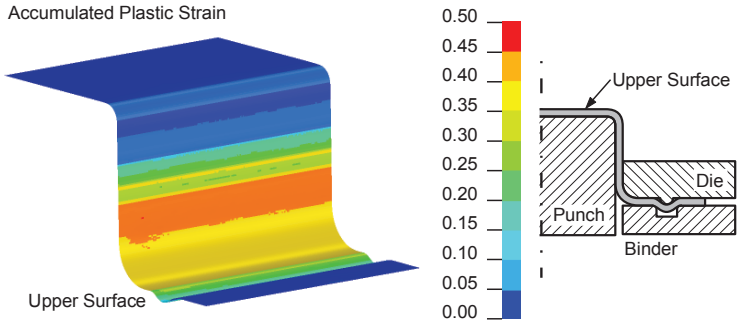

Figure A.6: U-Profile experiment; Field of the accumulated plastic strain on the upper surface.

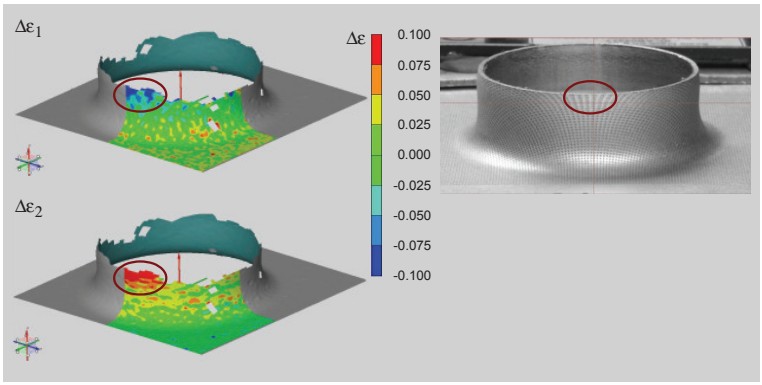

Figure A.7: Hole extrusion experiment; Comparison of the predicted and measured strain field.

Appendix B

Tensor analysis

The subsequently presented symbols and tensors are taken from [60], [62] and [116].

B.1 Symbols

$\cdot$	$\mathbf{a} \cdot \mathbf{b}$	Contraction of the inner indices; Example: $\mathbf{a}$ and $\mathbf{b}$ are vectors a_i, b_j; The contraction of the inner indices is identical with the scalar product $a_i b_i$.
:	$\mathbf{a} : \mathbf{b}$	Double contraction of the inner indices; Example: $\mathbf{a}$ and $\mathbf{b}$ are second-order tensors (a_{ij}, b_{kl}); The double contraction of the inner indices is given by $a_{ij} b_{ij}$.
$\otimes$	$\mathbf{a} \otimes \mathbf{b}$	Dyadic product; $\mathbf{a} \otimes \mathbf{b} := a_i b_j$
$tr\,(\bullet)$	$tr(\mathbf{a})$	Trace of a tensor; Example: For a second order tensor $\mathbf{a}$ the trace is given by $tr(\mathbf{a}) = a_{ii}$
$\|\bullet\|$	$\|\mathbf{a}\|$	L_2 Norm of a vector, which is the Euclidean distance and defined by $\|\mathbf{a}\| = \left(\sum_{i=1}^{n} a_i^2\right)^{\frac{1}{2}}$

B.2 Tensors

$(\mathbf{1})_{ij} = \delta_{ij}$	Second-order identity tensor; Example: For a vector $\mathbf{a}$, the following equation applies: $\mathbf{1a} = \mathbf{a}$.
$(\mathbf{I})_{ijkl} = \frac{1}{2}(\delta_{ik}\delta_{jl} + \delta_{il}\delta_{jk})$	Fourth-order symmetric identity; Example: For a second-order tensor $\mathbf{a}$, the relation $\mathbf{I} : \mathbf{a} = \mathbf{a} : \mathbf{I} = \mathrm{sym}(\mathbf{a})$ is valid.
$(\mathbf{1} \otimes \mathbf{1})_{ijkl} = \delta_{ij}\delta_{kl}$	For a second-order tensor $\mathbf{a}$, the identity satisfies $(\mathbf{1} \otimes \mathbf{1}) : \mathbf{a} = \mathrm{tr}(\mathbf{a})\,\mathbf{1}$.

Appendix C

Shape functions

As an example, the shape functions of an eight-node hexahedral element are given below [60]. Figure C.1 summarizes the constants of expression (C.1) and shows a visualization of the element.

$$N_{\mathbf{I}}(\boldsymbol{\xi}) = N_{\mathbf{I}}(\xi,\eta,\zeta) = \frac{1}{8}(1+\xi_{\mathbf{I}}\xi)(1+\eta_{\mathbf{I}}\eta)(1+\zeta_{\mathbf{I}}\zeta) \;; \qquad \mathbf{I} = 1,\ldots,8 \tag{C.1}$$

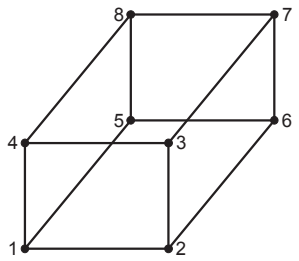

$\mathbf{I}$	$\xi_{\mathbf{I}}$	$\eta_{\mathbf{I}}$	$\zeta_{\mathbf{I}}$
1	-1	-1	-1
2	1	-1	-1
3	1	1	-1
4	-1	1	-1
5	-1	-1	1
6	1	-1	1
7	1	1	1
8	-1	1	1

Figure C.1: Left: Visualization of an eight-node hexahedral element; Right: Definition of the constants of the shape functions.

Appendix D

Numerical parameters LS-Dyna

All forming and springback simulations of this thesis are performed with the simulation system LS-Dyna. Table D.1 summarizes the choice of important numerial parameters.

Table D.1: Choice of numerical parameters.

Name Parameter	Value
Contact Tool/Specimen	
Geometric Boundary Condition	Soft 4
Dynamic Boundary Condition	Soft 0
Offset Type	Real
Shell Element Type	2
Integration Points In Thickness Direction	7
Type Integration In Thickness Direction	Gauss
Solution Scheme	
Forming Simulation	Explicit
Springback Simulation	Implicit

Bibliography

[1] C. Truesdell and W. Noll. *The Non-Linear Field Theories of Mechanics*. Springer Verlag, third edition, 2004.

[2] F. Barlat and J. Lian. "Plastic Behavior and Stretchability of Sheet Metals, Part I: A Yield Function for Orthotropic Sheets under Plane Stress Conditions". In *International Journal of Plasticity*, volume 5, pages 51–66, 1989.

[3] F. Barlat, J.W. Yoon, and O. Cazacu. "On Linear Transformations of Stress Tensors for the Description of Plastic Anisotropy". In *International Journal of Plasticity*, volume 23, pages 876–896, 2007.

[4] D. Banabic, H. Aretz, D.S. Comsa, and L. Paraianu. "An Improved Analytical Description of Orthotropy in Metallic Sheets". In *International Journal of Plasticity*, volume 21, pages 493–512, 2005.

[5] B. Plunkett, O. Cazacu, and F. Barlat. "Orthotropic Yield Criteria for Description of the Anisotropy in Tension and Compression of Sheet Metals". In *International Journal of Plasticity*, volume 24, pages 847–866, 2008.

[6] F. Yoshiha, T. Uemori, and K. Fujiwara. "Elastic-Plastic Behavior of Steel Sheets under In-Plane Cyclic Tension-Compression at Large Strain". In *International Journal of Plasticity*, volume 18, pages 633–659. Pergamon Press, 2002.

[7] J.L. Chaboche and G. Rousselier. "On the Plastic and Viscoplastic Constitutive Equations - Part I: Rules Developed with Internal Variable Concept". In *Journal of Pressure Vessel Technology*, volume 105, pages 153–158, 1983.

[8] R. Hill. "A Theory of the Yielding and Plastic Flow of Anisotropic Metals". In *Proceedings of the Royal Society of London, Series A*, volume 193, pages 281–297, 1948.

[9] R. Hill. "Constitutive Modelling of Orthotropic Plasticity in Sheet Metals". In *Journal of the Mechanics and Physics of Solids*, volume 38, pages 405–417, 1990.

[10] S. Thieme-Marti. *Mikrostrukturelle Modellierung des Kaltumformens einphasiger metallischer Werkstoffe*. PhD thesis, Eidgenössische Technische Hochschule Zürich, 1999.

[11] F. Barlat, D.J. Lege, and J. C. Brem. "A Six-Component Yield Function for Anisotropic Materials". In *International Journal of Plasticity*, volume 7, pages 693–712, 1991.

[12] E. Doege, H. Zenner, H. Palkowski, A. Hatscher, R. Schmidt-Jürgensen, S. Kulp, and C. Sunderkötter. "Influence of Elastic Material Characteristics on the Properties of Forming Parts". In *Materialwissenschaft und Werkstofftechnik*, volume 33, pages 667–672, 2002.

[13] T. Bäck. *Evolutionary Algorithms in Theory and Practice*. Oxford University Press, 1996.

[14] M.T.M. Emmerich. *Single- and Multi-Objective Evolutionary Design Optimization Assisted by Gaussian Random Field Metamodels*. PhD thesis, Universität Dortmund, 2005.

[15] Noesis Solutions. *OPTIMUS Theoretical Background*. 2008.

[16] M. Emmerich and A. Deutz. *Multicriteria Optimization and Decision Making: Principles, Algorithms and Case Studies*. LIACS Master Course, 2006.

[17] E. Zitzler, M. Laumanns, and L. Thiele. "SPEA2: Improving the Strength Pareto Evolutionary Algorithm". In *TIK-Report 103*, 2001.

[18] K. Deb, A. Pratap, S. Agarwal, and T. Meyarivan. "A Fast and Elitist Multi-Objective Genetic Algorithm: NSGA-II". In *IEEE Transactions on Evolutionary Computation*, volume 6, pages 182–197, 2002.

[19] N. Beume, B. Naujoks, and M. Emmerich. "SMS-EMOA: Multiobjective Selection Based on Dominated Hypervolume". In *European Journal of Operational Research*, volume 181, pages 1653–1669, 2007.

[20] C. Igel, N. Hansen, and S. Roth. "Covariance Matrix Adaptation for Multi-objective Optimization". In *Evolutionary Computation*, volume 15, pages 1–28, 2007.

[21] M. Ehrgott. *Multicriteria Optimization*. Springer Verlag, second edition, 2005.

[22] E.C. Harrington. "The Desirability Function". In *Industrial Quality Control 21*, pages 494–498, 1965.

[23] G. Derringer and R. Suich. "Simultaneous Optimization of several Response Variables". In *Journal of Quality Technology*, volume 12, pages 214–219, 1980.

[24] H.-P. Schwefel. *Evolution and Optimum Seeking*. Wiley, 1995.

[25] F. Jarre and J. Stoer. *Optimierung*. Springer Verlag, 2004.

[26] I.N. Bronstein, K.A. Semendjajew, G. Musiol, and H. Mühlig. *Taschenbuch der Mathematik*. Harri Deutsch Verlag, seventh edition, 2008.

[27] H.-G. Beyer and H.-P. Schwefel. "Evolution Strategies, A Comprehensive Introduction". In *Journal Natural Computing*, volume 1, pages 3–52, 2002.

[28] O.M. Shir. *Niching in Derandomized Evolution Strategies and its Applications in Quantum Control*. PhD thesis, University Leiden, 2008.

[29] A.E. Eiben and J.E. Smith. *Introduction to Evolutionary Computing*. Springer Verlag, second edition, 2007.

[30] R. Li. *Mixed-Integer Evolution Strategies for Parameter Optimization and their Applications to Medical Image Analysis*. PhD thesis, University Leiden, 2009.

[31] C.M. Bishop. *Pattern Recognition and Machine Learning*. Springer Verlag, 2007.

[32] H. Rinne. *Taschenbuch der Statistik*. Harri Deutsch Verlag, fourth edition, 2008.

[33] N. Hansen. "The CMA Evolution Strategy, A Tutorial". 2008.

[34] N. Hansen and A. Ostermeier. "Adapting Arbitrary Normal Mutation Distributions in Evolution Strategies: The Covariance Matrix Adaptation". In *Proceedings of the 1996 IEEE International Conference on Evolutionary Computation*, pages 312–317, 1996.

[35] A. Ostermeier, A. Gawelczyk, and N. Hansen. "A Derandomized Approach to Self Adaptation of Evolution Strategies". In *Evolutionary Computation*, volume 2, pages 369–380, 1994.

[36] A. Ostermeier. *Schrittweitenadaptation in der Evolutionsstrategie mit einem entstochastisierten Ansatz*. PhD thesis, Technische Universität Berlin, 1997.

[37] N. Hansen. *Verallgemeinerte individuelle Schrittweitenregelung in der Evolutionsstrategie*. PhD thesis, Technische Universität Berlin, 1998.

[38] L. Fahrmeir, R. Künstler, I. Pigeot, and G. Tutz. *Statistik*. Springer Verlag, sixth edition, 2007.

[39] D.F. Shanno. "Conditioning of Quasi-Newton Methods for Function Minimization". In *Mathematics of Computation*, volume 24, pages 647–656, 1970.

[40] E. Doege and B.-A. Behrens. *Handbuch Umformtechnik, Grundlagen, Technologien, Maschinen*. Springer Verlag, 2007.

[41] W.F. Hosford and R.M. Caddell. *Metal Forming Mechanics and Metallurgy*. Cambridge University Press, third edition, 2007.

[42] I. Heinle. *Automatisierte Verbesserung von Werkzeugziehanlagen durch Aufsprungsimulation*. Technische Universität München, 2002.

[43] J. Meinhardt, A. Lipp, I. Heinle, and M. Ganser. "Simulations- und Messdatenbasierte Rückfederungskompensation". In *Tagungsband des 29. EFB-Kolloquiums Blechverarbeitung*, 2009.

[44] M.L. von Schwerin, J. Meinhardt, and I. Heinle. "Entwicklung einer Methodik zur optimierten Gestaltung von Umformwerkzeugen". In *10. Workshop Simulation in der Umformtechnik*. Institut für Statik und Dynamik der Luft und Raumfahrtkonstruktionen, Universität Stuttgart, 2007.

[45] H. Hoffmann, J. Meinhardt, M.L. von Schwerin, and I. Heinle. "Die Prozesskette schließt sich beim Auslegen von Werkzeugen". In *Blech InForm*. Carl Hanser Verlag, 2007.

[46] M.L. von Schwerin. *Entwicklung einer Methodik zur optimierten Gestaltung von Umformwerkzeugen*. PhD thesis, Technische Universität München, 2008.

[47] H.-J. Bargel and G. Schulze. *Werkstoffkunde*. Springer Verlag, tenth edition, 2008.

[48] J. Lemaitre and J.-L. Chaboche. *Mechanics of Solid Materials*. Cambridge University Press, 1990.

[49] G. Backhaus. *Deformationsgesetze*. Akademie-Verlag, 1983.

[50] R. Hill. *The Mathematical Theory of Plasticity*. Oxford University Press, 1998.

[51] W. Schatt and H. Worch. *Werkstoffwissenschaft*. Deutscher Verlag für Grundstoffindustrie, eighth edition, 1996.

[52] K.G. Schmitt-Thomas. *Metallkunde für das Maschinenwesen, Band II: Gleichgewichts- und Ungleichgewichtszustände*. Springer Verlag, 1989.

[53] K. Lange. *Umformtechnik*. Springer Verlag, second edition, 1984.

[54] R.A. Higgins. *Engineering Metallurgy, Applied Physical Metallurgy*. Arnold, sixth edition, 1993.

[55] H. Schumann. *Metallographie*. Deutscher Verlag für Grundstoffindustrie, thirteenth edition, 1990.

[56] P. Stiaszny, A. Pichler, E. Tragl, H. Spindler, J. Szinyur, and M. Pimminger. "Höher- und höchstfeste Feinbleche: Legierungsdesign, Herstellrouten, Eigenschaften". In *Konferenz-Einzelbericht: Fügen von Stahlwerkstoffen*, pages 21–53, 2001.

[57] A. Spalek. *Entwicklung eines Prüfstandards zur Beurteilung des Bruchverhaltens schlagartig beanspruchter Tiefziehteile aus IF-Stählen*. PhD thesis, Technische Universität München, 2002.

[58] S. Traint. *Phase Transformations and Mechanical Properties of Low Alloyed Dual-Phase and TRIP-Steels*. PhD thesis, Technische Universität München, 2002.

[59] P. Haupt. *Continuum Mechanics and Theory of Materials*. Springer Verlag, second edition, 2002.

[60] T. Belytschko, W. K. Liu, and B. Moran. *Nonlinear Finite Elements for Continua and Structures*. Wiley, 2006.

[61] J.C. Simo and T.J.R. Hughes. *Computational Inelasticity*. Springer Verlag, second edition, 2000.

[62] E.A. de Souza Neto, D. Peric, and D.R.J. Owen. *Computational Methods for Plasticity, Theory and Applications*. Wiley, 2008.

[63] F. Barlat, J.C. Brem, J.W. Yoon, K. Chung, R.E. Dick, D.J. Lege, F. Pourboghrat, S.-H. Choi, and E. Chu. "Plane Stress Yield Function for Aluminum Alloy Sheets-Part 1: Theory". In *International Journal of Plasticity*, volume 19, pages 1297–1319, 2003.

[64] A.K. Sachdev and R.H. Wagoner. "Uniaxial Strain Hardening at Large Strain in Several Sheet Steels". In *Journal of Applied Metalworking*, volume 3, pages 32–37, 1983.

[65] H. Lanzerath, A. Bach, R. Schilling, G. Oberhofer, and H. Gese. "Failure Prediction of Hot-Formed Steels in Crash". In *VDI Report*, pages 599–624, 2006.

[66] P. Larour. *Strain Rate Sensitivity of Automotive Sheet Steels: Influence of Plastic Strain, Strain Rate, Temperature, Microstructure, Bake Hardening and Pre-Strain*. PhD thesis, Rheinisch-Westfälische Technische Hochschule Aachen, 2010.

[67] G.R. Cowper and P.S. Symonds. "Strain Hardening and Strain Rate Effects in the Impact of Loading of Cantilever Beams". In *Brown University Appl. Math. Report*, volume 28, pages 1–46, 1958.

[68] G.R. Johnson and W.H. Cook. "A Constitutive Model and Data for Metals Subjected to Large Strains, High Strain Rates and High Temperatures". In *Proceedings of the 7th International Symposium on Ballistics*, pages 541–547, 1983.

[69] P.J. Armstrong and C.O. Frederick. "A Mathematical Representation of the Multiaxial Bauschinger Effect". C.e.g.b. report rd/b/n 731, Berkeley Nuclear Laboratories, 1966.

[70] A. Krasovskyy. *Verbesserte Vorhersage der Rückfederung bei der Blechumformung durch weiterentwickelte Werkstoffmodelle*. PhD thesis, Universität Karlsruhe, 2005.

[71] P. Wriggers. *Computational Contact Mechanics*. Springer Verlag, second edition, 2006.

[72] P. Börner. *Statik, einschl. Reibung*. Georg Westermann Verlag, fifth edition, 1967.

[73] H.-J. Förster. *Statik, Reibung*. Carl Hanser Verlag, 1968.

[74] M. Steinicke. *Modifiziertes Reibgesetz für die Finite-Elemente-Simulation des Tiefziehens*. PhD thesis, Universität Stuttgart, 2003.

[75] P. Hora, T. Longchang, and J. Reissner. "Prediction Methods for Ductile Sheet Metal Failure using FE-Simulation". In *IDDRG*, 1994.

[76] P. Hora. *Numerische Simulationsmodelle zur Voraussage des Versagens bei duktilen Blechwerkstoffen*. PhD thesis, Eidgenössische Technische Hochschule Zürich, 1990.

[77] H. Gese and H. Dell. "Macroscopic and Mesoscopic Models for Fracture in Sheet Metal Forming". In *Procceding of Euromat*, volume 3. Wiley-VCH, 1999.

[78] S.P. Keeler. "Determination of Forming Limits in Automotive Stampings". In *Society of Automotive Engineers*, 1965.

[79] G.M. Goodwin. "Application of Strain Analysis to Sheet Metal Forming Problems in the Press Shop". In *Society of Automotive Engineers*, 1968.

[80] Z. Marciniak, J.L. Duncan, and S.J. Hu. *Mechanics of Sheet Metal Forming*. Butterworth-Heinemann, second edition, 2002.

[81] K. Nakazima, T. Kikuma, and K. Hasuka. "Study on the Formability of Steel Sheets". In *Yawata Technical Report, No. 284*, 1968.

[82] Z. Marciniak and K. Kuczynski. "Limit Strains in the Processes of Stretch-Forming Sheet Metal". In *Int. J. Mech. Sci.*, volume 9, pages 609–620. Pergamon Press, 1967.

[83] P. Wriggers. *Nichtlineare Finite-Element-Methoden*. Springer Verlag, 2001.

[84] T.J.R. Hughes. *The Finite Element Method*. Dover Publications, 2000.

[85] K.-J. Bathe. *Finite-Elemente-Methoden (Aus dem Englischen übersetzt von Peter Zimmermann)*. Springer Verlag, second edition, 2002.

[86] Y. Okan. *Sensitivity Analysis of Process- and Material Parameters of Elastic Springback in Car Components and Experimental Validation of the Results*. Technische Universität München, 2005.

[87] M. Bischoff. *Theorie und Numerik einer dreidimensionalen Schalenformulierung*. PhD thesis, Universität Stuttgart, 1999.

[88] M. Fleischer. *Absicherung der virtuellen Prozesskette für Folgeoperationen in der Umformtechnik*. PhD thesis, Technische Universität München, 2009.

[89] W. Panknin. *Der hydraulische Tiefungsversuch und die Ermittlung von Fließkurven*. PhD thesis, Technische Hochschule Stuttgart, 1959.

[90] S. Keller, W. Hotz, and H. Friebe. "Yield Curve Determination using the Bulge Test Combined with Optical Measurement". In *International Deep Drawing Research Group IDDRG, International Conference*, 2009.

[91] W. Volk, I. Heinle, and H. Grass. "Accurate Determination of Plastic Yield Curves and an Approximation Point for the Plastic Yield Locus with the Bulge Test". In *Proceedings of the 10^{th} International Conference on Technology of Plasticity, ICTP*, pages 799–804, 2011.

[92] A.D. Santos, P. Teixeira, A. Barata da Rocha, and F. Barlat. "On the Determination of Flow Stress Using Bulge Test and Mechanical Measurement". In *NUMIFORM 2010: Proceedings of the 10^{th} International Conference on Numerical Methods in Industrial Processes*, pages 845–852, 2010.

[93] W. Volk and I. Heinle. "New Approach for the Evaluation of Plastic Flow Curves for Large Strains with the Bulge Test". In *IV European Conference on Computational Mechanics*, 2010.

[94] A. Mutrux, B. Hochholdinger, and P. Hora. "A Procedure for the Evaluation and Validation of the Hydraulic Biaxial Experiment". In *Numisheet*, 2008.

[95] H. Aretz and S. Keller. "On the Non-Balanced Biaxial Stress State in Bulge-Testing". In *Steel Research International*. Wiley-VCH Verlag, 2011.

[96] K. Miyauchi. "A Proposal of a Planar Simple Shear Test in Sheet Metals". In *Scientific Papers of the Institute of Physical and Chemical Research*, volume 78, 1984.

[97] W. Hotz and J. Timm. "Experimental Determination of Forming Limit Curves (FLC)". In *Numisheet*, 2008.

[98] W. Volk and P. Hora. "New Algorithm for a Robust User-Independent Evaluation of Beginning Instability for the Experimental FLC Determination". In *Int. J. Material Forming*. Springer Verlag, 2011.

[99] I. Heinle, L. Kessler, T. Beier, H. Grass, J. Meinhardt, A. Lipp, and T. Bäck. "Challenges in Validation of Material Modeling for Forming Simulations". In *Proceedings AutoMetForm*, pages 83–99, 2010.

[100] L. Kessler, H. Gese, G. Metzmacher, and H. Werner. "An Approach to Model Sheet Failure after Onset of Localized Necking in Industrial High Strength Steel Stamping and Crash Simulations". In *SAE International*, 2008.

[101] H. Dell, H. Gese, and G. Oberhofer. *Users' Manual, MF GenYld + CrachFEM 3.8 Theory*. 2008.

[102] P. Ludwik. *Elemente der Technologischen Mechanik*. Springer Verlag, 1909.

[103] J.E. Hockett and O.D. Sherby. "Large Strain Deformation of Polycrystalline Metals at low Homologous Temperatures". In *Journal of the Mechanics and Physics of Solids*, volume 23, pages 87–98, 1975.

[104] H.W. Swift. "Plastic Instability under Plane Stress". In *Journal of the Mechanics and Physics of Solids*, volume 1, pages 1–18, 1952.

[105] E. Voce. "The Relationship between Stress and Strain for Homogeneous Deformation". In *J. Int. Metals*, volume 74, pages 537–562, 1948.

[106] O.W. Wetzell. *Wendehorst, Bautechnische Zahlentafeln*. B.G.Teubner, 27th edition, 1996.

[107] S. Thibaud, N. Boudeau, and J.-C. Gelin. "On the Influence of the Young's Modulus Evolution on the Dynamic Behavior and Springback of a Sheet Metal Forming Component". In *Numisheet*, 2002.

[108] J. Meinhardt, A. Lipp, H. Grass, I. Heinle, and T. Bäck. "Identification and Validation of Material Descriptions". In *Tagungsband des 30. EFB-Kolloquiums Blechverarbeitung*, 2010.

[109] J. Gerlach, T. Beier, L. Kessler, H. Grass, I. Heinle, and A. Lipp. "Identification and Validation of Yield Locus Parameters with respect to Industrial Forming Simulation Needs". In *Special Edition: 10^{th} International Conference on Technology of Plasticity, ICTP*, pages 732–737, 2011.

[110] T. Bäck, L. Kessler, and I. Heinle. "Evolutionary Strategies for Identification and Validation of Material Model Parameters for Forming Simulations". In *Proceedings Genetic and Evolutionary Computation Conference*, pages 1779–1786, 2011.

[111] W. Beitz and K.-H. Grote. *Dubbel Taschenbuch für den Maschinenbau*. Springer Verlag, 19th edition, 1997.

[112] M. Dyduch, A.M. Habraken, and S. Cescotto. "Automatic Adaptive Remeshing for Numerical Simulations of Metal Forming". In *Computer Methods in Applied Mechanics and Engineering*, volume 101, pages 283–298, 1992.

[113] M. Gee. *Remeshing für Finite Elemente Berechnungen mit großen Deformationen*. Universität Stuttgart, 1999.

[114] L. Kessler, J. Gerlach, T. Beier, H. Grass, I. Heinle, and A. Lipp. "Possibilities, Challenges and Risks in Creating Material Cards for Forming Simulations". In *Numisheet*, 2011.

[115] P. Hora, B. Hochholdinger, A. Mutrux, and L. Tong. "Modeling of Anisotropic Hardening Behavior based on Barlat 2000 Yield Locus Description". In *Forming Technology Forum*, 2009.

[116] H. Schade and K. Neemann. *Tensoranalysis*. Walter de Gruyter, second edition, 2006.

Samenvatting

In het afgelopen decennium is de toepassing van simulatie op basis van de eindige-elementenmethode (EEM) in de auto-industrie uitgegroeid tot een evaluatiestandaard voor metaalplaatvormingsprocessen. De technische en economische voordelen van simulatie op EEM-basis hangen sterk af van de nauwkeurigheid van de berekende voorspelling. Het voorspellend vermogen van simulaties op EEM-basis wordt in hoofdzaak bepaald door de gekozen natuurkundige theorie en de numerieke oplossing ervan. Deze dissertatie richt zich met name op materiaalmodellen die tot de groep der constitutieve wetten behoren. Voor elk materiaal moet een specifiek materiaalmodel worden aangewezen en geijkt. Dit materiaalmodel geeft de respons weer van de materie van een mechanisch systeem dat onder invloed van krachten wordt vervormd. In de afgelopen decennia is een variëteit aan materiaalmodellen voorgesteld om het elastoplastische materiaalgedrag van een metaalplaat te modelleren. Voor het kiezen van een materiaalmodel voor een gegeven materiaal is helaas geen algemene aanbeveling voorhanden. Dit werk heeft een drieledig doel: ten eerste het vaststellen van het potentieel van de materiaalmodellen teneinde het voordeel van de EEM-vormgevingssimulatie te maximaliseren; ten tweede het ontwikkelen van een identificatie- en validatieproces voor materiaalmodellen; en ten derde het onderzoeken welk effect de afwijkingen tussen de gemeten gegevens en de werkelijke waarden van de ijkexperimenten hebben op het voorspellend vermogen van materiaalmodellen.

De in dit werk geïntroduceerde experimenten zijn ontworpen ten behoeve van het onderzoek van materiaalmodellen en hun modelparameters. Onder ideale omstandigheden vertoont ieder experiment een andere gevoeligheid ten aanzien van het materiaalmodel en de daarmee samenhangende parameters voor het voorspellen van de gemeten grootheden. Deze gewenste eigenschap van de experimenten moet echter gewaarborgd zijn. Over het algemeen is het lastig om al deze gevoeligheidswaarden uitsluitend met theoretische beschouwingen te voorspellen. Op basis van de vastgestelde gevoeligheidswaarden en de kennis omtrent de keuze van de modelparameters die tot een nauwkeurige voorspelling van de meetgegevens leiden, kan men de onderzochte experimenten selecteren ten behoeve van identificatie en validatie van het geselecteerde materiaalmodel. Ter bepaling van de gewenste informatie kan een optimalisatieprobleem worden geformuleerd. Het doel is om de afwijking tussen de voorspelling van de simulatie

en de meetgegevens zo klein mogelijk te maken door de best mogelijke keuze van modelparameters te zoeken. Een tweede component van deze oplossing is het toepassen van evolutiestrategieën. Aangezien deze optimalisatiealgoritmen op statistische methoden berusten, wordt ook informatie over de gevoeligheid van de modelparameters gegeven.

Volgens de gepresenteerde resultaten leidt een complex materiaalmodel niet noodzakelijkerwijs tot grotere nauwkeurigheid van de vormgevingssimulatie. In deze dissertatie wordt bijvoorbeeld aangetoond dat het complexe vloeioppervlak volgens Barlat 2000 gunstig kan zijn in vergelijking met het veelgebruikte vloeioppervlak volgens Hill ´48 voor het modelleren van de materiaalrespons van staalkwaliteit DX54. De keuze van de exponent van het Barlat 2000-model kan meestal niet door de standaard ijkexperimenten worden bepaald. Deze parameter heeft helaas invloed van betekenis op het voorspellend vermogen van het materiaalmodel. Dit onderzoek toont aan dat het vloeioppervlak volgens Barlat 2000 zijn voordelen kwijtraakt als deze modelparameter ongeschikt wordt gekozen. De gevoeligheidswaarden die zijn verkregen uit op optimalisatie gebaseerde onderzoekingen in combinatie met een geschikt experiment, maken het mogelijk om een vereenvoudigde inverse bepaling van de vloeioppervlakexponent van het vloeioppervlak volgens Barlat 2000 te formuleren. Behalve de vloeioppervlakexponent worden ook andere modelparameters en uitbreidingen van het materiaalmodel in beschouwing genomen. Het beste voorspellende vermogen van de vormgevingssimulatie wordt verkregen als alle relevante effecten van de materiaalrespons door het materiaalmodel in beschouwing worden genomen.

Om de functionaliteit van het toegepaste materiaalmodel te waarborgen is een uitgebreide validatieprocedure noodzakelijk. Het geijkte materiaalmodel is pas bruikbaar als het een geslaagde voorspelling van de meetgegevens van alle validatie-experimenten oplevert. Aangezien het aantal validatie-experimenten beperkt is, moet de onderliggende validatie worden geïnterpreteerd als een indicatie van het voorspellend vermogen van de vormgevingssimulatie. Deze procedure mag echter niet worden gezien als een bewijs van de algemene validiteit van het gekozen materiaalmodel, de ijking daarvan, de overige mechanische wetten en de daarmee samenhangende numerieke oplossing.

De uit de ijkexperimenten verkregen meetgegevens zullen naar verwachting van de werkelijke waarden afwijken. Voor het onderzoek van de daarmee verband houdende gevolgen wat betreft de identificatie van het materiaalmodel en de ijking van de parameters daarvan wordt een op optimalisatie gebaseerde benadering voorgesteld. Het doel van de optimalisatie is om de voorspelling op basis van de slechtst mogelijke simulatie te bepalen door de onzekerheid ten aanzien van de uit de ijkexperimenten verkregen resultaten in beschouwing te nemen. Dit onderzoek toont aan dat men de kwaliteit van de inverse bepaling van modelparameters en de validatie van materiaalmodellen met deze procedure kan beoordelen.

Wat de in deze dissertatie gepresenteerde optimalisatietaken betreft, laat de $(1, \lambda)$-DR-ES onder de onderzochte algoritmen het beste resultaat zien. Een uitzondering vormt de ijking van het vloeioppervlak volgens Barlat 2000, welke een unimodaal optimalisatieprobleem binnen de onderzochte zoekruimte lijkt te zijn.

About the Author

Ingo Heinle, was born on Dezember 1st 1975 in Augsburg, Germany. His pre-university education lasted from 1982 to 1995 at the institutions Volksschule Neusäß, Realschule Neusäß and Staatliche Fachoberschule Augsburg. He studied civil engineering at the University of Applied Science of Augsburg and the Technical University of Munich. He received his diploma degree in civil engineering from the Technical University of Munich in 2002.

He began his professional career in 2002 at department of forming technology of the BMW Group as a computational engineer. He performed feasibility studies of forming tools in the early phase of the product development. Later, he coordinated the engineering of production processes within the department of forming technology. Afterwards, he developed processes including the corresponding automations for the compensation of the elastic springback of sheet metal parts and the prediction of press forces. Furthermore, he was engaged in research for the computation of the correspondence between CAD surfaces, the prediction of the elastic deformation of tools during the forming process and the computation of the geometry of assemblies in consideration of the elastic material behavior of parts. Today, he is responsible for the research in the fields of material modeling, springback compensation and press force computation. He is also a member of working groups for the standardization of experiments in the field of sheet metal processing.

Since 2008, he is a member of the group of Prof. Thomas Bäck as an external PhD student.

His current topics of interest include Optimization Methods, FEM Simulation, Material Modeling and Validation of Simulation Systems.